ScuDo
Scuola di Dottorato ~ Doctoral School
WHAT YOU ARE, TAKES YOU FAR

Doctoral Dissertation
Doctoral Program in Electronics Engineering (30^{th}cycle)

Where Integrated Electronics Meets Bio/Micro-Technology

From Synthetic Microstructures to Living Cells On-Chip

By

Beatrice Miccoli

******

Supervisor(s):
Prof. Danilo Demarchi
Prof. Fabrizio Candido Pirri

Doctoral Examination Committee:
Prof. Ayça Bal Öztürk , Referee, Istinye University
Dr. Luca Boarino, Referee, National Institute of Metrological Research (INRIM)
Prof. Marco Mazza, University of Applied Science - Western Switzerland
Prof. Valeria Chiono, Polytechnic of Turin
Dr. Luca Berdondini, Italian Institute of Technology (IIT)

Politecnico di Torino
2018

Declaration

I hereby declare that, the contents and organization of this dissertation constitute my own original work and does not compromise in any way the rights of third parties, including those relating to the security of personal data.

Beatrice Miccoli
2018

* This dissertation is presented in partial fulfillment of the requirements for **Ph.D. degree** in the Graduate School of Politecnico di Torino (ScuDo).

*"We give the name **scientist** to the type of man who has felt **experiment** to be a means guiding him to search out the deep truth of **life**, to lift a veil from its fascinating **secrets**, and who, in this pursuit, has felt arising within him a **love** for the mysteries of **nature**, so **passionate** as to annihilate the thought of himself".*

– M. Montessori
The Montessori Method,
Ch. 1, p. 8, **1912**.

Acknowledgements

The presented Ph.D. activity was for me one of the most exciting periods of my life and I will always remember it with happiness and a lot of emotion.

At first, I would like to genuinely thank my supervisor, Professor Danilo Demarchi, for welcoming me in his research group and for allowing me to do this extraordinary experience. Despite being a scientific supervisor, he was also a reference and mentor that I know I can always count on. Then, I'd like to deeply thank also all the colleagues that had to bear me during my research activity starting firstly with Dr. Alessandro Sanginario that has been another fundamental pillar of my research activity. I want to really thank him for his patience in helping me anytime I need, for listening to all my ideas and suggestion (even the bad ones) and for always being there for me. I would then like to continue by thanking Prof. Valentina Cauda for the unlimited scientific and personal support, Luisa Delmondo and Francesco Trevisan for sharing with me this amazing experience, and making me laugh also in the most stressful periods, Antonia Silvestri for being a trustworthy friend in addition to a great colleague, Dr. Giancarlo Canavese for the feedback on the thesis, and all the other people that in one way or in the other shared with me this path.

I would also like to acknowledge Professor Ali Khademhosseini and Dr. Su Ryon Shin for giving me the possibility to work to one of the most exciting project of my life and for initiating me to the world of cardiac cells. I want to devote a special thank to the irreplaceable friends, more than only colleagues, that I had to chance to meet and work with in Boston: Aica, my favorite laboratory mate and best friend, Ethan for the exquisite friendship and inexhaustible support, Emine, Ting, Serena, Xiaoyung, Elmira, Chiara, Alessandra, and all the others.

The time I spent in the group of Dr. Berdondini was also exciting and extremely scientifically fruitful. I would love to thank Luca and all is group for the warm welcome in their group especially Fabio, Giannicola, Hyder, Alessandro, Ermanno,

Stefano, Lidia, Marina and Davide. It was really a pleasure to be part of their group for few months.

I would also like to acknowledge Dr. Katarzyna Bejtka and Dr. Marco Fontana for all the FESEM characterizations as well as Dr. Angelica Chiodoni for the TEM ones.

At last, but not least, a big thank you to my family: Davide, the other half of the apple, mum and dad, for always supporting me during these years. In particular, I want to thank Davide for sharing with me this journey, always being there to hear and to comfort me, not only being patient during the numerous mobility periods but, also, always encouraging me to do new experiences, despite the sacrifices necessary from the personal point of view. Thanks also to my parents for always supporting me unconditionally in the bad and the good times.

This was an amazing journey for me, that gave me the opportunity to learn more things, meet more people people and do more life experiences than I would have ever expected.

Abstract

The always more predominant synergy between the biological and engineering worlds, is leading to an extremely fruitful mutual cooperation in which biology can benefit of engineering innovations and, vice versa. In this framework, unknown biological processes and complex bio-chemical dynamics can finally be unveiled, tremendously contributing to improve the current health-care and diagnostic paradigm. To reach this ambitious aim, it is fundamental to understand how these two worlds, apparently so distant, can efficiently and mutually integrate. My Ph.D. thesis was focused, specifically, on the interaction between electronics and cardiac cells, due to the intrinsic electrical activity of the latter. Due to the micrometer dimensional scale of the cells, it is advantageous to also use micrometer-scale electrodes, capable to interface with the living entities at their natural and functional dimensions where the most relevant processes happen. For this reason, I analyzed in depth also the use of electrical platforms, embedding micro-electrodes, both passive or with CMOS circuits directly underneath. Due to the complex nature of the problem of the cells viability on-chip, at first synthetic microstructures were used to test and optimize the sensing capabilities of the developed platforms. Specifically, zinc oxide (ZnO) micro-wires were at first deposited across the nanometric-spaced gap induced by exploiting the electromigration phenomenon on a micrometric gold metal wire. Thanks to the physical/electrical properties of ZnO microwires, the main goal was to create a multi-sensor capable to simultaneously detect variations of pH, temperature and UV-visible light, all important parameters to monitor in cell cultures. To improve the robustness of the system against electrical noise, the same microstructures were deposited across couples of micrometer electrodes, but this time fabricated on the surface of a CMOS chip. In this way, the electronic read-out of the variation of the electrical properties of the microstructure, according to the variation of the external parameters selected, was performed directly underneath the electrodes surface, hence reducing noise and parasitics. Specifically, 24 couples of

aluminum electrodes, were designed so to allow multiple measurements on the same chip. To improve the quality of the electrical contact between the microstructure and the aluminum electrode, easily oxidizing, a tailored electroless gold plating process was optimized to modify the electrodes surface to gold. The CMOS chip with deposited ZnO microwires was then used to investigate the UV-visible light sensing capabilities of the microstructure.

To understand the complex and multiple requirements of performing, instead, measurements of living cardiac cells on chip, a visiting period of 6 months was spent at the Kademhosseini laboratory in Boston (USA), part of the Harvard-MIT health science and technology division. During this time, the needs of primary neonatal rats cardiomyocytes were investigated by developing and electrically modulated bio-hybrid actuator, triggered by the beating activity of cardiac cells, and fabricated using bio-compatible hydrogels. After this extremely important intermediate step, preliminary experiments were done, at the end of the Ph.D. activity by measuring the electrical signals of cardiac cells directly on the surface of CMOS multi-electrodes arrays platforms. Some tests were performed also functionalizing the surface of the CMOS chips with the hydrogel developed in Boston for the bio-hybrid actuator. This activity was performed at the Italian Institute of Technology of Genova (Italy). The main focus of this activity was trying to evoke the firing of an electrical cardiac signal, commonly known as cardiac action potential, by applying an electrical stimulation. At the same time, the biologically-produced electrical signals were also recorded in real-time. Although the performed activity represented only an initial proof-of-concept, it provided an important insight to the challenges to be faced when living entities are deposited on electronic chips. At the same time, the preliminary experiments revealed the huge potentiality of active micro-electronic platforms for the monitoring, study and excitation of living cardiac cells. Thanks to these extremely multi-disciplinary studies it will be possible to significantly impact the current health-care and drug-development paradigms due to the possibility to investigate, previously unknown or not well characterized, biological processes, directly at their proper dimensional scale, with state-of-the-art integrated and hybrid electronic platforms.

Preface and Academic Mobility

Due to the extremely multidisciplinary nature of the present Ph.D. activity, different activities were performed in multiple laboratories (see schematic of Figure 1).

The predominant activity was related to the development of integrated passive and active (CMOS-based) sensing platforms at Politecnico di Torino (Italy). The main goal was to optimize these structures for the electrical sensing of multiple external parameters affecting the conductivity of ZnO microwires deposited on the chips surface.

Fig. 1 Academic mobility during the Ph.D. activity.

During the last year of Ph.D. more focus was instead given to the possibility of integrating living microstructures, i.e. cardiac cells, on-chip and not only of synthetic microstructures. To understand the basics of cardiac cell cultures and how it is possible to effectively grow living cells on synthetic materials, embedding also electrical stimulation, the author spent 6 months at the Khademhosseini Laboratory, part of the Harvard-MIT Division of Health Sciences and Technology, Biomaterial Innovation Research Center, Department of Medicine, Brigham and Women's Hospital (Boston, Massachusetts, USA).

At last, preliminary results about the interface of cardiac cells directly with CMOS circuits was performed during 2 months of experimental activities at the Microtechnologies for Neuroelectronics laboratory of the Italian Institute of Technology (IIT) of Genova (Italy), managed by Dr. Luca Berdondini.

Contents

List of Figures

List of Tables

Nomenclature

Roman Symbols

1D	One Dimensional
ADC	Analog to Digital Converter
APTES	(3-Aminopropyl)triethoxysilane
ATP	Adenosine Triphosphate
CAD	Computer Aided Design
CNT	Carbon Nanotube
CVD	Chemical Vapor Deposition
DAPI	4',6-Diamidino-2-Phenylindole
DE	Dielectric Elastomer
DIV	Days in Vitro
DMEM	Dulbecco's Modified Eagle Medium
DoE	Design of Experiments
DRIE	Deep Reactive Ion Etching
EDTA	Ethylenediaminetetraacetic Acid
EIBJ	Electromigration Induced Break Junction
FBS	Fetal Bovine Serum
FDA	Food and Drug Administration
FESEM	Field Emission Scanning Electron Microscopy
FPGA	Field Programmable Gate Array

FTO	Fluorine-doped Tin Oxide
GelMA	Gelatin Methacryloyl Hydrogel
HBSS	Hank's Balanced Salt Solution
HEPES	4-(2-hydroxyethyl)-1-PiperazineEthaneSulfonic Acid
HRTEM	High-Resolution Transmission Electron Microscopy
ID	Inner Diameter
Irgacure 2959	2-hydroxy-1-[4-(2-hydroxyethoxy)phenyl]-2-methyl-1-propanone
ITO	Indium-doped Tin Oxide
MA	Methacrylate Groups
MEA	Multi-Electrodes Arrays
MEMS	Micro Electro Mechanical Systems
MMP	Matrix Metalloproteinases
MOCVD	Metal Organic Chemica Vapor Deposition
mqH_2O	Milli-Q Water
MTTF	Mean Time to Failure
NEMS	Nano Electro Mechanical Systems
NiTi	Nickel Titanium
PBS	Phosphate-Buffered Saline
PCB	Printed Circuit Board
PCL	Poly(caprolactone)
PDLO	Poly-dl-ornithine
PDMS	Polydimethylsiloxane
PEG	Poly(ethylene glycol)
PEGDA	poly(ethylene glycol) diacrylate
PEN	Polyethylene Naphthalate
PI	Photoinitiator

PIV	Pixel Intensity Variation
PMMA	Poly(methyl methacrylate)
PVA	Poly(vinyl alcohol)
PVD	Physical Vapor Deposition
RF	Radio Frequency
RGD	Arginine-Glycine-Aspartic Acid
SBF	Simulated Body Fluid
SEM	Scanning Electron Microscopy
SMA	Shape Memory Alloys
SNR	Signal to Noise Ratio
TEM	Transmission Electron Microscopy
TMAH	Tetramethylammonium Hydroxide
TMSPMA	3-(Trimethoxysilyl)propyl methacrylate
VLS	Vapor Liquid Solid
XRD	X-Ray Diffraction
ZnO	Zinc Oxide

Chapter 1

Introduction

Chapter Abstract *In the present chapter, the main motivations for the present thesis work will be presented with the support of a brief literature review. The state of the art about the different specific topics studied in the Ph.D. work will also be reported, more in details, at the beginning of each chapter. At first, a comparative introduction (Section 1.1) will underline why the synergy and interaction between the synthetic and natural worlds at the micro/nano-scale is of extreme relevance in the current literature and how they are related in the present work. Then, the overall structure of the present thesis work will be shown in Section 1.2.*

1.1 Nature and Synthetic Micro-Worlds: a comparative Introduction

In the last decades, engineers, biologists but also chemists and medical doctors have worked together to bring the advantages of engineered new technologies into medicine and, vice versa. Indeed, always more often scientists are taking inspiration from nature for the design of innovative devices like actuators [5], bio-hybrid robots [6] or, also, innovative materials like super-hydrophobic self-cleaning surfaces [7]. For example, Nawroth *et al.*, designed a cutting-edge bio-hybrid robot, capable to autonomously swim mimicking the propulsion of jellyfish [6]. As depicted in Figure 1.1 a, at first the jellyfish propulsion was reverse engineered by studying and simulating the structural movement, conformation and feeding dynamics. Then, a silicone polymer medusoid was fabricated and seeded with rat cardiac cells, the main responsible of the robot actuation. They were hence able to mimic the jellyfish motion with artificial tissue engineering.

Apart from the dynamics of living animals, tremendous knowledge can also be gained from the observation of nature at the micro/nano-scale. The predominance of

surface forces at the micro/nano-scale above volume ones, is what allows to gerridae insects (also known as pond skaters or water bugs) to actually walk on the surface of water. Likewise, the spherical shape dewdrops on lotus leaves is mainly due to the super-hydrophobic nature of the leaf surface. The super-hydrophobicity is due to the presence of numerous pillar-like roughnesses capable to push away contaminants by the wheeling of water drops on their surface [7]. This is why, besides being referred as "lotus effect", this is also mentioned as "self-cleaning" ability. Examples of self-cleaning surfaces related to the lotus effect can also be found in rice leaves, butterflies wings, sharks or fishes skins and, also, in mosquito eyes [7].

The conjugation of living entities and engineering is also extremely useful in the field of energy production from natural sources. Among them, biological fuel cells are gaining always more attention thanks to the possibility of obtaining electrical power from the metabolic activity of biological entities, like, e.g., bacteria or enzymes. These devices are able to transform several food substrates into electrical charges. The main advantages of this choice are not only related to their high scalability but also to the fact that they can be intrinsically biodegradable with almost no trace in the environment after their use and disposal [8]. Furthermore, since they can conceivably be autonomous after a small food input they are extremely promising for powering devices in survival or harsh environments. Just as an example, Higgins *et al.*, combined together both the bacteria- and enzyme-based approaches by developing a hybrid lactate/air bio-fuel cell [8]. They associated a microbial anode, embedding the bacterium *Shewanella MR1*, to a lactate-based enzymatic cathode (see Figure 1.1, b). In this way, electrons are transferred both at the anode, where *Shewanella MR1* will metabolize lactate and at the laccase-functionalized cathode.

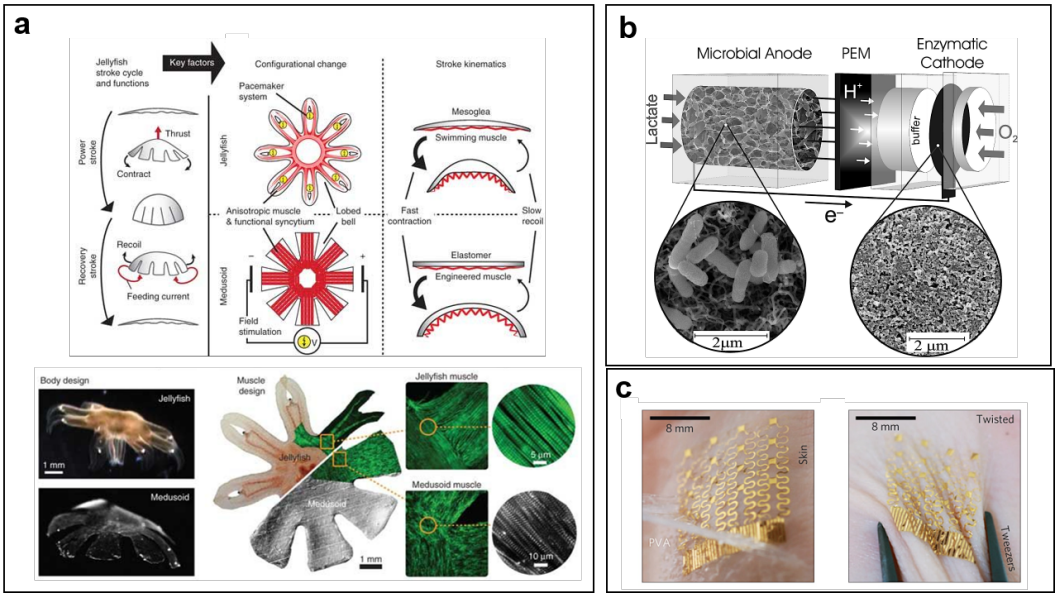

Fig. 1.1 (a) Main design elements of the tissue-engineered medusoid mimicking the propulsion dynamics of jellyfishes. After a first study and modeling of the jellyfish swimming and eating dynamics, a hybrid hydrogel-based robot was fabricated using silicone polymer and isolated rat cardiac cells (adapted by permission from Macmillan Publishers Ltd: Nature Biotechnology, reference [6], copyright 2012). (b) Schematic of the hybrid bio-fuel cell. Direct transfer of electrons is possible both at the anode, thanks to the metabolic activity of *Shewanella MR1*, and at the laccase-functionalized air-breathing cathode (adapted from [8]). (c) Ultra-thin gold sensor of skin thermography. The sensor, attached to the skin through water-soluble adhesive, is capable to function also in case of skin swirling (adapted by permission from Macmillan Publishers Ltd: Nature Materials, reference [9], copyright 2013).

The coupling between the engineering and biology worlds culminates in the integration of advanced engineered devices directly embedded in the human body. Although implantable devices have been studied for a long time, e.g., the first pacemaker was implanted in 1958 [10], what is changing in the recent decade is their operational paradigm. The outburst of internet-of-things as an intricated network of devices, electronics, sensors/actuators and wireless connectivity all embedded together, has raised new requirements also in the medical field. This is also strongly connected to the development of wearable technologies as answer to the escalating requests of self-care devices, capable to sense, measure, analyze and transmit data at the same time and of preventive medical screening. The knowledge demand in terms of new technologies, electronics and materials, as well as their functional integration all together is highly challenging. This is the reason why always more attention has been devoted to engineer new methodologies and materials combinations that allow an easier and strategic alliance of these different worlds. One compelling example

is the development of ultra-thin skin-like arrays for continuous monitoring of skin temperature by Webb *et al.* [9]. As shown in Figure 1.1 c, each array is constituted by micrometric gold serpentines (50 nm thin and 20 μm narrow) encapsulated, on both sides, in 1.2 μm-thick films of polyimide necessary both to electrically insulated the device and to protect it from external moisture. The device is then attached to the skin by using a poly(vinyl alcohol) based adhesive tape. As visible from Figure 1.1 c-right, the combined choice of the materials, the microfabrication and micro-structuration of the device, allows it to correctly adhere also in case of skin twisting, as expected in *in vivo* applications. As anticipated what makes this possible is the co-design of the electronics, of the materials science and of the biological function at the same time that make possible the rising of these state-of-the-art hybrid bio-medical devices.

There is a specific motivation why the synergy between micro/nano-fabrication techniques, as well as micro/nano-structures, is particularly effective for bio-medical applications. The reason is that the micro/nano-scale is the actual dimensional scale of the majority of biological entities as well as of their intrinsic activity. Figure 1.2 wants to show and explain this concept by comparing natural or artificial entities in a dimensional scale from few armstrongs to few millimeters. In both cases, atoms and small molecules represent the starting point. Just few armstrongs after, we can find antibodies and viruses e.g., bacteriophages, which arises from hundreds of armstrongs to 100 nm. These are among the main actors of the scientific literature in the fight against infectious or immune diseases which can give a crucial contribution in the continuous improvement of health-care. But, observing Figure 1.2, it can be noticed how this is exactly the dimensional scale of metal, semiconducting, polymeric or even hybrid nanoparticles directly synthesizable in chemical laboratories. At the boundaries between the nano-metric and micro-metric scales, bacteria, cells as well as their intrinsic and functional units like vesicles or organelles can be found. Their dimension allows them not only to interact with functional synthetic nano/micro-particles e.g., for drug delivery or diagnostics but, also, to be comparable in size with nano/micro-electromechanical systems (NEMS/MEMS) and CMOS technology. Therefore, they are not only capable to interact with them in their natural dimensional scale but, they can also take advantage of the strong improvements introduced by NEMS/MEMS and CMOS in terms of electrical and mechanical measurements, sensitivity, limit-of-detection, power consumption, just to list a few.

This dimensional affinity between the biological and the nano/micro-technology worlds paves the way for the design of an inexhaustible number of experiments in which synthetic nano/micro-particles or smart nano/micro-devices can interact directly with these biological entities at the same scale where they express their functionality. In this way, biological phenomena can be observed, studied and interrogated as close as possible unveiling details inaccessible in the past.

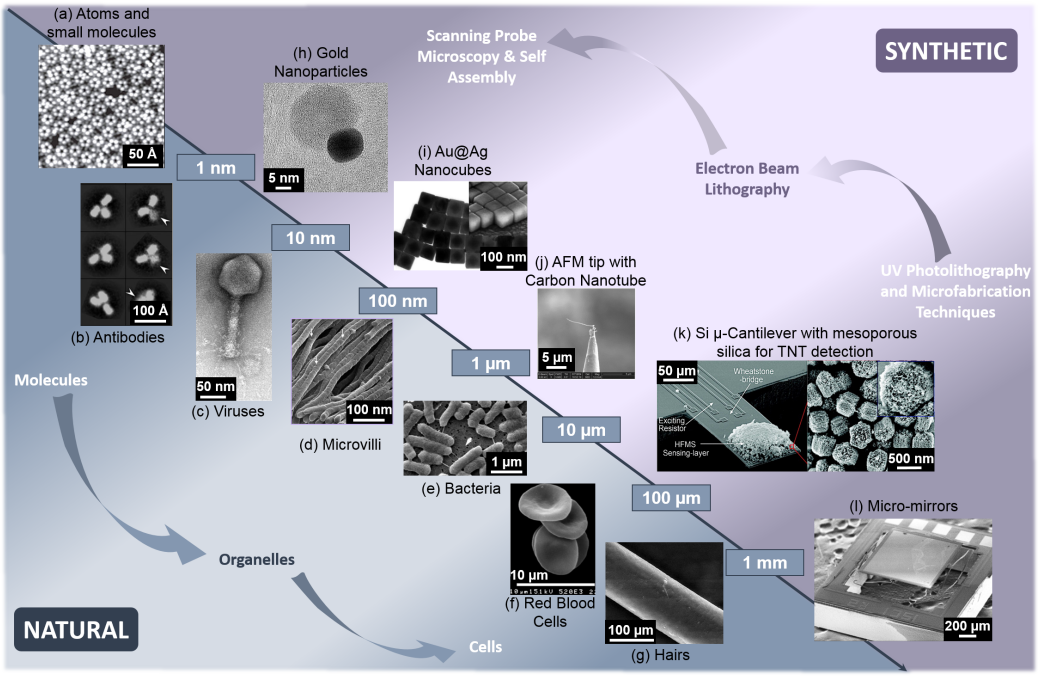

Fig. 1.2 (a) Scanning tunneling microscope images of FcCOOH molecular structure (adapted by permission from Macmillan Publishers Ltd: Nature, reference [11], copyright 2014). (b) IgG1 antibodies 3D (adapted from [12], licensed under a CC-BY 4.0 license). (c) Electron micrography of F386 bacteriophage (adapted from [13], licensed under a CC-BY license). (d) Microvilli of rat kidney (adapted from [14], licensed under a CC-BY license). (e) *Salmonella* Seftengerb bacteria (adapted from [15], licensed under a CC-BY 4.0 license). (f) Human red blood cell (reprinted from Advanced Drug delivery Reviews, Vol 60, F. Pierigè, S. Serafini, L. Rossi, M. Magnani, Cell-based drug delivery, 286-295, Copyright 2008, with permission from Elsevier [16]). (g) Horse hair (adapted from [17], licensed under a CC-BY-NC-ND 4.0 license). (h) Gold nanoparticle (black) with polymeric coating (gray) (adapted from [18], licensed under a CC-BY 3.0 license). (i) Au@Ag nanoparticles (adapted with permission from [19]. Copyright 2013 American Chemical Society). (j) Atomic force microscopy tip functionalized with a carbon nanotube (Reprinted from Journal of the Mechanics and Physics of Solids, Vol 53, C.H. Ke, N. Pugno, B. Peng, H.D. Espinosa, Experiments and modeling of carbon nanotube based NEMS devices, Pages 1314-1333, Copyright 2005, with permission from Elsevier [20]). (k) Silicon microcantilever loaded with hexafkuoro-2-propanol (HFIP) functionalized mesoporous silica (inset) (adapted with permission from [21]. Copyright 2011 American Chemical Society). (l) Electrothermally actuated micromirror (adapted from [22], licensed under a CC-BY 4.0 license).

More in details, numerous examples of interactions of living cells with microstructured platforms [23] or nanoparticles [24] can be found in the literature. For example, Viela *et al.* designed a polycarbonate microstructured platforms with hundreds of nano- and micro-pillars (diameter x height: 500 nm x 2 μm and 2 x 10 μm, respectively) to investigate the mechano-biology of stem cells [23]. After growing

mouse neuronal C17.2 stem cells on the two pillar structures (see Figure 1.3 a and b) they were able to measure different cells traction forces on the two different layouts. The cells grown on the nano-pillars resulted in less cellular confinement, higher mobility and lower traction forcer than the ones grown on the micro-pillars. These fundamental studies are crucial in the field of regenerative medicine for designing smart platforms capable to induce stem cell differentiation [23]. Besides interacting with object comparable or bigger than their size, living cells can also effectively combine with smaller particles that can both penetrate or just decorate the cellular membrane. Plascencia-Villa *et al.*, studied the dose-dependent cytotoxic effect of metal oxide nanoparticles made of CeO_2, TiO_2 and ZnO [24]. Specifically they focused on their effect on macrophages, fundamental cells of the immune system. In figure 1.3 c, is reported a field emission scanning electron microscope (FESEM) image of ZnO nanoparticles (single particle 5-10 nm, hydrodynamic diameter 86 nm) adsorbed on the cell surface and resulting in intense modifications of the cellular membrane that would then lead to invaginations and nanoparticles endocytosis [24]. After 24 h from ZnO nanoparticles internalization, programmed cellular death, through apoptosis was observed. While in case of loading with CeO_2 and TiO_2 nanoparticles no signs of necrosis or apoptosis were observed after 24 h. These studies are crucial to understand the effect of nanomaterials internalized in living cells, e.g., for drug delivery or cancer treatment.

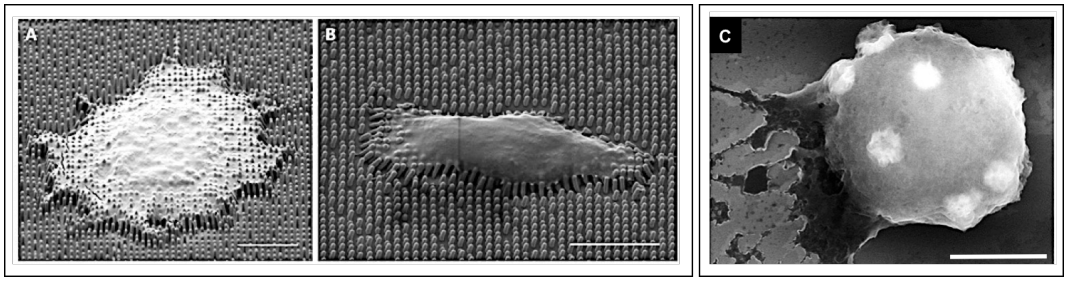

Fig. 1.3 Scanning electron microscope image of unpolarized (a) and polarized (b) mouse neuronal C17.2 stem cell on 500 nm polycarbonate pillars. Scale bars 10 μm ((a) and (b) reproduced with permission from [23], copyright 2016 WILEY-VCH). (c) FESEM image of ZnO nanoparticles-loaded macrophage cells. Scale bar 5 μm (Adapted in part from reference [24] with permission of The Royal Society of Chemistry, http://dx.doi.org/10.1039/C2IB20172K).

The study of synthetic microstructures, like e.g., zinc oxide microwires studied in the present work, presents a double significance. At first, as anticipated in the paragraph above, they can be designed with the right dimension in order to functionally interact with the biological entities. But this, at the same time implies that if it is possible to design a device capable to interact with synthetic microstructures to measure a physical quantity or to stimulate/modify that structure, it is also possible that the same approach can be then useful in case of biological/living micro-entities. The study of biological/living micro-entities introduces a great number of additional

challenges to be faced related to biocompatibility, contamination and survival issues. Moreover, numerous issues are also related to the high aggressiveness of biological fluids with respect to electronics.

Therefore, the design of exploratory platforms necessary to understand how to interact with a nano/micro-structure, how to measure its physical properties and their variation upon specific stimuli, as well as the requirements for measurements in liquids or in *in vivo*-like environments represent a fundamental phase. This is why, the present work started from the design and test of multi-functional platforms for sensing of physical properties of microstructures. Afterward, the physiological necessities for the survival and functional proliferation of living cells, specifically, cardiac cells, have been throughly investigated. This step was necessary also in order to understand how it is possible to employ biocompatible materials to recreate environment conditions *in vitro* as close as possible to *in vivo* ones. At last, as proof-of-concept of the integration of the two activities together, cardiac cells were studied on-chip paving the way for the design of new multi-functional platforms embedding on the same chip the stimulation, sensing and optimal cell survival and functional proliferation environment, on the same chip.

1.2 Aim of the Work and Thesis Structure

The present Ph.D. thesis reflects the high multidisciplinary nature of the topics introduced in Section 1.1. The main building blocks of the work are outlined in Figure 1.4.

At first, the electrical properties of synthetic microstructures, i.e., ZnO and $Mo_6S_4I_6$ microwires, were studied on microelectrodes platforms, with and without CMOS circuits underneath. In order to substitute synthetic microstructures with living ones, it is fundamental to understand the needs and the requirements of living entities in order to functionally survive and proliferate on engineered devices. For this reason, at first electrogenic cells, specifically, cardiac cells, were selected due to their electrical activity. Then, the use of biocompatible hydrogels as scaffolds for the functional growth of cardiac cells was investigated during the visiting period at the Khademhosseini Laboratory in Boston (USA), as already introduced in the . This activity was focused on the design and fabrication of a hydrogel-based actuator, actuated by the beating activity of cardiac cells growing on its surface, fabricated using bioprinting techniques.

At last, in order to merge the two activities, a preliminary proof-of-concept about the electrical sensing of cardiac cells on CMOS multi-electrodes arrays, with and without intermediate hydrogel coating was investigated during the two months visiting period at the IIT of Genova (Italy).

The structure of the thesis is organized in two principal sections. The first one (Part I) reports about the different research techniques and methodologies adopted, while, the second one (Part II) is more focused on the experimental results obtained.

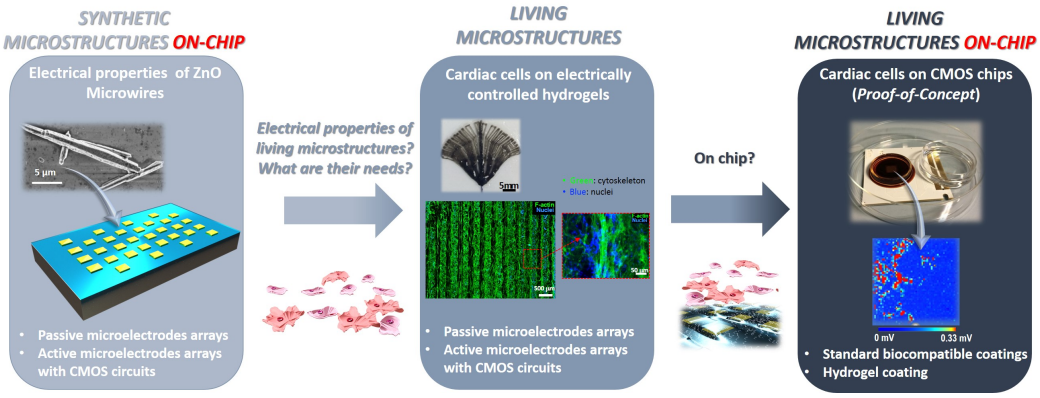

Fig. 1.4 Main building blocks of the Ph.D. Thesis. At first, the electrical properties of synthetic microstructures are studied on both passive and active microelectrodes arrays. Then, the needs of living microstructures for electrical sensing application were investigated by developing a bio-hybrid hydrogel-based actuator actuated by neonatal rats cardiac cells. At last, a proof-of-concept of the union of the two world was designed by measuring the electrical activity of cardiac cells on CMOS chips with and without hydrogel coating.

More in details, initially, the selected synthetic and living microstructures will be presented in Chapter 2, along with their most relevant electrical properties.

The passive and active microelectrodes-based sensing platforms will instead be presented in Chapter 3 and 4, respectively.

Then, the selected hydrogels for the fabrication of the bio-hybrid actuator, actuated by cardiac cells, along with the experimental setup used for the bioprinting experiments will be presented in Chapter 5.

In Part II, instead, at first the experimental results of the electrical sensing of the selected microstructures on the passive and active electrodes platforms optimized in the present work will be presented in Chapter 6.

In Chapter 7, the electrical modulation of the living cardiac cells grown on the bioprinted hydrogels will be described.

At last, the preliminary proof-of-concept results about the electrical sensing of cardiac cells growing on the CMOS multi-electrodes arrays, developed at the IIT of Genova in collaboration with 3Brain (3Brain GmbH, Switzerland), will be shown in Chapter 8.

Part I

Research Techniques and Methodologies

Chapter 2

Synthetic and Living Micro-Structures

Chapter Abstract *In Chapter 2 the synthetic and living microstructures studied in the present work will be presented. Synthetic zinc oxide microwires, their properties (Section 2.1), synthesis, both the ones reported in the literature (Section 2.1.1) and the adopted one (Section 2.1.1.1), will be described in details. Zinc oxide microwires represent the main protagonists of the synthetic microstructures world here presented. After a short introduction about another synthetic microstructure investigated, i.e.,* $Mo_6S_4I_6$ *microwires, cardiac cells will be extensively described as constituents of the world of living microstructures (Section 2.3). Specifically, Section 2.3.1 will describe their fundamental structure and properties, while, Section 2.3.2 will report the experimental protocols adopted to isolate cardiac cells from animal tissue.*

2.1 Zinc Oxide Microstructures

Zinc oxide (ZnO) micro-structures have been widely investigated in the literature due to their highly tunable physical, chemical and electro-mechanical properties [25, 26]. This allows for the development of advanced integrated solutions for numerous applications like electronic nanodevices, such as field effect transistors [27, 28], energy nanogenerators [29, 30] and solar cells [31], biosensors [32] and photodetectors [33, 34]. ZnO is a direct wide band-gap semiconductor, with an energy band-gap of 3.35 eV at 300 K. This implies that the material presents high break-down voltages being electrically robust when high electric fields are present. Moreover, it presents a high thermal conductivity, an elevated exciton binding energy, it is biocompatible [26] and, recently, also its anti-bacterial activity have been investigated [35].

ZnO micro-structures can be synthesized in a large variety of morphologies like e.g., nano-helix [36], flower-like [37] and fractal-like microstructures [38] or hollow nano-tubes [39] (Figure 2.1).

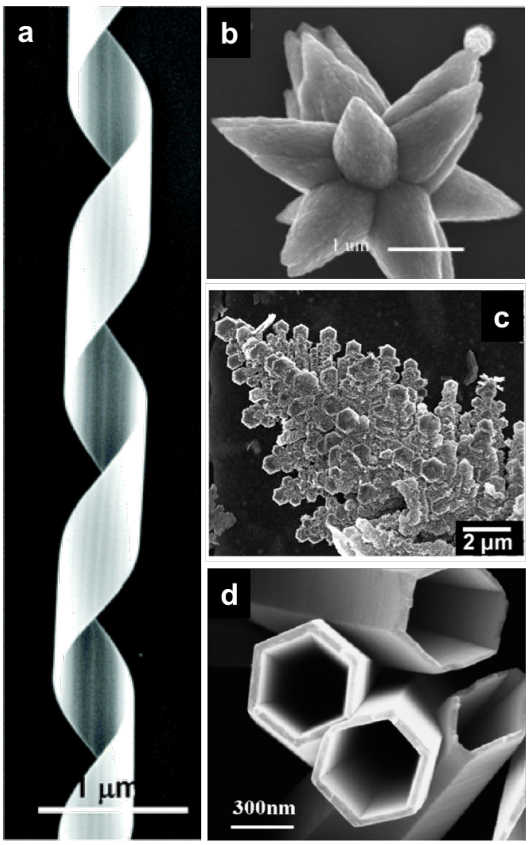

Fig. 2.1 Examples of different ZnO nano- and micro-structured morphologies like (a) nano-helix (adapted with permission from [36]. Copyright 2006 American Chemical Society), (b) flower-like (adapted with permission from [37]. Copyright 2005 American Chemical Society), (c) fractal-like (adapted with permission from [38]. Copyright 2009 American Chemical Society) and (d) nano-tubes (adapted with permission from [39]. Copyright 2009 American Chemical Society).

Among them, one-dimensional microwires have been widely investigated in the literature due to their peculiar opto-electronic properties favorable for the development of cutting-edge integrated nano/micro-devices [40]. Microwires are 1-dimensional (1D) microstructures, i.e., they are quantum confined only in two dimensions. The quantum confinement effect is one of the main responsible of the peculiar properties of micro-materials with respect to bulk ones. This effect is observed when one, two or all three the dimensions of a material are so reduced that they become comparable with the wavelength of electrons, therefore, they directly influence the band structure of the material itself leading also to the discretization of

the allowed electrons energy levels [41]. ZnO microwires are n-type semiconducting 1D micro-structures. Their ionicity is considered intermediate between ionic and covalent semiconductors. The crystal impurities due to oxygen vacancies and zinc interstitials not only define the purity of the material itself but, in addition, acting as donors of electrons, they strongly influence its electrical properties by introducing additional allowed energy levels in the forbidden band-gap in proximity of the conduction band.

The versatility of ZnO in a broad range of applications is also related to its polymorphism. More precisely, this material can be found in multiple crystal structures: cubic rocksalt, cubic zinc blend and hexagonal wurtzite (Figure 2.2).

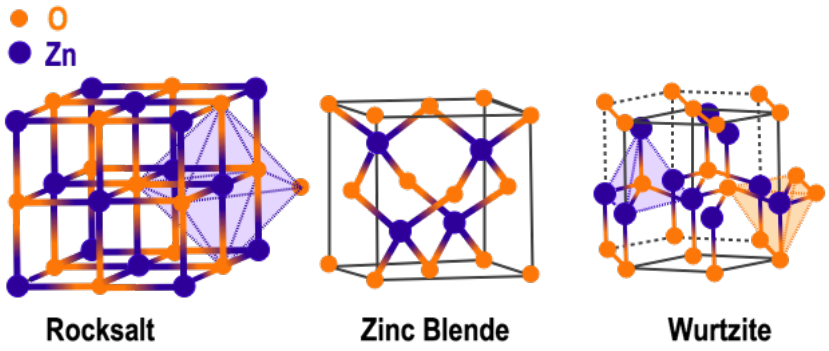

Fig. 2.2 Schematic view of the different crystal structures of ZnO: cubic rocksalt, cubic zinc blende and hexagonal wurtzite.

The cubic structures, rocksalt and zinc blende, are the less thermodynamically stable at ambient conditions. This is also why, in nature, ZnO is present in the mineral form as *zincite* ($(Zn,Mn^{2+})O$), that has an hexagonal crystal structure [42]. If the lattice spacing is reduced, so that inter-ionic Coulomb forces are more in favor of ionicity than covalent nature, a phase transition between wurtzite and rocksalt is possible at pressures around 10 GPa. Differently, the zinc blende crystal structure can be synthesized only by guiding the crystal growth starting from a cubic lattice substrate. This heteroepitaxial growth helps to deviate the growth of the crystal from its deeply-routed wurtize structure. The unit cell of the zinc blende structure presents 4 atoms with a tetrahedral coordination. In fact, its geometry is formed by the interpenetration of two face-centered-cubic (fcc) sub-units shifted by one quarter. Also the wurtzite lattice presents a tetrahedral symmetry but, this is obtained from the interpenetration of two hexagonal-closed-packed (hcp) sub-units leading to an hexagonal unit cell [43]. As detailed in Figure 2.2, in the wurtzite structure, each oxygen atom is at the center of a tetrahedron with zinc atoms at its vertices while, at the same time, each zinc atom is at the center of a tetrahedron with oxygen vertices.

Despite the intrinsic structural differences, all the presented crystal structures are non-centrosymmetric. Consequently, a spontaneous crystal polarization is not

only possible but, also, it is the reason behind the piezoelectricity of ZnO, i.e., the capability of the material to mutually convert mechanical energy into electrical signals and *vice versa*. Considering, e.g., the wurtzite phase, its overall structure is formed by the repeated alternation of planes made only by oxygen or zinc atoms along the c-axis (or [001] direction) with no inversion symmetry (see Figure 2.3 a). This leads, as a result, to a preferential crystal growth along the c-axis thus making the material strongly anysotropic. This feature can be easily recognized in ZnO micro/nano-wires or rods (Figure 2.3 b) in which the strong anysotropic growth along the c-axis produces highly elongated structures, with recognizable hexagonal section.

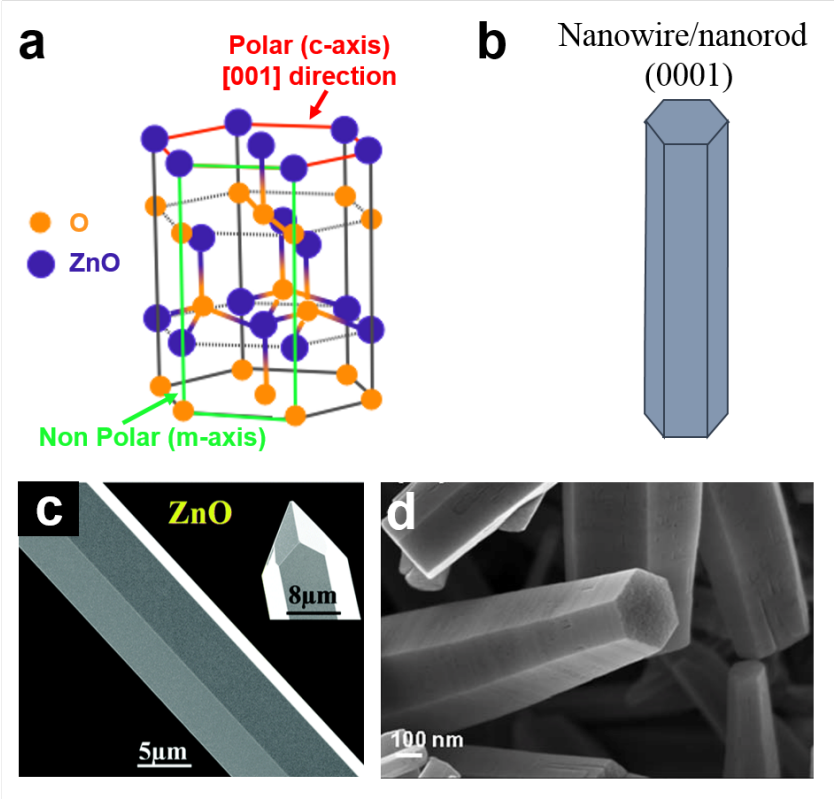

Fig. 2.3 Schematic view of the anisotropic growth of ZnO wurtzite structure along the c-axis.(a) Stick and ball diagram of the alternate of zinc and oxygen planes in the wurtzite anysotropic crystal structure. (b) Schematic morphology of a ZnO wire/rod structure growing along the [001] direction. SEM images of (c) ZnO microwires with the typical pencil-like tip (Adapted from [44] with permission of The Royal Society of Chemistry, http://dx.doi.org/10.1039/C6TC05568K) and, (d) ZnO microrods with flat ends (Adapted from [45] with permission of The Royal Society of Chemistry. http://dx.doi.org/10.1039/C4RA08462D).

According to different procedures, as it will be described in details in the Section 2.1.1, the synthesis of this kind of materials can result in different linear morphologies such as ZnO microwires, with the typical pencil-like end (see Figure 2.3 c), or as ZnO microrods with flat ends (see Figure 2.3 d). Due to the fact that on one side the material always terminates with an oxygen plane while, on the other side, it terminates with a zinc one, an intrinsic polarity is present in the crystal due to the opposite polarities at the extremes [26]. The intrinsic polarity of ZnO is not only intimately connected to its piezoelectricity but, also, to a large number of other properties like, e.g., plasticity, etching rate and defects propagation [43].

2.1.1 Zinc Oxide Microwires Synthesis

The versatility of ZnO can be also recognized in the numerous and different methods that can be adopted for its synthesis. Both dry or wet-chemical approaches can be used [25, 26, 40]. Dry techniques for this kind of applications relies generally on vapor-phase transport processes in which vapors, precursors of the element to be grown/deposited, are, at first produced. Then, they react in a closed chamber, usually made of quartz or alumina, leading to the condensation of the target material on a specific substrate. The way in which the vapors are produced define two major families of vapor-phase deposition processes: physical vapor deposition (PVD), in case of extraction from solid sources, and chemical vapor deposition (CVD), in case of vapor generation by the reaction of gaseous precursors.

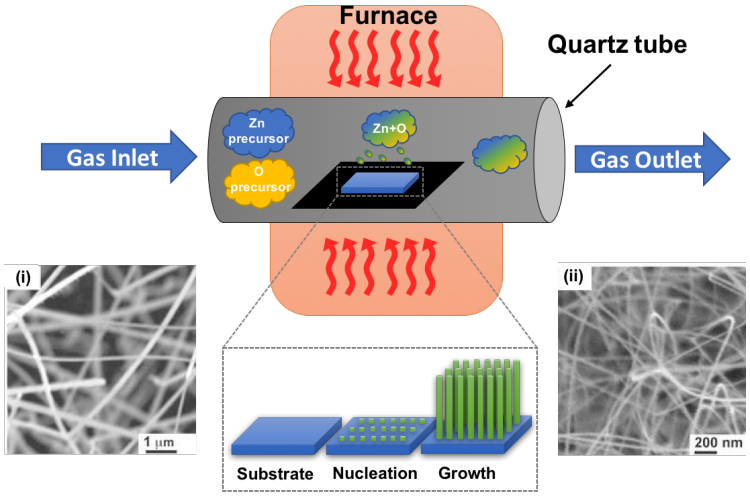

Fig. 2.4 Schematic outline of the fundamental steps and constituents of a CVD apparatus for ZnO micro/nano-wires synthesis.Insets (i) and (ii), (adapted from [46], license CC-BY-NC), show two SEM images of ZnO wires synthesized using this approach.

One of the most investigated processes for ZnO microwires growth is CVD and, more specifically, thermally activated CVD in which very high temperatures (above 500 °C) are employed to trigger the chemical reaction of the precursor gases [26]. As outlined in Figure 2.4, for the growth of ZnO micro/nano-wires both a zinc and an oxygen precursors are necessary. Usually, powder forms of ZnO or metallic Zn are chosen as Zn precursors and, then, oxygen is also added in the furnace stream [26]. Also the decomposition of the source of the target material into vapors is the motivation behind the high temperature required for the process since usually it is around 1975 °C for ZnO powders or around 420 °C in case of metallic Zn [25]. A lower decomposition temperature can be obtained e.g., by using a mixture containing also graphite as precursor of Zn as reported by Yu *et al.* in which the temperature was lower to 900 - 1000 °C [46].

The primary growth mechanism of ZnO microwires is due to the adsorption of atoms/molecules on the substrate surface followed by their consequent nucleation and growth. Different materials can be used as substrates like sapphire [25], silicon or also transparent materials like fluorine-doped tin oxide (FTO) glasses as shown in the work of Yu *et al.* (See Figure 2.4 (i)-(ii)) [46]. In order to improve the control on the spatial growth of the structures, as well as their size and uniformity, a catalyst is often used to guide the process. Usually they are metals like Fe, Sn, Cu or also Au, preferred in case of ZnO micro/nano-wires growth [25].

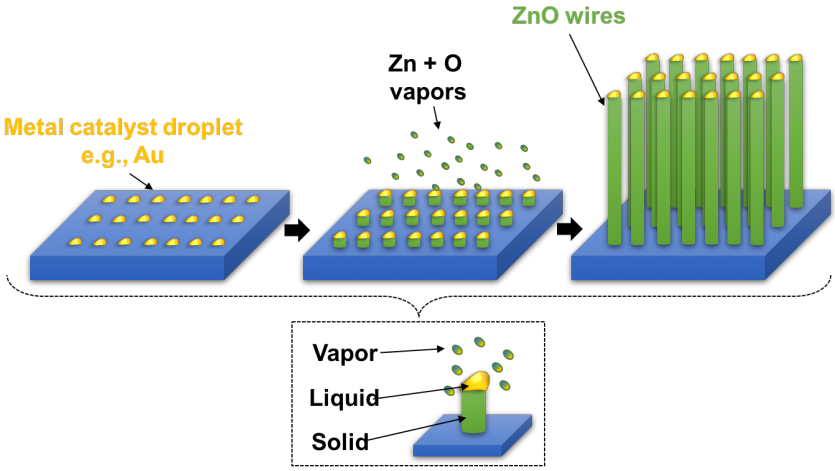

Fig. 2.5 Schematic outline of the fundamental steps during a VLS process.

When metal drops of a catalyst material are deposited on the substrate surface, the vapor-phase transport process is called vapor liquid solid (VLS). As outlined in the schematic of Figure 2.5, droplets of a specific metal, acting as a catalyst for the micro/nano-structure growth, are patterned on the substrate surface with a specific geometry. When the substrate is heated, the droplets will melt (*liquid*), accelerating and easing the adsorption of the precursors molecules (*vapor*) and their subsequent

nucleation and growth (*solid*). This process is based on the super-saturation of the precursors vapors inside the metal droplets leading to a precipitation phenomenon that will initiate the growth of the micro/nano-structure quicker than in the case of direct vapor adsorption on the solid substrate [47]. This approach can be also used to pattern islands or specific geometries of ZnO nanowires on a substrate only in specific regions. For example, Huang *et al.*, developed ZnO nanowires arrays for room-temperature nanolasers applications [48]. As shown in Figure 2.6-left, they patterned the vapor-phase growth of the nanowires on a sapphire substrate only on specific islands, with rhomboidal shape, by creating a Au-coating with the desired shape.

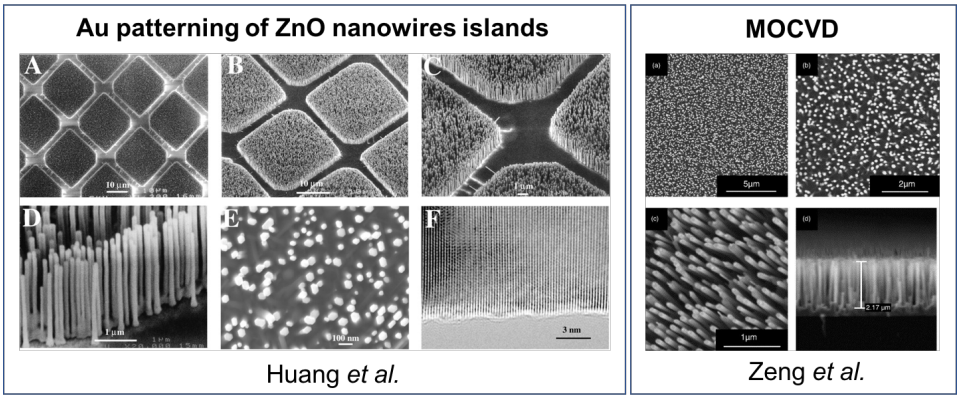

Fig. 2.6 Left side (a)-(e), scanning electron microscope images of ZnO nanowires patterned on Au islands on a sapphire substrate and, (f) high-resolution transmission electron microscope image of the [001] growth direction of a single nanostructure (From ref. [48]: Room-Temperature Ultraviolet Nanowire Nanolasers, by M. H. Huang *et al.*, Science, 2001, pp. 1897-1899. Reprinted with permission from AAAS.). Right side, field emission scanning electron microscope images of ZnO nanowires grown on Si substrate by MOCVD (Reprinted from Applied Surface Science, Vol. 250, Y.-J. Zeng, Z.-Z. Ye, W.-Z. Xu, L.-P. Zhu, B.-H. Zhao, Well-aligned ZnO nanowires grown on Si substrate via metal–organic chemical vapor deposition, Pages No. 280-283, Copyright 2005, with permission from Elsevier [49]).

Nevertheless, the presence of the metal catalyst can decrease the crystal purity of the final structures due to the unwanted contamination of the micro/nano-structures with catalyst impurities [50]. For this reason, recently, metal-organic CVD (MOCVD) was lately developed in order to have not only an efficient CVD, with lower temperatures as in the VLS case, but, also, no catalysts in order to further increase the quality of the final structure [50]. This technique is based on the use of precursors made by organometallic compounds and hydrides which can be decomposed at temperatures between 200 and 400 °C [26]. For example, Zeng *et al.* reported about the catalyst-free MOCVD of single crystal ZnO nanowires onto Si substrate for advanced optical applications [49]. The zinc precursor was diethyl zinc, a highly pyrophoric organometallic compound. The obtained nanostructures

were uniform in size and distribution, as confirmed by scanning electron microscopy analysis (see Figure 2.6-right), and, the typical hexagonal section of the single crystal configuration was observed.

One of the main motivations behind the continuous effort to decrease the temperature of vapor-phase processes is the necessity to perform the deposition processes also on a wider category of substrates that are not be able to withstand high temperatures like flexible substrates made of e.g., polymers or even paper-based materials. For this reason, despite sometimes they lead to a lower crystal quality, wet-chemical approaches are preferred [26]. The most used methods are based on the sol-gel approach, like aqueous chemical growth, hydrothermal growth and template-assisted growth. However, also numerous different approaches are possible like, e.g., electrodeposition which takes advantage of a three-electrodes setup to control the diffusion of charged reactive particles, using an electric field, in order to assemble the desired microstructure on a specific conductive substrate [26]. A solution-phase synthesis approach presents several advantages related to its reduced cost, if compared with vapor-phase synthesis, since no specific equipment is necessary, and to its low process temperature. Nevertheless, this approach is more time-consuming with respect to the previous one since the reaction time can extend also to several hours while, using the vapor-phase synthesis, also few minutes can be enough. Moreover, the precise tuning of crystal properties and the final purity are more challenging [25]. For these reasons, the best approach for the microstructures growth must be chosen specifically for the application requirements, e.g., in case of metrological studies, a vapor-phase process can be preferred due to the superior crystal purity.

In a solution-phase synthesis using the hydrothermal approach, the key factors affecting the final outcome are the initial reagents used and their mutual ratio. In fact, in a sol-gel process, solid materials, nano/micro-structures or also hydrogels or aereogels, are obtained from precursors in the solution-phase [51]. Inorganic salts are generally used for ZnO synthesis as Zn sources like zinc acetate ($Zn(OAc)_2$) or zinc nitrate ($Zn(NO_3)_2$). When hydrolyzed in water or alcohols, these precursors produce Zn^{2+} ions that will combine with OH^- anions generated from the hydrolysis of a hydroxide (e.g., sodium hydroxide, NaOH, or potassium hydroxide, KOH). Several hydroxyls will be generated by their reaction, and, specifically, $[Zn(OH)_4]^{2-}$ will condense in the form of ZnO [40]. This process is guided by the initial formation of ZnO nuclei, due to a supersaturation condition. The formed nuclei will then be exploited for the generation of bigger particles. This process is referred as Oswald ripening or coarsening [52]. Due to the highest reactivity of ZnO crystallographic planes in the [001] direction ($\pm(0001)$ planes in case of wurtzite structure), on that surfaces the growth rate will be higher in order to minimize the total energy of the system, thus leading to the formation of anisotropic rod-like structures [53].

Using the described method, stand-alone ZnO microstructures can be obtained in powder form. If the goal is, instead, to have a forest-like growth of microstructures on a specific substrate the aqueous chemical growth method can be instead used. These kind of structures are of particular interest for energy applications [54] . When a suitable substrate is immersed in a solution with precursors of Zn^{2+} and OH^{-} ions, at a specific temperature (usually below 100 °C), in a closed container for several hours ZnO wires will grow vertically on the substrate surface forming a forest-like structure [26]. A large variety of substrates can be used, due also to the low process temperature, depending on the specific final application like e.g., silicon wafers, with and without a thin metallic layer on the surface, or bare and FTO-coated transparent glass slides as well as flexible polymeric substrates like kapton or polyurethanes [40]. Although the length of the microstructures can be modulated by changing the reaction duration, the final outcome of the crystal structures is instead strongly influenced by the substrate choice. For example, Xu *et al.*, optimized the growth of long ZnO nanowires (bigger than 30 μm in length) on a indium-doped tin oxide (ITO) glass for applications in dye-sensitized solar cells where transparent substrates are required [55]. Differently, Quin *et al.*, functionalized a flexible textile fiber with ZnO nanowires in order to be able to harvest energy in presence of vibrations or different disturbances (e.g., air flow, heartbeats, environmental noise), task much more difficult using hard substrates [56]. Sometimes, an additional seed layer made also of ZnO can be deposited on the substrate prior to the microwires growth. Usually, the growth of the ZnO seed layer develop along the c-axis and, as in the case of no ZnO seed layer, its properties strongly influence the final crystal wires [40]. For example, Laurenti *et al.* investigated the different wettability of ZnO nanowires as a function of different deposition methods of the seed layer [57]. As shown in Figure 2.7, different water contact angles (insets) were obtained, for the synthesized ZnO nanowires forest, changing the seed layer deposition parameters.

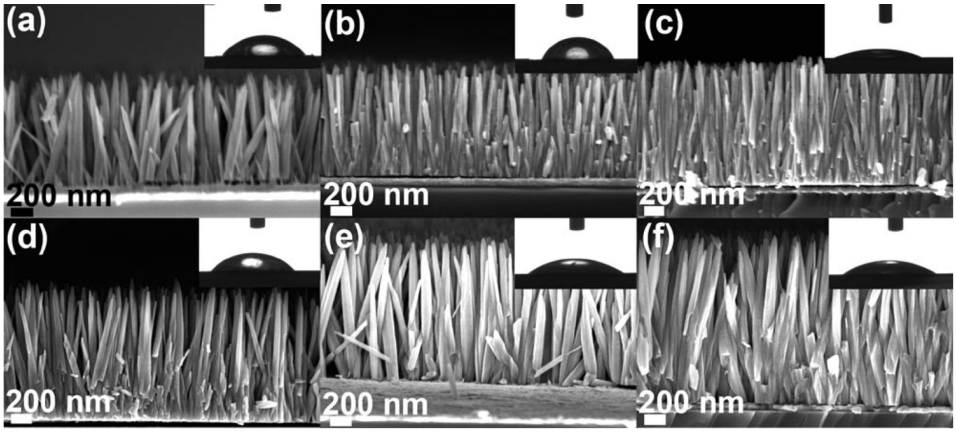

Fig. 2.7 Field emission scanning electron microscope images of ZnO microwires grown, on differently treated ZnO crystals seed layers. Three concentrations of the precursors solution were tested ((a) and (d) 5 mM, (b) and (e) 10 mM, (c) and (f) 20 mM) in case of both fresh ((a), (b), (c)) and two weeks old ((d), (e), (f)) seed layers (reproduced with permission from [57], Wiley 2013).

2.1.1.1 Experimental Protocol

In the present work, ZnO microstructures were synthesized in order to be singularly deposited between a couple of metal electrodes for sensing applications. For this reason, the hydrothermal sol-gel approach was preferred to the aqueous chemical growth. As anticipated in Section 2.1.1, this method is based on the hydrolysis of Zn and O precursors in Zn^{2+} and OH^{-} ions and on their subsequent condensation in different hydroxyls that will then lead to the growth of ZnO microstructures [58]. As outlined in Figure 2.8, at first, 3.35 g of potassium hydroxide (KOH, 60 mmol, Merk) and 1.48 g of zinc nitrate hexaydrate, ($Zn(NO_3)_2 \cdot 6H_2O$, 5 mmol, Sigma-Aldrich) are dissolved in 10 mL of bi-distilled water (Millipore) each.

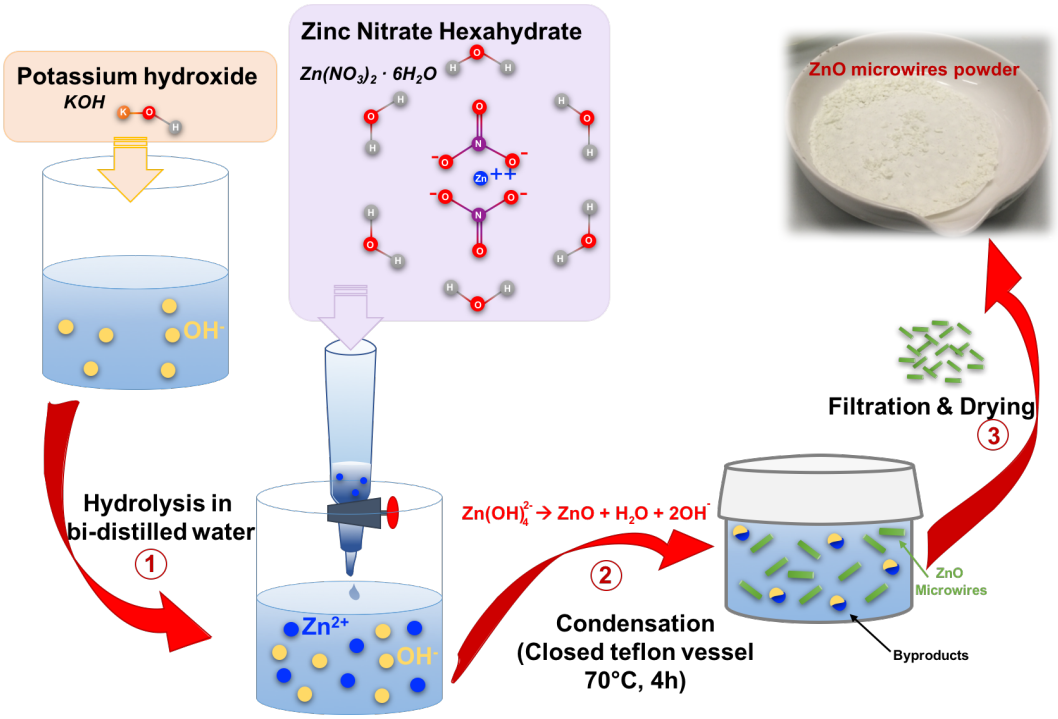

Fig. 2.8 Schematic of the hydrothermal hydrolysis and condensation reaction for ZnO microwires synthesis. At first, the solution of potassium hydroxide and zinc nitrate hexahydrate are dissolved in water hydrolyzing in Zn^{2+} and OH^- ions. When the nitrate solution is slowly add drop-by-drop to the potassium one, intermediate hydroxides will form and, specifically, $[ZnOH_4]^{2-}$ will condense in ZnO. After a thermal treatment in a teflon vessel at 70 °C for 4 hours, the solution is washed and filtered to neutralize pH. A last drying step is then performed to obtain a dry powder of ZnO microwires.

Then, the zinc nitrate solution is added drop-by-drop to the potassium hydroxide one using a cylindrical separatory funnel under vigorous magnetic stirring. The Zn^{2+} cations will react with the OH^- anions forming intermediate hydroxyls like $ZnOH^+_{(aq)}$, $ZnOH_{2(aq)}$, $ZnOH_{2(s)}$, $ZnOH_{3^-(aq)}$ and $[ZnOH_4]^{2-}$ [40]. The last hydroxyl, $[ZnOH_4]^{2-}$, it the one that will condense leading to the formation of ZnO nuclei or nuclei aggregates. The complete chemical reaction can be observed in Equations 2.1 and 2.2.

$$Zn^{2+} + 4OH^- \rightarrow [Zn(OH)_4]^{2-} \tag{2.1}$$

$$[Zn(OH)_4]^{2-} \rightarrow ZnO + H_2O + 2OH^- \tag{2.2}$$

The vigorous stirring is necessary since the addition of zinc nitrate will quickly lead to the formation of a gel due to the condensation of $[ZnOH_4]^{2-}$. This process,

can be observed with naked eyes since the solution will quickly change from being transparent to opaque and denser, often requiring an increase of the magnetic stirrer velocity (Figure 2.9). At this stage, the ZnO crystal growth along the c-axis will slowly start leading to the formation of anisotropic microwires due to energy minimization, as described in details in the section 2.1.

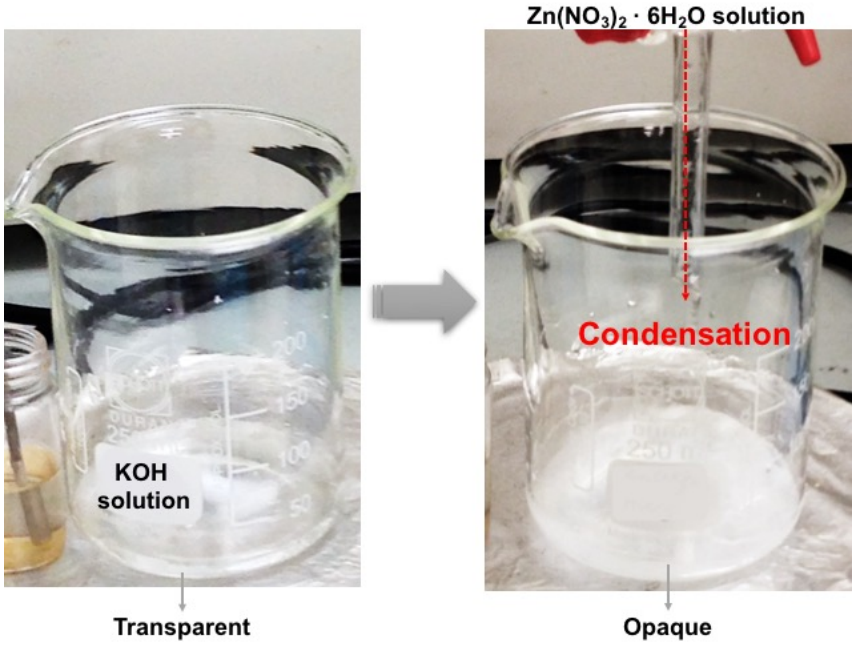

Fig. 2.9 Gelatination of the potassium hydroxide solution (left) after the drop-by-drop addition of zinc nitrate hexahydrate solution (right).

Thereafter, the solution is transferred in a closed Teflon bottle and heated at 70°C for 4 to 5 hours. This thermal treatment is necessary not only to favor the crystal growth but, also, to improve its crystal purity and quality. The solution was then filtered and accurately washed using bi-distilled water in order to remove the reaction by-products or unreacted reagents and to neutralize pH. This step was performed pouring the solution into and Erlenmeyer flask through a ceramic funnel covered with filtering paper. At last, the solution was dried overnight at 60 ° obtaining a white powder (see Figure 2.8).

As unveiled by FESEM microscopy analysis, the synthesis resulted in the growth of ZnO microwires with hexagonal section, width between 300 nm and 2 μm and length between 5 and 15 μm (Figure 2.10).

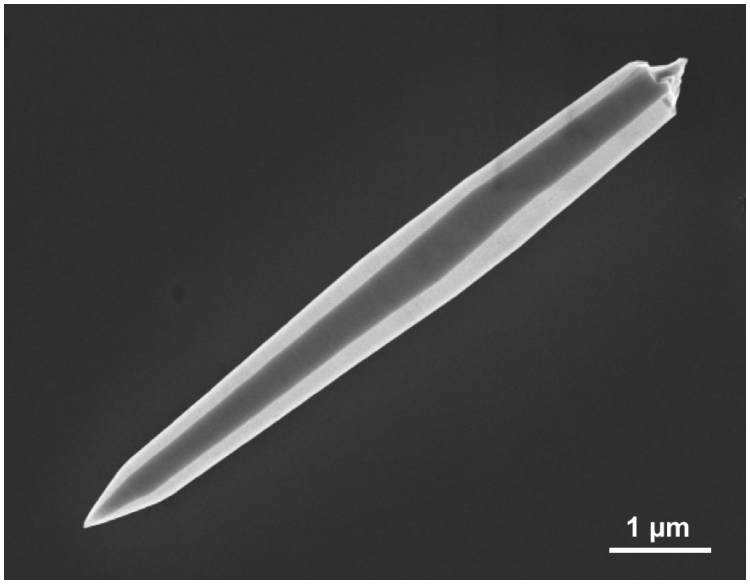

Fig. 2.10 FESEM image of a single ZnO microwire synthesized by the hydrothermal route.

Interestingly, the two extremes of the microstructures showed pencil-like terminations. As reported also in [26], this phenomenon can be attributed to the erosion of the already formed ZnO microwires by excess OH^- anions due to the consumption of the complete zinc cations source in the solution. This feature underlines how the solution concentration and pH play a crucial role in the synthesis outcome. In fact, as also reported by Cauda *et al.* [58], changing the ratio of the potassium hydroxide in solution, different micro-structured morphologies can be obtained. In case of ZnO microwires synthesis, the molar ratio between the moles of zinc nitrate hexahydrate and potassium hydroxide is 12:1. If this ratio is reduced to 8:1, ZnO multi-pods are obtained, and, if the ratio if further reduced to 2:1, flower-like ZnO structures, similar to desert roses, are obtained (Figure 2.11).

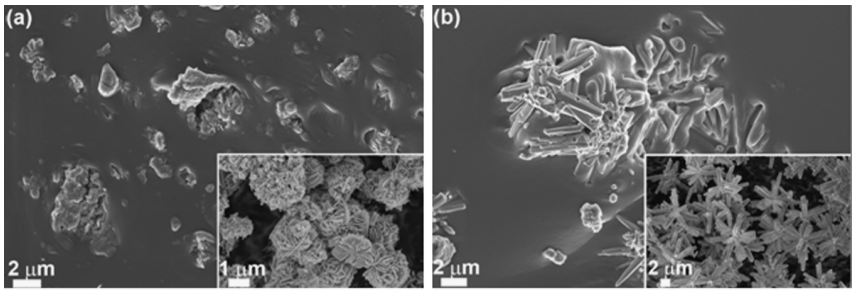

Fig. 2.11 Scanning electron microscope images of (a), ZnO multipods and (b) ZnO desert-roses embedded in a polydimethylsiloxane matrix or pristine (insets) (Reprinted from Nano Energy, Vol. 18, V. Cauda, S. Stassi, A. Lamberti, M. Morello, C. F. Pirri, G. Canavese, Leveraging ZnO morphologies in piezoelectric composites for mechanical energy harvesting, Pages No. 212-221, Copyright 2015, with permission from Elsevier [58]).

This behavior can be explained based on the variation of OH^- ions in the synthesis solution due to different amounts of potassium hydroxide, at a fixed Zn^{2+} ions concentration. In case of ZnO microwires, a higher number of nuclei will be formed since numerous OH^- ions are present. The growth will then proceed along the c-axis, as previously mentioned in Sections 2.1 and 2.1.1. When, instead, less OH^- ions are present, not only a smaller number of ZnO nuclei will form but also their growth will be slow down due to the less abundance of constituents [58]. This will cause an aggregation of the forming crystals. In case of multi-pods, the OH^- ions concentration is still sufficient to maintain the wire structure, although not stand alone but with numerous wires aggregating to the same center. While, in case of desert-roses, petal-like crystal structures will form and aggregate each other.

As widely reported in the literature [59–61], and throughly discussed in Section 6.2, ZnO microwires can be effectively used as pH sensors thanks to the variation of its surface charge in presence of electrolytes [59]. The variation of the surface charge is caused by the protonation/deprotonation of specific hydrogen ions bonding sites, e.g., oxygen vacancies, on the surface of the microstructure [60]. As reported by Cauda *et al.*, the pH sensitivity of the ZnO microwires can be further enhanced by functionalizing their surface with amino-propyl groups ($-NH_2$) that will contribute with additional reversible protonation/deprotonation activity in an electrolyte solution [59].

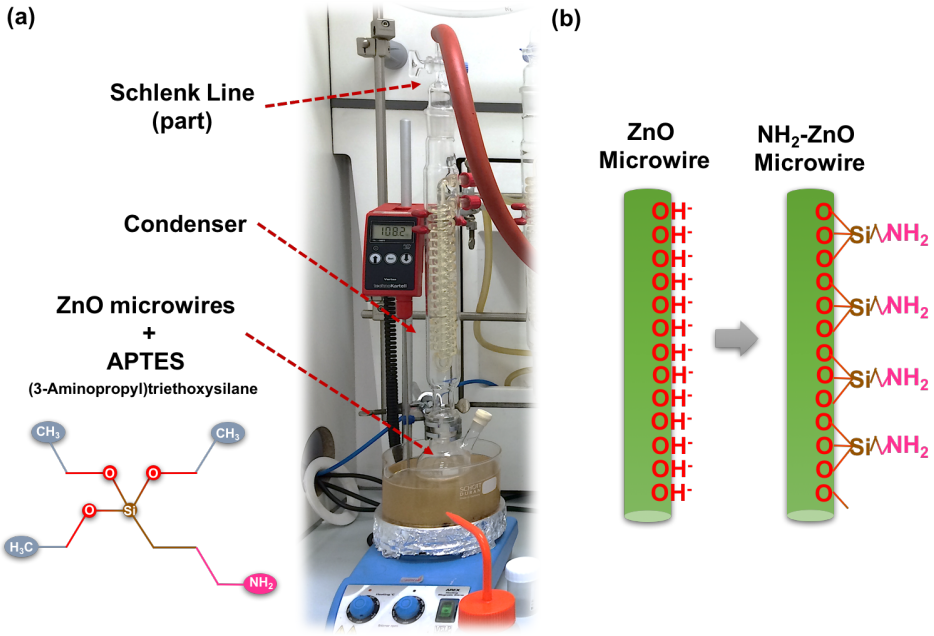

Fig. 2.12 Overview of the amino-propyl group functionalization of ZnO microwires. (a) Experimental setup used for the functionalization. A Schlenk line and a glass condenser tube are used for the 24 hours reflux of the solution composed by ZnO and APTES. (b) Schematic diagram of the ZnO microwires surface before and after functionalization with NH_2 groups.

The functionalization was carried out using (3-Aminopropyl)triethoxysilane (APTES) as functionalizing agent, and, specifically, 10 mol% of APTES are used, with respect to the total molar amount of ZnO (Figure 2.12). At first, 500 mg of ZnO microwires powder was outgassed in a round flask connected to a Schlenk line in order to remove the water molecules naturally adsorbed on the wires surface. Since the molecular weight of ZnO is 81 mg/mmol, 6.17 mmol of ZnO are present in 500 mg of powder. Then, the atmosphere is modified from vacuum to inert nitrogen flux, and 113 μL of APTES (corresponding to 0.0617 mmol) are added. The obtained solution is kept under reflux for 24 hours, always in nitrogen atmosphere. After the reflux, the resulting solution is washed with acetone and, at last, washed with bi-distilled water and dried overnight, exactly as in case of ZnO microwires synthesis. The confirmation of the correct -NH_2 functionalization of ZnO microwires using this procedure was previously verified by thermogravimetric analysis and published in [59].

The variation of the electrochemical properties of ZnO microwires according to specific external stimuli, is of great interest for the development of cutting-edge sensors, field-effect-transistors, energy harvesting devices and memories. Moreover their wire geometry is suitable for their integration in state-of-the-art microdevices. The use of ZnO microwires for UV-visible light, pH and temperature single and multi-parameter sensing, will be presented and discussed in Chapter 6.

2.2 $Mo_6S_4I_6$ Microwires

Another group of inorganic microstructures, $Mo_6S_4I_6$ microwires, was also studied using the electronic platforms developed in the present work. $Mo_6S_4I_6$ microwires are transition-metal dichalcogenide microwires, of the molybdenum-sulfur-iodine systems. This type of systems have been studied mainly for industrial applications thanks to their physical and chemical properties [62]. Moreover, $Mo_xS_yI_z$ ternary composites, can be the precursors for a less cumbersome synthesis of MoS_2 nanotubes, widely studied in the literature due to their applications in the fields of extreme low-friction lubricants [63], catalysts in desulfurization processes [64] and wear-resistant additives [62].

The ternary compounds $Mo_xS_yI_z$ can be synthesized with different stoichiometries obtaining materials with different electro-chemical and mechanical properties. Just as an example, $MoS_2 - I_x$, $Mo_6S_4I_6$ and $Mo_6S_2I_8$ microstructures have completely different electrical properties being semiconductors, wide band-gap semiconductors and metals, respectively [62]. Some of them can be also functionalized on along their surface. $Mo_6S_yI_z$ ($8.2 \leqslant y+z \leqslant 10$) nanowires were functionalized with gold nanoparticles and then modified into gold-decorated MoS_2 nanotubes by Kovič *et al.* [65]. The functionalization with gold nanoparticles strongly enhance the

performances of inorganic nanowires as sensors or bio-sensors. Kis *et al.*, instead, focused on the study and comparison of $Mo_6S_3I_6$ and $Mo_6S_{4.5}I_{4.5}$, both belonging to the general categories of $Mo_6S_{9-x}I_x$ nanowires. Besides simulating their atomic structure (Figure 2.13, a), using density functional theory calculations, they also performed transmission electron microscope (TEM) characterizations (Figure 2.13, c-d) as well as nano-mechanical ones to obtain the Young's Modulus [66]. $Mo_6S_3I_6$ are the $Mo_xS_yI_z$ microstructures more investigated in the literature. A typical scanning electron microscope (SEM) image of $Mo_6S_3I_6$ nanowires can be observed in Figure 2.13, b. Not only their synthesis is straightforward (it consists only of one step) [67] but, they can be useful to increase the electrical conductivity of polymeric compounds [68], as additive in synthetic-based oils, like polyalphaolefin [69], or, as innovative tool for molecular electronics if functionalized with small concentrations of mercury [70].

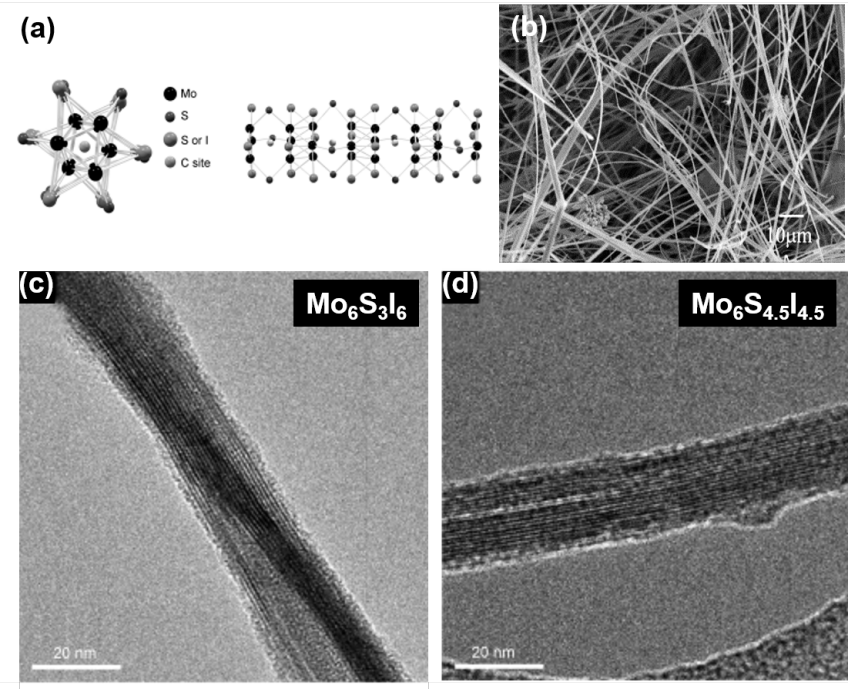

Fig. 2.13 (a) $Mo_6S_{9-x}I_x$ atomic structure viewed perpendicularly (left) or parallel (right) to the nanowire axis (reproduced with permission from [66], copyright Wiley, 2007). (b) SEM images of $Mo_6S_3I_6$ nanowires (Reprinted from Journal of the European Ceramic Society, Vol. 27, D. Vrbanic, S. Pejovnik, D. Mihailovic, Z. Kutnjak, Electrical conductivity of $Mo_6S_3I_6$ and $Mo_6S_{4.5}I_{4.5}$ nanowires, Pages No. 975-977, Copyright 2007, with permission from Elsevier [71]). (c)-(d) TEM images of $Mo_6S_3I_6$ and $Mo_6S_{4.5}I_{4.5}$ nanowires [66] (reproduced with permission from [66], copyright Wiley, 2007).

Although several methods can be chosen to synthesize this kind of microstructures like sulfurization, template assisted growth or precursors pyrolysis, the quicker,

simpler and mostly used one is the direct synthesis from the vapor phase [72]. This technique is based on the creation of a super-saturated vapor phase that, if the correct reaction/condensation kinetics are recreated, will initiate a chemical reaction responsible for the initial nucleation of nanometric particles [73]. The further condensation of the super-saturation will then lead to the agglomeration of new particles on the formed nuclei, hence forming different types of nano/micro-structures. One of the easiest methods to obtain a super-saturation phase involves the heating-induced evaporation of a solid material into a background gas [73]. Usually, for the synthesis of $Mo_6S_4I_6$ microwires, molybdenum, sulfur and iodine powders are evaporated in quartz furnaces with a specific molar ratio equal to 6:3:9 [74].

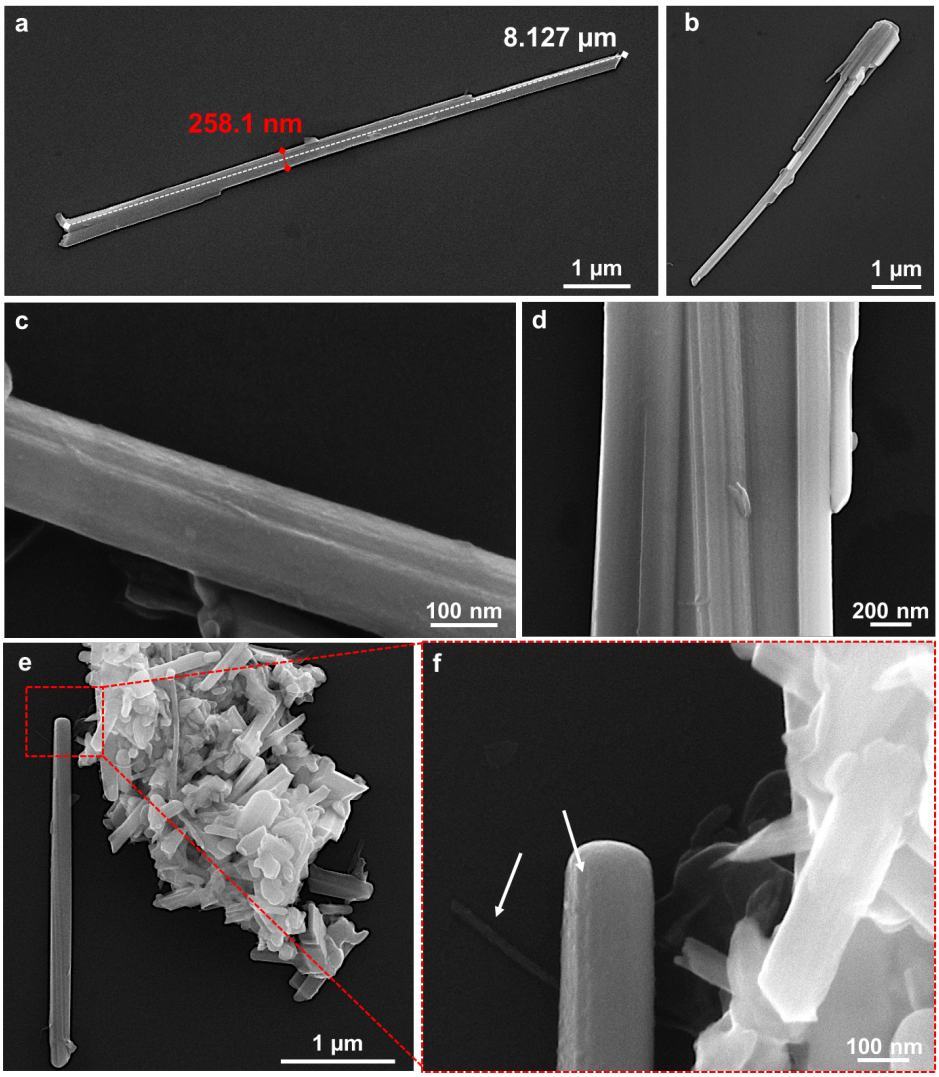

Fig. 2.14 Scanning electron microscope images of $Mo_6S_4I_6$ microwires. The microwires are formed by bundles of wires between 200 nm and 800 nm width and between 8 μm and 15 μm long ((a), (c)). The width of each bundle corresponds to $\sim$ 1 μm ((b), (d)). The smaller pieces of microwires formed due to the sonication process tend to aggregate together (e), while, in some cases the sonication is able to isolate individual wires of nanometric size that can be also observed embedded in the bigger bundles (f).

The $Mo_6S_4I_6$ microwires characterized in the present work were kindly supplied in powder form by Prof. Dr. Irena Drevenšek Olenik from the Faculty of Mathematics and Physics, University of Ljubljana within the COST Action COINAPO. The microwires powder was then dispersed in isopropanol (2-propanol, Sigma Aldrich, USA) in order to be handled and to disrupt microwires aggregations. If characterized with SEM, see Figure 2.14, they appear as a bundle of multiple microwires aligned one next to the other (width between 200 nm and 800nm, length between 8 μm and

15 μm). The typical dome termination, identified also by Remskar *et al.* [74], can be clearly recognized.

The bundle structure of $Mo_6S_4I_6$ was also reported by Hassanien *et al.*, although they reported about bundles of wires with width between 2 nm and 5 nm [62]. This can be related both to the extended sonication time of the microwires solution (between 2 and 3 days) and to the fact that, after the sonication, only the top most solution was collected, i.e., the one containing the smaller structures. In the present work, the sonication time of the solution of $Mo_6S_4I_6$ microwires was of only 2 - 3 minutes since the focus of the work was to deal with micro- and not nano-structures. Moreover, the sonication of the solution causes the formation of aggregates deriving from the combination of broken wire fragments (Figure 2.14). The higher is the number of these aggregates and the more it will be necessary a filtration procedure in order to collect only the desired wire structures. If higher magnifications are reached (Figure 2.14 (d) and (f)), the nanometric-size wires identified by Hassanien *et al.* can also be recognized either as stand alone (Figure 2.14 (f), left arrow) or as embedded in the bigger bundle (Figure 2.14 (f), right arrow).

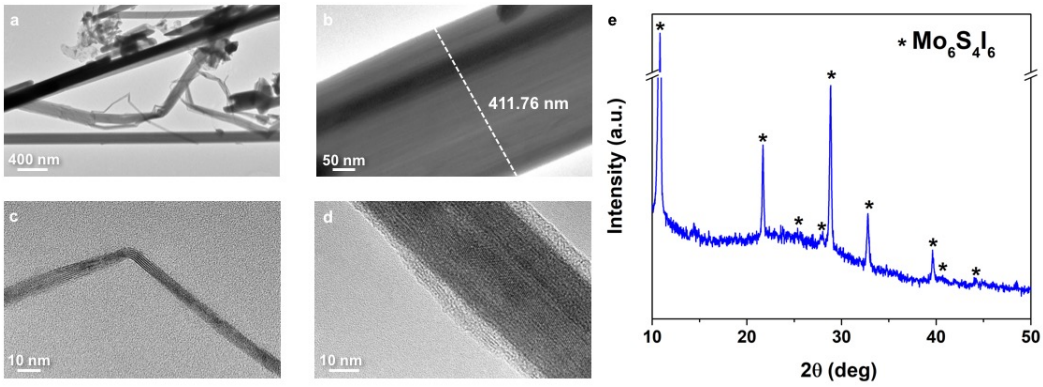

Fig. 2.15 TEM images (a)-(d) and XRD spectrum (e) of $Mo_6S_4I_6$ microwires.

The bundle morphology can also be appreciated from TEM imaging (2.15, a-d). Both wires of 10 nm of diameters and bigger bundles of 400 nm can be observed at lower magnification. The crystal nature of $Mo_6S_4I_6$ wires, reported also in the literature [74], was clearly recognizable from high-resolution TEM (HRTEM) images shown in Figure 2.15, c and d. The X-ray diffraction (XRD) pattern of $Mo_6S_4I_6$ microwires disclosed the presence of five sharp peaks of high intensity at 2θ values of about 10.81°, 28.85°, 21.71°, 32.79° and 39.72° (in order of decreasing intensity), corresponding to $Mo_6S_4I_6$ (International Center for Diffraction Data, ICDD, database, software PC-PDFWIN, PDF N. 390574). These well defined peaks can be associated to big crystals that seems expanding along the microwire length. The broader smaller peaks at about 25.30°, 28.01°, 40.69° and 44.21° revealed, instead, that also some smaller nano-crystals were present (Figure 2.15,

c-d). Nevertheless, due to the lack of literature about the exact crystal structure of $Mo_6S_4I_6$ microwires, it was not possible to extract also the detailed crystal planes indexing of the material. Further studies are required to fill this gap so that e.g., with additional and more resolved HRTEM imaging the exact distance between crystal planes can be revealed.

In Chapter 6, the the variation of the electrical properties of $Mo_6S_4I_6$ microwires will be studied using the customized electronic platform developed in the present work.

2.3 Cardiac Cells

In sections 2.1 and 2.2 different microstructures, whose variation of the electrical properties can be of high interest for sensing applications were presented. But, what happen if the same paradigm is applied to "living microstructures", i.e., cells? Necessarily, numerous additional challenges must be faced related to the need of keeping the microstructure not only alive, but, also, healthy, so that all the physiological characteristics and functions remain unchanged.

As anticipated in Chapter 1, in the last decades, scientists with completely different backgrounds have cooperated to integrate engineering in medicine and viceversa. Specifically, regarding the field of cardiac engineering, extensive studies have been performed at the border between electrical engineering and cardiology due to the electrical activity of cardiac cells. This subject has been studied from several points of view resulting in different branches of knowledge like, e.g., cardiac tissue engineering [75], implantable devices like pacemakers [76], vascular stents [77] or stretchable electronics *in vivo* patches [78], as well as CMOS-based multi-electrodes arrays for the stimulation and read-out of the electrical activity of cells [79–81]. For example, Xu *et al.* 3D printed an elastic multi-functional membrane, with embedded electrical, thermal and optical stimulation sites as well as sensors for pH, temperature and mechanical strain [78] (Figure 2.16-a), that can be directly applied on the heart. Therefore, they integrated metals, oxide or not, in order to help clinical cardiologists and fundamental researcher to map and stimulate multiple physiological parameters of the heart with high density and reliable physical *in vivo* coverage.

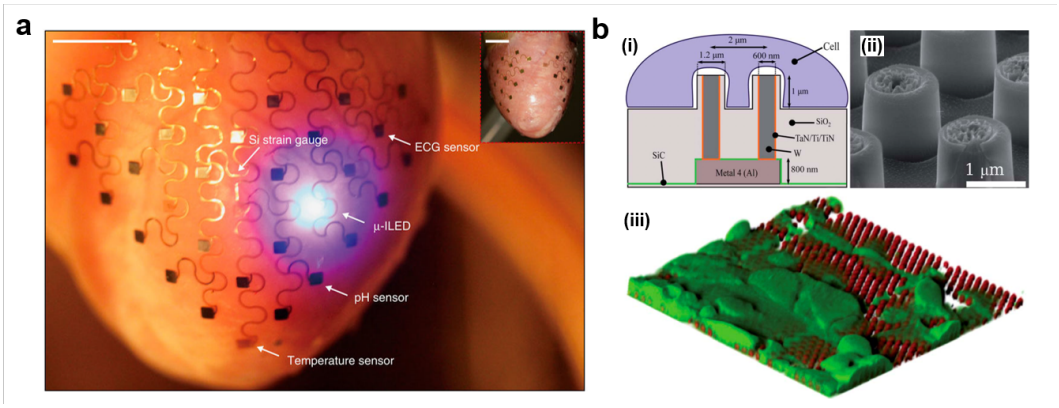

Fig. 2.16 Examples of integration between electronics and biology. (a) 3D elastic electrodes membrane enveloping a rabbit's hearth for multi-parametric mapping and stimulation of physiological parameters (Adapted by permission from Macmillan Publishers Ltd: Nature Communications, reference [78], copyright 2014). (b) CMOS multi-electrodes array for sensing and stimulating single cardiac cells. The micro-nail structure (ii) allows the stimulation of individual cells (adapted from [80] with permission of The Royal Society of Chemistry).

Differently, Abiri *et al.*, designed a miniaturized pacemaker, with a diameter of 3.8 ± 0.7 mm, that could be remotely controlled exploiting inductive power transfer in order to obtain a lead-less device hence, getting rid of the side effects related to the use of leads [76]. This was possible by designing the logic circuitry within the transmitting parts. Moreover, the extreme miniaturization allows the implant to be placed in the anterior cardiac vein hence avoiding mechanical failure points where, instead, standard implants need to be included in. Electrical engineering can also give a powerful contribution in the study and understanding of fundamental behaviors and mechanisms of cardiac cells thanks to the development of integrated multi-electrode arrays platforms capable to read-out intra- and extra-cellular electrochemical signals cells while also stimulating them. This technique is of particular interest for elctrogenic cells like cardiac cells and neurons. These systems, are able to take advantage of the miniaturization of CMOS circuits to perform, in few millimeters, advanced and multiple complex operations, like reading extremely noisy electrical signals from liquid environments while at the same time applying an electrical stimulation. For instance, Huys *et al.*, reported about an array of 16384 active sensors integrated on a 0.18 μm CMOS chip for recording electrical signals and stimulating individual cardiac cells [80]. The electrodes surface was patterned with thousands of micro-nails, ranging from 1.2 to 4.2 μm (see Figure 2.16-b), in order to achieve single-cell electrical stimulation. More details about CMOS multi-electrodes arrays for cardiac cell stimulation and recording will be presented in Chapter 4.

Before entering going in further details about the potentialities of the integration of electronics and medicine, the structural properties and fundamental electromechanical activity of cardiac cells will be described in Section 2.3.1.

2.3.1 Cardiac Cells Structure and Properties

The aim of this section is to introduce the fundamental structures and functionalities of cardiac cells of interest for the experimental work performed in the thesis. Specifically, as described in details through the next sections of the manuscript, the goal is to interface cardiac cells, extracted from rats at first, with polymeric scaffolds, in order to clearly understand their behavior and their needs (Chapters 5 and 7), and, then, to use these information to electrically characterize them more efficiently using CMOS circuits potentialities (Chapters 4 and 8). For this reason, after a brief introduction about the heart structure and functions, more attention will be given to the intrinsic and structural conformation and activity of specific cardiac cells and their signaling pathway.

The heart is the indispensable motor in our body responsible for blood circulation. Thanks to the contraction of the cardiac tissue, the heart will keep contracting constantly around 3 billion times in an entire lifetime [82]. This powerful behavior is controlled by specific electrochemical signals called action potentials. These signals trigger the release of calcium ions stored inside the cellular membrane that will then stimulate the contraction of the cardiac muscle cells, i.e., cardiomyocytes.

Four chambers form the heart. Two chambers are on the right side, constituting the right atrium and the right ventricle, and two are instead, on the left side, i.e., the left atrium and the left ventricle. The two atria are in the upper part, one next to the other, while, the two ventricles are in the bottom (Figure 2.17). It is important to notice that the pumping activity of the atria only involves pumping the blood from the upper to the lower chamber. This is the reason why their size is smaller than the one of ventricles which, instead, need to pump the blood outside the heart towards the lungs or the whole body [83]. Consequently, as it will be described in Section 2.3.2, during the isolation of cardiomyocytes from rats hearts, in some cases, only the ventricles will be selected for the experiments for a higher cell quality efficiency. As the other organs, also the heart is surrounded by a membrane, called pericardium, mainly composed by connective tissue. The main internal wall, instead, is called myocardium and it is a complex structure mainly responsible of the heart contraction. It is predominantly composed by cardiomyocytes but also, collagen fibers, for structural support, blood vessels and fibroblasts are present [83]. Fibroblasts are the principal cells forming connective tissue and, one of their most important task is to produce the constituents of the extracellular matrix, like, .e.g, collagen, which represents the structural and biochemical support to every type of cell. In Figure 2.17, the complex muscular conformation of the heart can be observed. It can be appreciated how, muscle cells envelope and surround the heart cavities twirling in a spiral fashion. This twirling is what allows to the heart to pump blood with an extremely higher efficiency if compared to a straight conformation [83].

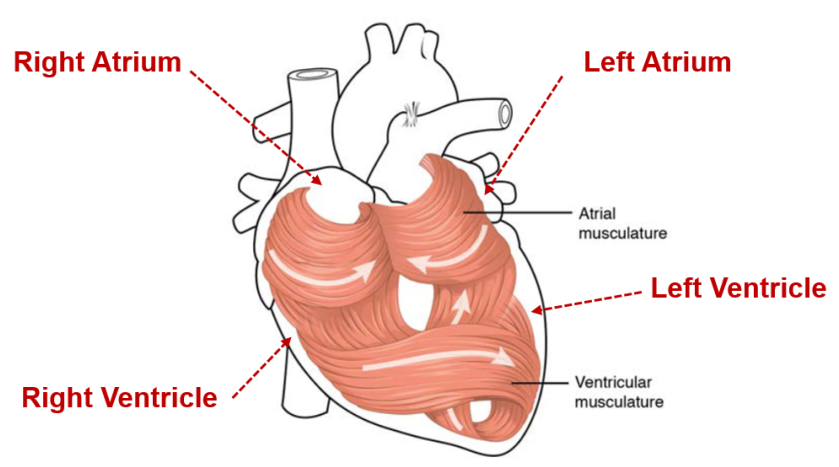

Fig. 2.17 Schematic diagram of cardiac muscles twirling in the 4 different heart's chambers sustaining the correct blood pumping activity (adapted from [83], licensed under a CC-BY-4.0 license, download for free at https://openstax.org/details/books/anatomy-and-physiology).

One of the main characteristics that regulates the contraction and relaxation of cardiomyocytes is their excitability, i.e., their membrane can change its electrical state propagating an electrical wave called action potential. For cardiac cells, this trigger can be both initiated by the nervous system but, at the same time it can be influenced by other local stimuli, e.g., hormones.

Cardiomyocytes are composed by several fibers, myofibrils, able to stretch and recover their shape according to the beating behavior they have to sustain (see Figure 2.18). The Greek word "*sarco*", which means flesh or muscle, gives a specific name to the cellular membrane (sarcolemma) and to the cytosol of cardiomyocytes (sarcoplasm). As detailed in Figure 2.18, myofibrils are encapsulated in the sarcoplasmatic reticulum responsible of regulating the exchange and storage of calcium ions related to their electrical activity. Specific prolongations of the sarcolemma, called T-tubules, where the calcium ions channels are located, are embedded in between the sarcolemma and the sarcoplasmatic reticulum and, they are the main responsible of the action potential propagation. Nevertheless, the real fundamental core for cardiomyocytes activity are sarcomeres. These functional units have a cylindrical shape and are formed by an ordered arrangement of thin (actin) and thick (myosin) contractile proteic myofilaments that, sliding one on the other, will result in the physical contraction of cardiac cells [83]. These are the responsible of the striated appearance of cardiac cells, as it can be observed from the histology image reported in Figure 2.18 a. The darker lines (A bands) correspond to myosin while, the lighter ones (I bands) to actin. When relaxed, the average length of an individual sarcomere can range between 1.8 and 2.4 μm [84]. The area at the center of a sarcomere and of the A band where the thick myosin filaments are not overlapped with actin ones, it's called H zone. The anchoring of the sarcomere to the cytoskeleton is possible thanks

to specific regions, exactly at the center of the H band, called M lines (see Figure 2.18).

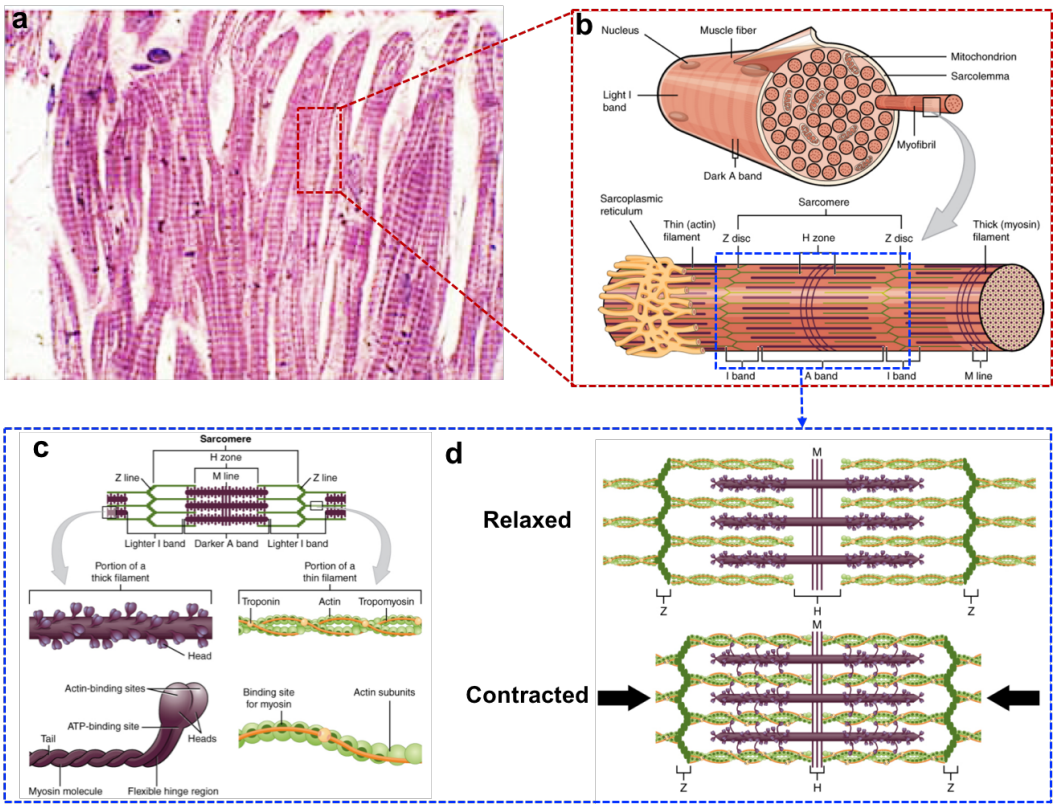

Fig. 2.18 (a) Histological examination under light microscopy of cardiac tissue myectomy (surgical procedure that removes the overgrown cardiac tissue in hypertrophy pathology). Cellular components, e.g., nuclei are marked in dark blue (adapted from [85], licensed under a CC-BY license). (b) Schematic diagram of a muscle fiber with details about the actin and myosin filaments behavior, (c)-(d), according to the sliding filaments model (adapted from [83], licensed under a CC-BY-4.0 license, download for free at https://openstax.org/details/books/anatomy-and-physiology).

As outlined in Figure 2.18, each sarcomere is delimited by two transversal structures, called z-discs, that also function as anchor points for actin and myosin. Two specific proteins, troponin and tropomyosin, on the surface of actin filaments, are responsible of the regulation of thin and thick filaments behavior. More precisely, myosin expose on its surface numerous globular heads (see Figure 2.18 c). Each globular head has both an actin and an adenosine triphosphate (ATP) binding site [84]. ATP is an energy-carrying molecule able to transfer its phosphate groups to other molecules, through a specific enzyme, producing energy that is then used where needed. Similarly, actin filaments also present some myosin binding sites, called G-actin monomers, in addition to their main backbone structure (F-actin). When the

sarcomere is relaxed, the actin binding sites are covered by tropomyosin protein, thus preventing its connection to the actin filament (Figure 2.18 c and d, up). Tropomyosin is also complexed with troponin hence completely passivating the myosin binding sites on actin. When calcium ions are present, they will bind to a specific sites on troponin hence leading to a conformational change and to the exposure of myosin binding sites on the actin filament [83]. The myosin head will be then attracted to the actin G-monomers where it will create a complex in presence of ATP thus leading to the shortening of the sarcomere [84]. This continuous process requires an extremely demanding amount of ATP. Since mithocondria are responsible for ATP production, it is not surprising that they represent 40% of the total cardiomyocytes volume [84]. All the different structures of sarcomeres can be directly observed through electron microscope analysis on tissue samples as shown in Figure 2.19.

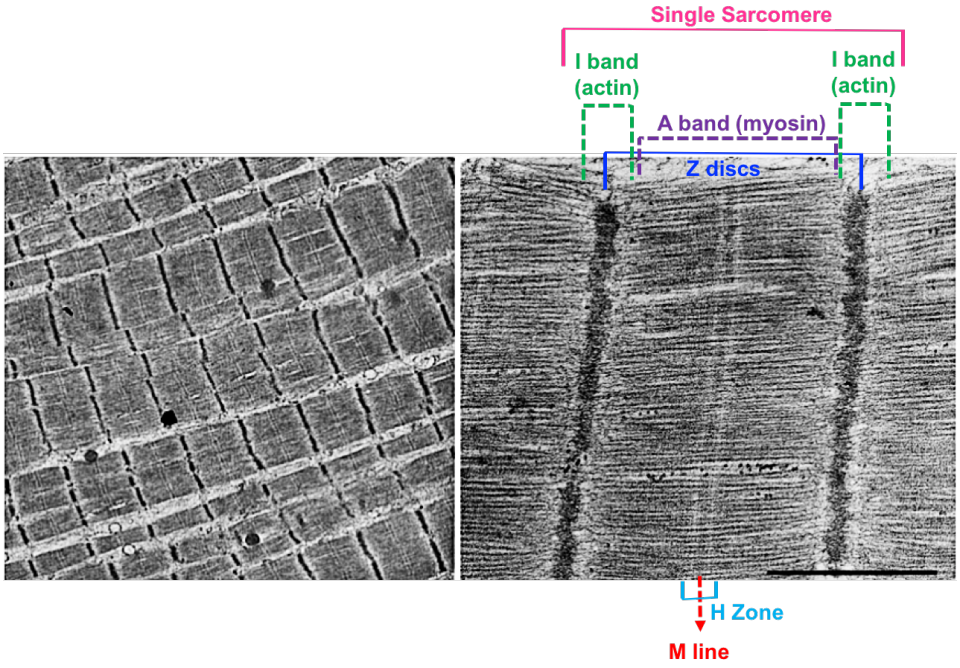

Fig. 2.19 Scanning electron microscope of cardiac myectomy samples at low (left) and high (right) magnification. All the components of the sarcomere structure like z disks, I and A bands, H zone and M line can be recognized. Scale bar 1 μm (adapted from [85], licensed under a CC-BY license).

Cardiac fibers are formed by numerous sarcomeres one next to the other, and, different fibers are joined together, at the sarcolemma, through intercalated disks which not only are the responsible of the wave-like contraction of muscle cells but, also, the contain two fundamental entities for a synchronized contraction: gap junctions and desmosomes (Figure 2.20).

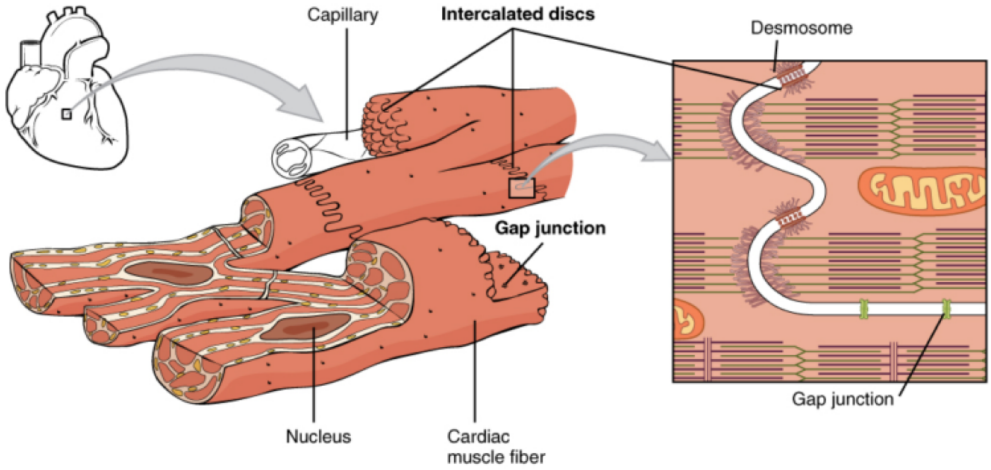

Fig. 2.20 Schematic diagram of intercalated discs joining together different cardiac fibers. The inset reports a detail about gap junctions and desmosomes, the two main constituents of intercalated disks. Adapted from [83], licensed under a CC-BY-4.0 license, download for free at https://openstax.org/details/books/anatomy-and-physiology.

Gap junctions are small molecular channels linking the sarcoplasm of different cardiomyocytes hence allowing the passage of the calcium ions current in order to have a synchronized contraction of the whole heart. When a group of cardiac cells are electrically coupled one with the other they for a bigger synchronized contracting unit called syncytium [83]. Specific antibodies can be used to mark different gap junction proteins through phosphorilation reactions in order to image gap junctions using fluorescence microscopy. Specifically, in the present work the markers for the gap-junction protein Connexin-43 will be used. This choice was supported by the fact that this is the most present connexin in mammalians hearts [82]. The analysis of this factor is important to understand the electrochemical coupling of a population of cardiomyocytes. Understanding the internal detailed structure of cardiac cells is fundamental in order to correctly interpret the results of fluorescent imaging characterization hence clearly observe not only the structure and health status but also the metabolic and electrical activity of the cells cultured *in vitro*. Plenty of antibodies, specific markers or phosphors can be used to achieve this task. When antibodies are used for the fluorescent imaging, the technique is often referred as immunostaining. In Figure 2.21 are shown different literature examples of fluorescent stainings of different details of cardiomyocytes exploiting the coupling of the target marker with a specific phosphor. In Figure 2.21 a, for example, wheat germ agglutinin (WGA) coupled to the commercial fluorescent dye Alexa Fluor 488 (AF-488) which emits at 519 nm, is used to mark the whole cardiomyocyte membranes. This is possible due to WGA ability to selectively bind to glycoproteins of the cell membrane hence it is often use to image the cross-section image of cardiac tissue [86]. Usually the nucleus is stained using specific fluorescent

markers capable to overcome the cell membrane and bind to the cell DNA. One example, shown in Figure 2.21-a and extensively used in the present work, is 4',6-Diamidino-2-phenylindole (DAPI) that emits strong blue light when bounded to the nucleus.

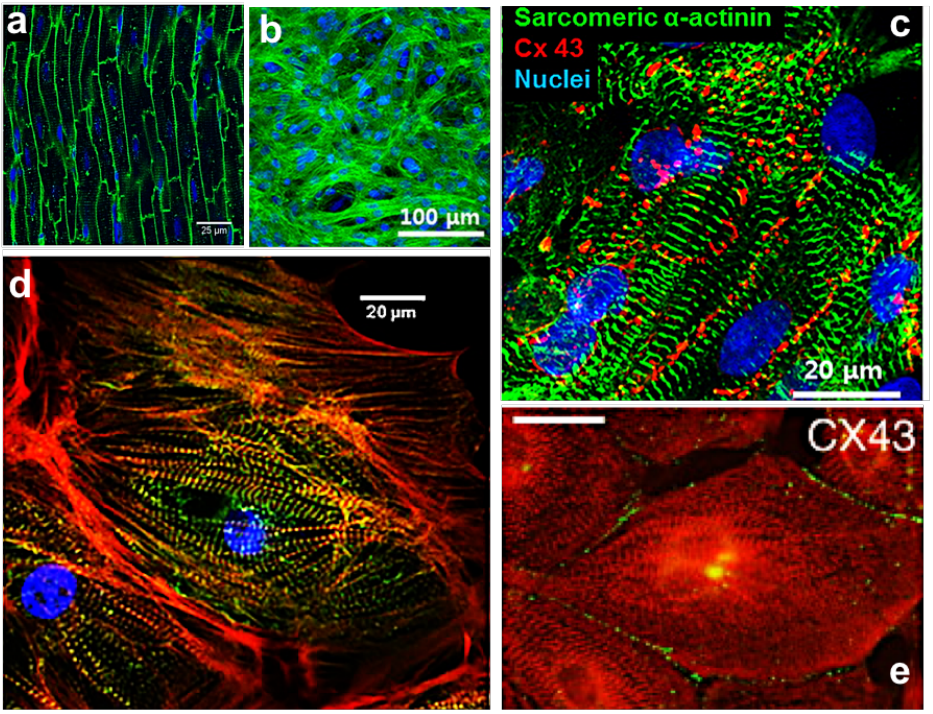

Fig. 2.21 (a) Cardiomyocytes histological section in which the nuclei are stained in blue using DAPI and the cell membrane in green using WGA-AF488 (adapted from [86], licensed under a CC-BY 4.0 license). (b) Confocal fluorescence microscope images of cardiomyocytes. F-actin filaments are stained in green while nuclei in blue (adapted with permission from [87]. Copyright 2013 American Chemical Society). (c) Immunostaining of cardiomyocytes after 8 days of culture. Sarcomeric-α-actinin is marked in green, nuclei in blue and connexin-43 in red (adapted with permission from [87]. Copyright 2013 American Chemical Society). (d) Immunostaining of cardiomyocytes showing sarcomeric-α-actinin in green, F-actin in red and nuclei in blue (adapted from [88], copyright 2016, the American Physiological Society). (e) Immunostaining of connexin-43 in green and sarcomeric-α-actinin in red. Scale bar 25 μm (reprinted from Stem Cell Research, Vol. 1, Marie-José Goumans *et al.*, TGF-β1 induces efficient differentiation of human cardiomyocyte progenitor cells into functional cardiomyocytes in vitro, Pages No. 138-149, Copyright 2008, with permission from Elsevier [89]).

The elongation of actin filaments can be also clearly imaged (Figure 2.21 b). They appear as long interconnected filaments representing one of the main portion of the cell cytoskeleton. At high magnification, it is also possible to observe the regular

pattern of cardiomyocytes z-disks by using a marker for the protein sarcomeric-α-actinin, present on their surface and linking the z-disks to the actin filaments (Figure 2.21 c-e). This is one of the staining protocol used more often since it can clearly reveal the conformation of cardiac cells sarcomeres. In Figure 2.21 c, the z-lines of sarcomeres, and their regular repetition along the muscle fiber can be clearly observed in green. Moreover, the red fluorescent signal, represents the antibody specific for connexin-43, thus indicating the location of the gap-junctions electrically coupling different cardiomyocytes. The distribution of gap-junctions at the connection points between different cardiomyocytes can be also clearly recognized by the green fluorescent signal in Figure 2.21 e. By choosing opportunely different fluorescent dyes for different targets of interest multiple stainings can be done at once in order to have a more comprehensive overview of the cellular structure. As an example, in Figure 2.21 d, nuclei are marked in blue, sarcomeric-α-actinin in green and F-actin in red. Specifically, the co-localization of actin filaments and sarcomere z-disks can be appreciated.

As it will be deeply discussed from Chapter 5 on, fluorescent immunostaining is an extremely important tool in order to understand the interaction, proliferation and activity of cardiomyocytes with synthetic materials like, e.g., polymeric scaffolds. Moreover, as it will be explained in Section 2.3.2, when cardiomyocytes are extracted directly from animal tissues, different populations of cells may be present at the same time, mainly cardiomyocytes, cardiac fibroblasts and red blood cells. Immunostaining can be a powerful tool to be able to examine the quality and characteristics of the final outcome of the cell extraction procedure. When cardiomyocytes are cultured *in vitro*, the immunostaining of connexin-43 and, more precisely, its spreading and density all over the culture is one of the key factors to understand of the grown cardiomyocytes effectively connect and electrically couple one with the other forming a synchronized cardiac tissue. As anticipated, this is related to the ability of gap-junctions to allow the passage of ions between different cells, i.e., the propagation of the electrical signal. Calcium ions are the main responsible of the electrical conductivity, i.e., contractility of cardiac cells. The ions balance of the cell defines a specific resting potential from the inside of the cell and relative to the outside that is usually around -80 or -90 mV for contractile cardiac cells [83]. The main ionic channels involved are sodium, calcium and potassium ones. In resting condition, potassium channels are opened, constantly leaking potassium ions, while, calcium and sodium ionic channels are closed. The trigger of an action potential will make the fast sodium channels to open leading to a fast depolarization of the cardiac cell (3-5 ms [83]). When the membrane potential will reach -40 mV, slow calcium channels will open leading to a slow influx of calcium ions in the cell. When the membrane potential will further increase up to around 30 mV, the sodium channels will close and a plateau condition is reached (see Figure 2.22 a). In this condition, the membrane potential slowly decrease due to the opening of a small number of potassium channels that will cause a slow out-flux of potassium ions. Due to the slow

dynamics, this plateaus is relatively long, around 175 ms [83]. When the membrane potential reach 0 mV, calcium channels will close while the remaining potassium channels will open thus leading to the cell repolarization in about 75 ms. At this point the cycle with repeat. The increase of the sarcoplasmatic concentration of calcium ions will cause the binding of these ions to troponin, hence allowing the binding of actin and myosin, previously described in this section, that will cause the cell contraction. An increase of calcium ions concentration from the nanomolar to the micromolar regime is sufficient to trigger this process [84]. The slow dynamics of the plateau, also referred as refractory period, is thus necessary in order to allow the cardiac cell to fully contract before the subsequent action potential [83]. This is important in order to allow the ventricle to fully deplete of blood before the next contraction.

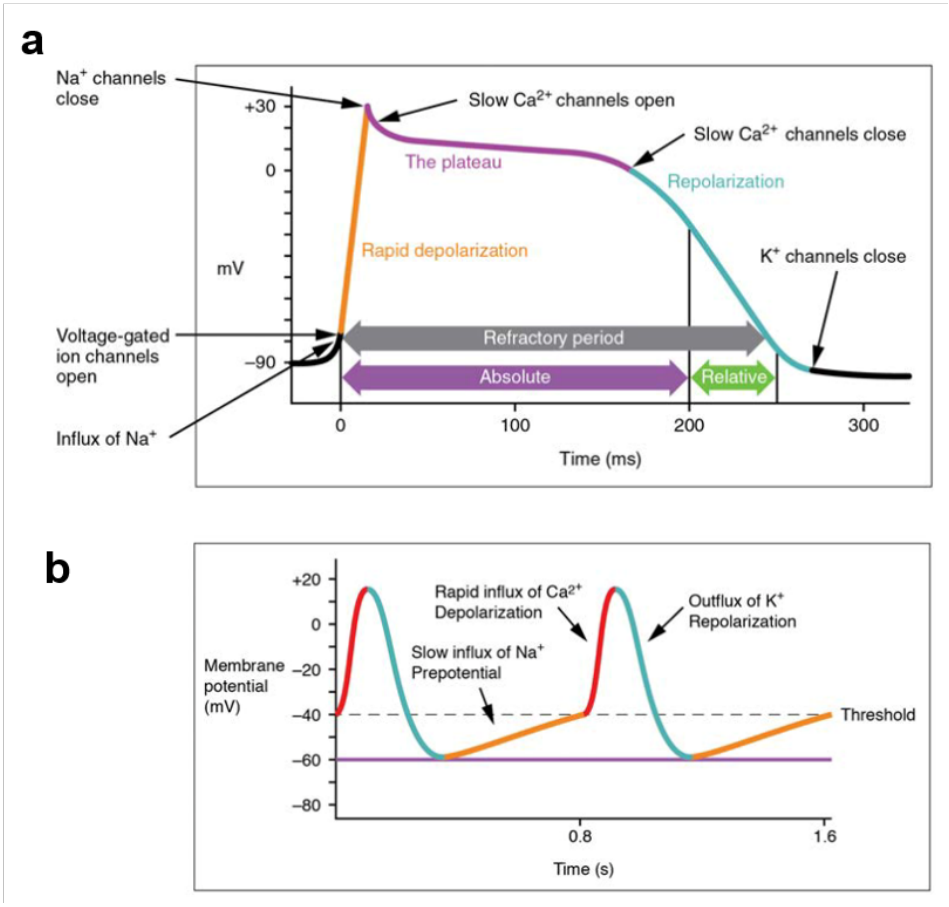

Fig. 2.22 Schematic behavior of the action potential of a contractile (a), and pacemaker (b), cell. Adapted from [83], licensed under a CC-BY-4.0 license, download for free at https://openstax.org/details/books/anatomy-and-physiology.

The described conduction mechanism is the one displayed by cardiac contractive cells. Nevertheless, there is a different family of cardiac cell, called cardiac conductive or pacemaker cells, which exhibit spontaneous repolarization. This means that they do not need external stimulation to initiate an action potential. This is possible due to the instability of their membrane potential. Since they have fewer potassium channels than contractive cardiomyocytes, their resting potential usually is never higher than -60 mV (Figure 2.22 b). Their membrane potential instability is due to specific sodium channels which are always open and grants a slow influx of sodium ions. When the potential reaches -40 mV the (spontaneous) depolarization occurs, and a repolarization mechanism similar to the one of contractile cells will occur [83]. It is important to underline as the dynamics of pacemaker cells is much faster than contractile ones and they are the ones that will define the heart rate since, as previously underlined in this section, all cardiomyocytes are coupled through gap junctions. When one cardiomyocytes depolarize all the neighboring ones will follow in a chain reaction. The faster pacemaker cell will cause the depolarization of neighboring pacemaker and contractile cells, leading to their depolarization, i.e., propagating the action potential.

In the next section, Section 2.3.2, the experimental protocol adopted in the present work in order to isolate cardiomyocytes from animal tissue will be described.

2.3.2 Cell Isolation From Animals: Experimental Protocol

The reliability of electrophysiological studies on cardiomyocytes strongly depends on the quality and organization of the cell culture. At first, it is important to underline how the 2D intrinsic nature of *in vitro* studies leads to several limitations deriving from the 2D tissue conformation that differs from its natural 3D one *in vivo*. This is why, biocompatible materials, originated from the same constituent of living tissues can be extremely important. Not only they can improve the reliability of *in vitro* studies but, also, they can be engineered in 3D-like cell culture substrates closer to *in vivo* conditions than standard cell culture supports. Nevertheless, numerous models have been developed by scientists during the years to study cardiomyocytes. Among them, there are two main branches. The first one is based on the use of primary cardiomyocytes, hence, for each experiment the cells are directly extracted from animal tissue while, the second one makes use of commercial cell lines. In the first case, as it will be discussed in details at the end of this section, specific enzymes are used in order to cleave the bondings between cells, hence releasing them from the extra cellular matrix forming the animal tissue. Usually, the most used animal models are neonatal rats cardiomyocytes, even if also embryonic or adult rats are used. Cardiomyocytes have been reported to be extracted also from other animal models like mouse, chick or zebrafish [90]. Nevertheless, the mouse-derived cardiomyocytes are much more fragile than the rats counterpart, the chick-

derived ones are suitable only up to the embryonic stage while, the zebrafish hearts presents only two chambers, instead of four [90]. Regarding instead rats-derived cardiomyocytes, sometimes also adult rats are selected for the cell isolation [91]. Although adult rats cardiomyocytes present a rectangular shape, closer to *in vivo* conditions, while in neonatal ones sarcomeres are not completely organized yet, they are not always considered the best choice since they can be cultured only for a very short time [90]. This is due to their difficulty to adhere and proliferate to plastic cell culture supports, if not properly additionally functionalized, and to the fact that their natural beating activity will quickly stop if not artificially stimulated [92]. Moreover, the cardiac cells isolation is more laborious than in case of neonatal ones. It requires a specific system, called Langendorff apparatus, to extract cells of high quality, that involves the perfusion of the enzymatic digesting solution through the entire hearth through a cannula inserted in the aorta instead of being just mixed with minced heart pieces as in case of neonatal rats [91]. Human-induced pluripotent stem cells can be additionally used to derive cardiomyocytes. But, besides being highly expensive, their physiology and architecture remains still immature, up to now, making them more suitable for stem cell differentiation studies than for fundamental electrophysiologial ones [90, 93]. Several cell lines can be found commercially but, none of them is capable to faithfully reproduce healthy *in vivo* cardiomyocytes being more similar to skeletal muscle cells configuration instead like, e.g., the rat embryonic-derived H9c2 line [90]. One of the most used is the cell line called HL-1 that is derived from the atria of tumor lineage mice. Although, contrarily to primary cardiomyocytes that cannot duplicate in culture but just grow in size, HL-1 cells can be passaged indefinitely, they are artificially engineered and they still resemble early stage immature embryonic cardiomyocytes [90].

The trade-off between a simple experimental procedure and a good yield and reliability of cell culture is the reason why, in the present work, mainly neonatal or embryonic rats cardiomyocytes have been used. Moreover, they are less sensitive to calcium ions variations, that may occur during the isolation process reducing the process complexity [94]. Only for a specific subset of experiments, where cardiomyocytes were deposited on CMOS chips, embryonic rats cardiomyocytes have been selected due to the lower percentage of cardiac fibroblast and death cells present.

Cell Isolation Protocol - Neonatal Rats. The presented protocol was optimized at the facilities of the Khademhosseini Laboratory in Boston (see the Preface for the complete affiliation list). The protocol was adapted and optimized from [5] and the procedures with experimental animals were approved by the Institute Committee on Animal Care. The animal sacrifice was performed by Professor Yi-Chen Li (Associate Professor, School of Light industry and Engineering, South China University of Technology), while, the remaining steps of the cell isolation, were carried

out by the author. At first, all the metallic tools used for the dissection were bleached, cleaned with 70% ethanol and then autoclaved at 120 °C for a complete sterilization. Moreover, all the solutions were filtered through a 0.22 μm Millipore filter to avoid contamination. After the extraction from two days old Sprague–Dawley neonatal rats (previously sacrificed by decapitation), the hearts were washed in a Hank's balanced salt solution (HBSS, Gibco, USA) with no calcium and no magnesium (see Figure 2.23). The HBSS is a solution of different salts, like e.g., KCl (potassium chloride), $NaHCO_3$ (sodium bicarbonate) or NaCl (sodium chloride). It is frequently used as pH buffer for cell cultures that require a pH between 7.0 and 7.4 in order to allow cells to grow and proliferate especially when the cell culture is exposed to normal atmosphere out of the incubator. In fact, due to its poor reactivity and low salts concentration, the buffer ability of HBSS is quickly saturated in the CO_2-enhanced atmosphere of cell culture incubators. It is is important to underline that the specific HBSS used for cell isolation is without calcium and magnesium since they both are inhibitors for the subsequent first digesting enzyme: trypsin. Therefore, by maintaining or washing the dissected tissue with HBSS, with no calcium and magnesium, it is possible to both stabilize the pH, avoiding tissue damages, and to decrease the concentration of excess divalent cations and proteins that inhibit trypsin activity.

After the washing with HBSS, necessary also to remove the excess blood remained from the surgery, the aorta and the upper atrial part of the hearts were removed in order to reduce the contamination of non-beating species in the final culture, e.g., connective tissue. Afterwards, the hearts were transferred in a solution of HBSS with 0.05 % trypsin (Gibco, USA) where they were cut in small pieces, around 0.5 - 1 mm^3, with sterilized scissors (Figure 2.23, 3). Trypsin, is a protease, i.e., an enzyme capable to cleave the covalent bonds linking two amino acids, called peptide bond, and, usually, the commercial one is extracted from porcine pancreas [94]. More specifically, it is a pancreatic enzyme selective to lysine and arginine amino acids which play a crucial role in membrane proteins activity and molecular exchanges [95]. It is extensively used in cell culture to detach cells from culture plastic substrate since it cleaves the bonds that cells develop to attach to the substrate. After mincing in a sterile 60 mm x 15 mm petri dish, the heart pieces were shaked overnight at 4 °C on an orbital shaker, for the tissue pre-digestion step, after throughly sealing the container with parafilm, in order to avoid contaminations (Figure 2.23, 4). The next day, after maximum 15-16 hours from the pre-digestion, in order to avoid trypsin to start damaging the cells, a second digestion step, of higher intensity, was started using a different and more effective enzyme: collagenase type II (Worthington Biochemical Corporation, Lakewood, NJ). Also collagenase is a protease but its activity affects the triple helix bonds of collagen fibrils constituting the extracellular matrix [94]. Briefly, collagenase is capable of cleaving the bonds linking the cells to the extra cellular matrix network, that establishes the animal tissue, hence isolating individual cells. Numerous types of collagenase, with slightly different characteristics and performances, can be found commercially like type I,

type II, type III and type IV, just to list a few. For the isolation of neonatal rats cardiomyocytes,collagenase type II was selected, which is extracted from the colH gene of the bacterium *clostridium histolyticum* and, due to its highest enzymatic activity, is specifically useful for highly fibrous tissues digestion like the heart one.

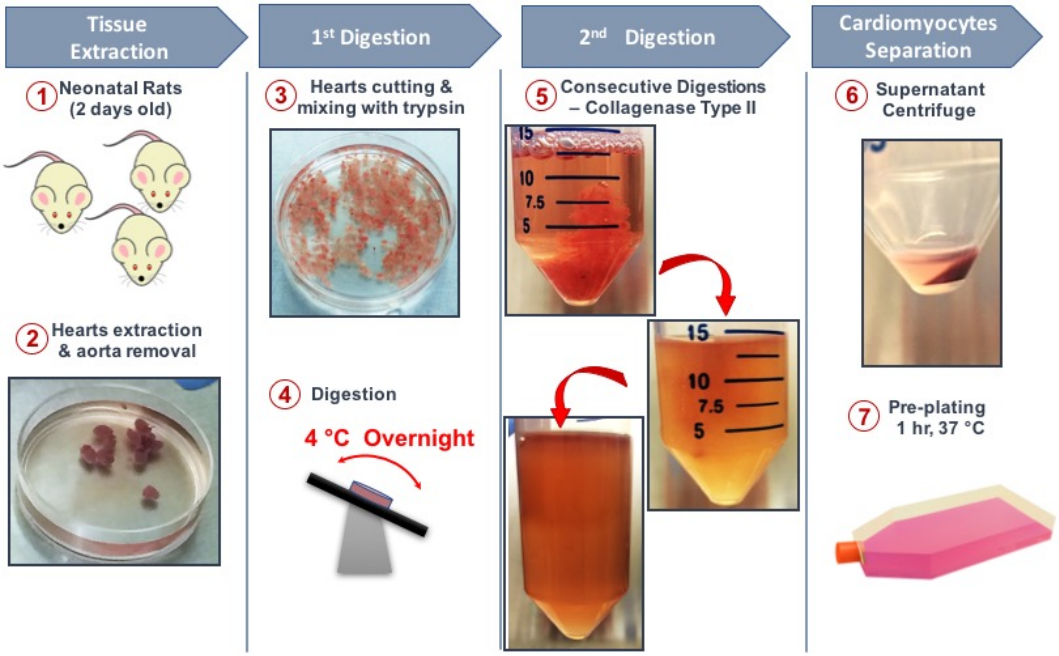

Fig. 2.23 Schematic diagram of the experimental protocol used for cardiac cells isolation. At first, whole hearts are extracted from neonatal rats and the aorta is removed (1-2). Then, the hearts are minced in pieces of about 1 mm^3 in an HBSS solution with 0.05 % trypsin with no EDTA and shaked overnight at 4 °C (3-4). The next morning, after consecutive digestions in a solution of HBSS with 0.1 wt. % of collagenase type 2, the hearts pieces are completely digested (5). The obtained solution is then centrifuged at 1000 rpm for 5 minutes and the resulting pellet is then plated in a cell culture flask and incubated for 1 hour at 37 °C to allow cardiac fibroblast to adhere to the flask (6). At last, the supernatant is collected from the flask and ready to be seeded on the samples (7).

More in details, 30 mg of collagenase type II were dissolved in 30 mL of HBSS (0.1 wt.%) and then filtered through a 0.22 μm filter for removing bacteria or contaminants eventually present. Then, the minced heart pieces were collected, trying to minimize the amount of trypsin collected, and moved to a 50 mL conical tube with 10 mL of cardiac cell culture medium (Figure 2.23, 5). The cardiac medium was prepared starting from basic Dulbecco's modified eagle medium, (DMEM, Gibco, USA) with the addition of 10% of fetal bovine serum (FBS, Gibco, USA), rich of cellular growth factors, 1% of 200 mM L-glutamine (Gibco, USA) an amino acid important for cell growth and gene expression as well as for cardioprotection [96], and 100 units mL^{-1} of penicillin-streptomycin (Gibco, USA). Then, the first of four

digestion steps started by slowly swirling the solution at 37 °C for 7 minutes in a water bath. When completed, the majority of the solution was carefully removed from the conical tube leaving only 1 - 3 mL containing the mixture of tissue and released cells. After the addition of other 10 mL of fresh collagenase solution, the process was repeated other 3 times. As it can be observed from Figure 2.23 5, during the consecutive digestions, the turbidity of the solution was constantly increasing, due to the higher number of cells released from the tissue, while, at the same time, the tissue pieces in solution were becoming smaller and smaller up to the complete digestion. To avoid loosing cardiomyocytes during the changes of the collagenase solutions, during the last two digestions the solution was not removed with the pipette gun but, all the solution was filtered using a cell strainer of 70 μm is order to allow the cells to pass through while stopping the mucous tissue debris remained after cells removal. After centrifugation at 1000 rpm and 37 °C for 5 minutes, the resulting pellet was seeded in a T175 cell culture flask with 15 mL of cardiac medium, pre-heated at 37 °C, and it was incubated for 1 hour into the cell incubator. This step is called pre-plating, and it is necessary in order to allow all the non-myocytes species, like fibroblast and endothelial cells, to adhere to the flask substrate (see Figure 2.24). In fact, the adhesion dynamics of cardiomyocytes is much slower than the one of fibroblast and endothelial cells, and they can be found in suspension also after several hours from plating. Although, exceeding 1 or 2 hours of pre-plating would lead to a purer cardiomyocyte final culture, it would also cause some cardiomyocytes to start adhering to the flask substrate hence reducing the final cardiomyocytes yield. In the present, work, due to the demanding number of cells to be seeded on the 3D-like scaffold, a pre-plating time of only 1 hour was preferred although some cardiac fibroblasts were still present in the final culture. Nevertheless, if the cell isolation was carried out correctly, the number of fibroblasts was not so high to damp the beating activity of cardiomyocytes, due to their faster growth that would surpass the myocytes one and, instead, was helping to recreate an environment closer to the *in vivo* one.

After the pre-plating step, the cardiomyocytes can be collected from the flask by just carefully collecting all the supernatant. They can then be seeded on the desired sample or, they can be centrifugated and then re-suspended in cardiac medium if a higher concentration is needed. As it can be observed in Figure 2.24, the cardiac fibroblasts continue to grow and proliferate in the flask after cardiomyocytes removal. They can be cultured with standard procedures. They can be passaged up to 5 times and they can also be frozen. They grow on standard cell culture substrates with an extremely flat conformation, that can be particularly appreciated from bright field images (Figure 2.24, b). The fluorescent staining (after fixation with 4% paraformaldehyde) of F-actin filaments (Alexa Fluor 488® phalloidin, Invitrogen™, USA) and nuclei (DAPI, Invitrogen, USA) revealed a strongly interconnected elongated F-actin network with long filapodia, as expected from the literature [97]. Filapodia are elongated projections of the cytoplasms and they are

the main responsible of cells adhesion and movement. The nucleus is elliptical and surrounded by a branched cytoplasm. This intricated cytoskeleton evolution is strongly related to their important function of forming sheets that link and sustain together all the heart by lying along the cytoskeleton of the cardiomyocytes network [97].

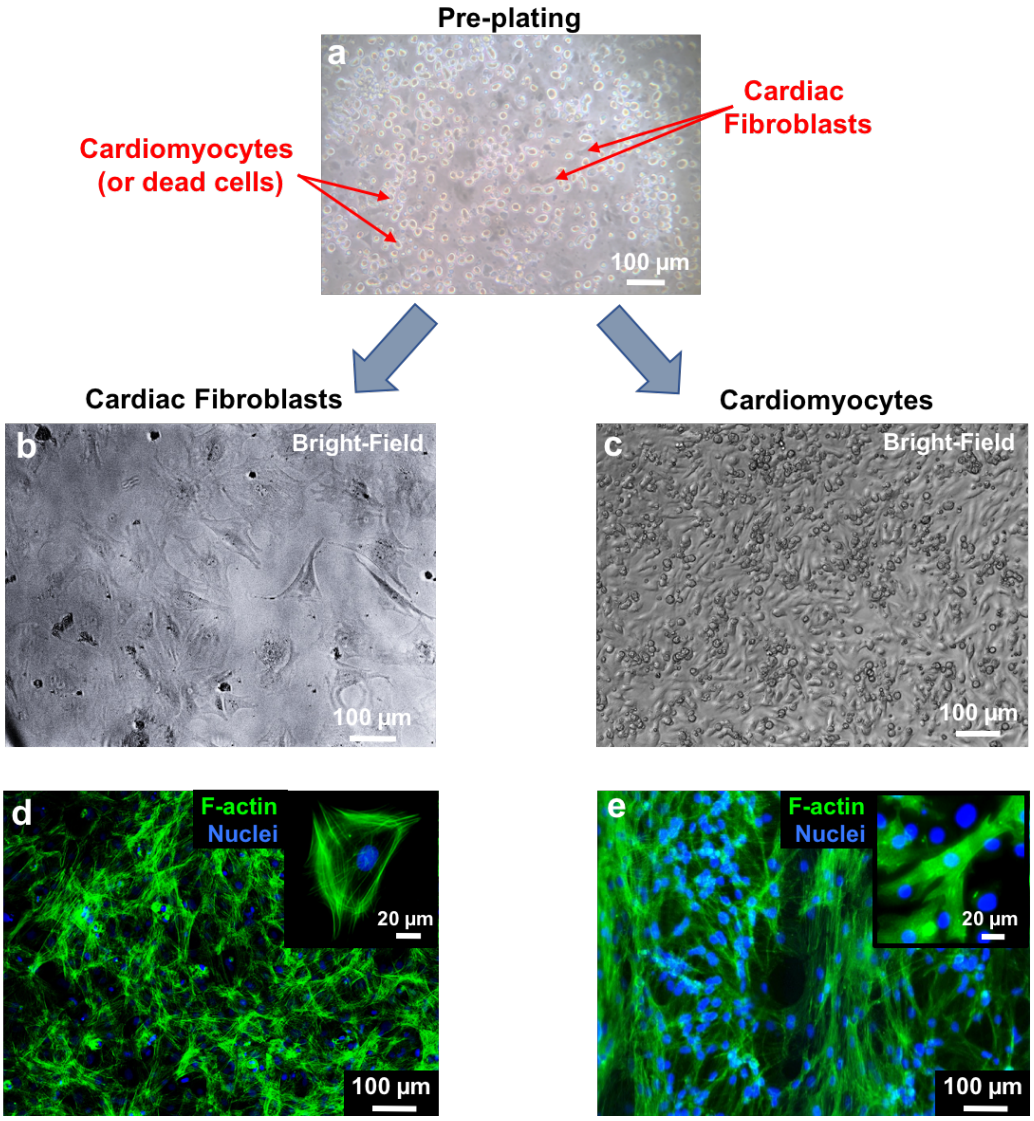

Fig. 2.24 Experimental results of the cardiac cells isolation from neonatal rats. At first, during the pre-plating step, (a), the cardiac fibroblasts adhere to the cell culture flask after 1 hour of incubation while, the majority of cardiomyocytes is still in suspension. When the supernatant is collected from the flask, the cardiac fibroblasts continue to grow and proliferate on the flask, showing their typical extremely flat conformation ((b) and (d)). The collected supernatant cardiomyocytes, instead, can be then seeded on appropriate supports where they can also grow and expand ((c) and (e)).

Differently, cardiomyocytes showed a more accentuated 3D conformation, also easily noticed from bright field imaging (Figure 2.24, c). The more elongated and rectangular actin filaments conformation can be observed in the F-actin and DAPI staining (Figure 2.24, e). Cardiomyocytes are slightly smaller than cardiac fibroblasts and, differently from the latter, they cannot reproduce. Their number is fixed at the early stage of the animal heart development (after some weeks from birth) [97], i.e., when cultured they grow in size but not in number. They are usually not passaged and extra-care and special medium should be use if they have to be frozen. In the present work, cardiac fibroblast were used fro preliminary tests, while, freshly isolated cardiomyocytes were chosen for later experiments. As it will be deeply discussed in Chapter 5, from day 1-2 after seeding, cardiomyocytes showed spontaneous beating activity up to day 7-9.

Cell Isolation Protocol - Embryos Rats. The presented protocol was adapted from [98] at the Neuroscience and Brain Technologies facilities of the IIT of Genova, Italy (see the Preface for the complete reference to the laboratory). The experiments involving animals were executed conforming to the European Communities Council (86/609/EEC) regulations. Also in this case, Sprague-Dawley rats were chosen but, instead of neonatal, 18-days embryos (E18) were selected (the average gestation period of rats is 22 days). The embryos extraction and sacrifice through decapitation was performed in sterile conditions by IIT personnel. Afterward, sterilized forceps were used to open the chest and extract the hearts. After removing debris of pulmonary tissue, eventually still present, the hearts were cut at about 2/3 of their longitudinal direction in order to remove the atria and the vessels in the upper part. During these steps, the tissue was maintained in the buffer dissection medium, similar to the HBSS used in case of neonatal rats, described in [98] and kept ice-cold. Specifically, the solution was formed by 100 mM NaCl, 10 mM KCl, 1.2 mM KH_2PO_4, 4 mM $MgSO_4$, 50 mM Taurina, 20 mM Glucose, and 10 mM 4-(2-hydroxyethyl)-1-piperazineethanesulfonic acid (HEPES) as pH buffering agent. As in case of neonatal rats, the hearts were then minced in small pieces, around 0.5 - 1 mm^3. Then, they were digested in a digesting solution composed always by collagenase type II (0.2%, Invitrogen, USA) but with the addition also of 0.4% of pancreatin (Sigma-Aldrich, USA). Both collagenase and pancreatin were dissolved in the buffer solution described previously. A total of three digesting cycles in 50 mL conical tubes were performed, always in the water bath at 37 °C, for 10 to 15 minutes. The supernatant collected from the conical tubes was then added to a second conical tube containing DMEM-GlutaMax^{TM} (Invitrogen, USA) which already includes glutamine, with the addition of 10% FBS (Sigma-Aldrich, USA). Each tube was then centrifuged for 8 minutes at 1200 rpm. The obtained pellets were then pooled and resuspended in cardiac medium ready to be plated on a Petri dish for the pre-plating step. In this case, the cardiac medium was composed by (4:1) DMEM-GlutaMax^{TM} (Invitrogen, USA), 6% horse serum, 4% FBS and 10 μg/mL

of Gentamycin antibiotic. The addition of the horse serum is thought to help to slow down the proliferation of cardiac fibroblasts that remain after the cell isolation in the cardiomyocyte culture. After a pre-plating step of 2 hours, the media of the Petri dish containing predominantly cardiomyocytes was collected, centrifuged and resuspended in fresh cardiac medium in order to be then used for the experiments.

Chapter 3

Passive Metal Nano-Junctions for Electrical Sensing: Nanogap Chips

Chapter Abstract *In Chapter 3 the layout and structure of the passive microelectrodes chip, also defined as Nanogap chip, will be described in details in Section 3.2. By turning in an advantage the problem of electromigration of metal lines in electronic circuits the nanometric-spaced gap creation will be outlined (Section 3.3). After, the dielectrophoresis technique adopted for the microstructure alignment will be presented in Section 3.4. This is an easy-handling and low-cost approach if compared with the use of standard micro-manipulators e.g., embedded in electron microscopies and, based only on the use of alternated electric fields to create a dipole in the microstructure and attract it to the wanted region. Part of this chapter was also published by the author in [3] and in [2], and reported in the Master Thesis [99]. Moreover, part of this work was also developed during the supervision of the Master Thesis of Francesco Capua [100].*

3.1 Passive Metal/Microstructures Junctions for Electrical Sensing: an Overview

Passive metal/microstructures junctions have been widely investigated in the literature as powerful tools for the fabrication of state of the art sensing platforms [61] but also non-volatile memories [101] or devices for energy accumulation [102]. For example, Liao *et al.* engineered a p-type field effect transistor based on the contacting of CuO nanowires with gold contact pads [103]. The developed was also capable to perform CO gas sensing hence leading to the development of a multifunctional integrated sensing platform.

One of the main limitations of these approaches is related to the fabrication of a functional contact between the microstructure and the electrodes [2]. Often nano/micro-manipulators embedded in complex instruments like atomic force or scanning electron microscopes are employed to position the, often individual, microstructure across the electrodes [104]. This approach is usually referred in the literature as pick-and-place, and can be extremely time-consuming, despite necessarily requiring the use of specific equipment [2]. Despite being time-consuming, these equipments, e.g., SEM microscopes, can be extremely expensive, from several hundreds of thousands euros up to some million, and they require Trained operators capable to use them, further increasing the overall cost. Therefore usually, different methodologies like the random deposition [105] or the growth on the microstructures directly on the electrodes chip [106] are preferred. Nevertheless, also in this case, numerous details and issues should be taken into consideration. For example, the random dispersion method necessarily undermines the reproducibility of the final deposition process as well as preventing any control over the microstructure placement and orientation [2]. On the other hand, the direct growth method, despite presenting a higher control over the microstructure positioning, still requires a precise tuning and strictly constraints on the growth process as well as on the allowed materials [2].

Another common issue to be faced is related to the quality of the metal/microstructure junction. In fact, not optimal contacting of the microstructures on the underlying electrodes will impede the correct operation of the electrical and sensing measurements, in some cases also completely blocking the transmission of the electrical signals [2]. Therefore, additional metal contacts can be often added at the extremes of the microstructure in order to improve the quality of the electrical contact [105, 107]. Despite the higher reproducibility and quality of the metal/microstructure contact, this approach also presents several disadvantages as again the need of specific instrumentation, like electronic microscopes or high resolution lithographic steps, the reduction of the overall sensing area of the microstructure, as well as the impossibility to re-use the electrodes platform with different microstructures or for different tests [2]. Another important issue is also linked to the fact that the addition of different metal layers may modify the behavior (e.g. Schottky or Ohmic) of the original metal/microstructure junction, hence affecting the final performances of the final sensor [2]. This detail was also experienced in the present work when, the addition of platinum contacts to the extremes of $Mo_6S_4I_6$ microwires deposited on the passive microelectrode array, led to the modification of the junction behavior from Schottky to Ohmic, as it will be discussed in details in Section 6.3.

From the above discussion it is evident how the effective interface of microstructures across metal electrodes it is not straightforward and, instead, numerous details need to be taken into account according to the selected application. In the next section, Section 3.2, the selected methodologies and techniques adopted in the present work to overcome the presented technological issues will be explained in details.

3.2 Nanogap Chip: Layout and Features

The interface of microstructures with the electrodes is a cumbersome step in the development of integrated devices for advanced sensing applications. Therefore conceiving novel platforms and techniques to overcome this barrier is highly important. In some cases, completely innovative approaches are necessary, but, sometimes, just a different approach and usage of old methodologies can be advantageous, like e.g., the dielectrophoresis theory, described in Section 3.4. The starting point of the present work was the employment of a passive microelectrodes array chip in order to study the electronic properties of ZnO microwires, at first, and $Mo_6S_4I_6$ microwires, later. The detailed introductions of these two microstructures are reported in Chapter 2.1 and 2.2, respectively. As anticipated, this device is also referred as Nanogap chip due to the presence of nanometric-spaced metal gaps on its top surface.

In Figure 3.1 a, it is reported a picture of the whole microelectrodes array mounted on a custom printed circuit board (PCB). The active area of the chip is 5 x 5 mm^2, while the total dimension of the PCB is 16 x 25 mm^2. The chip was fabricated using conventional photolithography, as described also in [3] and in [2], by depositing a stack of different materials on a p-doped silicon (Si) wafer (Figure 3.1 b). Since its only function was to be a support, the specific doping of the Si wafer was not relevant. Then, 200 nm of silicon dioxide (SiO_2) were deposited by thermal oxidation on the wafer. During this thermal oxidation process part of the original Si wafer surface was consumed at the Si/SiO_2 interface. A 10 minutes bath in piranha solution was then executed in order to remove any trace of contaminants. Piranha solution is a 3:1 mixture of sulfuric acid (H_2SO_4) and hydrogen peroxide (H_2O_2). It is commonly used in fabrication processes to remove organic contaminants due to its highly oxidizing nature.

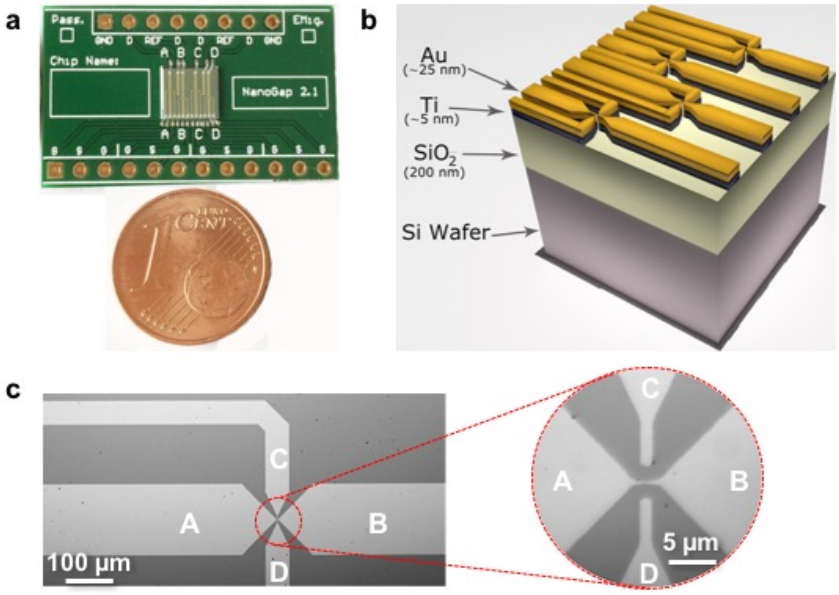

Fig. 3.1 Layout of the Nanogap chip (a) and cross-section schematic of the superposition of the different layers forming the chip (b) (Adapted with permission from [3]). (c) Detail of one butterfly probe before the nanometric gap formation with magnification of the central junction region (inset) (reproduced from [99]).

Next, ∼5 nm of titanium were deposited as adhesion layer for the subsequent gold thermal evaporation. The rapidity with whom Ti forms oxides nitrides or carbides with adjacent layers, makes it an optimal candidate as adhesive layer. A final layer of ∼25 nm of gold resulted as top layer after the thermal evaporation which was then patterned, with standard photolithography, in a column of four butterfly-like electrodes (see Figure 3.1). Gold was chosen because it is a noble metal with high conductivity ($\sigma = 4.1\text{x}10^7$ S/m at 20°C) and because of its strong resistance against oxidation in time.

Four nanometric-spaced gaps, i.e., nanogaps, can be created on each chip. Each structure is, in turn, formed by four metal microwires labeled A, B, C and D in Figure 3.1 c and d. Two of them are aligned horizontally (A and B) and two vertically (C and D). Just after the evaporation, before the nanometric-spaced gap is created, the microwires A and B form a single metal line with a thinner width in the central region (∼2 μm instead of ∼250 μm of the outer regions). As it will be described in details in Section 3.4, this different geometry was designed in order to induce a higher electric field in the central region of the nanometric-spaced gap, so that, the microstructure alignment would happen at the center.

After the fabrication, the chip was glued and wire bonded on a custom designed PCB board (Figure 3.1). Due to their fragility, the aluminum bonding wires were then covered with epoxy resin (1k-epoxy casting resin, Delomonopox®6093).

The PCB presents one through-hole contact for each A-, B-, C- and D-type metal probe so that they can be externally accessed with common electronics laboratory equipment. This is a key factor in order to provide a easy-handling and low-cost platform for microstructures interface and measurements with no need of complex micromanipulators and probes embedded e.g., in SEM or focus ion beams (FIB) microscopes.

In Section 3.3 the theory (Section 3.3.1) and experimental apparatus (Section 3.3.2) used to create the nanometric-spaced junction between electrodes A and B will be presented. While, in Section 3.4 the theoretical model (Section 3.4.1) and the experimental results of dielectrophoresis will be outlined.

3.3 Nano-Junctions Fabrication: Electromigration Induced Break Junction Technique (EIBJ)

The fabrication of nanometric spaced metal gaps, also referred as nanogaps, brings countless advantages in the field of sensing and biosensing [108]. In this way it is possible to directly interface nano/micro-particles even down to single molecules therefore extremely improving the final sensitivity and selectivity. The closer the electrodes are to the structure and the less noise and interference will be introduced. This is particularly important in the field of molecular sensing where a noise higher of just some pA can overcome the target signal. In the present work, these structures were used to characterize the variation of the electrical properties of the selected microstructures according to the variation of external stimuli. Therefore, a precise nanometric control of the nanogap dimension was not necessary since also gaps between 1 and 3 μm were acceptable.

In literature, numerous techniques can be find to fabricate nanogaps like electron-beam [109] or focused ion beam [110] lithography, scanning probe and atomic force microscopy [111] or also electrochemical plating [112] or mechanically break junctions [113]. Nevertheless, these techniques require highly specialized equipment, therefore increasing the final cost, and in some cases, they require etching processes which strongly restrict the categories of materials that can be used [114]. This is why, in the present work, a more versatile, easy-handling and low-cost approach was chosen based on electromigration induced break junction (EIBJ). This technique, take advantage in a positive way of an important problem of metal lines in integrated circuits: electromigration. Electromigration, as detailed in Section 3.3.1, is related to a net mass transport in a conductor caused by elevated current densities. Although a specific probe geometry is required, in order to achieve the wanted goal, this technique requires low-cost but *ad hoc* electronics circuits, it can be parallelized so that multiple junctions can be formed at the same time. Moreover, it can be easily

controlled in therms of the applied voltages, through a feedback system (see Section 3.3.2).

3.3.1 Theory of Electromigration

Electromigration was deeply investigated in the literature to asses interconnections reliability in integrated circuits [115]. When an electric field is applied to a conductor, the induced motion of electrons will randomly transfer some motion quantity to the ions, forming the crystal lattice, through scattering phenomena. The number of scattering collisions is strongly dependent on both the available number of electrons, i.e., current density, and the conductor temperature, since electron scattering is enhanced by thermal vibrations [99]. Under specific circumstances, the electron can transfer its energy to the ion inducing a transport of the ion itself. All together, the moving ions will form an electronic wind [115]. Nevertheless, no modification of the conductor geometry will happen if this flux of ions is constant. When instead a divergence of the flux is present, voids or hillocks can be created (see Figure 3.2). The constant removal of metal ions from a specific region of the interconnect may cause the formation of voids which may lead to an interruption of the metal line, i.e., an unwanted open circuit (Figure 3.2, up). While, the continuous accumulation of metal ions can cause hillocks which, in turn, can short circuit two adjacent metal lines (Figure 3.2, down). Both these condition will cause a circuit malfunction.

Flux divergences, responsible for the formation of hillocks and voids, are mainly caused by lattice defects or by the poly-grains that constitute the majority of metallic films [115]. The different diffusivity on the poly-grains, higher at the interface and lower in the center of the grain itself, will cause, as well as temperature a variation of the diffusion coefficient, hence, flux divergence.

A quantification of the influence of the current density and of the temperature on electromigration can be obtained by considering the Black's Law (see Equation 3.1). This model was empirically developed and provides the mean time to failure (MTTF), i.e., the time-duration that the metal interconnects is considered to be working correctly. This law was originally developed to estimate the reliability of integrated circuits, but, later, it was also applied to electromigration studies.

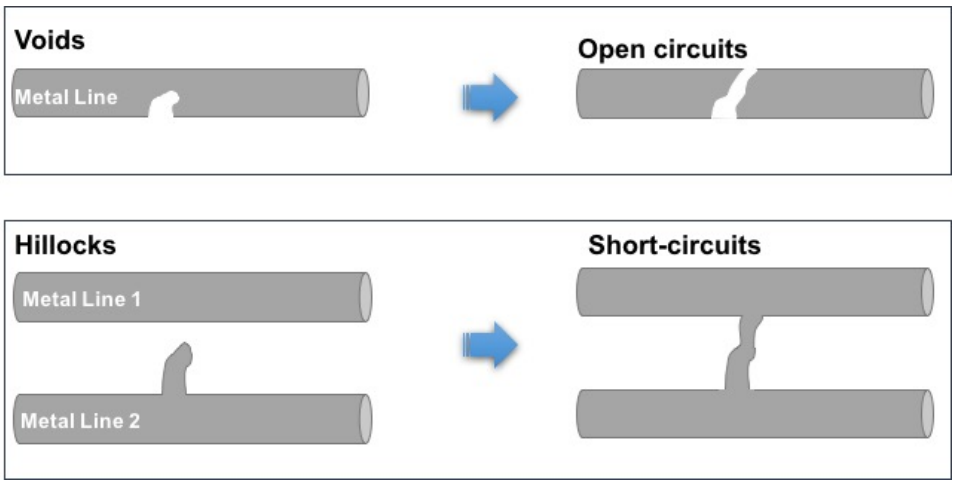

Fig. 3.2 Schematics of voids (up) and hillocks (down) formation in metal interconnects caused by electromigration leading to open circuits of short-circuits, respectively.

$$MTTF = \frac{A}{J^n} e^{\frac{E_a}{KT}} \tag{3.1}$$

In Equation 3.1, A is the Black's constant associated with the material geometry, E_a is the electromigration activation energy, K is the Boltzmann constant, T is the temperature in Kelvin, J is the average current density and n is an exponent varying between 1 and 2 dependent on the type of material [116]. It is important to notice that in the Black's equation there is a linear relationship with the current density while, an exponential decrease of the MTTF with respect to a temperature increase. This underlines how also the temperature, and not only the current density, plays a crucial role in electromigration. The thermal energy provided to the lattice ions will increase their vibration around their defined position increasing the probability of a collision with electrons. In case the motion quantity transferred by an electron to a metal ion is sufficiently high, a vacancy in the crystalline lattice can be created by the ion removal hence resulting also in an ion flux inside the material. More in details, as underlined by Demarchi *et al.* there are three different forces acting on the moving ions (as reported schematically in Figure 3.3, a). The electronic wind, already anticipated, due to the collision of electrons with ions, the electrostatic force, exerted by the external electric field and the backflux force which is related to the effect of different ions concentrations in a finite volume and it represents a feedback mechanism for the electrostatic wind.

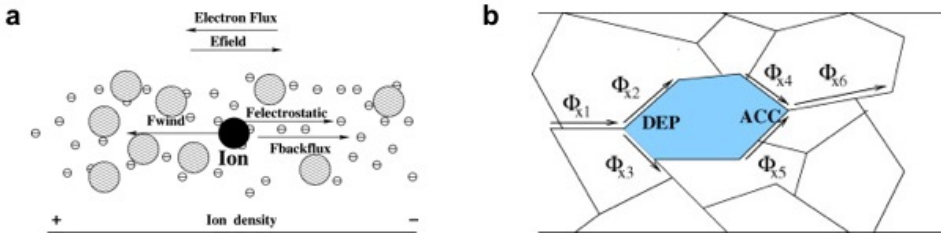

Fig. 3.3 Schematics of the different forces acting on the metal ion (a) and of the effects of triple points on depletion and accumulation phenomena on a metal grain (b) (Reprinted from Electrochimica Acta, Vol. 54, D. Demarchi, P. Civera, G. Piccinini, M. Cocuzza, D. Perrone, Electrothermal modeling for EIBJ nanogap fabrication, Pages No. 6003-6009, Copyright 2009, with permission from Elsevier [115]).

The backflux force describes also the effect of grain dimension on the overall electromigration process. A higher backflux force will be produced in a smaller grain for the same ions displacement [115]. This is an important factor to consider since the grain size may vary considerably depending on the deposition process. The points where three different grains meet are called triple points (Figure 3.3, b) and they are one of the main responsible for electromigration process since they are points of critical mechanical stress. This is because, at triple points ion fluxes can sum up, leading to ions accumulation, or become equal to zero, hence causing a depletion region. It's clear now how this can lead to the formation of hillocks and voids in the meal line.

By taking advantage of the voids creation mechanisms of electromigration the EIBJ technique was developed in order to create controlled nano/micro-metric ruptures of metal wires. Nevertheless, an accurate control of the current density and of the temperature are necessary in order to be able to accurately control this process that, if uncontrolled, would lead to an extended melting of all the metal line. In case of gold metal wires, like in the present work, the minimum current density to be reached to start electromigration is $10^8 \mathrm{A/cm^2}$ at room temperature [117]. A crucial factor is also related to the geometry of the wire, as anticipated in Section 3.2. The wire is fabricated with a smaller width in the central region so that, at the same applied voltage, the current density will be higher in the center hence increasing the probability that the right temperature and current density conditions are reached exactly in the the central thinner region where the nanogap needs to be created.

3.3.2 EIBJ Experimental Apparatus

To electromigrate the metal wires on the nanogap chips, a custom hardware-software platform, called NanoCube, developed at the Micro & Nano Electronic Systems (MiNES) laboratories of Politecnico di Torino, and published in [117], was used.

The NanoCube, see Figure 3.4 a, is an embedded modular system capable to take advantage of the electromigration phenomenon to fabricate nanogaps using EIBJ. The *ad hoc* developed PCB boards, allow complete modularity and personalization of the system upon new needs or improvements. It runs real-time Linux operating system and the presence of Wi-Fi communication (IEEE 802.11 WLAN link) increases its versatility and functionality. The core of its operation is the implementation of specific real-time R/V curves which include all the significant informations about the ongoing electromigration process. The voltage applied to the metal wire, i.e., the flowing current, is constantly increased, starting from an initial value, up to the occurrence of electromigration. One example, published in [117], is shown in Figure 3.4 b, and it will be described in details in the present section. Their significance resides in the fact that they enclose the instantaneous variation of the resistance that is intrinsically linked with the removal of metal ions from the metal wires. In fact, when a nanogap is created, an open circuit condition is measured at the extremes of the original metal wire.

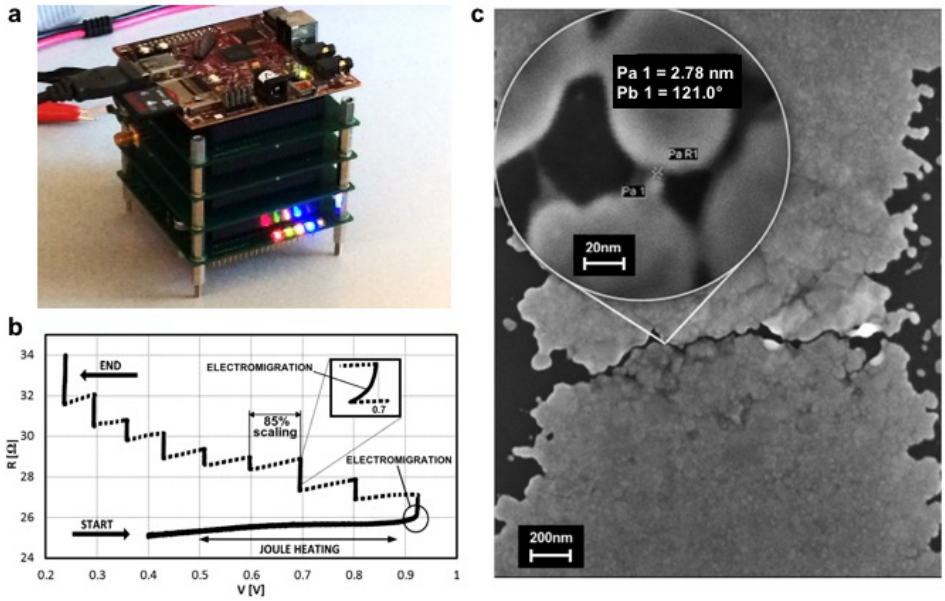

Fig. 3.4 (a) Image of the NanoCube apparatus used for the electromigration of the nanogap chips. Resistance versus voltage plot during an experimental electromigration (b) and FESEM image of an obtained nanogap (c) as reported in [117] (©2014 IEEE).

Since the EIBJ process is almost instantaneous, a precise control of the current density and of the temperature at the junction, it's fundamental in order to successfully create a nano-junction. An literature example of a nanogap ($\sim$ 2.78 nm spaced in its closest point) created with the NanoCube is shown in Figure 3.4 c. To achieve these results, two separate algorithms for feedback control of both current density and temperature, are implemented. They both manage the voltage

applied to the junction. Nevertheless, the temperature feedback is capable to predict and estimate the junction's temperature, thanks to real-time simulations, in order to further improve the voltage value [117]. An initial guess of the applied voltage is necessary as well as the size of the voltage increase for each step. In the present work these values were chosen as 0.9 V and 2 mV, respectively.

The current feedback control is based on controlling the change of the electrical resistance which in turn, is proportional to the atoms moving in the material [117]. Therefore, the current feedback algorithm constantly increases the voltage applied to the metal wire using the indicated step-size, while at the same time measuring the resistance of the metal wire. When a resistance value corresponding to the inverse of the quantum conductance, G_0, is reached, it is assumed that the last gold atom is removed, leading to the gap formation (specifically, $1/G_0 = 13$ kΩ) [117].

The temperature estimation, instead, is fundamental to avoid the melting of the metal wire rather than the nanometric-spaced gap formation. In fact, as the metal wire section decreases, due to the atoms removal process, the temperature must be carefully controlled to avoid that an overheating, despite the wire melting, can provoke surface tension effects responsible of larger gaps and metal islands accumulation [117]. Since the exact architecture of the NanoCube apparatus was not the main goal of the present work, just a brief schematic overview will be given of the complex implementation of the temperature feedback algorithm. Specifically, upon a measurement of the current density in the metal wire, the algorithm exploits this measurement as a key to search a hash table reporting, for each current density the correspondent value of the temperature obtained through Spice simulations. If, for a specific measurement, the temperature is higher than the one predicted from the the electrothermal model developed by the authors, then the software will decrease the applied voltage of a specific percentage (95% in the present work, 85% in [117]) hence leading also to a temperature reduction. This process can be clearly recognized from Figure 3.4 b. At first, as the voltage increases, the resistance also increases with a linear dependency, as expected from the Joule heating effect. But, as the current density is close to the threshold value for electromigration, around 10^8 V, the resistance increases exponentially with the applied voltage, as visible from Figure 3.4 b. Each time an exponential increase of resistance is detected, the applied voltage is reduced of the percentage specified at the starting point (85% in this case). Then the process is repeated again: the voltage is slowly increased up to another exponential resistance increase. This slow sequential process is necessary in order to have a controlled rupture of the metal wire. It is important to notice that after the reduction of the voltage, the value of the resistance is almost unchanged, this means that electromigration started to occur. The process will then stop when the quantum conductance limit will be reached.

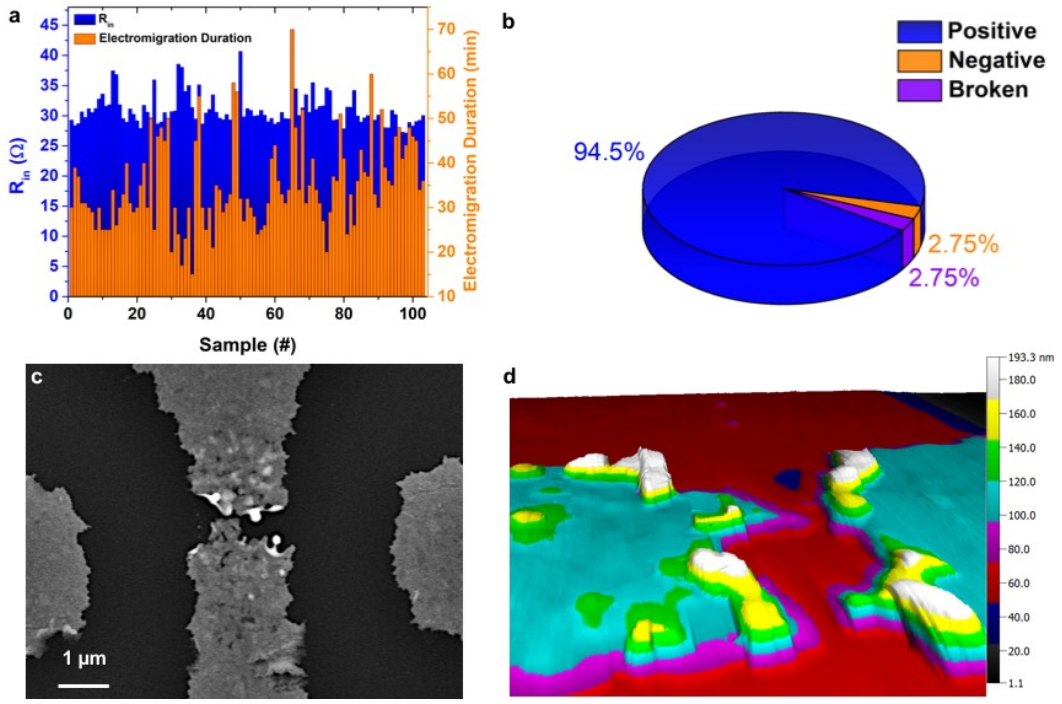

Fig. 3.5 Initial resistance value and electromigration duration on a series of 103 experiments (a) and statistics about the positive or negative outcome of the electromigration on nanogaps (b). Just 2.75% of the probes, were originally broken before the process started. SEM (c) and AFM (d) characterizations of a nanogap.

In Figure 3.5 a, the initial metal wire resistance and electromigration duration are shown for a series of 103 electromigration experiments. The initial wire resistance varied between 27 and 38 Ω, due to process variations. While, the electromigration time ranged between a shorter time of 20 min up to 1 hour. In average, this process lasts around 30 - 40 min, that is much shorter if compared with traditional methods that have time durations around 1 - 2 hours [117]. This is possible thanks to the implementation of both the current and temperature feedbacks instead of only the indirect measure of the conductance and power dissipation on the wire, as reported in the literature [118].

On the total 103 electromigration experiments, 94.5% resulted positive while, the remaining ones where either negative, 2.75%, or the probe was originally already broken, 2.75% (see Figure 3.5 b). A first verification of the correct outcome of the process was obtained by measuring with a source meter (34411A 6.5 Digit Multimeter, Agilent, USA), an open circuit condition. Nevertheless, a more accurate proof was obtained by performing FESEM or atomic force microscopy (AFM) imaging. The AFM imaging was performed by the author using an A100 AFM from A.P.E. Research, Italy. Two examples are reported in Figure 3.5 c and d, respectively, where it can be observed the irregular features of the nanogap borders. This is typical

of EIBJ processes in which the rupture is dominated by the physical processes and dynamics of electromigration. For the applications addressed in the present work the irregular border is not a negative feature but, instead, it represents an advantage since the irregularity allows higher surface contact area of the microstructure with the electrodes. Moreover, since the main focus of the present work was to use these gaps to interface microstructures, and not e.g., single molecules or nanoparticles, gaps of the order of hundreds of nm were acceptable, hence a precise tuning and optimization of the electromigration process was not part of this study.

Once that each of the four probes of every nanogap chip was correctly electromigrated, the next step was the alignment of the microstructure using alternated electric fields, i.e., dielectrophoresis, as discussed in Section 3.4.

3.4 Microstructures Alignment: Dielectrophoresis

As extensively described in Chapter 1, the integration of microstructures with microelectrodes it is not a straightforward task. Numerous details must be taken into account to be able not only to perform a measurement but, also, to obtain a reliable result. In addition, to develop portable and versatile devices, the deposition method must not be too cumbersome or long so that the overall device adavantages are lowered. For example the pick-and place approach [104] requires the use of micromanipulators usually embedded in highly complex, expensive and not portable equipment like e.g., FIB microscopies. To overcome these issues, often the direct grow [106] or random dispersion [105] methods are employed. Nevertheless, they also present several disadvantages like the rigorous constraints of the synthesis process, along with electrodes poor re-usability, low yield and scarce reproducibility [2]. Sometimes, additional metal contact enforcements are necessary in order to create an optimal electrical contact between the microstructure and the electrodes. For example Kind *et al.* used electron-beam lithography to deposit additional gold contacts at the extremes of ZnO nanowires [105], while Das *et al.* exploited the same technique to deposit Ti/Au contact on one side of a ZnO nanowires and Pt contact on the other [107]. Despite producing junctions of high electrical quality, this approach in the majority of the cases also requires the use of complex equipment in order to locally deposit the metal contact only at the extremes of the microstructure. These are the reasons why, as anticipated in details in Chapter 1, in this work the dielectrophoresis deposition method was selected. Exploiting this method it is possible to create microwire/electrodes junctions just taking advantage of the microstructure polarization due to the presence of alternated electric field. Only a function generator is necessary, much cheaper than FIB or electron-beam lithography apparatus and, no contact enforcements are necessary.

In Section 3.4.1, a brief introduction about the theory of dielectophoresis is reported while, in Section 3.4.2 the adopted experimental procedure will be described.

3.4.1 Theory of Dielectrophoresis

The word dielectrophoresis derives from the Greek word *phorein* which describes the transport of a particle due to dielectric forces [119]. It was first introduced by J. H. A. Pohl only in 1951 in the framework of carbon-black filler removal from polyvinyl chloride samples, for industrial applications. Specifically, he was studying the motion of particles suspended in a solvent caused by alternated electric fields. The dielectrophoresis is described by the dielectrophoretic force (in case of a spherical particle) reported in Equation 3.2.

$$F_{DEP} = 2\pi\varepsilon_m R^3 CM(\nabla E^2) \tag{3.2}$$

$$CM = \frac{\varepsilon_p - \varepsilon_m}{\varepsilon_p + 2\varepsilon_m} \tag{3.3}$$

In Equation 3.2, ε_m is the absolute permittivity of the enclosing medium, R is the radius of the particle, CM is the a factor, called Clausius-Mossotti, connected to the particle polarizability while, ∇E^2 is the gradient or the root mean square amplitude of the particle and medium electric field. The Clausius-Mossotti term, relates the absolute permittivity with the permittivity of the dielectric medium, ε_m (Equation 3.3) [119].

From Equation 3.2 it can be noticed that the dielectrophoretic force is equal to zero in case of uniform electric fields. Considering all the quantities constant, bigger particles will experience higher force. Moreover, it is important to notice that the force can be attractive or repulsive depending on the sign of the CM factor. If the particle permittivity is greater than the medium one, the dielectrophoretic effect will be attractive, i.e, the particle will be attracted in the region of higher electric field. In the opposite case, instead, the dipole moment will be aligned against the applied field, hence causing a repulsion of the particles. The dependency of the force from the square of the electric field, implies that both AC or DC fields ca be effective. At last, the geometry of the electrodes plays a crucial role for obtaining the desired effect on the particle. In fact, since the dimensional units of the electric field term are $\mathrm{V}^2/\mathrm{m}^3$, scaling the electrodes size down to the microscale allows to reach values of this term around 10^{12} $\mathrm{V}^2/\mathrm{m}^3$, enough e.g., to align biological cells, just applying external voltages of the order of 1 V [119]. In the specific case of the nanogap chips, this means that a higher attractive force will be present in the junction region,

due to the smaller dimension of the metal probes, hence increasing significantly the probability of attracting the microstructure in the central region of the gap.

Although Equation 3.2 provides a correct picture of the dielectrophoretic force, numerous modifications should be taken into consideration in the experimental applications due e.g., to particle inhomogeneity, net charges and conductive losses [119]. Moreover, usually cells are cultured in the cell culture medium, which presents numerous electrolytes making the surrounding medium conductive. In this case a complex permittivity must be considered in the equations. A disturbance of the dielectrophoretic force can also be caused by boundaries or surrounding particles that are in the proximity of the electrodes [119]. All these examples, explain why numerous theoretical models have been and are currently developed in order to correctly quantify the dielectrophoretic force for each different experimental condition. For example, Schnelle *et al.* analyzed how 3D multi-electrodes systems induce the dielectrophoretic force on dielectric particles of cells [120]. While, Voldman *et al.* established a simulation tool capable to estimate the performances of quadrupole dielectrophoretic traps [121].

In the present work, a COMSOL Multiphysics® basic simulation of the electric field acting on the nanogap was developed [3] (Figure 3.6).

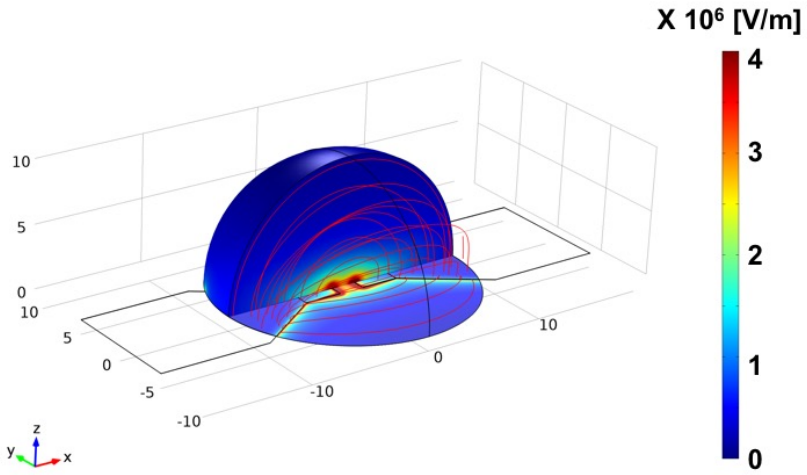

Fig. 3.6 COMSOL Multiphysics simulation of the dielectrophoretic field on the nanogap chips layout (adapted with permission from [3]).

Due to the specific geometry, not only the region of higher electric field coincides with the center of the gap, but, also, an intensity of the order of 10^6 V/m is obtained by applying just 3 V_{pk-pk} on the electrodes hence achieving extreme efficiency.

In Section 3.4.2, the experimental procedure here adopted to align microstructures in the gap region of the nanogap chips will be presented.

3.4.2 Dielectrophoresis Experimental Setup

Thanks to the versatility and easy-handling of dielectrophoresis the only instrumentation needed is a function generator. Moreover, by performing the process under an optical microscope, the dielectrophoresis can also be monitored optically in real-time.

Preliminary, the target microstructures must be dispersed in a solvent, therefore both ZnO and $Mo_6S_4I_6$ were dispersed in isopropyl alcohol (2-propanol, Sigma Aldrich, USA) with concentrations between 0.6 - 0.8 mg/mL. One nanogap chip was then fixed under an optical microscope (Zeiss, Axio Scope.A1) and the connecting wires of the selected nanogap were then connected to a function generator (Agilent-Keysight 33210A) using crocodile cables (see Figure 3.7).

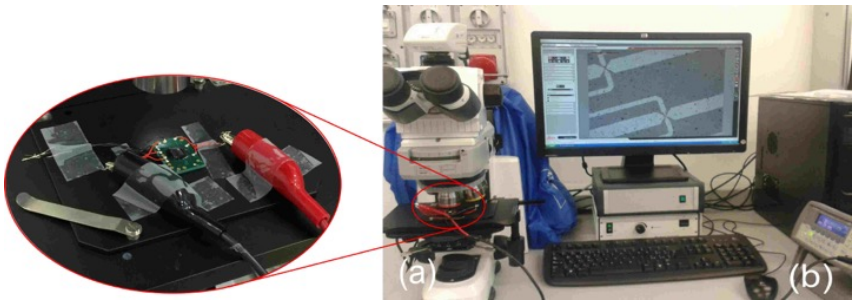

Fig. 3.7 Experimental setup used to deposit microstructures on nanogap chips using dielectrophoresis. The nanogap chip is positioned under the optical microscope (a) and then the dielectrophoretic signal is applied with the signal generator (b) (reproduced from [99]).

Then, 10 μL of microwires solution were dropped on the whole chip surface simultaneously with the application of the electrical signal. The electrical signal was applied until the complete solvent evaporation and it was an AC sinusoidal waveform with 0 offset, amplitude 3 V_{pk-pk} and frequency between 100 kHz and 10 MHz. Since, due to their dimension, the selected microstructures could be clearly imaged with an optical microscope, looking in real-time at the dielectrophoresis process can be an additional useful tool to monitor the overall success of the process. In Figure 3.8 are reported six frames of a dielectrophoresis video recorded with the optical microscope camera during the deposition of a ZnO microwire on a nanogap chip. At first, the pristine nanogap surface resulted clean with no relevant micrometric structures present. After that 10 μL of microwires solution were dropped on its surface, while applying the electrical signal, numerous microwires could be seen floating on its surface in the isopropanol solution following the force of the applied electric field. Due to the presence of the liquid, it was not possible to acquire an image perfectly focused. After few seconds from the drop deposition (Figure 3.8, time 15.49 s), some microwires resulted attached to the gold electrodes either in the gap region or along the electrodes border, like in the reported example. The

perpendicular alignment of the microwires with respect to the gold wire edges confirmed that the dielectrophoresis was working correctly since the wires aligned with the electric field lines (as simulated in Figure 3.6). The motion of a single ZnO microwire was followed in the experiment (red circle in Figure 3.8), although not perfectly on focus, due to its movement in the liquid in the x, y and especially, z directions. The selected microwire was attracted close to the gap at 15.49 sec after the drop deposition and then, in just approximately less than 2 sec it resulted positioned exactly at the center of the nanogap, only 17.16 sec after the process started.

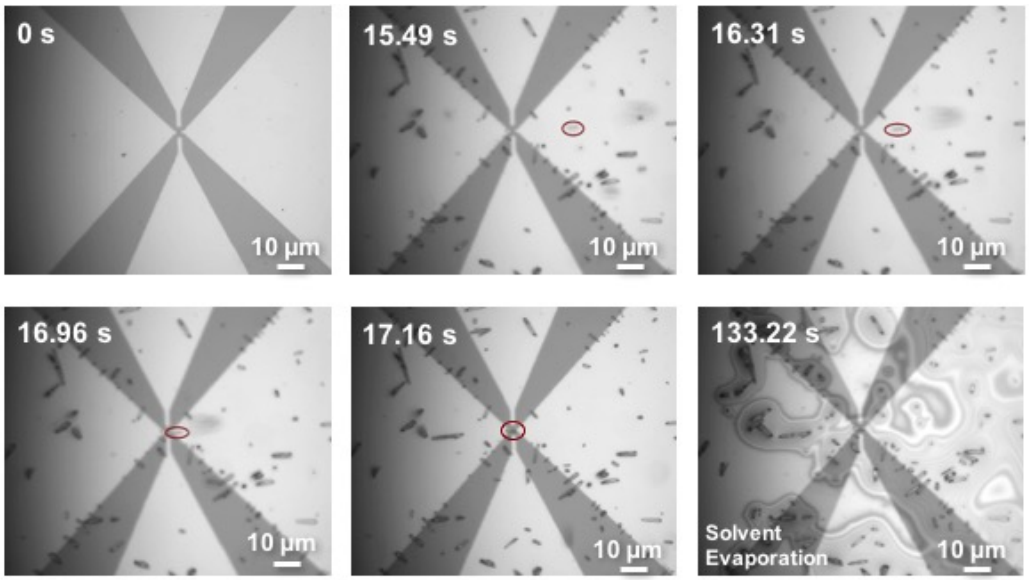

Fig. 3.8 Time frames of a single dielectrophoresis process of ZnO microwires, acquired with the optical microscope camera. The red circle highlight a ZnO microwire that is attracted in the central gap region by the field force. The poor focus in some images is due to the presence of a liquid solution on the chip (adapted from [99]).

After about 133.22 sec (2.22 min), the solvent was completely evaporated from the chip surface as visible from the shadows in Figure 3.8, 133.22 s. As it can be appreciated from the experimental results, the microwire deposition using dielectrophoresis is easy-handling and extremely fast, if compared with other discussed techniques like pick and place or direct growth. Moreover, the process time is also strongly dependent on the concentration of the microwires solution. The higher the number of microwires in the solvent and the faster one of them will be attracted in the gap region. Nevertheless, increasing too much the microwires concentration will often lead to have agglomerates of microwires in the gap region, instead of a single one, hence making the further electrical characterization of the microstructure not reliable. The selected concentration was chosen as the optimal trade-off between the process duration and the deposition of a single microstructure.

On a total of 31 dielectrophoresis experiments performed with ZnO microwires on the nanogap chips, i.e., on overall 124 electrodes pairs (four for each chip), in the 84% of the cases a ZnO microwire was aligned between a couple of gold electrodes ("successful alignment" in Figure 3.9). A successful alignment was assumed when a ZnO microwire was bridging two gold electrodes in at least one of the four junctions of each nanogap chip. In this case the percentage of success will be, for that chip, of 25%. The remaining 75% will belong to the "No Alignment" category since associated with the remaining 3 not-bridged gaps. If all the four junctions of a single nanogap chip present two electrodes bridged by a microwire, 100% of success will be considered [3].

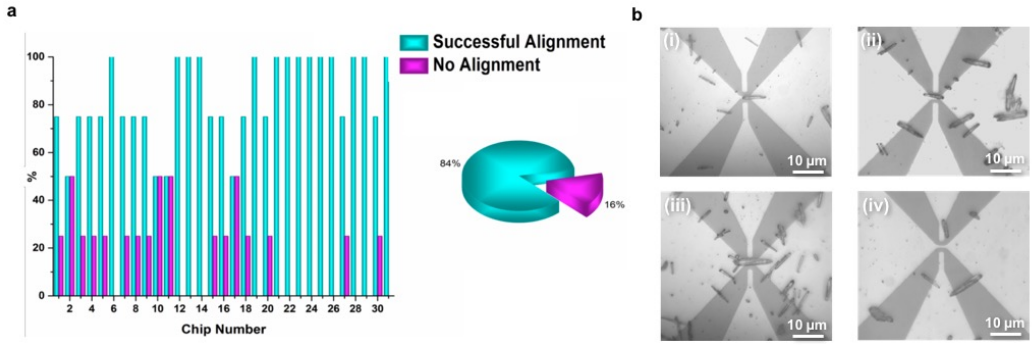

Fig. 3.9 (a) Successful ZnO microwire alignment percentage on 124 electrode couples, i.e., 31 nanogap chips (reproduced with permission from [3], Supplementary Information). (b) Optical microscope images of successful dielectrophoresis experiments.

It must be underlined how, in case of micro- and not nano-structures, a correct alignment is considered even if the structure is bridging two couples of electrodes that are not necessarily the electrodes of type A and B (according to the legend in Figure 3.1), where the nanogap is formed with electromigration. One example of this aspect is reported in Figure 3.9 b-(iv) where a ZnO microwire is bridging the bottom electrode with the right one (electrodes of types B and D). The electrodes of type C and D had been originally designed to act as gates on the microwire/gold junction present at electrodes of type A and B. Nevertheless, this feature was not considered in the present work, and, electrodes of type C and D where considered equivalent to the one of type A and B for the purpose of the electrical characterization of the microstructure. Other examples can also be observed in the FESEM images reported in Figure 3.10. The FESEM characterization of the microwire/gold junction can provide additional informations regarding the actual formation of the junction. In fact, the presence of microwires fragments or of unwanted slopes, not visible from the optical microscope, can impede the formation of an actual electrical junction. In this case, even if from a first examination with the optical microscope the microstructure seemed correctly positioned, no electrical signals can be recorded. Therefore, the FESEM characterization is an extremely useful tool in order to asses the quality

of the formed junctions or to understand the nature of the conduction problems, if present.

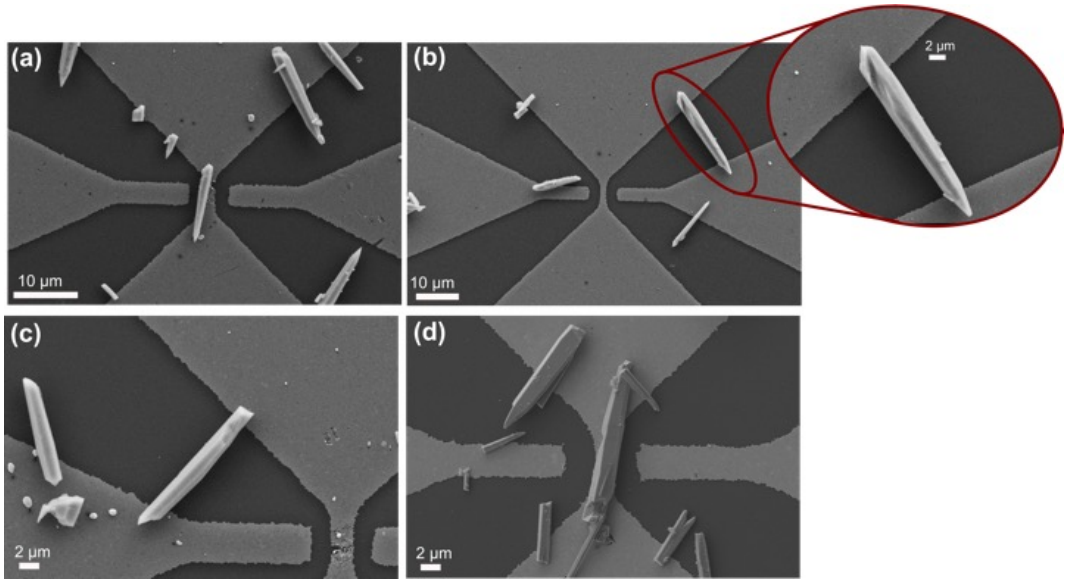

Fig. 3.10 FESEM images of ZnO microwires deposited on nanogap chips using dielectrophoresis (reproduced with permission from [3], Supplementary Information).

The same methodology was applied in case of $Mo_6S_4I_6$ microwires. Interestingly, the same parameters of the sinusoid signal used in case of ZnO microwires were effective also for the alignment of these structures. In Figure 3.11 the correct alignment of $Mo_6S_4I_6$ microwires across the nanogap is shown using both optical and FESEM imaging.

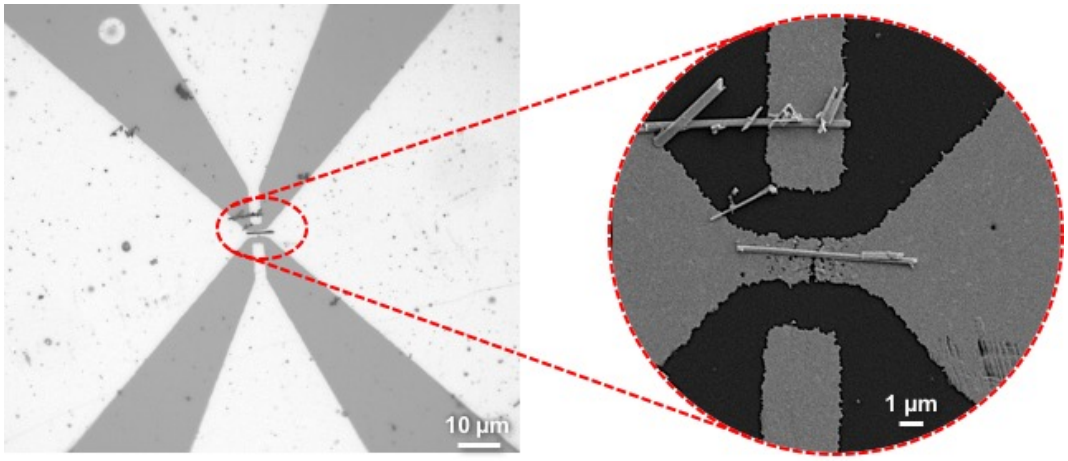

Fig. 3.11 Optical microscope (left) and FESEM (right, zoomed) images of $Mo_6S_4I_6$ microwires deposited on nanogap chips using dielectrophoresis (also reported in [100]).

In both cases, ZnO and $Mo_6S_4I_6$ microwires, the nanogap chip surface could be cleaned, in case of unfavorable microstructure alignment, by a 15 minutes ultrasonication treatment in isopropyl alcohol.

Chapter 4

Active Integrated Microelectronics for Nanosensing

Chapter Abstract *In this chapter the active microelectronic device used for sensing of microstructures will be presented. These CMOS chips are called Micro-for-Nano (M4N) since they provide a microscale electrodes platform for nano/microsensing. After introducing the main concept and design motivations (Section 4.1), the two core circuits for both integrated dielectrophoresis and impedance measurement on-chip, will be qualitatively presented. Thanks to the CMOS circuits, directly underneath the sensing and stimulating electrodes, the noise and interconnections parasitics are strongly reduced. To improve the quality of the electrical contact between the microstructure and the integrated aluminum electrodes, an electroless gold CMOS post-process was developed (Section 4.1.1). At last, a brief overview about the LabVIEW-based graphic user interface (GUI) developed will be presented in Section 4.1.2. Part of this work was published by the author in [4] and in [122], while, the CMOS Post-Processing was optimized in collaboration with the Master Thesis work of V. Allegra [123]. The electronic design of the M4N chips, was not developed in the present work and it was previously published in [124]. While, the CMOS post-process and the effective alignment and measurement of the electrical properties of ZnO microwires had been directly addressed by the author. In the second part of the present Chapter, instead, the adavantages of culturing electrogenic cells, specifically cardiomyocytes, on CMOS chips will be presented. This work represents the initial proof-of-concept linking the different works performed in the present Ph.D. activity. In fact, the author started by using multi-electrode-arrays platforms, with or without CMOS circuits, for the investigation of the electrical properties of synthetic microstructures and how their variations can be exploited for advanced sensors fabrication. Then, after understanding the needs and the potentialities of electrogenic living microstructures, i.e., cardiac cells, the author focused the last part of the Ph.D. activity on understanding the power deriving from*

the link between cardiac cells and CMOS electronics. This work was intended as a future perspectives at the conclusion of the Ph.D. activity, therefore, due to the lack of time, a preliminary study was performed on commercial CMOS MEA devices developed by the 3Brain company (Switzerland), described in Section 4.2.1. This activity was performed at the Microtechnology for Neuroelectronics laboratory, part of the Italian Institute of Technology (IIT) of Genova (Italy), and directed by Dr. Luca Berdondini. The preliminary experimental results where CMOS MEA were integrated not only with cardiac cells, but also, with the GelMA hydrogel synthesized at the Khademhosseini Laboratory in Boston, will then be presented in Chapter 8

4.1 Micro-for-Nano Chip: Design and Features

The characterization of materials at the nano/micro-scale, both synthetic or living ones, or their use for sensing/biosensing applications, requires the development of nano/micro-devices capable on one sides, to efficiently interface with them and, on the other side, to provide their functional interrogation and/or stimulation. In this framework, the use of passive microdevices, i.e., devices which need external instrumentation to perform sensing or stimulation, introduces several limitations in terms of portability and of interconnections noise and parasitics that, in some cases can cover or alter the target signal. Therefore, as anticipated in Chapter 1, designing the electronics, i.e., the functionality of the chip, closer to the target structure, can bring countless advantages. Specifically, there will be improvements of the device performances and portability, hence widening its operational applicability. In fact, when dealing with signals of the order of pA - μA, the presence of wide interconnections can cause important noise coupling phenomena, which strongly decrease the final sensitivity of the device. Nevertheless, upgrading from passive to active microdevices introduces a high number of additional challenges to be faced. These not only include the design of *ad hoc* integrated CMOS circuits but, also, the optimization of significant post-processing of the circuits themselves. The post-processing of CMOS circuits, i.e., the processing after their fabrication, is a fundamental requirement in order to both protect the electronics from the sensing environment, just consider all the measurements that must be performed in liquids, often also conductive, and to make the electrodes surface suitable and optimal for the microstructure to be integrated on and for the specific measurement to be performed.

The Micro-for-Nano (M4N) chip here presented, represents a step further in the design of smart devices capable to interface with microstructures for sensing applications. With respect to the nanogap chips, discussed in Chapter 3, the M4N chips integrate on top of the CMOS electronics an array of metal microelectrodes where microstructures, like the ZnO microwires presented in this work, can be aligned, thanks to the embedded dielectrophoretic (DEP) circuits, and, then, the

variation of their impedance can be monitored in real-time upon variation of external physical/chemical stimuli like UV light (see Chapter 6). Custom read-out circuits (ROCs) had been developed in order to transform the variation of the microstructure properties into digital signals, so that it can be compliant with standard electronic devices [4]. As anticipated in Chapter 2, the scaling of electronic devices has brought electronic components always closer to the dimensional scale of nano/micro-structures hence making CMOS technology the optimal candidate for this kind of applications.

The M4N chips were designed using 130 nm CMOS technology and then they were wire bonded on a custom-fabricated PCB board (Figure 4.1, a and b). On the chip's surface, the aluminum top electrodes (AlTEs), i.e., the metal lines of the top layer of the chip, were also the bonding pads can be found, were exposed to open air in order to be interfaced with the selected microstructures. Directly underneath, the circuits for the dielectrophoresis and the read-out can be found. Specifically, 8 unit cells are exposed on the chip surface (Figure 4.1, c), each one formed by three couples of facing microelectrodes (Figure 4.1, d). The distance between them slightly varies between about 1 up to 3 - 4 μm in order to be able to contact structures with different sizes. Each unit cell has its own dielectrophoresis circuit and 3 ROCs, one for each couple of electrodes. Therefore, the overall device belongs to the multi-electrodes array (MEA) devices since an array of 24 active sites are available on its surface for multiple sensing applications.

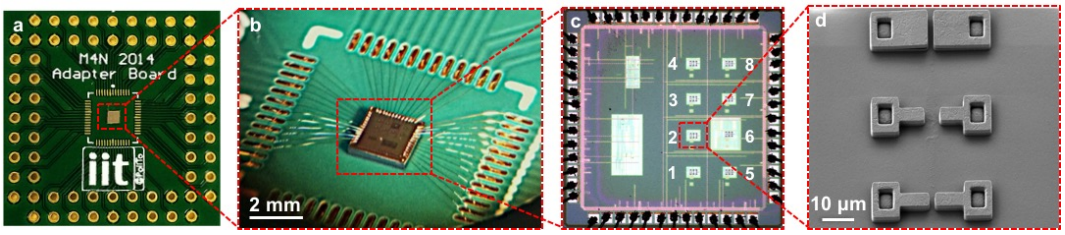

Fig. 4.1 M4N chips mounted (a) and wire bonded (b) to a custom PCB board. Each chip has 8 electrodes unit cells (c), each one with 3 couples of facing Al microelectrodes (d). Figure (d) was adapted from [122].

The dielectrophoresis circuits are constituted by digitally-controlled triangle-wave oscillators (supplied at 3.3 V) which generate a triangular wave signal with amplitude 3 V_{pk-pk} with oscillation frequency between 50 kHz and 1 MHz [124]. This frequency range was designed in order to widen the range of microstructures that can be integrated and measured on the chip. The ROCs, instead, were design using high speed 130 nm CMOS transistors since they required a smaller supply voltage, 1.2 V, hence decreasing the overall power consumption (only of 14.82 μW) [124]. Both the DEP and ROC circuits, are connected with the same couple of facing AlTEs (see 'A' and 'B' in Figure 4.2, a). For this reason, while one circuit is active,

the other one is completely isolated and vice versa [124]. This switching process, and all the other configurations, are managed by an external microcontroller, that, according to the instructions programmed by the user in its registers enables either the DEP circuit or the ROCs ones.

The microcontroller is also responsible to process the frequency-modulated 1-bit quasi-digital output signal produced by the ROCs [124]. Specifically, the output signal of the ROCs is a square wave signal (see Figure 4.2, a, top) whose discharging time, T_1, is proportional to the resistance and to the capacitance of the microstructure deposited between the electrodes, while, the charging time, T_0, is mainly related to its capacitance [124]. By processing in real-time the obtained signal, e.g. using the LabVIEW based GUI described in Section 4.1.2, the resistance and the capacitance of the microstructure, i.e., its impedance, can be extracted. This approach belongs to the family of the event-based architectures in which an analog information (continuous signal) is acquired, processed and transmitted in a digital (discrete) signal [125]. In the standard sample-based approaches (see Figure 4.2, b), the information carried by the continuous signal, needs to be carried through a sampled representation of the signal itself, leading to both the transmission of a high number of data and to a loss of information due to the sampling. They are usually based at first on the amplification of the analog signal obtained from the measurement and, then, on its conversion into a N-bit value. In this case often analog blocks with high demand in terms of power consumption and device size are necessary, e.g., analog to digital converters, which make not feasible the use of these circuits for highly integrated MEA chips [125].

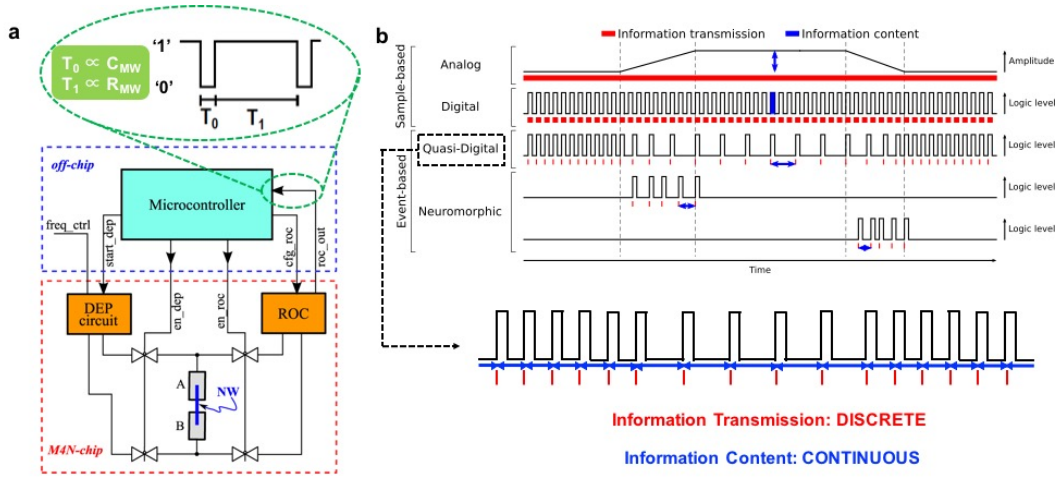

Fig. 4.2 (a) Block diagram of the circuits of a single couple of electrodes with external microcontroller interface and output signal (adapted from [124], ©2015 IEEE). (b) Scheme of the quasi-digital approach used for the design of the ROCs and its comparison with both the common sample-based and the neuromorphic systems (adapted from [125], ©2017 IEEE).

Instead, in the event-based approaches the information (blue lines in Figure 4.2, b) is marked and embedded in the timings of the signal itself, as outlined by the red bars in the figure. In fact, while in traditional approaches the information is mapped with an amplitude value (both in the analog or digital case), in the event-based ones, the information carrier is the time itself [125]. For example, for the M4N chips, a variation of the square wave time T_1 brings the information about the variation of the measured microwires resistance and, this information is not encoded in the signal amplitude. This means that a continuous information is transmitted by a digital signal. In this way it is possible to take the advantages of both analog signals, capable to retain the complete acquired information, and of digital ones, hence reducing the amount of transmitted and processed data i.e., the circuit complexity and power consumption. Besides the quasi-digital signals also the neuromorphic ones belong to the event-based category. These signals are called neuromorphic since their working mechanism is inspired to the signal transmission architecture of neurons and perceptive cognitive systems. In this case, the signal is always to the logic '0' except when a variation of the information occurs, while, in the quasi-digital approach the information is continuously transmitted. This is why, as observable from Figure 4.2 b, the quasi digital signal is represented by a continuous square wave while, the neuromorphic one by a series of spike trains (related to a variation of the measured quantity). Nevertheless, in the neuromorphic case there is a significant reduction of the processed and transmitted data that may cause some loss of information. Moreover usually, these type of ROCs are often analog CMOS circuits with analog memory elements. Instead, in the quasi-digital approach not only the information content is continuous and there are no information losses, but, also, mainly mixed analog/digital components are used, or also fully-digital designs can be found, leading to smaller circuits that allow higher integration hence the addition multiple sensing sites on the same chip [125].

Since the main focus of the present work was to use the M4N chip to measure the variation of the electrical properties of ZnO microwires, no further details will be given about the circuits architecture and design. Instead, more attention will be devoted to the post-processing processes and to the sensing measurements. In fact, the M4N chips cannot be used as produced from the foundry but, several procedures are necessary to prepare the surface for the microstructure deposition.

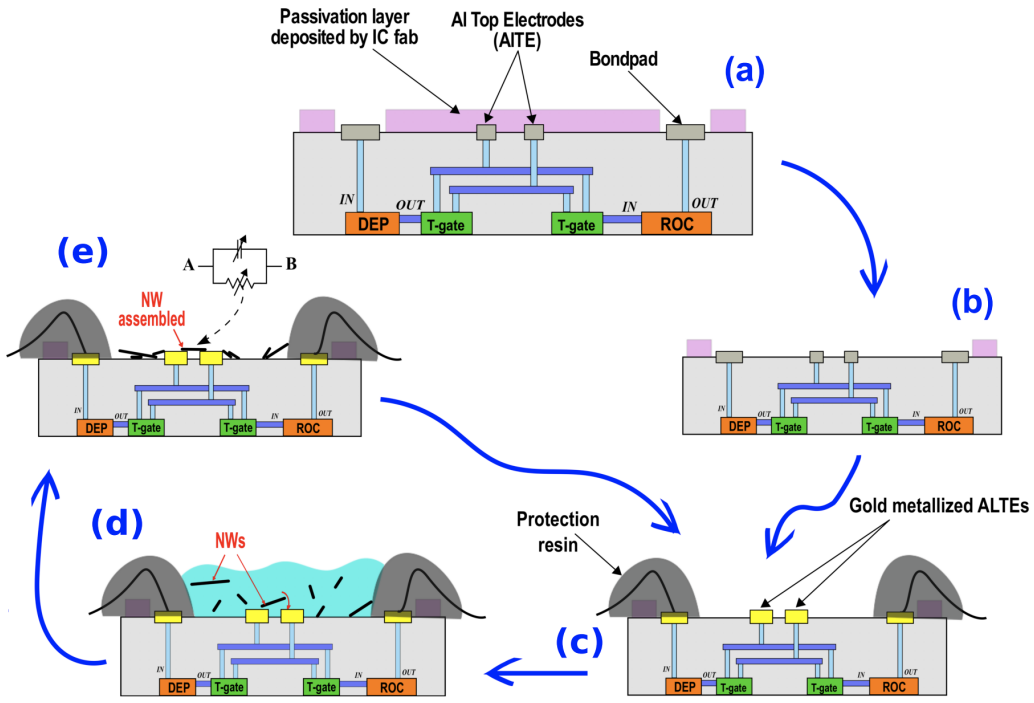

Fig. 4.3 Process flow of the integration and sensing of microstructures on the M4N chips. After the removal of the passivation (a), the AlTEs are plated with gold and the bonding pads are protected with epoxy resin (b-c). The microstructures can then be deposited exploiting the embedded DEP circuits (d) and their impedance can be at last measured using the ROCs (e) (reproduced from [4], licensed under a CC-BY 4.0 license).

The overall process flow designed and implemented for the integration and sensing of microstructures on the M4N chips is shown in Figure 4.3. At first, it must be considered that, the integrated circuits produced with CMOS technology, present a passivation layer on the top-most surface in order to protect the circuits from damages, dust and contaminants [4]. For the M4N chips, the top passivation is formed by 400 nm of phosphosilicate glass (PSG) and 500 nm of silicon nitride (Si_3N_4), as outlined in Figure 4.3 a. It was therefore necessary to expose the surface of the AlTEs initially buried in the passivation. As described in the next paragraph, this step was performed by a dry etching technique (Figure 4.3, b). Nevertheless, once the AlTEs were exposed to open air, a thin insulting layer of aluminum oxide, Al_2O_3 would rapidly form on their surface. Due to the reduced contact area between the microstructure and the metal electrodes, this thin insulating layer can be enough to compromise the electrical measurement. For this reason, an electroless gold metalization plating was developed in order to modify the electrodes surface from aluminum to gold, less prone to oxidation and biocompatible (Figure 4.3, c). Then, the chip was wire bonded on a custom-designed PCB board and the bonding wires where then protected by 1-k epoxy resin, as in the case of the nanogap chips. From

this point on, the chip is ready to be programmed at first to enable the DEP circuits, to align the selected microstructures and, then, to read-out in real-time the variation of their impedance through the embedded ROCs (Figure 4.3 d and e, respectively) [4]. The microwires can then be removed by a quick ultrasonic bath (10 - 20 min) in isopropanol leaving the chip ready for another use. The reusability of the chip is one powerful intrinsic advantage of the dielectrophoresis deposition method.

Before proceeding to the next section (Section 4.1.1), where the electroless metalization process will be throughly discussed, few other important details need to be specified about the passivation removal process. Usually, the standard fabrication processes for integrated circuits allow the opening of apertures on specific regions of the passivated chip surface. This is necessary, e.g., to create apertures for the bonding or the I/O pads. However, due to the strict design rules governing the standard CMOS fabrication process, these holes need to be at least bigger than 60 μm x 60 μm and in any case smaller than the underlying metal area so that some passivation is always left between two different top metal lines (see Figure 4.4, b). These constraints, not only strongly reduce the maximum number of unit cells that can be integrated on a single chip, due to the large aperture, but, also they do not remove the passivation between a couple of facing electrodes, hence impeding the alignment of the microstructure on their surface. For these reasons, instead of designing additional lithographic masks to be integrated in the fabrication process, hence strongly increasing the final cost of the device, a reactive ion etching (RIE) process was preferred [4]. RIE includes both a chemical etching, thanks to a reactive plasma generated e.g. by a radio-frequency (RF) field, and a physical one caused by the highly energetic ions of the plasma that attack and react with the substrate surface. In the case of M4N chips, SF_6 gas was used to etch the PSG and Si_3N_4 passivation on the whole chip surface. Once the aluminum surface is reached, the aluminum itself will act as a stop layer for the RIE process hence allowing the opening of the area between different metal electrodes without damaging them (Figure 4.4, c).

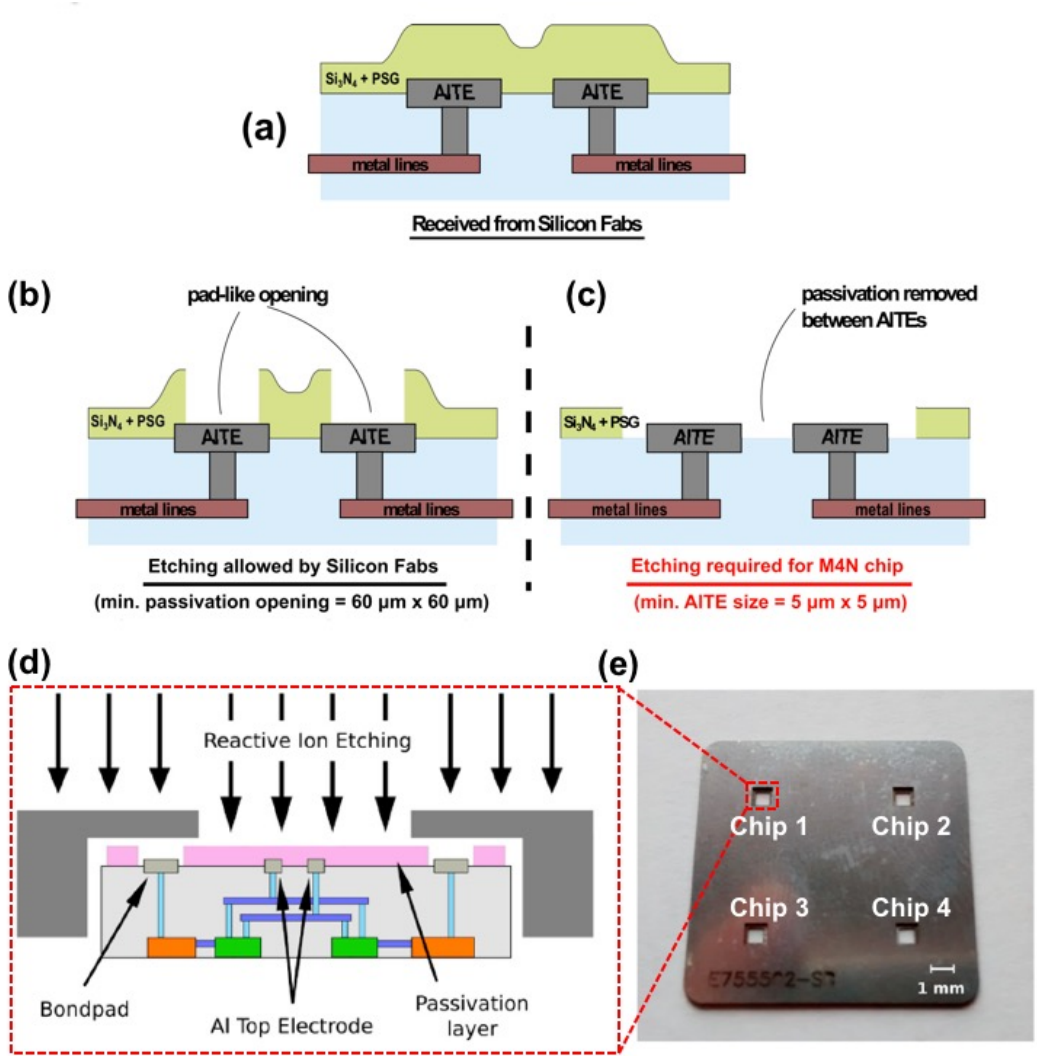

Fig. 4.4 RIE of the M4N native passivation layer (a). (b) Standard solutions used to open windows on integrated circuits like e.g. bonding pads opening. (c) etching required for the correct operation of the M4N chips. This is achieved through RIE (d) after that the chip's bonding pads had been covered by a custom stainless steel mask (reproduced from [4], licensed under a CC-BY 4.0 license).

During the RIE process, the ring of boning pads surrounding the chip active area (see Figure 4.1, c) need to be protected from the attack in order to avoid the etching of the passivation layer insulating two different bonding pads. For this purpose, a custom stainless steel mask was fabricated capable to cover just the area of the chip where the square ring of bonding pads is located (Figure 4.4 d and e). With a single mask, 4 M4N chips can be processed at once. Specifically, 16 sccm of SF_6 gas were used for a single process at a chamber pressure of 75 mTorr and using a RF power of 150 W. The overall process duration was of 13 minutes. As published in [4], the

confirmation of the success of the RIE process was obtained using energy dispersive X-ray spectroscopy (EDX) analysis which revealed the presence of aluminum on the electrodes surface.

In Section 4.1.1, after an initial literature review about CMOS post-processing in general, an introduction about the electroless nickel gold immersion (ENIG) metalization process will be presented (Section 4.1.1.1) and then, the experimental protocol adopted will be discussed in details (Section 4.1.1.2).

4.1.1 CMOS Post-Processing

The modification of the surface of CMOS circuits is of high interest for the fabrication of state-of-the-art multi-functional devices capable to integrate on the same chip both the electronics and other application-driven features like microfluidics, bio-functional coatings or also moving mechanical parts. By optimizing CMOS-compatible fabrication processes high-performing conditioning electronics e.g., with digital ROCs can be directly incorporated in the final device [126]. This is particularly relevant in the field of MEMS and NEMS where CMOS circuitry can be also embedded on-chip leading to CMOS-MEMS devices and, especially, sensors/actuators with improved performances and, also, higher miniaturization [127].

Depending on when the modification of the CMOS chip is performed (before, during of after the integrated circuits fabrication), these processes can be referred as pre-CMOS, intra-CMOS and post-CMOS [127]. In pre-CMOS processes, all the non-standard features are defined prior to the fabrication and buried in a recess trench then covered by a dielectric material. If part of the device must interact with the external environment, usually a post-processing etching step is required in order to expose the target area. Since these processes require additional lithographic masks not only they considerably increase the final cost of the device but, also, the final thickness of the microfabricated structures is limited by the resolution of the photolithographic step [127].

If the additional features are fabricated through the deposition of additional polysilicon thin layers, then micromachined and, if needed, released to create suspended structures, the process is called inter-CMOS [127]. These precesses were developed in the United States around the 1990s by the Analog Devices Inc. for the production of MEMS gyroscopes and accelerometers [127]. They are currently employed in the volume production of smart tire pressure monitoring systems [127].

However, one of the most adopted approaches is the post-CMOS, also called CMOS post-processing. This approach is based on the modification of the CMOS chip surface after its fabrication process is completed and, most of all, it can be performed externally to the foundry. If compared with the pre- and inter-CMOS ones, this method offers several advantages. At first, since the chip is processed after

its fabrication, no specific modifications of the foundry manufacturing operations are needed, hence reducing the final cost of the devices if compared with the pre- or intra-CMOS approaches [127]. Secondly, the processing of polysilicon requires elevated temperatures, above 800 °C, in order to reduce the induced stresses on the material itself, hence increasing the probability of damaging the CMOS circuits [128]. Therefore, thanks to their more versatile implementation and cost effectiveness, CMOS post-processing approaches are gaining always more interest in the literature [127].

CMOS post-processes can be either additive, where the necessary materials and structures are added on the chip surface, or subtractive, hence requiring etching steps to remove selected portions or layers of the chip [127]. In the present work, both additive and subtractive CMOS post-processes were adopted in order to properly prepare the chip surface for the interaction with the selected microstructures. At the dawn of the CMOS MEMS fabrication, the subtractive method was at first employed based on wet etching techniques [127]. The etching step can be performed both at the front- or at the back-side of the chip and usually, in case of silicon etching KOH or tetramethylammonium hydroxide (TMAH) are selected [127]. In order to accurately control the etching mechanism, two approaches can be used. In case a small process variation can be tolerated on the final structure, the etching mechanism can be tuned by controlling the etching time and properly calibrating the etching rate. If, instead, a higher precision is required, automatic etch-stop layers can be employed [127]. In time, a gradual switching to a dry etching technique, like the RIE adopted in this work, was preferred. This was mainly due to the higher versatility, precision and performances of these methods allowing for the fabrication of a wider spectrum of CMOS-MEMS [127].

The flexibility of the CMOS post-processing allows it to be performed both at the wafer or die level, i.e., before or after the wafer dicing, respectively. Usually, at the wafer level, the process is performed after the deposition of a passivation layer to protect the top metalization and before the chip dicing [129]. Despite its adaptability and versatility, numerous precautions must be taken in order to avoid wafer damages during the post-processing step. As already anticipated, the experimental temperature should be below 450 °C in order to avoid the degradation of the underneath metalizations [129]. Plasma treatments may charge the MOS transistors while, the added layers could cause the mechanical stress on the final device to increase above the critical point, hence causing the malfunctioning of the interconnects and the device itself [129].

One of the firsts and most relevant examples of wafer-level CMOS post-processing is the digital micromirror device developed by Kessel *et al.* [130]. The core of the device is an array of tilting micro-scale mirrors on the surface of a CMOS chip which are used for projection display systems. Each mirror can be in two stable positions switched by electrostatic forces stored in one bit of a static random access memory

(SRAM) directly underneath the mirror [130]. The mirrors holders are fabricated by consecutive depositions and patterning processes. The releasing of the mirror itself, instead, occurs just before the wafer dicing step by removing a specific sacrificial layer of photoresist using RIE [130].

Nevertheless, in case of multi-wafer-projects, in which dies are received from the foundry instead of the whole wafer (as in the present work), more caution is needed. This is not only related to the individual chip handling but, also, to the fact that some processes, working properly at the wafer level may be not be so effective also at the die level. Just as an example, obtaining a uniform photoresist coating of a very small surface is highly cumbersome leading often to the presence of important border effects. For this reason, Chang *et al.* suggest in their paper to avoid the use of photolithography for die-level CMOS post-processing [131]. To pattern the active area of the open-gate field effect transistor they developed two different approaches based on wet etching of metal stacks or RIE, respectively. Using both the methods they were able to remove the different passivation layers on top of the gate so that it could be exposed to the target sensing solutions [131]. Despite being useful for die-level post-processing, RIE and, especially, deep-RIE (DRIE) techniques are extremely useful to achieve high aspect ratio structures on chip [126]. DRIE, also known as Bosch process, is a RIE improvement in which etching cycles are alternated with passivation steps which, protecting the surface from further ions attacks, allow the fabrication of true-vertical walls, not always possible with other approaches [126]. Thanks to the high anisotropic nature, DRIE it widely used in MEMS/NEMS fabrication to have high-aspect-ratio structures, indeed between 20:1 and 30:1 [126]. This leads to the fabrication of advanced devices like e.g., comb-like actuators with combs deep up to 100 μm and comb distance of 15 μm [126].

The CMOS post-processing techniques, described up to now, have been intended for applications on rigid substrates. However, flexible electronics is becoming a key requirement for an increasing number of applications like tactile sensors for robotics hands or wearable applications [132]. In this case, the post-processing temperature is an even more critical problem since flexible substrates are often able to withstand only low temperatures [132]. This is one of the main reasons that makes impractical the direct fabrication of CMOS circuits or CMOS-MEMS devices on flexible substrates. To bypass this issue, hybrid approaches, based on smart packaging and post-processing of the CMOS dies using flexible materials are preferred. One of the most adopted approach is the incorporation of CMOS chips in flexible skin technologies using silicon islands structures [132]. After fabrication, the chips are post-processed both on the front and on the back side so that the chip can be completed encapsulated into a polymeric substrate made e.g, of polyimide or polydimethilsiloxane (PDMS). Usually, at first a polymeric layer is deposited on the front side of the chip and, after a back-side etching to reduce the thickness of the final chip, another polymer is deposited on the back side so that the chip is completely

encapsulated [132]. In this way, silicon islands, incorporating the functional CMOS electronics, can be patterned on extended polymeric substrates to form smart flexible skins for different applications. At the early stage, this technology was employed to fabricate flexible arrays of diode-based temperature sensors for robotic or biomedical usage [133]. Numerous improved implementations of this approach have been then reported in the literature. For example, Xu *et al.* developed integrated circuits-based flexible shear-stress sensor skin for unmanned vehicle applications [134] while, Katragadda *et al.* fabricated a novel intelligent textile where sensing and computational components were embedded into textiles without compromising the fabric flexibility and wearability [135].

The versatility of CMOS post-processing, along with the great advantages introduced by the silicon islands approach, can be used as foundation for the design and fabrication of other types of CMOS-based devices, in addition to smart textiles. For example, starting form the silicon islands approach, different groups developed implantable neural probes for the investigation of neural disorders [132]. These studies are based on the interconnection of silicon islands by polymeric cables then folded to form a 3D structure where also microfluidics channels can be embedded to enable e.g. chemical stimulation or drug delivery studies [136, 137]. Other biomedical applications involved, e.g., intelligent medical catheters and waveguides [132].

CMOS post-processing and bio/chemical-compatibility When dealing with clinical and biological applications of CMOS-based post-processed devices, it is extremely important to pay specific attention to biocompatibility issues. This is a two-way process since, on one side, the synthetic device must be biocompatible and electrochemically stable, so to avoid damages to the biological entities present, but at the same time, the electronics must be protected by the extremely harsh and aggressive environment constituted by biological fluids and tissues [138]. This is extremely important not only in case of implantable devices for *in vivo* applications but, also, for the development of cell-based biosensors e.g., used for new drugs testing or electrophysiological studies. One of the main obstacles is the presence of aluminum and its oxide, in the CMOS fabrication process flow as conventional material for metalization lines [138]. As described in Section 4.1, also the M4N chips here presented expose top aluminum metal vias. Aluminum is a material that reacts strongly with the oxygen present in air environments forming a natural Al_2O_3 (alumina) amorphous and insulating oxide layer. This is caused by its highly negative Gibbs free energy (-791.15 kJ/mol) [138]. When exposed to low or high pH conditions, aluminum and its oxide will also undergo chemical modifications by forming Al^{3+} or AlO_2^-, respectively. These two species are the main responsible of corrosion phenomena [138]. Although the pH value of physiological solutions is close to neutrality, corrosion phenomena still occur due to the creation of localized acidic pH conditions at the electrodes surface as a consequence of the adsorption

of the Cl^- ions present in solution on their surface [138]. Therefore, aluminum CMOS electrodes must be carefully passivated or protected with *ad hoc* coatings from the different physiological solutions. Despite the potential damages for the electronics, the corrosion of aluminum or alumina is also extremely dangerous for the biological environment due to its cytotoxic nature [138]. In addition, alumina was found also to be a thrombogenic agent, hence responsible for undesirable blood clotting [139]. This is why, for *in vivo* applications, aluminum is coated with the more electrochemically stable titanium nitride [139]. Additional sources of toxicity are also constituted by the formation of the insoluble compound $Al(OH)_3$ or by the creation of $AlCl_3$ [140].

When the CMOS chip needs to be interfaced with living cells to characterize their electrical communication, an optimal adhesion of the cells on the electrode surface is necessary in order to measure a reliable signal. As it will be discussed in Section 4.2 and in Chapter 8, CMOS post-processing employing biocompatible and bioactive coatings can be a successful strategy to improve the cellular adhesion on the electrodes. Usually adhesion proteins can be selected like the arginine-glycine-aspartic acid (RGD) peptide sequence [138]. This coating is particularly successful with different cells type, including cardiomyocytes, but, it is not very effective with neurons for which other coatings, like polylysine, are preferred [138].

It is now clear why the aluminum top electrodes of the M4N chips do not represent an optimal surface for sensing applications. Not only the spontaneous formation of the insulating aluminum oxide layer decreases the quality of the electrical contact between the electrodes and the target microstructure, but also, it constitutes a cause of toxicity in case of biological applications. Therefore, an electroless nickel immersion gold metalization process was selected and optimized in order to modify the electrodes surface from aluminum to gold, a metal with known biocompatibility and that is less prone to oxidation [141]. After a short literature review about electroless nickel immersion gold metalization processes in general (Section 4.1.1.1), the experimental metalization protocol optimized in the present work will be discussed in details in Section 4.1.1.2.

4.1.1.1 Electroless Nickel Immersion Gold (ENIG): Introduction and State of the Art

As anticipated in Section 4.1 and 4.1.1, a RIE step was performed on the M4N chips in order to remove the passivation layer, deposited by the foundry, hence exposing the underlying aluminum electrodes. Nevertheless, the native aluminum oxide forming on the aluminum surface after air exposure is responsible of the increase of the contact resistance between the electrode itself and the microstructure that will be deposited [142]. Therefore, a plating with a metal more robust against oxidation, like e.g., gold, is a necessary step to improve the final sensor performances.

One of the most used techniques to cover the surface of a metal with a different metal is the electrodeposition [4]. This process is based on the application of a voltage difference between two electrodes in an electrolytic bath. One of the two electrodes will act as donor of metal ions (cathode) while, the other one (anode) will be plated with the donated material after that the ions are transported close to its surface, by the applied potential. Specifically, the transported metal ions react with the electrons present in the solution hence converting the metal ions in metal atoms at the anode surface [143]. In case of the M4N chips, this technique requires that all the AlTEs are connected to the same ground potential to allow the correct current flow, necessary for the electrodeposition, which is not possible due to the chip circuits configuration[4]. For this reason, in this work, an electroless deposition process was preferred. Electroless plating involves the auto-catalytic reduction of metallic ions in an aqueous solution that are then deposited on the surface of another metal immersed in the solution, without requiring external electrical energy [144]. The uniformity of the deposition is increased since the process is not influenced by the external current distribution [145]. This is why this approach can be used for a wider family of materials, than electrodeposition, including also fabric or insulators as plastics or rubbers [144]. Moreover, employing electroless processes, not only the physical and mechanical properties of the final metal are strongly improved, if compared with electrodeposition but, at the same time, sharp edges or deep holes can be plated with uniform spatial thickness [144]. For these reasons, in addition to its high selectivity and high resistance against wear and corrosion, this technique has been widely used in flip-chip packaging applications, MEMS, powder metallurgy as well as jewelery plating [144, 4, 145].

In case of electroless deposition of gold layers on aluminum, usually a stack of different metals is used to improve the catalytic gold deposition, as well as its adhesion. The stack is formed in order by aluminum $\rightarrow$ zinc $\rightarrow$ nickel $\rightarrow$ gold and this is why this technique is called electroless nickel immersion gold (ENIG). Briefly, ENIG is based on the immersion of the aluminum electrodes in a strong alkaline solution of zinc that, reacting with the aluminum electrodes, will form a zinc surface. The zinc surface will then be a catalytic layer for the subsequent nickel and then gold plating [142]. Precise tuning of the process concentrations, temperatures and times are necessary in order to achieve the desired coating. This is particularly important when dealing with micrometric electrodes, that differently from macroscale ones, for which the industrial processes are already developed, require *ad hoc* process adaptation and optimization.

In Section 4.1.1.2, the experimental procedure optimized for the ENIG plating of the M4N AlTEs will be described in details.

4.1.1.2 ENIG Experimental Process Optimization

The ENIG process reported in the present work, was optimized to allow slow and stable growth rates, suitable for the plating of the micrometric AlTEs of the M4N chips. One of the major complications was achieving an uniform and complete plating avoiding the growth of a short-circuit between the couples of facing electrodes, spaced only by few microns. All the solutions used for the ENIG process were purchased from Technic Inc. (USA). As anticipated in Section 4.1.1.1, the ENIG process here presented involved the deposition of a stack of metals, in order zinc (Zn), nickel (Ni) and at last gold (Au), on the surface of the AlTEs. A total volume equal to 20 mL was prepared for each of the ENIG process solution, as detailed in Table 4.1. As anticipated in the chapter abstract, the optimization of the ENIG process was performed in collaboration with the Master Thesis work of V. Allegra and published by the author in [4].

Before starting the plating, the chip surface must be cleaned so that contaminants, eventually present from the fabrication and the chip handling will not interfere with the deposition process. Therefore, the chip is at first immersed in an alkaline chemical degreasing solution, TECHNIC TSC 1500, responsible of removing all the grease and oil present on the electrodes surface. The solution contains sodium silicates compounds and it is in white powder form. It must therefore be dissolved in Milli-Q water (mqH_2O), also called ultra-pure water, with 5% concentration, until the solution appears completely transparent (see Figure 4.5 a). It has a working temperature between 60°C and 83°C and a working time between 1 min and 5 min, according to the technical data-sheet provided. In the present work, the minimum working time was selected, 1 min, due to the micrometer size of the electrodes, while the temperature was optimized to 68°C.

To remove the silicates residues due to the TECHNIC TSC 1500 solution, a next immersion of the chip in an ammonium bifluoride-based solution, TECHNIC REMOVA 1700, was necessary. TECHNIC REMOVA 1700 appears in a solid crystalline form, and must be also dissolved in mqH_2O with 0.8% concentration. The solution is very acidic, the measured pH was close to 1, and it is operative at room temperature. If this solution is used to clean silicates residues, as in the present case, according to the technical data-sheet, it must be mixed with nitric acid (HNO_3). The optimal concentration of HNO_3 chosen to be effective, but, at the same time, to avoid electrodes damages was 1%. Therefore, the final solution was formed at first by dissolving 0.16 g of TECHNIC REMOVA 1700 in 20 mL of mqH_2O and then, by adding 200 μL of HNO_3 (see Figure 4.5 and Table 4.1). This step was also important to activate the surface for the subsequent Zn deposition. Due to the aggressiveness and strong acidity of the solution this step lasted only 1 sec.

Step	Chemicals	Solution Details
1-Degreasing	***TECHNIC TSC 1500***	20 mL mqH_2O + 1 g TSC (5%)
2-Acid Activation	***REMOVA 1700 + Nitric Acid***	200 μL HNO_3 (1%) + 0.16 g REMOVA (0.8%) + 20 mL mqH_2O
3-Zn Plating	***TECHNIC EN ZINCATE***	15 mL mqH_2O + 5 mL EN ZINCATE (25%)
4-Acid Desmutting	***Nitric Acid***	200 μL HNO_3 (1%) + 20 mL mqH_2O
5-2nd Zn Plating	***REMOVA 1700 + Nitric Acid***	200 μL HNO_3 (1%) + 0.16 g REMOVA (0.8%)+ 20 mL mqH_2O
6-Ni Plating	***TECHNIC EN NICKEL AT 5000, Part A and B***	15.8 mL mqH_2O + 1.2 mL EN NICKEL A(6%)+3 mL EN NICKEL B (15%)
7-Au Plating	***OROMERSE SO, Part A and B***	18.68 mL OROMERSE A(93.4%) + 1.32 mL OROMERSE B(6.6%)

Table 4.1 Detailed composition of the 7 solutions employed in the ENIG plating of the M4N chips.

In order to be able to plate other metals on aluminum, the native oxide formed after the RIE process must be carefully removed. This can be done by using a strong sodium hydroxide (NaOH) solution containing also zincate ions ($Zn(OH)_4^{2-}$) [146]. In this way, Al_2O_3 will dissolve due to NaOH while, at the same time, Zn will deposit on the aluminum surface due to a displacement reaction [146]. Therefore, it is important to notice that the zincation is not entirely an additive process but, more precisely a substitutionary one where aluminum atoms on the chip surface are substituted by Zn ones. To achieve this goal the TECHNIC EN ZINCATE solution, specifically developed by Technic Inc. for this step of the process was used. This solution is then diluted in mqH_2O with a final concentration of 25% (5 mL diluted in 15 mL of mqH_2O, see Table 4.1). As visible from Figure 4.5 a, the obtained solution is yellow and transparent, moreover, it works at room temperature and the immersion time can be varied between 15 sec up to 2 min. Here, the immersion time was optimize, during successive experimental trials to 1 min. As reported in the literature, to improve the adhesion of the zinc layer, as well as the smoothness of the final surface, multiple zincation steps can be useful [145]. This requires an intermediate acid attack between the two zincation steps. Therefore, as visible from the table in Figure 4.5 c, during the ENIG plating of the M4N chips, two zincation steps of 1 min were performed, intermediated by a 1 sec long nitric acid (1%) attack.

The double-zincation step prepared the surface for the subsequent Ni plating. To start electroless Ni plating, the electrodes must be immersed in a solution containing Ni ions and specific reducing agents [144]. The temperature plays also a crucial role to allow and maintain a stable reaction dynamics. The electroless nickel-phosphorous alloy TECHNIC EN NICKEL AT 5000 product was selected for this task.

a

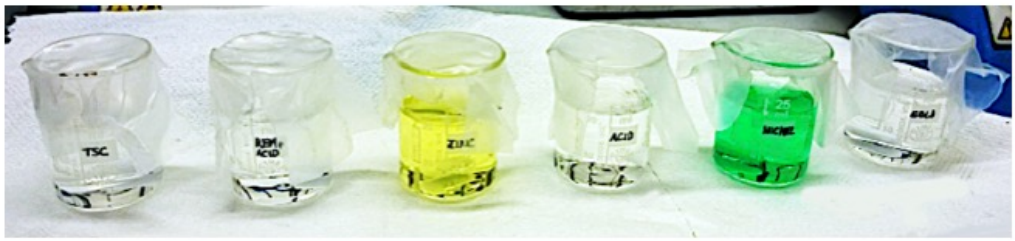

b

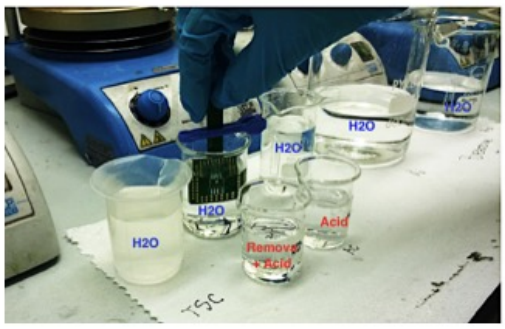

c

Step	Time	Temperature	Stirring
Degreasing (TSC)	60 s	68 °C	200 rpm
Rinse	60 s	Room Temp.	/
Remova + HNO_3	1 s	27 °C	/
Rinse	60 s	Room Temp.	/
Zinc	60 s	27 °C	200 rpm
Rinse	60 s	Room Temp.	/
Acid (HNO_3)	1 s	27 °C	/
Rinse	60 s	Room Temp.	/
Zinc	60 s	27 °C	200 rpm
Rinse	60 s	Room Temp.	/
Nickel	120 s	86 °C	200 rpm
Rinse	60 s	Room Temp.	/
Gold	120 s	73 °C	200 rpm
Rinse	60 s	Room Temp.	/

Fig. 4.5 Experimental ENIG plating process of the M4N chips. (a) The different plating baths to be prepared are, in order: TSC, REMOVA with 1% HNO_3, EN ZINCATE, 1% HNO_3, EN NICKEL and OROMERSE SO. (b) Washing step of the M4N chip during the ENIG process. (c) Summary of all the steps of a complete ENIG process of a M4N chip reporting also the chip immersion time, solution temperature and stirring.

The product is formed by two components, part A and part B. Part A is the primary source of Ni ions, it contains nickel sulfate and it is what gave the green color to the solution (see Figure 4.5 a). Part B, instead, contains sodium hydroxide and it is the main source of the reducing agent, sodium hypophosphite. Although all the solutions, except the acid steps, are kept under vigorous stirring at around 200 rpm, for the Ni plating the stirring is a mandatory requirement for the plating to be effective. The two solutions, A and B, need to be diluted in mqH_2O with percentage concentration of 6% and 15%, respectively (see Table 4.1). The operational temperature range is between 82°C and 87°C (86°C in the present work), since a lower temperature may slow down too much the deposition rate, while, a higher temeprature may result in the degradation of some constituents of the solution. To have a uniform Ni plating of the electrodes, an immersion time of 2 min was experimentally optimized.

At last, the gold plating was performed by using the OROMERSE SO plating solutions (Part A and Part B), specifically optimized for plating on Ni-covered surfaces. Part A contains sodium hydroxide while Part B is the main source of Au ions. The reaction is guided by the following equation: $2Au^{+} + Ni \rightarrow 2Au + Ni^{2+}$ [147]. Part B must be diluted in part A with final concentration of 6.6% (see Table

4.1). Also in this case, the working temperature is extremely important for the success of the plating process and it must be kept between 70°C and 73°C.

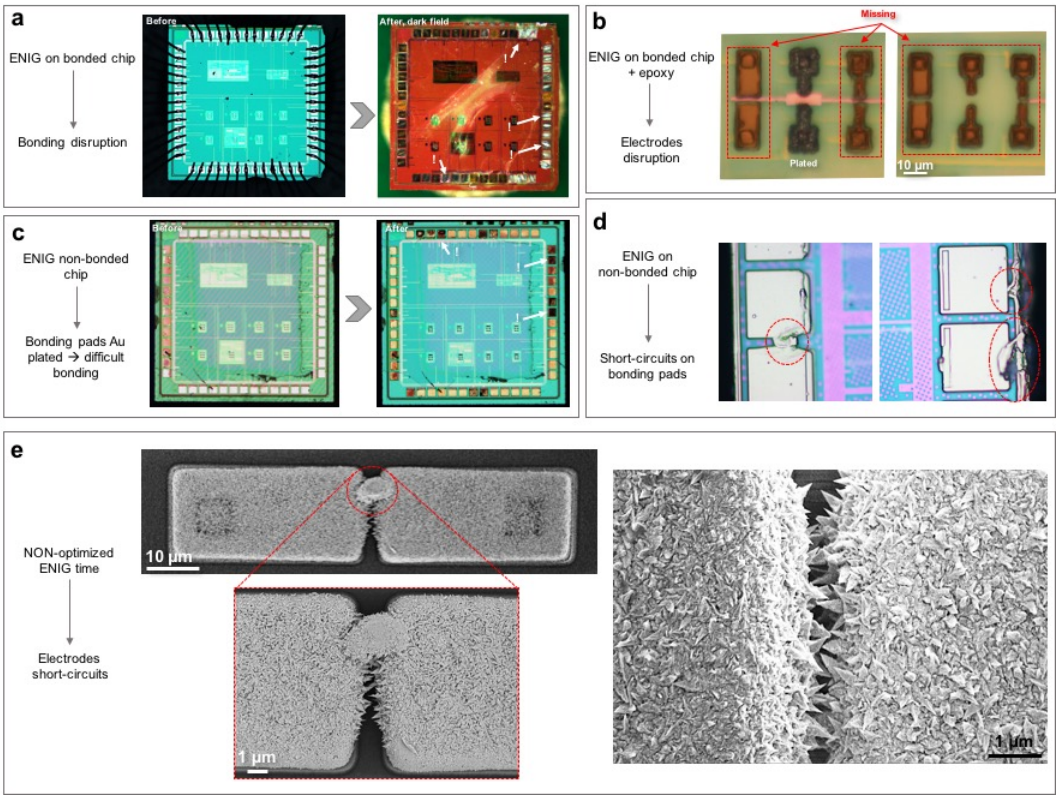

Fig. 4.6 Experimental problems encountered during the ENIG plating of M4N chips. (a) Disruption of the bonding wires if exposed to the ENIG process. (b) Electrodes disruption if the process is done with the bonding wires protected with the epoxy resin. In this case only an electrode halo remains in the majority of the cases. The ENIG process on non-bonded chips causes the Au plating also of the bonding pads (c), which may cause unwanted short-circuits (d). (e) FESEM images of the final surface in case of Au extra-growth between the electrodes gap forming unwanted short-circuit.

As anticipated and summarized in the table reported in Figure 4.5, each solution requires a specific working temperature and stirring condition. For this reason, the TSC, Zn, Ni and Au solutions are placed each one on a separate AREX-heating magnetic stirrer at 200 rpm and 68°C, 27°C, 86°C and 72°C, respectively. The remaining solutions, REMOVA and nitric acid, do not need specific operating conditions, and therefore, are placed directly on the hood bench. Each plating step is followed by a 1 min rinsing in mqH_2O (see Figure 4.5 b). After the last rinsing step, the chip is dried under nitrogen flux. The total ENIG process time is very quick, just 14 min, and the whole process cost for one chip is less than 1€, thus making the process suitable for quick and low-cost experiments [4].

Nevertheless, in addition to the optimization of the solutions concentrations, working time and working temperature, which where experimentally adjusted starting from the data-sheet guidelines, numerous other unpredictable operating conditions needed to be optimized for a successful process. The most important are shown in Figure 4.6. In order to be handled, the M4N chip was directly attached to the final PCB board that was previously designed with an holding tab to ease the immersion of the chip in the different baths (see Figure 4.5 b). The tab was then removed at the end of the ENIG process. At first, the chip was not only glued on the PCB but also bonded. Nevertheless, as visible from Figure 4.6 a, the bonding wires were not able to withstand the chemical process and, due to the residues remained on the bonding pads, no further bonding was possible on the plated chip. To solve this issue the chip was plated after covering the bonding wires with the epoxy resin described in Section 4.1. However, although the mechanism is not clearly understood yet, it is supposed that a chemical interaction occurred between the epoxy resin and the plating baths leading to the disruption of the M4N electrodes during the process. In fact, as shown in Figure 4.6, the majority of the AlTEs were removed from the chip surface leaving only a halo, recognizable from the orange contrast with no three-dimensionality under the optical microscope, instead of the real electrode. This problem was no more observed when the process was performed on the chip just glued on the PCB with no bonding and no epoxy resin. At this stage, even if the electrodes were gold-plated, still other minor issues needed to be taken care of. Since the bonding pads were also made of Au, the growth of gold during the ENIG process was occurring also on their surface (see Figure 4.6 c). This growth, was clearly observable under the optical microscope since a brown contrast and higher roughness were present on the plated bonding pads. This not only made impossible the bonding of the chip with too high surface roughness but, also, caused unwanted short-circuits between adjacent pads or between the pad and the surrounding metal ring of the chip (see Figure 4.6 d). In both the cases, it was not possible to use the chip from the electrical point of view. The formation of short-circuits caused by the overgrowth of gold on the electrodes surface was also present in some cases between different couples of facing electrodes, as shown in Figure 4.6 e. From the FESEM images it can be recognized how the growth of excess gold on the electrodes surface causes the formation of pyramidal crystals oriented from the inner wall of one electrode towards the other electrode and vice versa.

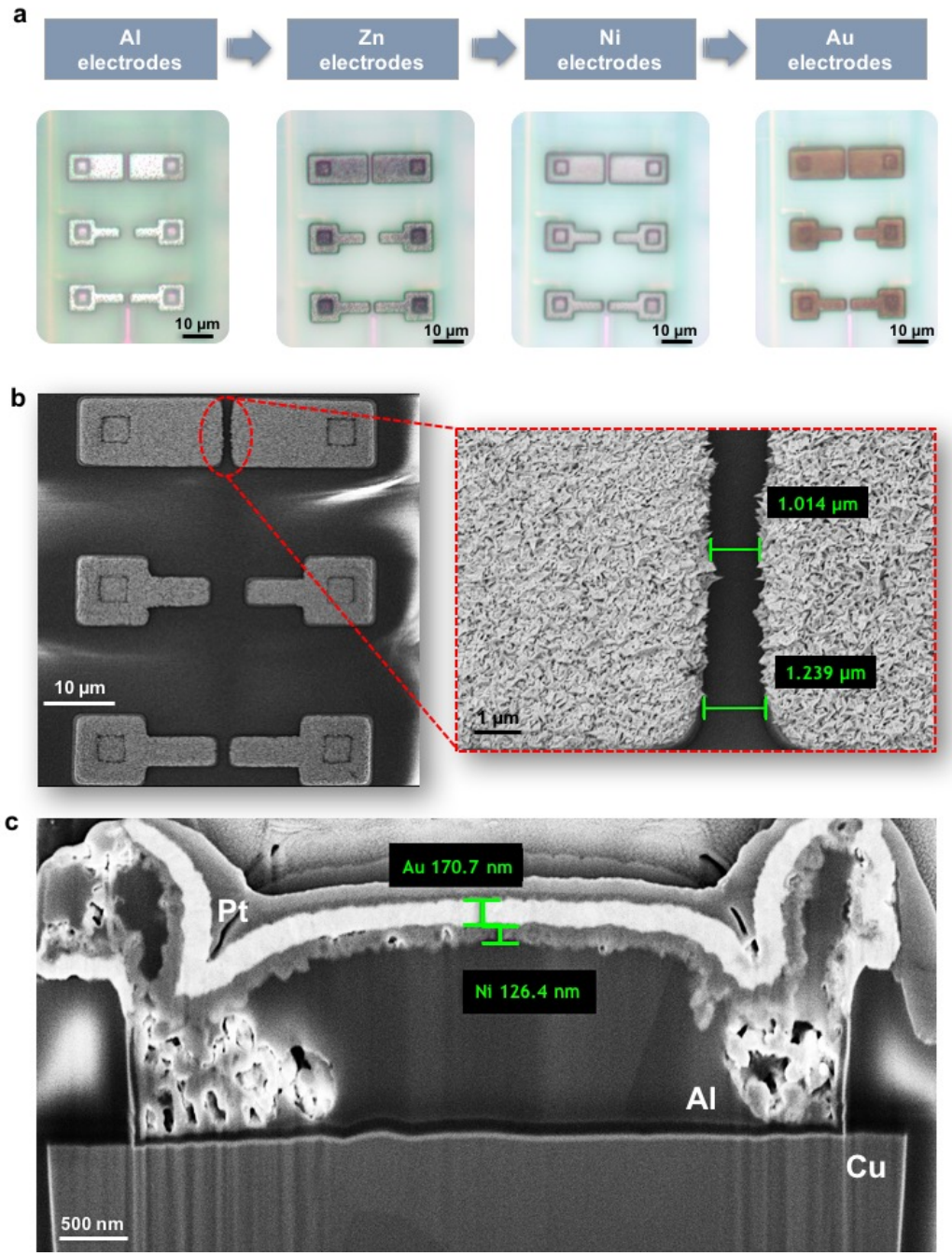

Fig. 4.7 (a) Optical microscope images of the AlTEs during each step of the ENIG process. (b) FESEM images of the final gold-plates surface of one cell of the M4N chip. (c) FIB cross-section of one AlTE after the ENIG process. The zinc layer is not visible, due to its small thickness, while, the nickel and gold ones are clearly recognizable with thicknesses of 126.4 nm and 170.7 nm, respectively (image (c) adapted from [4], licensed under a CC-BY 4.0 license).

In some cases, this extra growth caused the formation of gold bumps that were connecting electrically the couple of facing electrode hence making not possible anymore the microstructure deposition and characterization. For all these reasons the plating time of both Ni and Au baths was carefully tuned starting from 10 min, then reduced to 5 min and, at last, to 2 min. It is worth to note that, characterized with the FESEM microscope, the final gold surface showed sharp pyramidal nano-crystals randomly oriented contributing to increase the surface roughness. This is a positive feature for increasing the contact area of the microstructure on the electrodes.

The results of the optimized ENIG plating of the M4N chips can be observed in Figure 4.7. Each plating step, besides being verified by EDX analysis (as reported in [4]), was also recognizable from the optical microscope (Figure 4.7 a). In Figure 4.7 b, a successful gold plating process on a single M4N cell is characterized with the FESEM microscope. The typical pyramidal-like surface roughness can be observed uniformly on all the electrodes. The magnification of the upper couple of electrodes revealed a gap of about 1 μm, with no critical points for short-circuits formation. Analyzing the FIB cross-section of one plated electrode (Figure 4.7 c), the Au thickness was found to be around 170.7 nm while the Ni one around 126.4 nm corresponding to growth rates of 85.35 nm/min and 63.2 nm/min, respectively. The platinum (Pt) layer visible on top of the gold layer was deposited *in situ* only for the cross-section measurements. The Zn layer cannot be observed from the image due to its substitution nature that leads to extremely reduced additional thickness.

In Chapter 6, the electrical characterization of ZnO microwires deposited on the gold-plated M4N chips will be described in details as well as the variation of their electrical properties under varying UV-visible light.

4.1.2 LabVIEW Graphic User Interface

In order to control the circuits of the M4N chips, e.g., to enable or disable the DEP or the read-out circuits, a communication with the integrated circuits must be established. To achieve this aim, an Arduino Due interface was selected [4]. Arduino Due is a low-cost open source electronic platform, with embedded an ARMCortex Sam3x microcontroller, capable to make the sensing from the M4N chips a plug-and-play solution so that the acquired data can be monitored in real-time on a standard working station (see Figure 4.8). To interface the M4N chips with the Arduino Due a custom-fabricated PCB adapter board is developed. Then a graphic user interface (GUI), is necessary in order to easily configure the M4N chips and acquire the measurement data. The GUI must be able to both enable the DEP circuits when a DEP experiments want to be performed and, to read-out the measured impedance from the selected electrode couple. Due to the system modularity, each of the 8 unit cells can be independently configured so that multiple experiments can be performed on the same chip.

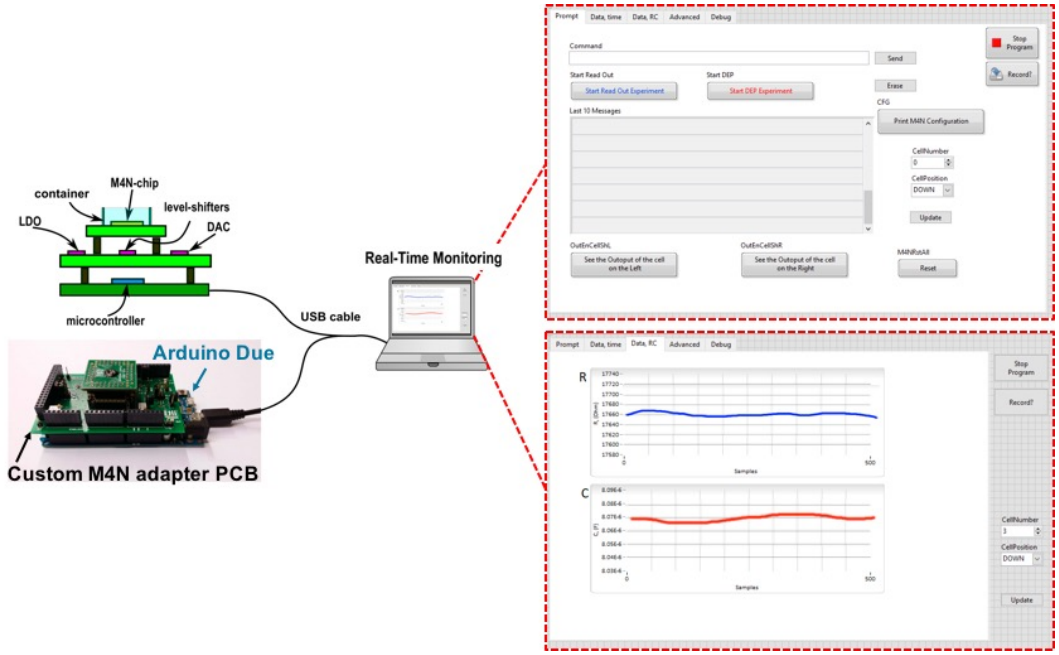

Fig. 4.8 Overall sensing setup for the M4N chip consisting in a interface board and in a Arduino Due directly connected to a working station for real time monitoring with the LabVIEW interface (adapted from [4], licensed under a CC-BY 4.0 license).

The programming language selected to build the GUI was the Laboratory Virtual Instrument Engineering Workbench, i.e., LabVIEW, a visual programming language from National Instruments^{TM}. The developed software represents a serial interface to read and write data from and to a serial port and it directly interfaces with the functions of the chips firmware. Thanks to its versatility, this software can be used for the communication with any type of serial port, and not just with the Arduino Due one, like in the present case. The building blocks of the software are 5 modules, each one responsible for a specific task:

1. *Serial Module*: controlling the communication with the serial port.
2. *GUI Module*: for data visualization.
3. *Event Handler Module*: detecting the commands defined by the user.
4. *Recording Module*: saving data on external files.
5. *Control Module*: managing all the other four modules.

The serial module is a state machine that controls the communication on the serial port. A state machine is an abstract machine that, at each time, can be exactly in one of a finite number of states. The change between one state and another,

called transition, is triggered by external instructions. The state machine of the serial module receives commands through an input queue and, after their execution, it loads the answers into an output queue. Specifically, if an instruction is present in the input queue, the serial module writes this instruction on the serial port, and then it reports the answers obtained from Arduino in the output queue. These answers may include both output configuration or errors messages and raw data, i.e., the values of T_0 and T_1.

The GUI module, is responsible of displaying on the GUI the data requested by the user. It can both show the last 20 strings sent by Arduino on the serial port and, plot the real-time variation of the resistance and the capacitance of the microstructure deposited between the selected couple of electrodes (see Figure 4.8). Also the real-time visualization of the signal timings, T_0 and T_1, can be selected if preferred, by switching to the proper tab on the GUI. The recording module will then be responsible to save on an external text file the acquired data, if necessary.

On the command prompt of the GUI several buttons are present so that the user can decide which action to perform like, e.g., enabling the ROCs of a specific cells, resetting the whole M4N or saving the data on a text file (Figure 4.8). This procedure is handled by the event handler module, which, whenever the user press a button, sends the related instructions to the proper module. At last, all the information exchanged by the four modules here presented, are managed by the control module.

The modularity of the software architecture allows the different modules to be readily re-used for other applications. Moreover, it allows an easier debugging in case of errors and a quicker implementation of new functionalities.

4.2 Cells-on-CMOS MEA

As anticipated in Chapter 1, CMOS electronics can provide an enormous contribution to biological and clinical studies. Not only it can contribute to unveil fundamental biological cues, not estimable with standard techniques (ref) but, it can also contribute to create high-throughput screening device that can significantly change the clinical and health-care global paradigm [138]. In this framework, as anticipated in Chapter 1 and 4, multi-electrodes array (MEA) platforms prevail thanks to the possibility of recording simultaneous signals from more than ten thousands of electrodes, in some cases, hence not only allowing the study of large population of cells and tissues but, at the same time, allowing the parallelization of multiple analysis on the same chip [148, 149].

As expected, and anticipated in Chapter 2, the research and development of this type of devices is extremely multidisciplinary ranging from state-of-the-art IC design to advanced biology. Therefore, a basic understanding of cellular physiology is an

important prerequisite and this justifies not only the six months visiting period at the Khademhosseini laboratory, but also, the extensive introduction about cardiac cells presented in Chapter 2.

CMOS MEA act as transduction mechanism for the signals produced by the cells, usually electrogenic ones. When an electrical signal is transmitted by the cells, i.e., an action potential, the related variation of the ions flowing in/out the cells provoke a voltage pulse that can be then recorded by the underlying electrodes [150]. This type of measurement is referred as *extracellular* recording since, only the signal propagated outside the cellular membrane can be recorded. Thanks to its low-invasiveness, without the need of breaking the cell membrane as in case of patch-clamp techniques traditionally used in the literature to measure intracellular action potentials [150], extracellular measurements allow for long measurements, also lasting more than 1 month, over large population of cells, while at the same time, allowing also for single-cell resolution if necessary and if the electrodes are designed small enough [150, 80]. This is extremely useful in case of new drugs development tests or in the modeling of the diseases evolution [150, 138]. Moreover, as already anticipated in Chapter 1, the use of active circuits not only strongly reduces the noise and parasitics effects but, also, it allows for a higher integration of the system[150].

In order to effectively and functionally culture cells on CMOS electrodes, the modification of the electrodes surface, as it comes directly from the foundry is a key feature (as extensively discussed in Chapter 1 and Chapter 4). Despite the biocompatibility and cytotoxicity issues, already discussed in Chapter 4, another important parameter to be considered is the electrodes impedance. In order to be able to record the electrical signals produced by the cells, a good electrical coupling between the cells and the electrodes is necessary which, in turns, is strongly influenced by the electrodes impedance, that should be ideally as small as possible [149]. Therefore the electrodes materials and geometries play a crucial role in the final electrical read-out. Nevertheless, a trade-off is necessary between the reduction of the impedance and the MEA density [149]. To have high-throughput devices, the density of the MEA chip need to be increased as much as possible, therefore requiring a reduction of the size of the electrodes. This, however, will result in an impedance increase. Numerous strategies have been developed in the literature to overcome this issue, mainly involving the use of micro/nano-structuration to increase the electrodes surface area or roughness like, nanostructured sponge-like platinum or titanium nitride layers [150, 149].

Numerous equivalent models have been reported in the literature about the electrochemical interactions between the cells and the electrodes, mainly based on the one originally developed by Hodgkin and Huxley in the 1952 [151, 149, 150]. Although a complete description of the equivalent electrical models of the cells-electrodes interface is beyond the scopes of this work, a brief description of the principal mechanisms involved will be here given, for clarity sake and completion.

Basically, the cell membrane is associated to a membrane capacitance, while, the ionic channels are modeled as tunable resistors with non linear conductances [151]. The cleft between the cell and the electrode can be instead modeled as a resistance while, the electrodes/electrolytes interface is usually modeled with a resistance/-capacitor parallel [150]. When an action potential is produced by a cell, the ions concentration in the close surrounding environment will be strongly modified. This will modify the charges accumulated at the electrodes/electrolyte interface, hence the capacitive part of the electrode, thus being recorded as a voltage variation [150]. When, instead, the cells are stimulate using the CMOS electrodes the reverse process occurs. The artificial modification of the capacitive element of the electrode induced by the electronics will modify the charge distributed at the electrodes/electrolyte interface. This, in turns, will affect the ionic currents flowing inside/outside the cells, therefore inducing an artificial depolarization state. The advanced description of the electrochemical mechanisms established the the cells/electrodes interface in an electrolyte solution can be found, e.g., in the Helmholtz planes and in the Gouyu-Chapman theories [152], that, nevertheless, due to the preliminary nature of this section, are beyond the objective of this thesis. Nonetheless, it is important to underline how, the more accurate are the electrical signals extracted from the cells and the more informative will be the results. In fact, the modification of the action potential shape, of its regularity or inter-spike intervals, as well as of the duration of the re-polarization phase (often found in the literature as QT interval prolongation [150]) can carry enormous amounts of information for drugs assessments and cardiotoxicity tests [150]. For example, the QT interval prolongation is a common side effect associated to the administration of numerous drugs, also not cardiac-related, and therefore, it represents one of the main challenges to be solved in the current drugs discovery research where CMOS MEA can provide a significant contribution [153].

Several examples of CMOS MEA devices recording the extracellular action potentials of cardiac cells can be found in the literature for different applications like cardiac pharmacological screening [154] or fundamental electrophysiology studies [155, 156]. Several devices commercial devices can also be found like the high-density MEA by 3Brain with 4096 electrodes [157], described in Section 4.2.1, the MEA2100 CMOS chips by Multichannel Systems, embedding 60 MEA electrodes [158] or the medium throughput MED64 system by Alpha MED Scientific Inc., with 64 electrodes [159]. Nevertheless, despite these few exceptions, the majority of MEA systems already available commercially are passive systems with the need of a commercial conditioning electronics [150]. Therefore, a consistent amount of research efforts are nowadays directed towards the optimization and development of innovative CMOS MEA systems that, in the near future, will be able to surpass the MEA technologies commercially available nowadays hence boosting the use of MEA systems in everyday clinical applications [149].

In Section 4.2.1, the commercial high-density CMOS MEA system, developed by the 3Brain company [157], and used in the present work to perform preliminary experiments linking the electronic and the biological worlds will be presented.

4.2.1 Introduction about 3Brain Chips

The CMOS MEA chips selected in the present work for the preliminary investigation of cardiac cells on CMOS circuits were the BioChip 4096E fabricated by the 3Brain Company (3Brain GmbH, Switzerland [157], see Figure 8.2). These chips allow both the real-time recording of the electrical action potentials of the cells from 4096 electrodes (sampled at 18 kHz) and the cell culture stimulation through 16 on-site stimulating electrodes. In this way, both the spontaneous beating activity of cardiac cells and the evoked cardiac potentials can be analyzed on the same chip.

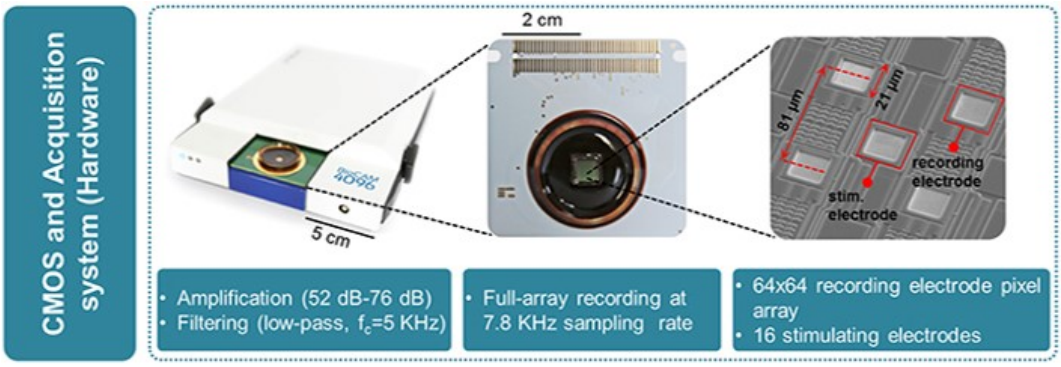

Fig. 4.9 3Brain CMOS MEA setup and overview of the chip structure (adapted with permission from [160], licensed under a CC-BY 4.0 license).

The 4096 recording and the 16 stimulating electrodes presented the same size, 21 x 21 μm^2, but different pitch, 81 μm and 1246 μm, respectively (see Figure 8.2). The total active area of the chip, instead,is of 5.12 x 5.12 mm^2. It is important to notice that, dimensions of the electrodes, as well as of their pitch, is smaller than other devices reported in the literature, usually around hundreds of um [81]. Therefore, assuming an average cardiomyocytes length to be in the range of 60 μm, sub-cellular processes can be easily monitored with the presented devices [81].

The real time acquisition of the recorded signals was performed with a customized-version of the commercial BioCam system, always provided by the 3Brain company, with embedded temperature control to keep the temperature of the culture stable at 37°C during the measurements.

To achieve the electrical stimulation of the cardiac culture, the 16 stimulating electrodes were connected to a 16-channels electrical stimulator (Plex-Stim Electrical

Stimulator 2.0 System, Plexon Inc., USA). As it will be explained in Chapter 8, to replicate the stimulation paradigm of the cardiac tissue on the bio-hybrid actuator, described in Chapter 5, square wave signals with frequency between 0.5 Hz and 3 Hz were selected. Nevertheless, in this case the stimulation was current-based, instead of voltage-based, due to the experimental setup configuration, with pulses of peak-to-peak amplitude between 300 $\mu A_{peak-peak}$ and 600 $\mu A_{peak-peak}$.

In order to be able to widen the applicability range of the chip, and use them with other types of electrogenic cells, e.g., neurons, the dynamic range of the system was designed to allow a suitable gain modulation [81]. In this way, both the mV-ranged cardiac action potential as well as the one from neurons, usually around 100 $\mu V_{peak-peak}$ in case of dissociated cortical rats, can be measured with the same chip [81]. Each electrode is multiplexed on parallel output channels so that the simultaneous readout from numerous electrodes can be obtained allowing a high spatial resolution [81]. Specifically, the 4096 electrodes are multiplexed in groups of 256 on 16 output analog channels, instead of on a single one, then sampled using analog to digital converters (ADCs). The converted digital signals are then processed through a field programmable gate array (FPGA), responsible also of the timing of the system and of a preliminary filtering step of the signals [81]. The complete details of the CMOS MEA design and architecture can be found in [81].

In Chapter 8, the preliminary experimental results obtained by culturing primary cardiomyocytes on the chip surface will be presented in details.

Chapter 5

Cardiac Cells Characterization and Actuation on Soft Hydrogels

Chapter Abstract *Chapter 5 introduces the research activity performed during the 6 months visit at the Khademhosseini Laboratory part of the Harvard-MIT Division of Health Sciences and Technology, Biomaterial Innovation Research Center, Department of Medicine, Brigham and Women's Hospital in Boston (USA). The activity was based on designing, fabricating and testing a multiple-hydrogels-based bioactuator actuated by freshly isolated neonatal rat cardiomyocytes with embedded microelectrodes. This was a fundamental step for the work here presented in order to understand the functional needs of cardiomyocytes in favor of the next electrical sensing on-chip. After a short introduction about soft actuators and their main applications (Section 5.1), more attention will be given to cells-based hydrogel soft actuators (Section 5.2). The selected hydrogels and the experimental synthesis procedure adopted is detailed in Section 5.2.1 and Section 5.2.3, respectively. Then, the preliminary work based on the development of a UV photolithography-based cardiomyocytes soft actuator with embedded microelectrodes is presented in Section 5.3. This work was previously developed in the Khademhosseini Laboratory and the author contributed just to achieve its final completion. This was the starting point for the design and development of a bioprinted soft actuator with wireless electrical stimulation (Section 5.4). This activity was done in collaboration with the Master Thesis work of A. Defeudis [161] and S. Bruni. The design and fabrication of the wireless stimulating electrodes was instead developed in collaboration with the Ph.D. activity of L. Pirrami (University of Applied Sciences and Arts Western Switzerland, Fribourg and Politecnico di Torino, Italy). At last, part of this work was also published by the author in [1] and, different parts of the cited articles are verbatim quoted in this chapter with permission (a starting and an ending footnote will be present at the beginning and at the end of the quoted sections, see Appendix A for the complete copyright rights and permission).*

5.1 Soft Actuators: Introduction and Stimulation Techniques

Conventional engineered actuators and robots are devices capable of autonomous and independent actions or movements. Their standard fabrication process relies mainly on the use of rigid materials, like metals or hard plastics, with Young's modulus usually between 10^9 Pa – 10^{12} Pa [162]. To push the performances of these devices always more forward, scientists are recently paying specific attention to design robots/actuators capable to mimic natural systems. This is principally due to their ability to intrinsically display exceptional performances, if compared with engineered ones, often with a simpler structure and organization [162]. One other key advantage is that their body is often formed by soft materials, perhaps with flexible joints, hence enhancing their overall agility and degrees of freedom as well as exceptional deformation and adaptation, also in confined environments [162]. Therefore, merging the advantages of biological robots/actuators soft bodies with engineered artificial systems would enable the fabrication of unprecedented state-of-the-art hybrid systems.

Therefore, a new branch of study was recently born, specifically focusing on developing soft actuators, i.e., actuators whose body is constituted by materials with Young's modulus in the range of soft biological materials between 10^4 Pa – 10^9 Pa [162]. For example, the Young's modulus of human skin varies between 0.42 MPa and 0.85 MPa (in case of torsion tests) [163] while, the one of ventricular myocardium in adult rats is between 20 kPa and 54 kPa [87]. In Figure 5.1, the Young's modulus of several biological and synthetic materials are reported [162].

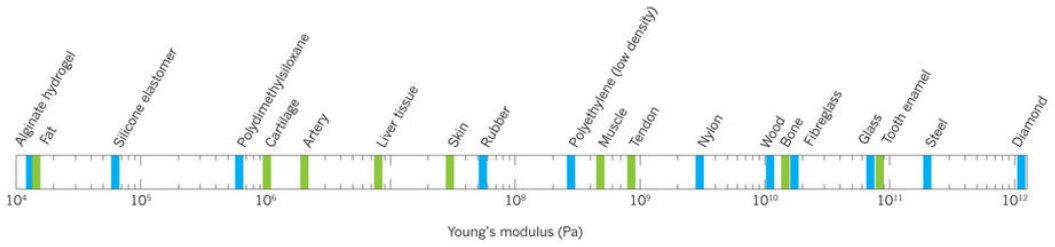

Fig. 5.1 Comparison of Young's modulus of common biological and synthetic materials (reprinted by permission from Macmillan Publishers Ltd: Nature, reference [162], copyright 2015).

The choice of materials for soft robots/actuators hence usually resides in the ones with Young's modulus comparable with the one of biological materials, usually always less than $\sim$ 1 GPa [162]. Furthermore, the use of materials analogous to the biological ones makes soft robots safer alternatives, in terms of accidental damages

that can be caused, if compared with standard rigid robots, in all those applications that requires direct interaction with humans [162].

One of the key features for soft bodies to actually become state-of-the-art robots/actuators is to be able to embed sensing as well as computation, power storage and communication that can make these bodies smart and functional [162]. In this way, the advantages of both mimicking nature potentialities and of advanced engineering tools can be combined in a unique cutting-edge devices. The applications of these types of systems branch out in diverse fields for instance biotechnologies, like artificial muscles [164], environment assessment [165], robot autonomous locomotion [166] and objects manipulation [167], as well as soft cyborgs [168].

The triggering of the actuator can be achieved with numerous methods like pneumatic actuation, tendons length variation or electrical stimulation [162]. In the first case, usually, channels are embedded in the synthetic soft material; the expansion of these channels due to an increased air pressure or flow rate of a fluid will define and control the actuation dynamics [162]. In this case, precise tuning of the pressure-regulating elements is essential for the correct functioning of the device. For example, Suzumori *et al.* developed a pneumatic rubber-bodied swimming robot whose motion was controlled by properly tuning the pressure in two internal flexible chambers of the actuator itself (see Figure 5.2, a) [169]. Being fabricated only by rubber, the presented soft-robot exhibited a smooth and wavy motion dynamic close to the one of living creatures [169]. Seok *et al.*, instead, took inspiration from the peristaltic locomotion of *Oligochaetes* worms, to fabricate a worm-like soft robot with embedded nickel titanium (NiTi) actuating coils [170]. NiTi belongs to the category of shape memory alloys (SMA), i.e., the material is capable to generate mechanical work as a consequence of a phase variation [170]. Specifically, a 7% strain change can be observed during the heat-induced transition from its martensite to its austenite phase [170]. As depicted in Figure 5.2 b, NiTi micro coils were wrapped around a soft-braided body. When a specific temperature was applied, the NiTi phase change triggered the propagation of a traveling contraction wave along each segment of the actuator, from the head up to the tail, resulting in worm-like peristaltic locomotion [170].

A less cumbersome architecture is instead possible by choosing an electrical actuation. Electro-active polymers are the main candidates for these applications, i.e., polymers that can change their shape in response to an electrical stimulus [162]. These materials can be coupled and interposed together with dielectric materials to fabricate state of the art integrated soft-robots capable of exceptional locomotion, especially in water-based harsh environments, like the fast-moving soft electronic fish developed by Li *et al.* [171]. As shown in Figure 5.2 c, they designed a fish-shaped actuator driven only by the electro-active properties of its soft-body, formed by both a dielectric elastomer and a ionically conductive hydrogel, up to a speed of 6.4 cm/s [171]. Also in this case, the authors took inspiration from the pectoral fin structure

of the manta ray for the design of their electronic fish. The fish muscles were formed by dielectric elastomeric (DE) membranes while, the fin and the soft body where fabricated using a silicone thin film and a silicone frame, respectively (see Figure 5.2 c). In the rest state, the fish showed a specific equilibrium bended state but, when a voltage was applied, the Maxwell stress induced by the accumulation of positive and negative charges on both the sides of the elastomer caused a deformation of the DE membranes [171].

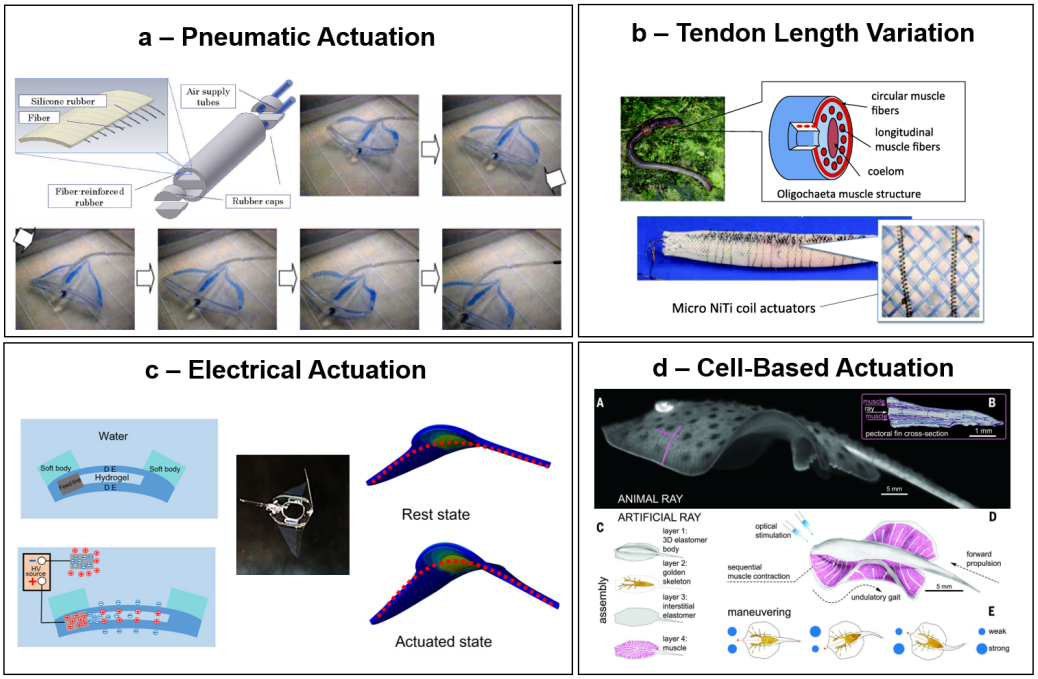

Fig. 5.2 (a) Fundamental pneumatic structure of a rubber-bodied manta and example of its pneumatic swimming dynamics (adapted from [169], ©2007 IEEE). (b) Soft robot with peristaltic locomotion inspired to the muscular structure and motion dynamics of *Oligochaetes*. The actuation is based on NiTi SMA coils phase change (adapted from [170], ©2013 IEEE). (c) Soft electro-active fish operational mechanism based on a dielectric elastomer and a ionically conductive hydrogel (adapted from [171], licensed under a CC-BY-NC 4.0 license). (d) Soft-robotic ray light-actuated by employing optogenetic-modified rats cardiac cells (from Park, S.-J. et al., Phototactic guidance of a tissue-engineered soft-robotic ray. Science vol. 353, pages 158–162, 2016 [172]. Reprinted with permission from AAAS).

It is worth noting that, the majority of the examples of soft robots/actuators reported so far aim to mimic the muscular structure and/or motion dynamics of living animals. This is always more relevant when moving from hard-bodied to soft-bodied actuators thanks to the ability of soft materials to be more suitable and more effective in mimicking Nature's creations. Therefore, the choice of soft and flexible materials as fundamental components for the fabrication of soft actuators paves the way for the

design of innovative devices capable to reproduce always more complex dynamics and mechanisms belonging to the natural world, but new to the engineering one, hence enormously increasing not only the performances but also the potentialities and applicability range of this kind of devices. Moreover, as observed by Li *et al.*, aquatic animals emerge as one of the most popular sources of inspiration due to the high soft and flexible portion of their body as well as to their agility [171].

The same considerations are true also for an emerging new class of soft actuators, also called muscle-based actuators, whose actuation is triggered by living cells. Despite their enormous advantages for *in vivo* medical applications, cell-based soft actuators allow for the investigation of devices with superior energy efficiency and potential auto-repairing features than the synthetic counterpart [173]. The physical support of this type of actuators is often formed by polymeric materials and/or hydrogels, as it will be introduced in details in Section 5.2. A strong biocompatibility of the materials used is a key requirement to guarantee not only the survival of the living structures, but, also, their functional proliferation and growth. The alternative name 'muscle-based actuators' is due to the fact that the most popular types of cells used for these purposes are muscle cells like cardiomyocytes or skeletal muscle cells [173, 174]. If compared to skeletal cells, cardiomyocytes are slightly more of interest due to their ability to show spontaneous beating, i.e., potential spontaneous actuation, as detailed in Chapter 2. Nevertheless, numerous challenges still need to be further studied and solved like having a precise and controlled temporal and spatial resolution of the electrical stimulation of muscle cells, in order to obtain the desired actuation, as well as their functional growth on both 2D and 3D substrates [173]. One technique often exploited to improve the local control of electrogenic cells excitation is based on the engineering of the single muscle cells so that their ionic channels show light-dependent activity [175]. This approach is called optogenetics and it is also widely used in case of neurons studies. One of the most relevant examples of the utility of this approach in the field of cell-based bioactuators is the phototactic-guided tissue-engineered ray by Park *et al.* [172]. In their work, the authors designed and fabricated an artificial swimming ray, with a PDMS backbone and with optogenetically-modified rats cardiomyocytes as functional layer growing on its surface [172] (see Figure 5.2, d). The motion of the artificial ray was actuated by the beating activity of the cardiomyocytes growing on its surface which, in turns, was guided by the external light, due to the optogenetic-modified cells [172]. By activating a serpentine-patterned light guide (see 'weak' and 'strong' blue circles in Figure 5.2, d), an ondulatory locomotion, similar to the one of the real sting ray was achieved [172]. Nevertheless, in the present work, an electrical stimulation through flexible microelectrodes was preferred to the optogenetic one, in order to control the electrical activity of cardiac cells growing on the soft-actuator (see Section 5.3). One of the immediate advantages of this approach is that no gene-engineering is necessary to be performed on the cells, hence speeding up the transfer of the obtained *in vitro* results to clinical applications. Moreover, as outlined also in [1] and in [176],

optogenetics requires complex and time consuming techniques and procedures, the use of chemicals with potential toxicity as well as extremely long-term expression techniques to be able to decrease the power of the excitation light hence reducing possible damages to the cells. The power of the excitation light is one of the main obstacles to be overcome in order to transpose the optogenetic results *in vivo*. In fact, one of the most powerful application of cell-based soft actuators, in the clinical field, is the *in vivo* implant of this materials as patches or scaffold e.g., to promote tissue regeneration in case of cardiac failure [177] or of brain injuries [178]. On one side, the light power must be high enough in order to penetrate deeply in the tissues with cell-level resolution but, on the other side, often the necessary excitation power cannot be reached due to potential tissue damages [179]. To balance this excitation light trade-off, new photonic devices are currently being studied and developed [179].

From the discussion reported in the present section, it can be understood how soft actuators can be extremely useful tools in very disparate fields ranging from ocean missions to implantable cardiac patches. Moreover, despite the final application, soft actuators represent a unique tool for cell-based studies where cells can find a flexible and soft support and environment where they can grow and proliferate similarly as many cells to in the living body hence enhancing the reliability of the performed studies.

In Section 5.2, bio-compatible polymers and hydrogels predominantly employed for cell-based soft actuators will be introduced. Then, in Section 5.2.1 and 5.2.2 the materials selected in the present work will be detailed in addition to their experimental synthesis procedure (Section 5.2.3).

5.2 Bio-Hydrogels for Cell-Based Soft Actuators

Hydrogels are a sub-category of polymers with large swelling and liquid retention capabilities when in contact with water or also other biological fluids [180, 181]. This property is mainly related to the presence of abundant hydrophilic functional groups on the hydrogel backbone [180]. Despite the large volume of fluid that can be absorbed, these materials do not dissolve in water due to the presence of cross-links between the different polymeric chains present which hold the structure in place regardless of the deformation [180]. One example of hydrogel swelling due to water absorption can be observed in Figure 5.3, a. In this example, α-elastin hydrogel, an oxalic acid-solubilised modification of elastin protein to increase its solubility, swelled in water up to a ratio of 21-35 g H_2O/g protein [182].

Similarly to living tissues, also hydrogels are soft, contain high amounts of water/biological fluids and can have a specific porosity [181]. This is the reason why they can be considered among the best candidates to interact with and to reconstitute

biological tissues [181]. Several hydrogel-based products are already present in the market like contact lenses, wounds dressings and hygiene products to absorb fluids [181]. In Figure 5.3 b, is shown a dressing, by Neoheal®, used for burns and other types of skin wounds [183]. Hydrogel-based dressing can bring numerous advantages to wounds healing thanks to their aid in eliminating dead tissue (also called, autolytic debridement), in maintaining a high moisture level in necrotic wounds as well as in boosting the generation of collagen [181].

The polymers constituting hydrogels can both be of natural origin, like gelatin, chitosan, agarose, collagen and hyaluronic acid or derived from synthetic materials like poly(ethylene glycol), poly(vinyl alcohol) and polypeptides [181]. Also mixtures of natural and synthetic hydrogels are possible.

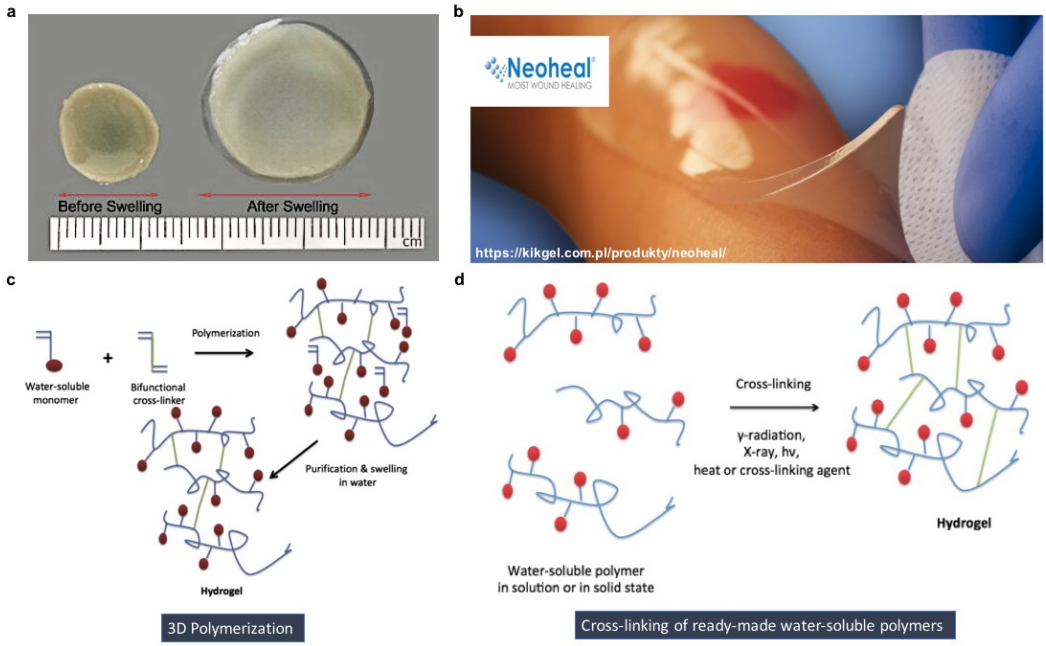

Fig. 5.3 (a) Example of elastin hydrogel swelling (Reprinted from: Biomaterials, Vol. 30, N. Annabi, S. M. Mithieux, A. S. Weiss, F. Dehghani, The fabrication of elastin-based hydrogels using high pressure CO_2, Pages No. 1-7, Copyright (2009), with permission from Elsevier [182]). (b) Commercial product based on hydrogels: Neoheal® sterile dressing for burns and other types of skin wounds by Kikgel (reproduced from [183], https://kikgel.com.pl/produkty/neoheal/). Schematic diagrams of the hydrogels synthesis through 3D polymerization (c) or through cross-linking of water-soluble polymers (d) (adapted from [181], licensed under a CC-BY 3.0 license).

Usually, there are two predominant methods to synthesize hydrogels differing by the nature of the precursors. If a hydrophilic monomer polymerizes, due to the activity of a cross-linker agent, the process is called 3D polymerization and a purification step is necessary in order to wash out the unreacted monomers, that

may often be toxic (see Figure 5.3, c) [181]. The purification step may be eluded if the starting material is already a water soluble polymer that is then crosslinked using different energy sources like radiation, light, heat or also cross-linkers (see Figure 5.3, d) [181]. The starting polymers can be selected among biocompatible and non-toxic materials so that they do not need to be filtered out from the system hence eliminating the need of the washing step [181].

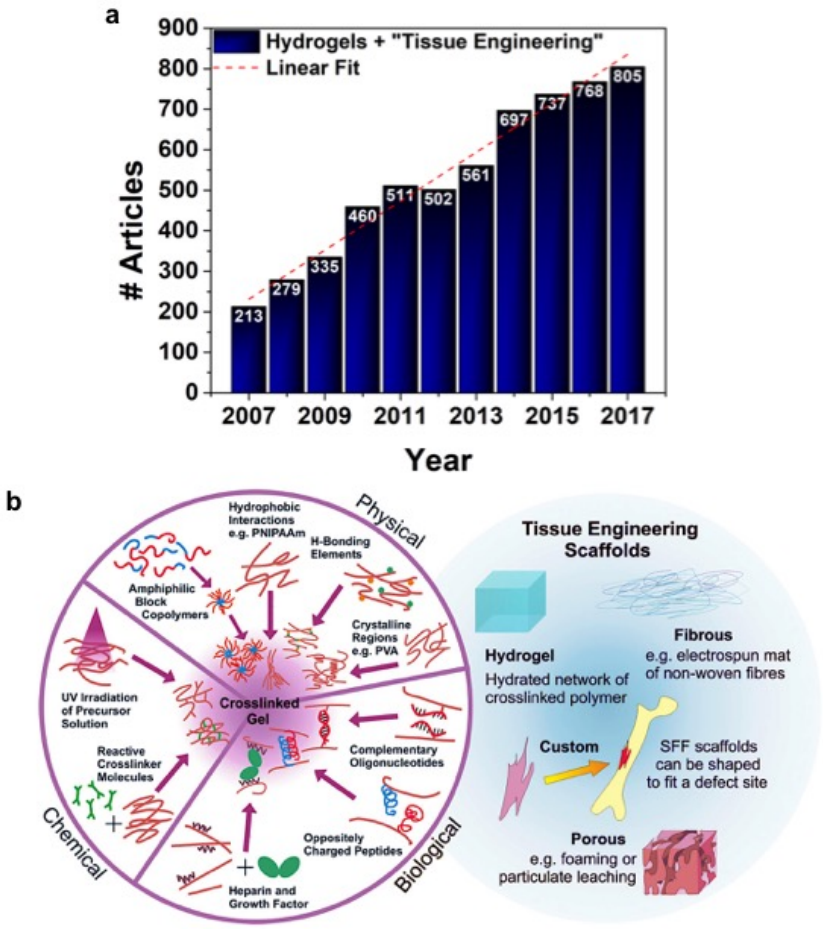

Fig. 5.4 (a) Number of published articles listed in the Scopus database including the keywords "hydrogels" and "tissue engineering" from 2007 to 2017 [184]. (b) Schematic diagram of the different possible crosslinking methods for hydrogels like physical, chemical or biological (left). Different morphologies of scaffolds for tissue engineering (right). Reproduced from [185] with permission of The Royal Society of Chemistry, http://dx.doi.org/10.1039/B811392K.

Despite the commercial applications already listed, hydrogels are gaining always more interest among the scientific community for more advanced applications as tissue engineering. As elucidated by Annabi *et al.*, and anticipated in Section 5.1,

tissue engineering is related to the substitution of damaged organs, or part of them, with artificial tissues [182]. This includes implants originated both from *in vitro* cultures, in some cases using cells extracted from the patient himself, and implants directly developing *in vivo* and starting from an inserted scaffold where cells can penetrate and trigger the growth of tissues [182]. Looking at the number of published articles listed in the Scopus database in the last 10 years, from 2007 to 2017, including the keywords "hydrogels" and "tissue engineering", an ongoing linear growth can be observed (see Figure 5.4, a) [184]. The field of tissue engineering is inherently linked to the one of cell-based soft actuators. Indeed, cell-based soft actuators can serve as preliminary testing platforms to deeply study the dynamic and the behavior of the scaffold, prior to *in vivo* trials. Likewise, the knowledge gained during the development of materials for tissue engineering can provide massive information for the application and/or transposition of these materials into soft-actuators.

The hydrogels for these applications can originate in different ways (see Figure 5.4, b, left). The first type permanently crosslink, forming covalent bonds, due to the interaction with an energy source e.g., light, or due to the action of specific crosslinkers moieties, as already anticipated in this section. These materials are called chemical hydrogels [185]. If the bonding between the different polymeric strings is of non-covalent nature, the hydrogels are referred as physical ones [185]. If the main responsible of the crosslinking of the polymeric chains are biological molecules or entities, e.g., interacting peptides with complementary charges or oligonucleotides sequences, the physical hydrogel becomes a biological one (see Figure 5.4, b, left) [185]. One crucial consideration, important both for the use of these materials in soft-actuators and in tissue engineering, is related to their morphologies. In fact, besides being bare hydrogels, these materials can be engineered in different shapes and morphologies like fibers, porous materials or structures with customized shapes (see Figure 5.4, b, right), to optimally adapt to the target application [185].

Despite a complete and detailed description of all the hydrogels used for tissue engineering is beyond the scope of this work, in order to provide a general overview, in Table 5.1, the most common hydrogels, both synthetic or natural, used for this purpose are listed with their most relevant applications. Poly(ethylene glycol), PEG, is one of the main protagonist due to its high biocompatibility and superior solubility in various solvents [185]. It is a ethylene oxide based polymer. It is also approved by the Food and Drug Administration (FDA) federal agency for clinical, cosmetic and pharmaceutics applications [186]. One of the key-properties of PEG is that it is naturally repulsive for proteins [185]. This implies that it can act as inert substrate e.g., to define regions where a lower cell adhesion is wanted, despite guaranteeing overall biocompatibility, as done in the soft actuator developed in the present work (see Section 5.3). At the same time, PEG bio-active surface functionalizations are required if this material wants to be used as primary scaffold for cells adhesion. The lack of sites that promotes cell adhesion and proliferation,

like e.g., the RGD sites described in Chapter 2, is one of the main issues of synthetic hydrogels. This is also the main reason why much attention has been devoted to natural hydrogels as well as to mixtures of synthetic/natural materials [187, 186, 1]. Other relevant synthetic hydrogels are e.g., poly(vinyl alcohol) (PVA), that due to its non-degradability is limited to be used only on permanent implants, if its degradability is not chemically enhanced; similarly, the non-degradable poly(methyl methacrylate) (PMMA) is widely used as bone cement while poly(caprolactone) (PCL), showing a high degradability, is instead used for degradable sutures or stents (with FDA approval) [185].

Origin	Material	Pros/Cons	Applications	Source
Synthetic	Poly(ethylene glycol) PEG	Proteins repellent effect	Inert background	[185]
	Poly(vinyl alcohol) PVA	Non-degradable	Permanent implants	[185]
	Poly(caprolactone) PCL	Degradable, hydrophobic: need treatment to increase wettability	Degradable sutures, stents	[185]
	Poly(methyl methacrylate) PMMA	Non-degradable	Bone cement	[185]
Natural	Keratin	Promotes epithelialization, can be extracted from patient hairs/nails	Wound repair	[181, 188]
	Alginate	Poor bio-degradation and poor cell adhesion: modifications required	Drug delivery of proteins for regeneration of mineralized tissue	[189]
	Agarose	Promotes axonal regeneration, biomechanical properties similar to native cartilage	Optimal for neural cells, stem cells and chondrocytes	[187, 186] [190]
	Gelatin	Cell-responsive, similar to molecules in the living tissues (ECM)	Microvessel growth, cardiac cells	[186]

Table 5.1 Summary table with some of the most common hydrogels, both synthetic or natural, for tissue engineering applications.

Although synthetic hydrogels can be extensively optimized and they show a high flexibility in terms of tuning of their physico-chemical properties, their potential cytotoxicity as well as the need of surface bio-activation are some of the main reasons promoting the study of natural hydrogels and synthetic/natural hybrids materials [186]. The inclusion of hydrogels derived from natural sources, like skin or algae, introduces native sites that can promote not only cell adhesion and proliferation in the optimal way possible, since it is the same methodology adopted by Nature, but, also it favors their functionalities. Some of these materials can also be derived directly from patients biological materials like keratin hydrogel, a promoter of epithelial cells growth, that can be synthesized starting from hair and nails (see Table 5.1) [188]. Other hydrogels can be derived from plants like alginate, synthesized from brown algae, or agarose, derived from seaweeds. The properties of these materials make each of them suitable for specific applications like the drug delivery of proteins helping the regeneration of bone tissue, in case of alginate [189], or like the promotion of axons regeneration as well as the generation of tissues with mechanical characteristics similar to cartilage, in case of agarose hydrogel

[187, 186, 190]. At last, also different parts of animals body can be exploited for the generation of natural hydrogels, like e.g., gelatin hydrogel, which deriving from collagen, can be extracted from several sources such as porcine skin. Gelatin-derived hydrogels show properties similar to the ones of the extra-cellular matrix of cells making them optimal candidates for cells growth and functional proliferation. More details about specific gelatin-based hydrogels will be given in Section 5.2.1 and 5.2.2.

By properly tuning the physical, chemical, biological and mechanical properties of synthetic/natural hydrogels, it is possible to design and fabricate supports, acting as scaffold for tissue engineering or as backbones for cell-based soft actuators, with tailored properties as required by the final application. For example, Nawroth *et al.*, engineered a biological-powered tissue-engineered mechanical device, mimicking jellyfish swimming, muscle-powered by cardiac cells [6] (see Figure 1.1, a). Instead, in the present work, different layers of distinct hydrogels, both PEG- and gelatin-based, where adopted to fabricate a soft actuators with a specific motion mimicking the swimming dynamics of manta batoid rays [1]. The desired motion dynamics was achieved thanks to a precise tuning of the hydrogels concentrations as well as to a specific patterning of the hydrogels thickness and superimposed geometries (See Section 5.3).

5.2.1 Gelatin Methacryloyl Hydrogel (GelMA)

As mentioned in Section 5.4 and in Chapter 2, gelatin-based hydrogels exhibit properties very similar to the ones of the ECM. This is strongly related to its natural origin directly from the partial hydrolysis of collagen, an ECM protein present in different parts of animals body like e.g., porcine skin. From a biochemical viewpoint, this similarity is translated in the presence of both RGD cell-adhering sites, and, also, of matrix metalloproteinases (MMP), main responsible for the degradation of ECM proteins i.e., cell adhesion, proliferation and migration [191]. Due to the high amount of cell binding sites and to its functional similarity to the ECM, gelatin-based porous hydrogel was chosen, in the present work, as best candidate for the development of a cardiomyocytes-powered soft actuator [1].

Although gelatin is capable to form on its own a physical hydrogel, thanks to its gelatination at low temperatures, to form chemical hydrogels, a modification of the material is necessary [191]. One possibility is to exploit the sides groups of gelatin, containing amine groups (NH_2), to graft additional methacrylate groups (MA), which, due to the presence of very reactive double bonds, easily crosslink forming a hydrogel in presence of a suitable initiator (see Figure 5.5, (i)) [191, 87]. In this case, the material is referred as gelatin-methacryloyl (GelMA) hydrogel (also called gelatin-methacrylate or gelatin-methacrylamide) [191, 87]. The approach selected in the present work was to use a photo-initiator, soluble in water-based solutions, to

have a photocrosslinkable GelMA hydrogel which can be patterned taking advantage of photolithographic techniques (as it will be described in Section 5.3). The photoinitiator selected is the commercial 2-hydroxy-1-[4-(2-hydroxyethoxy)phenyl]-2-methyl-1-propanone (Irgacure® 2959), which exhibits a low cytotoxic effect if compared with other commercially available photoinitiators [192] but also other initiators are possible like lithium acylphosphinate salt [191].

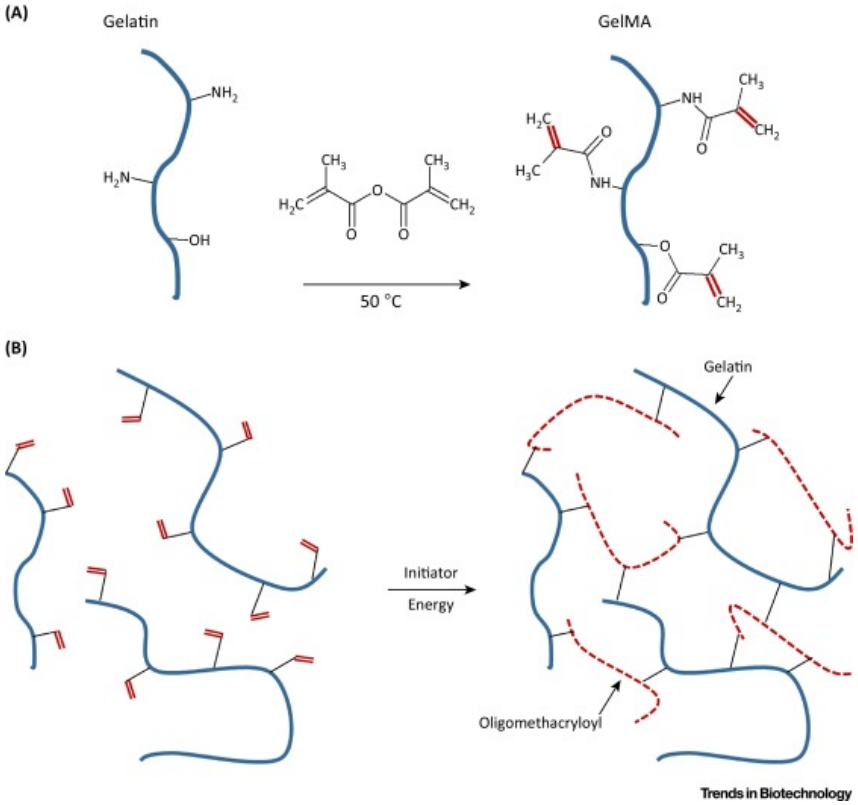

Fig. 5.5 Schematics of the synthesis and crosslinking of GelMA hydrogel. At first, methacryloyl groups are formed due to the reaction of gelatin and methacrylic anhydride at 50 °C (A), then, due to the radicals generated from the photoinitiator reaction, the chain polymerization of the substituted methacryloyl groups starts forming the crosslinked hydrogel network (B). Reprinted from Trends in Biotechnology, Vol. 34, B. J. Klotz, D. Gawlitta, A. J. W. P. Rosenberg, J. Malda, F. P. W. Melchels, GelatinMethacryloyl Hydrogels: Towards Biofabrication-Based Tissue Repair, Pages 394-407, Copyright (2016), with permission from Elsevier [192].

The first protocol for the synthesis of GelMA was developed by Van Den Bulcke *et al.* in 2000 [193]. The majority of the protocols found in the literature involve small modifications of the original protocol [191, 192]. Essentially, gelatin reacts with MA at 50°C in a phosphate-buffered saline solution (PBS, pH 7.4) and some methacryloyl groups are substituted on the gelatin backbone due to the interaction

with amine groups (see Figure 5.5, A) [191]. By diluting the solution with additional PBS, the substitution reaction can be stopped and, the GelMA can be dialyzed in deionized water for 5-7 days to remove any cytotoxic residues like unreacted MA or reaction byproducts [191]. The detailed procedure adopted in the present work to synthesize GelMA is reported in Section 5.2.3. It is important to notice that the RGD sites will not react with MA, hence the substitution process will not undermine the advantageous cell-interacting properties of the material [191]. After dissolving the photoinitiator in the solution, radical photo-polymerization can be triggered by light of a suitable wavelength (365 nm in case of Irgacure® 2959) so that GelMA chains can be connected by the poly-methacryloyl chains forming a crosslinked GelMA hydrogel (see Figure 5.5, B) [191, 192].

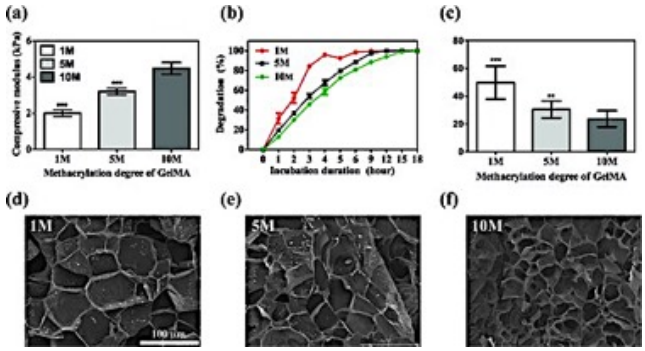

Fig. 5.6 Variation of the compressive modulus (a), degradation (b), pore size (c) and SEM images (d)-(f), of GelMA hydrogel with different methacrylation degree. Reproduced with permission from Advanced Functional Materials, Y.-C. Chen, R.-Z. Lin, H. Qi, Y. Yang, H. Bae, J.M. Melero-Martin, A. Khademhosseini, Functional Human Vascular Network Generated in Photocrosslinkable Gelatin Methacrylate Hydrogels, Vol.22, Pages 2027-2039, ©2012 WILEY-VCH Verlag GmbH & Co. KGaA, Weinheim [194].

By tuning the gel concentration, the physical properties of the final GelMA hydrogels as pore size, elastic modulus or bio-degradation can be strongly modified [191]. Chen *et al.*, published a study in which they compared 48.9%, 63.8% and 73.2% MA substitution degrees in GelMA hydrogels by tuning the molarity of the MA solutions to 1 M, 5 M and 10 M, respectively [194]. As outlined in Figure 5.6 a and b, they observed that by increasing the methacrylation substitution, the compressive Young's modulus almost doubled passing from 1 M to 10 M, while, the bio-degradation, measured as the percentage of GelMA residual mass after incubating it with collagenase solution, decreased [194]. Characterizing, instead, the material with the SEM microscope, the average pores size was observed to vary from 49.7 ± 11.8 μm in case of 1 M, to 30.13 ± 6.12 μm for 5 M and, finally, to 23.6 ± 5.85 μm for 10 M (see Figure 5.6, c-f) [194]. Therefore, the average size of the GelMA hydrogel pores was found to decrease by increasing the percentage of MA substitution. Form the reported results, it is clear how the physical properties

of the final synthesized GelMA hydrogel can be extensively customized, with high versatility and adaptation of the material to the target application selected. Further variability can be obtained by incorporating nano/micro-materials into GelMA [191]. In fact, tuning the synthesis process to optimize one parameter, e.g., increase the compressive modulus, may result in the alteration of also other properties like pore sizes and degradability that, instead, may not be wanted to change. In this case, synthesizing hybrid hydrogels in which nano/micro-materials are incorporated like gold nanoparticles [195], carbon nanotubes (CNTs) [87, 5, 1] or graphene oxide [196], can lead to a selective tuning of the mechanical and/or electrical properties of GelMA without heavily affecting the other physical parameters [191]. For the applications of GelMA in the field of electrogenic cells, like the cardiomyocytes objective of this work, the incorporation of conducive nano/micro-materials was found to strongly enhance the electrical activity of the cells seeded on the hydrogel substrate while, at the same time, optimizing its mechanical properties for the beating activity of cells [87, 5]. Therefore, in Section 5.2.2, the incorporation of CNTs into GelMA for improving cardiomyocytes culture will be discussed in details.

5.2.2 Carbon Nanotubes Reinforced GelMA Hydrogel (CNT-GelMA)

The incorporation of CNTs in the GelMA hydrogel was found to improve both the mechanical and the electrical properties of the hydrogel, for cardiac tissue culture applications [197, 87]. Moreover, by tuning the concentration of CNTs added to the GelMA pre-polymer solution (i.e. the GelMA solution before the photo-crosslinking) the properties of the final hydrogel can be further tuned. One key advantage is connected to the presence of hydrophobic tracts on the GelMA polymeric backbone [197]. These hydrophobic segments will interact with the sidewalls of CNTs acting as surfactant for the nanotubes dispersion in solution as well as mechanical stabilizers [197]. In fact, usually, biological-like solutions, like PBS or cell culture media, include different salts that can cause the precipitation of CNTs [197]. But, by encapsulating CNTs with a thin layer of GelMA (Figure 5.7, a) it was possible not only to successfully disperse them in a PBS-based solution by ultra-sonication (see Section 5.2.3) but, also, to limit their aggregation as well as their potential cytotoxicity [197, 198]. From the HRTEM imaging previously performed in [87] and shown in Figure 5.7 b, it is possible to recognize a thin layer of hydrogel completely encapsulating the CNTs surface. The diameter of the CNTs was found to increase from ~ 9 nm $\pm$ 8 nm for pristine CNTs to ~ 25 nm $\pm$ 12 nm in case of GelMA-coated CNTs [197]. By observing the porosity of the final hydrogel, no significant differences were observed in case of pristine GelMA or CNT-GelMA in terms of dimensions while, looking inside the pores, extensive CNTs fractal-like networks were found in case of CNT-GelMA (Figure 5.7 c) [87]. This grid formation

was supposed by the authors to be originated during the photo-crosslinking of the GelMA-coated CNTs [87].

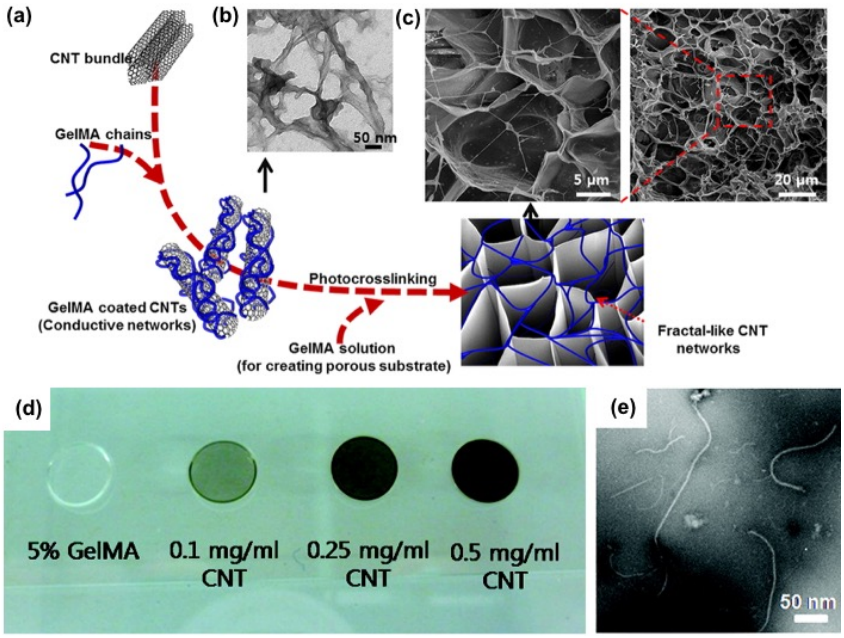

Fig. 5.7 (a) Schematics of the GelMA hydrogel functionalization with CNTs with TEM imaging of the GelMA-coated CNT bindle (b). (c) SEM characterization of the porous structure of a CNT-GelMA thin film with 1 mg/mL CNTs. In the inset, the fractal-like CNTs networks can be recognized inside the pores ((a)-(c) adapted with permission from [87]. Copyright 2013 American Chemical Society). (d) Color variation of the CNT-GelMA pre-polymer solutions with different CNTs concentrations. (e) HRTEM images of 0.5 mg/mL CNTs dispersion in the GelMA pre-polymer solution ((d) and (e) adapted with permission from [197]. Copyright 2012 American Chemical Society).

Shin *et al.* explained that the fractal-like CNTs network can have a function similar to the one of the pukinje fibers present in the heart muscles, that constitute a DC conductive network with conductivity ~ 0.1 S/m [87]. Indeed, the impedance of CNT-GelMA at low frequencies (below 0.1 kHz) was found by the authors to be notably inferior to the one of bare GelMA, due to the presence of additional resistive paths through the CNTs-network present [87].

As expected, the color of the pre-polymer solution darken as the CNTs concentration is increased (see Figure 5.7, d) leading also to a higher UV light absorption during the crosslinking of the hydrogel hence to a longer UV crosslinking time [197]. From the optical images of the pre-polymer solution (Figure 5.7, d) a first assessment of the homogeneity of the CNTs dispersion in the GelMA pre-polymer solution can be done due to the absence of any aggregation visible at the macro-scale [197]. Nevertheless, a more precise evaluation can be obtained by HRTEM characterization,

see Figure 5.7 e, in which individual CNTs can be recognized in the GelMA solution [197].

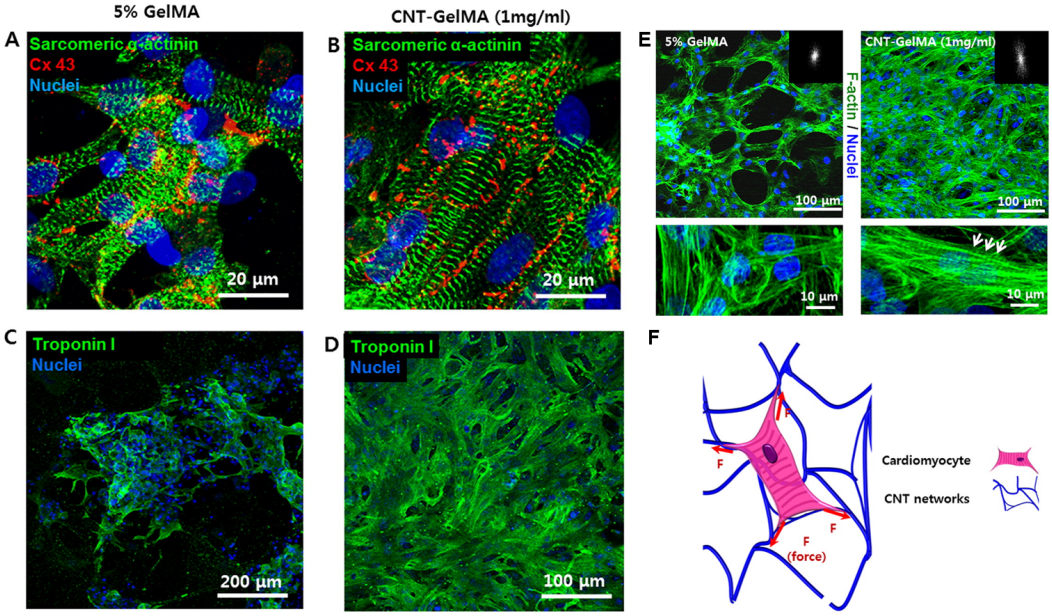

Fig. 5.8 Sarcomeric-α-actinin (green) and Cx-43 (red) immunostaining of cardiomyocytes cultured on 5% GelMA hydrogel (a) and 5% GelMA hydrogel with 1 mg/mL of embedded CNTS (b) after 8 days of culture. Improved sarcomeres alignment can be recognized in case of CNT-GelMA hydrogel. Similarly, improved and more aggregated Troponin I expression was observed on CNT-GelMA (d) if compared with pristine GelMA hydrogel (c). These assumption are confirmed also by confocal imaging of F-actin after 5 days of culture (e), where, 1 mg/mL CNT-GelMA resulted in a more homogeneous cell spreading as well as improved sarcomere linear alignment and cell elongation. (f) Schematic of the cell-CNT network interaction affecting the cardiomyocytes organization on the CNT-GelMA hydrogel. Adapted with permission from [87]. Copyright 2013 American Chemical Society).

The advantages introduced by embedding CNTs in the GelMA hydrogels are not limited only to an improved electrical coupling of the beating activity of the cells, due to the conductive paths introduced by the CNTs grid. In fact, also the compressive Young's modulus was found to increase from 10 kPa, in case of bare GelMA, to 32 kPa for 3 mg/mL CNTs-GelMA [87]. The obtained value is closer to the one of the ventricular myocardium of adult rats, that, as anticipated in Chapter 2, is between 20 kPa and 54 kPa [87]. Therefore, the CNTs network, embedded in the GelMA hydrogel, are responsible for the improvement of both the electrical and the mechanical properties of the scaffold fundamental for cardiac tissue engineering. These hypothesis were confirmed experimentally by Shin *et al.* in [87] where they compared the culture of freshly isolated neonatal rats cardiomyocytes on 5% GelMA hydrogel with and without CNTs (1 mg/mL). The most relevant results are shown in

Figure 5.8. Looking at the cardiomyocytes immunostaining (after 8 days of culture) with Sarcomeric-α-actinin and Cx-43 expression using the confocal microscope, it can be observed how an improved interconnected tissue, with superior cell-cell electrical coupling, was present in case of CNT-GelMA scaffold, showing also a higher uniaxial alignment of the sarcomeres (see Figure 5.8, a and b) [87]. The superior performances of CNT-GelMA hydrogels, if compared with bare GelMA hydrogels, can be recognized also in a more uniformly distributed expression of both Troponin I (Figure 5.8, c and d) and of F-actin filaments (Figure 5.8, e) [87]. Also in this case, not only the cardiac tissue was more dense and homogeneous, but also, the cell morphology looked more elongated in one direction, as in case of *in vivo* conditions, instead of being randomly oriented as for bare GelMA hydrogel [87]. Shin *at al.* hypothesized that the improved cardiac tissue organization in case of CNTs-loaded GelMA is related to the presence of the fractal-like CNTs network which presents strong similarities to the real structure of the ECM in the heart tissue hence guiding cell elongation and cardiac myofibers striation (see Figure 5.8, f) [87].

The preliminary results obtained by Shin *et al.* in [87] and in [197] supported the choice of CNT-GelMA hydrogel as backbone for the development of a cardiomyocytes-powered soft actuator, described in details in 5.3. Before focusing on the description and the designed of the aforementioned cell-based soft actuator, the experimental synthesis procedure adopted in the present work to synthesized GelMA and CNT-GelMA will be detailed in Section 5.2.3.

5.2.3 CNT-GelMA Exerimental Synthesis

In this section, the experimental synthesis procedure adopted at the Khademhossini Laboratory in Boston (see the Preface for the complete affiliation list) will be described. The mechanism of the synthesis was based on a modification of the original Van Den Bulcke protocol, as anticipated in Section 5.2.1 and published in [87], [1] and [197]. At first, a solution of PBS (Gibco®, USA), with 10% (w/v) gelatin from porcine skin (G2500 Sigma-Aldrich Inc., USA) was heated up to 50°C in an Erlenmeyer flask, under magnetic stirring (240 rpm) up the the complete dissolution of the gelatin (see Figure 5.9). Then, the substitution reaction of the MA groups in the gelatin backbone was initiated by slowly dropping 0.8 mL of methacrylic anhydride (276685 Sigma-Aldrich Inc., USA) per gram of gelatin. The solution was then left mixing at 50°C for 2 hours. Afterwards, the reaction was stopped by diluting the solution with additional warm PBS (pre-heated at 50°C), and, then, the mixture was separated into dialysis membranes with molecular weight cut off between 12 kDa and 14 kDa (Spectrum^{TM} Spectra/Por^{TM} 4 RC Dialysis Membrane Tubing 12,000 to 14,000 Dalton MWCO) and dialyzed at 40°C for 1 week in deionized water. The dialysis water was changed two times per day. This step was fundamental for the complete removal of all the unreacted MA and the

potentially toxic reactions byproducts. At last, the solution was freeze-dried for 1 week (see Figure 5.9).

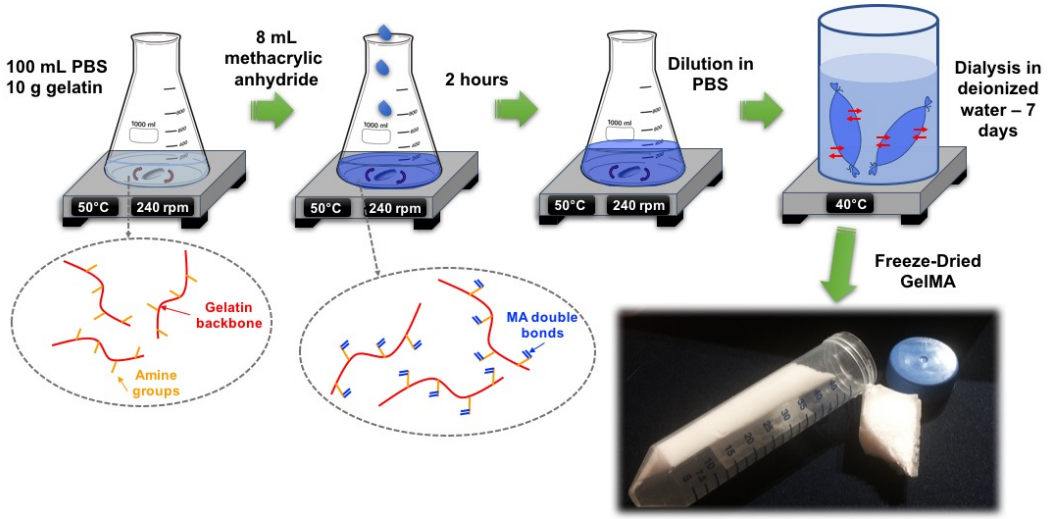

Fig. 5.9 Schematic diagram of the synthesis of GelMA hydrogel.

To prepare the GelMA pre-polymer solution the desired amount of GelMA was dissolved in PBS with the addition of 1% Irgacure® 2959 photoinitiator. To allow the complete dissolution of both GelMA and the photoinitiator the solution was quickly vortex and heated in dark conditions at 80°C for 10 - 20 minutes. In order to incorporate CNTs into the GelMA pre-polymer solution multiwalled CNT, functionalized with carboxyl acid groups (30 nm $\pm$ 15 nm diameter and 5 μm – 20 μm length, 95% purity, Nanolab Inc.) were added to a solution of 2% GelMA in PBS with a concentration of 1 mg/mL. Then, the solution was sonicated (VCX 400, 80 W, 2 s on and 1 s off) for 1 hour obtaining a final black solution with no aggregations visible. This solution was referred as "CNT-stock". In order to obtain the final CNT-GelMA hydrogel pre-polymer solution, the CNT-stock was further mixed with additional PBS, GelMA freeze-dried hydrogel and photoinitiator. The amount of PBS and GelMA freeze-dried precursor were selected according to the final concentration wanted (usually between 5% and 8% GelMA), while, the Irgacure® 2959 photoinitiator concentration was kept constant to 1%.

5.3 Preliminary Work: UV Photolithography- Fabricated Soft Actuator With Embedded Gold Microelectrodes

In this Section, the design and development of a PEG and CNT-GelMA hydrogels based hybrid actuator, actuated by the beating activity of cardiomyocytes growing on its surface will be described. The shape of the soft actuator was designed to mimic the muscular structure and motion dynamics of the manta batoid ray. Gold flexible microelectrodes were embedded in the soft actuator in order to electrically stimulate it *in loco*. As it will be detailed in Section 5.3.1.1, the soft actuator was fabricated using UV photolithographic techniques. Although the author has contributed only to the very final stage of this project during the Ph.D. activity, this work was fundamental for the successive step i.e., the design and fabrication of a bio-printed wireless-stimulated PEG/CNT-GelMA soft actuator actuated by freshly isolated cardiomyocytes. As anticipated in the Abstract of Chapter 5, this work was previously published by the author in [1] (a starting and an ending footnote will enclose the verbatim extracts from the published paper, see Appendix A for the copyright and permission).

5.3.1 Electrically Driven Microengineered Bioinspired Soft Robots

The content of this sections was previously published by the author in: S. R. Shin, B. Migliori, B. Miccoli, Y.-C. Li, P. Mostafalu, J. Seo, S. Mandla, A. Enrico, S. Antona, R. Sabarish, T. Zheng, L.Pirrami, K. Zhang, Y. S. Zhang, K.-T. Wan, D. Demarchi, M. R. Dokmeci, A. Khademhosseini: "Electrically Driven Microengineered Bioinspired Soft Robots", Advanced Materials. Year 2018. Pages 1704189. ISSN 1521-4095. Copyright WILEY-VCH Verlag GmbH & Co. KGaA, Weinheim, reproduced with permission (see Appendix A for the copyright and permission).

[1] To create a bioinspired soft robot with flexible microelectrodes, batoid fish can be a good model organism with several advantages as suggested in previous studies [172, 199]. The batoid fish, which are cartilaginous fish with dorsoventrally flattened bodies and extended pectoral fins, can be easily mimicked by simplifying its structure and movements among various living organisms in the ocean. In addition, the flexible microelectrodes are amenable for easy integration into flattened bioinspired robots.

[1] Starting point of the verbatim quote from [1], see Appendix A for the complete copyright and permission file.

However, various batoid fish exhibit different swimming styles that largely depend on their skeletal architecture (e.g., cartilage joint patterns), along with their aligned muscle tissues on their pectoral fins [199]. To create a natural motion, we intended to mimic the alignment of skeletal and muscular architecture of the batoid fish, in particular a stingray, which can modulate the movement of the robot in a biomimetic manner. Especially, the cartilage structure and arrangement are key criteria to consider in the design of an effective bioinspired soft robot as it will have a strong influence on the kinematic motion of the robot.

5.3.1.1 Fabrication Techniques

We designed and fabricated a bioinspired soft robot, which combined the mechanical and biological properties of a sting ray (Figure 5.10). The bioinspired soft robot was composed of four layers: aligned muscle tissue, micropatterned CNT-GelMA hydrogel, a flexible Au microelectrode, and a micropatterned PEG hydrogel layer. The first layer, which aimed to mimic the structure and function of the cartilage joint patterns (blue dot in Figure 5.10, a) of the skeletal architecture in a sting ray, was composed of a PEG micropatterned hydrogel (Figure 5.10, b). In this case, the PEG micropatterned hydrogel allowed for easy deformation of the construct under cell contraction and relaxation while maintain the mechanical stability of the whole structure when compared with a thin PEG hydrogel film [200, 201]. For the second layer, a network of flexible Au microelectrodes was integrated into the scaffold to stimulate the robot with precise control and efficient electrical signal propagation across the robot. The Au microelectrodes with nanometer thickness were designed with a meander line pattern, which helped dissipate the physical stress of the metal electrode during muscle actuation when embedded in the scaffold [202]. The third layer was designed to mimic the directional muscle alignment against the cartilage joint patterns of the stingray.

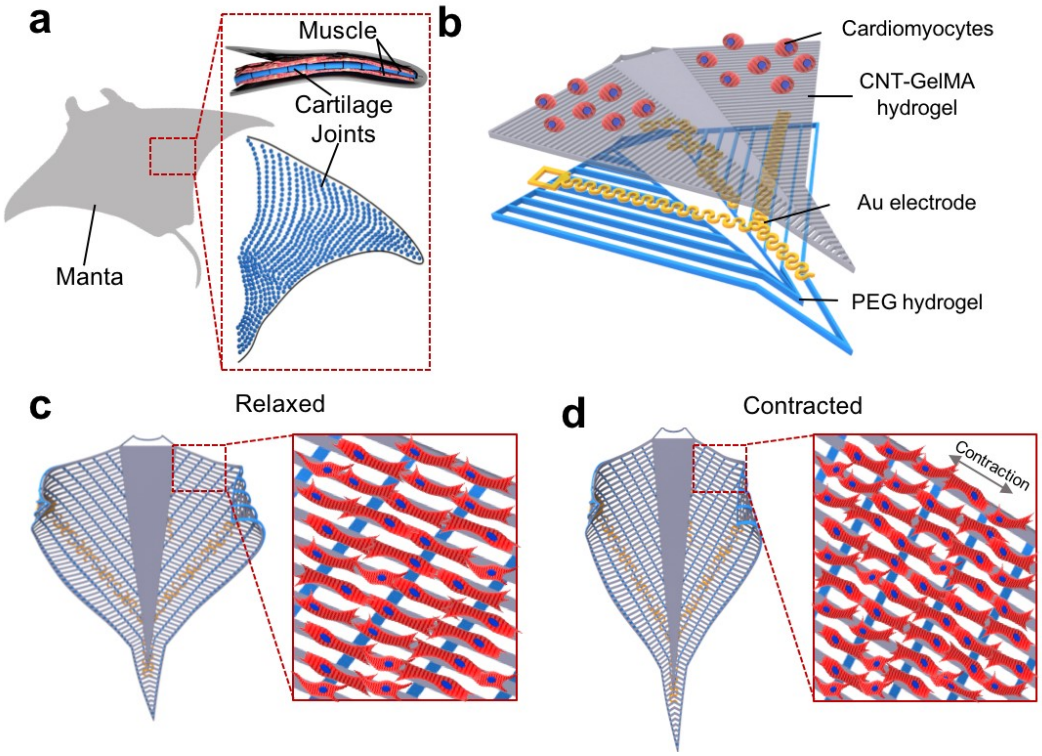

Fig. 5.10 Schematic of the device. (a) Schematic of the cartilage joints and muscle patterns of a string ray. (b) Schematic illustration of the layer-by-layer structure of the construct. The bottom layer was composed of a PEG hydrogel with vertical line patterns for alignment. The upper layer in contact with the cells was made of patterned CNT–GelMA hydrogel with a pattern, which was perpendicular to the PEG hydrogel patterns. The microelectrodes were embedded in between the two layers. (c)-(d) Schematic design of the sting ray movement in the macro and micro scale: relaxed cardiomyocytes (c) and contracted cardiomyocytes (d). Reproduced with permission from reference [1], ©2018 WILEY-VCH Verlag GmbH & Co. KGaA, Weinheim.

A CNT-GelMA micropatterned hydrogel, which acted at a biocompatible environment suitable for cardiomyocyte culture and alignment, was generated with a pattern perpendicular to the orientation to the PEG hydrogel pattern (Figure 5.11). Finally, the fourth layer consisted of neonatal rat cardiomyocytes seeded on top of the CNT-GelMA hydrogel pattern to obtain a sting ray-shaped bioinspired soft robot. After the maturation of the cardiomyocytes, the CNT-GelMA hydrogel pattern ensured contractions in the direction of cell alignment while the PEG hydrogel pattern could release the membrane tension following contraction, thus allowing the scaffold to return to its original shape (Figure 5.10, c and d). The detailed fabrication process of the bioinspired soft robot with the incorporated flexible Au microelectrode is presented and schematically illustrated in Figure 5.11. The spacing in between the microscale hydrogel patterns is an important factor affecting cell alignment and

cell-cell interactions, as reported in a previous study [203]. Three different pattern distances were tested for both the PEG (200, 300, and 500 μm) and the CNT-GelMA (50, 75, and 150 μm) hydrogels.

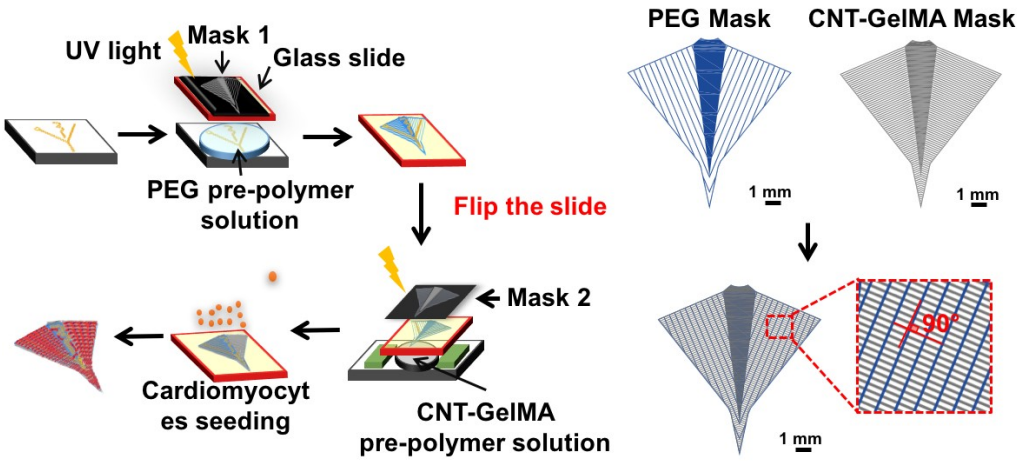

Fig. 5.11 (a) The Au electrode is peeled from the glass slides thanks to the assistance of the PEG hydrogel layer directly UV-crosslinked on its surface through a specific photolithographic mask. The structure is then flipped, and a CNT-GelMA hydrogel pattern is crosslinked on the other electrode's surface. Cardiomyocytes are then seeded on the CNT-GelMA hydrogel top layer. The angle between the PEG and CNT-GelMA hydrogel pattern line was of 90°. Reproduced with permission from reference [1], ©2018 WILEY-VCH Verlag GmbH & Co. KGaA, Weinheim.

Despite the inferior cell alignment, the spontaneous beating had higher rates and was more stable on the patterns with 75 μm spacing (frequency: 0.9 ± 0.1 Hz) than on the ones with 50 μm spacing (frequency: 0.5 ± 0.2 Hz) and 150 μm spacing (frequency: 0.2 ± 0.1 Hz) [1]. This could be related to the higher number of cell-cell interactions, which led to the higher beating synchronization and rates [204]. Furthermore, the geometry of the supporting PEG hydrogel pattern dramatically affects the function of the bioinspired soft robot in terms of both directional beating and overall structure folding. To prevent irreversible complete rolling of the soft robot during the dynamic beating of the cardiomyocytes, the pattern spacing of the PEG hydrogel support layer was varied between 200, 300, and 500 μm. A middle ground for the PEG hydrogel pattern density was found to be at 300 μm. With this dimension, the supporting PEG hydrogel layer was soft enough to follow the cardiomyocyte-induced bending of the soft robot, while remaining sufficiently stable to prevent irreversible folding of the substrate.

5.3.1.2 Cardiomyocytes Culture and Actuation Dynamics

After seeding neonatal rat cardiomyocytes on the optimized soft robot with CNT-GelMA and PEG hydrogel patterns with distances of 75 and 300 μm, respectively, the cells were stained for cardiac-specific biomarkers, including Sarcomeric α-actinin and connexin-43 (Cx-43)[205, 206] to observe the tissue morphology and phenotypes. Notably, in the case of the 75 μm spacing CNT-GelMA hydrogel spacing, cardiomyocytes on the top layer were observed to show alignment along the CNT-GelMA hydrogel pattern, and were interconnected between the patterned lines (Figure 5.12 a,b), leading to the formation of a pseudo-3D cardiac tissue construct. The obtained pseudo-3D cardiac tissue construct consisted of cardiomyocytes in layers, the (i-1 and -2) upper, (ii) middle, and bottom parts, based on aligned and random cardiomyocyte morphology. Both cell bodies and elongations were found to intrude the base and side CNT-GelMA hydrogel patterns (50 μm in width and thickness), which therefore served as pseudo-3D scaffolds instead of 2D substrates [87]. More specifically, as shown in the schematic in Figure 5.12 a, and confirmed by confocal fluorescent microscopy, a homogeneous distribution of Cx-43, and well-organized sarcomeric α-actinin structures were observed on the topmost tissue (Figure 5.12 b(i-1 and -2)). This tissue is primarily responsible for the synchronous beating of the whole construct. Alternatively, in the middle and bottom parts sarcomeric α-actinin expression resulted in partially aligned and organized tissue along the muscle-like hydrogel structure (Figure 5.12 b(ii),(iii)), which was found to not only enhance the synchronous contractile properties of the structure but also to guide the actuation dynamics parallel to the direction of the CNT-GelMA hydrogel pattern (Figure 5.12 a), inducing the swimmer-like movement of the bioinspired soft robot. The soft robot showed spontaneous and synchronous beating behavior when neonatal rat cardiomyocytes were cultured on the biomimetic scaffold starting at day 3 (beating frequency 1.0 $\pm$ 0.1 Hz) until day 9 (beating frequency 0.8 $\pm$ 0.1 Hz), with no significant reduction in beating rates (Figure 5.12 c). Interestingly, because of the patterned design of the PEG hydrogel substrate, the cultured cardiomyocytes on the biomimetic multilayer scaffold showed a similar beating rate compared to those on pristine CNT-GelMA hydrogels as shown in our previous work [87].

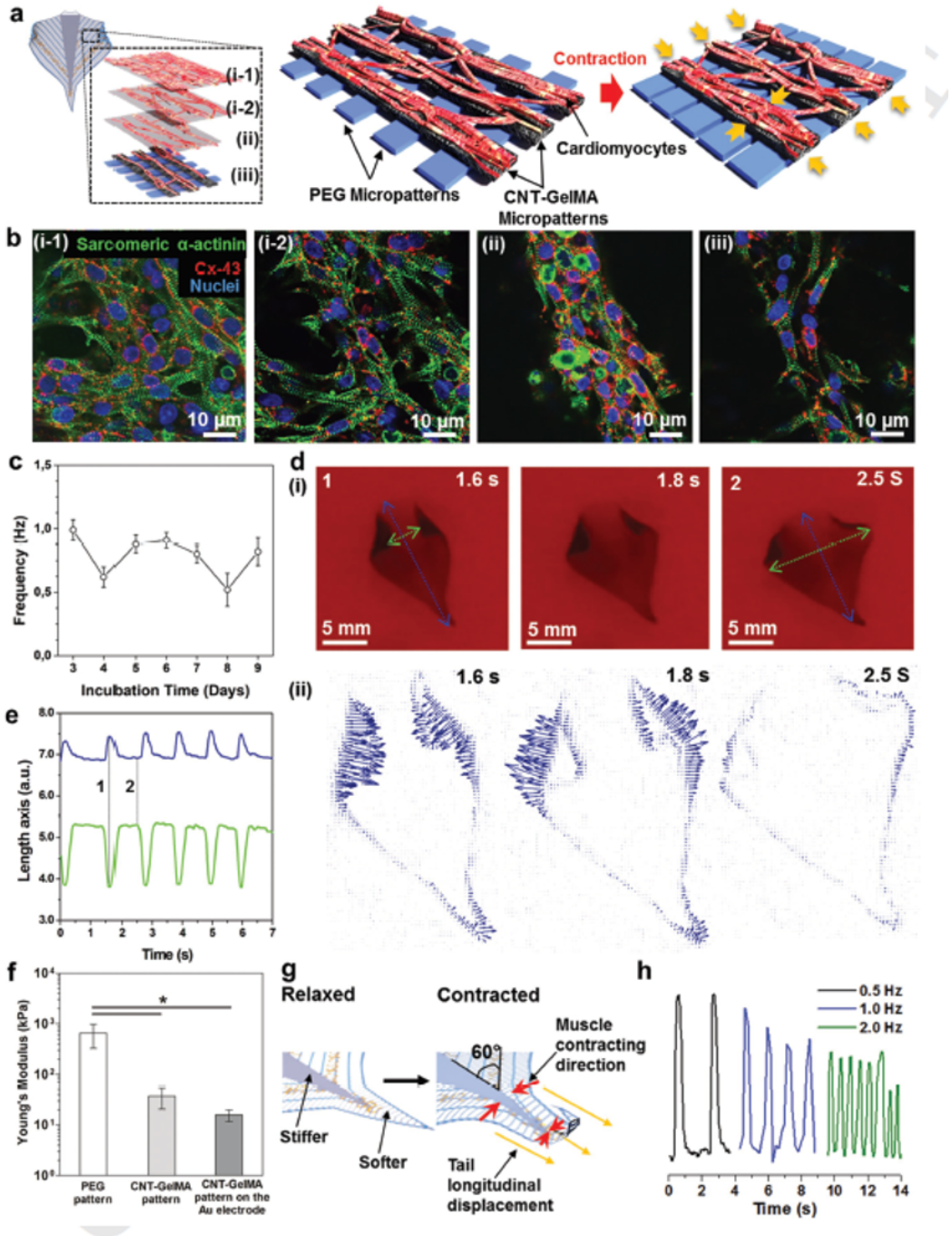
a
(i-1)
(i-2)
(ii)
(iii)
Contraction
Cardiomyocytes
PEG Micropatterns
CNT-GelMA Micropatterns
b
(i-1) Sarcomeric α-actinin
Cx-43
Nuclei
10 μm
(i-2)
(ii)
(iii)
c
Frequency (Hz)
Incubation Time (Days)
d
(i)
1
1.6 s
1.8 s
2
2.5 S
5 mm
(ii)
1.6 s
1.8 s
2.5 S
e
Length axis (a.u.)
Time (s)
f
Young's Modulus (kPa)
PEG pattern
CNT-GelMA pattern
CNT-GelMA pattern on the Au electrode
g
Relaxed
Contracted
Muscle contracting direction
60°
Stiffer
Softer
Tail longitudinal displacement
h
0.5 Hz
1.0 Hz
2.0 Hz
Time (s)

Fig. 5.12 The characterization of the cardiomyocytes on the bioinspired scaffold. (a) Schematic illustration of the contraction behavior of the cultured cardiac muscle tissue on the bioinspired scaffold. The cultured cardiac muscle tissue showed a pseudo-3D structure, which could be separated into four layers, the (i-1 and -2) upper, (ii) middle, and (iii) bottom, based on aligned and random cardiomyocyte morphology. (b) Confocal fluorescent images showed different morphology in the (i-1 and -2) upper, (ii) middle, and (iii) bottom of cardiomyocytes cultured on the bioinspired scaffold for day 5. (c) Spontaneous beating rates of the cardiomyocytes on the bioinspired scaffold from day 3 to day 9. (d) (i) Photograph of a free-standing bioinspired soft robot cultured for 5 d at 0, 0.18, and 0.3 s. The blue line represents the longitudinal axis displacement while the green line represents the transverse axis displacement. (ii) Particle Image Velocimetry measurement of the bioinspired soft robot spontaneously moved within 0.3 s. All arrows indicated direction and magnitude of the beating motion. (e) Displacement of the two major axes during stimulated contractions (2.0 Hz, 1 $V \cdot cm^{-1}$). The blue line represents the longitudinal axis displacement (corresponding to the blue line in Figure 3d) while the green line (corresponding to the green line in Figure 3d) represents the transverse axis displacement. The frame taken in correspondence to the lines marked with 1 and 2 are shown in Figure 3d. (f) Young's modulus of the PEG hydrogel pattern, CNT-GelMA hydrogel pattern, and the CNT-GelMA hydrogel pattern fabricated on the Au microelectrode. ($^{*}p < 0.05$). (g) Schematic of the mechanism of tail longitudinal displacement which induces the soft robot displacement along the vertical direction, mainly on the tail part, when the cells contract. (h) Beating response of the bioinspired soft robot when stimulated with an AC external electrical field at 1 $V \cdot cm^{-1}$ and with various frequencies from 0.5 to 2.0 Hz.Reproduced with permission from reference [1], ©2018 WILEY-VCH Verlag GmbH & Co. KGaA, Weinheim.

Consequently, the optimized micropatterns on the PEG hydrogel did not inhibit the cardiac muscle actuation on the substrate.

Finally, the fabricated bioinspired soft robot showed a unique self-actuating movement, but not yet forward propulsion. In Figure 5.12 d,e, longitudinal (blue line, stretching) and transverse (green line, contracting) axes on the soft robot showed actuation in opposite directions at the same time. A much higher contraction of the laterally patterned fins was observed in the transverse axes of the soft robot due to the strong muscle contraction of the aligned cardiac tissue along the CNT-GelMA hydrogel patterns (Figure 5.12 b(ii),(iii)). In addition, the micropattern of the stiff PEG hydrogel with a spacing of 300 μm may help to induce the easy deformation of the micropatterned soft CNT-GelMA hydrogel under cell contraction. The Young's modulus, derived from the force indentation data using a Hertzian model, of the micropatterned PEG hydrogel, was 651 $\pm$ 326 kPa, which was 30 times higher than that of the CNT-GelMA hydrogel (37 $\pm$ 16 kPa), as shown in Figure 5.12 f. On the contrary, the soft robot showed less deformation in the longitudinal axes (blue dot line), i.e., in the direction of the PEG hydrogel pattern. The longitudinal displacement can be mainly attributed to the 60° angle of the CNT-GelMA pattern

with respect to the main axes of the soft robot that induced a force component in the vertical direction (Figure 5.12 g). Hz.

The local control of the electrical stimulation of the soft robot was achieved through the encapsulation of a set of 200 nm thick Au microelectrodes in the structure. The Au microelectrodes (Figure 5.13 a) were deposited on a glass substrate by e-beam evaporation (see [1] for further details). Atomic force microscopy (AFM) characterization (Figure 5.13 b) revealed a root mean square roughness of 2.0 ± 0.4 nm, therefore providing compelling evidence of the high quality of the deposited electrode. The shape of the embedded Au microelectrodes was designed to allow the structure to maintain a high degree of flexibility necessary for the microelectrodes to not impede the beating of cardiomyocytes, and to generate a uniform electric field distribution across the scaffold, such that a wave-like displacement (arc segment angles: 120°), originating from the central region of the structure can be achieved. Direct UV crosslinking of the PEG and CNT-GelMA hydrogels on the surface of the microelectrodes not only prevented electrode delamination, but also allowed the microelectrodes to be directly incorporated between the two hydrogels. Successful transfer and encapsulation of the microelectrodes in the PEG hydrogels, was assessed using SEM (Figure 5.13 c,d) to ensure that there were no cracks at the interface between the microelectrodes and the hydrogel or surface damage of the microelectrodes. The Au electrode was then completely enclosed in the micropatterned CNT-GelMA hydrogel, which was assessed using optical imaging, as shown in Figure 5.13 e. It was confirmed experimentally that the Young's modulus of the micropatterned CNT-GelMA hydrogel on the Au electrode was similar to that of the micropatterned CNT-GelMA hydrogel only. Therefore, the CNT-GelMA hydrogel was successfully deposited on top of the Au microelectrodes; however, the Au electrode may have partially prevented crosslinking of the CNT-GelMA prepolymer under the microelectrodes since the opaque nature of the Au electrodes prevented the illumination crosslinking the material underneath them. Finally, we created a bioinspired soft robot with embedded Au microelectrodes between the hydrogel layers as shown in Figure 5.13 f. To further assess the stability of the electrodes in cell culture condition, its resistance was monitored for 5 d of incubation in cell culture media at 37 °C, (Figure 5.13 g). Only a slight variation of resistance was observed during the 5 d of culture, thus confirming the stability and adhesiveness of the electrode in the biological environment. In addition, the modulus of the electrical impedance was measured for the transferred microelectrodes on the PEG hydrogel layer, the encapsulated microelectrode within two hydrogel layers, and the entire soft robot with cultured cardiomyocytes (Figure 5.13 h). As expected, at frequencies higher than 0.1 kHz, the presence of the capacitive current strongly decreased the modulus of the impedance on the PEG/microelectrodes (from 630 to 251 Ω), PEG/microelectrodes/CNT-GelMA (from 280 to 61 Ω) and PEG/microelectrodes/CNT-GelMA/cardiomyocytes (from 318 to 89 Ω) samples between 0.1 and 82.5 kHz.

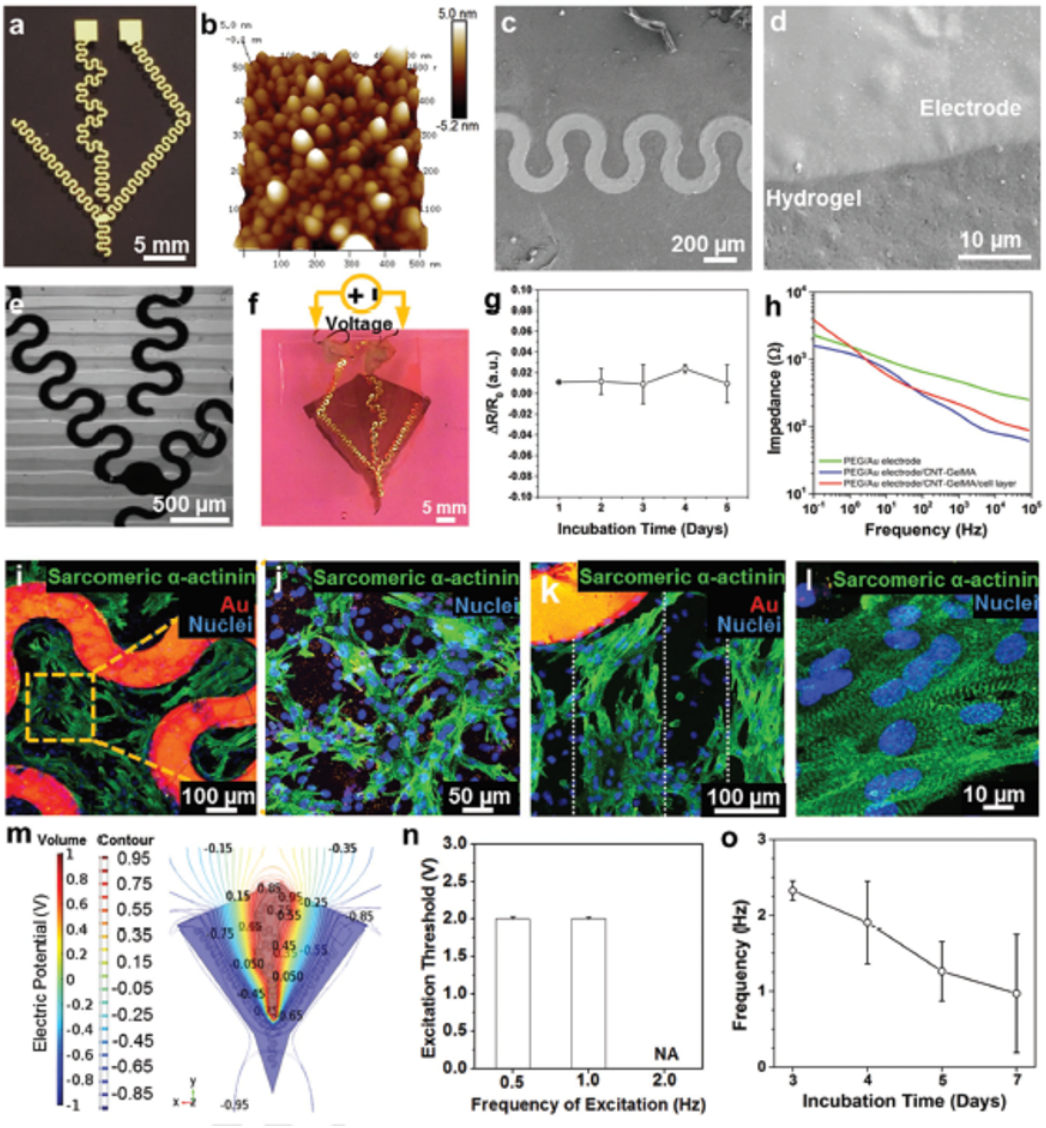

Fig. 5.13 Characterization of the Au microelectrodes and their incorporation into the bioinspired soft robot. (a) E-beam-evaporated Au microelectrodes with a serpentine pattern. (b) AFM image of the Au microelectrodes. (c,d) SEM image of the Au microelectrode successfully transferred onto the PEG hydrogel. (e) Optical microscope image of the Au microelectrodes successfully embedded in the CNT-GelMA hydrogel pattern. (f) Obtained bioinspired soft robot with embedded Au microelectrodes. Copper wires were connected to the structure using silver paste to make an electrical contact for local electrical stimulation. (g) Variations in the Au microelectrodes resistance embedded in the bioinspired scaffold during 5 d of incubation in cell culture media at 37 °C. (h) Measured impedance modulus of Au microelectrodes transferred on the PEG hydrogel pattern (green), embedded in between PEG and CNT-GelMA hydrogel patterns (blue), and PEG and CNT-GelMA hydrogel patterns with cardiomyocytes layer (red). (i) Confocal fluorescence image of the cardiomyocytes, randomly spread among the Au microelectrodes (red signal) on the unpatterned central body. (j) The cardiomyocytes exhibited a random network organization on the unpatterned central body. k) Well-elongated and aligned cardiomyocytes were showed on the CNT-GelMA hydrogel pattern which is indicated by the white dots. (l) Partial uniaxial sarcomere alignment and interconnected sarcomeric structure was observed on the patterned areas. (m) Top views of the numerically calculated electric potential contour plot volume distribution when a square wave signal (Peak Amplitude: 1 V, DC offset value: 0V, Frequency: 2.0 Hz, Pulse width: 50 ms, Duty Cycle: 10%) was applied to the embedded microelectrodes. (n) Excitation threshold voltage required at different frequencies (0.5, 1.0, and 2.0 Hz) when electrical stimulation was applied via the embedded Au microelectrodes. (o) Spontaneous beating behavior of the bioinspired soft robot with embedded Au microelectrodes after electrical stimulation.Reproduced with permission from reference [1], ©2018 WILEY-VCH Verlag GmbH & Co. KGaA, Weinheim.

Alternatively, at lower frequencies that are more representative of physiological conditions, an impedance modulus reduction could be observed when the CNT-GelMA hydrogel layer was added on the PEG/microelectrodes structure (from 2.3 to 1.6 kΩ at 0.1 Hz). This can be attributed to the presence of additional current paths through the CNTs incorporated in the GelMA hydrogel, and would therefore contribute to an efficient electrical signal propagation through the cardiomyocytes. When cardiomyocytes were seeded on the soft robot with the embedded Au microelectrodes, a moderate impedance modulus increase was noticed, likely due to the intrinsic resistivity of the cells. Moreover, to confirm the organization of cardiac tissue on the microelectrodes-incorporated soft robot, immunostaining of sarcomeric α-actinin and F-actin was investigated. As shown in Figure 5.13 i,j, we observed the random network formation of cardiac tissue with well-interconnected sarcomeric structures on the central body due to the absence of a pattern on the CNT-GelMA hydrogel. On the contrary, the cardiomyocytes were only partially aligned with the micropatterned CNT-GelMA hydrogels on the laterally patterned fins, as evident from Figure 5.13 k,l.

After cardiomyocytes seeding, the bioinspired construct with the embedded Au microelectrodes was able to efficiently maintain its original shape and integrity during the culture period. Moreover, to make use of the embedded microelectrodes, two copper wires were connected to the outermost end of the electrodes to electrically stimulate the bioinspired actuator. The copper to Au attachment was insulated from the culture media by a thin layer of PDMS (Figure 5.13 f). To investigate how an external voltage signal propagates and distributes via the embedded microelectrodes along the construct, finite element model simulations were performed using commercially available software (COMSOL Multiphisics), both in the case of the embedded microelectrodes and the external carbon rod electrode. When a square wave signal (AC peak voltage amplitude 1V, DC offset value 0V, frequency 2.0 Hz, period 50 ms, duty cycle 10%) was applied in the case of the microelectrode stimulation, the maximum voltage intensity was found to be 1 V in the central area of the structure (Figure 4m). The observed nonuniform electric potential distribution suggested a nonspontaneous electrical excitation of the cardiomyocytes. This nonuniform electric potential distribution could generate the electrical propagation of the pulse conduction from one cell to another. Therefore, this can result in a wave-like displacement of the whole structure, in which the movement originates from the central body, and propagates toward the outer fin regions, mimicking the physiological actuation of the muscles to achieve defined contraction of the entire structure. To control the beating rates of the soft robot at a specific target frequency (0.5, 1.0, and 2.0 Hz), a biphasic pulse waveform at various frequencies (pulse width: 50 ms, duty cycle: from 2.5% to 10%, peak voltage amplitude: from 0.5 to 6 V, DC offset value: 0V, frequency: 0.5, 1.0, and 2.0 Hz) was applied to the microelectrodes. We successfully tuned the beating behavior of the cardiomyocytes at 0.5 and 1.0 Hz, as shown in Figure 4n. However, we were unable to achieve a stimulation frequency

of 2.0 Hz, as the artificial tuning of the beating behavior could not be achieved for peak amplitudes smaller than 3 V, which was the maximum waveform amplitude we could apply. This indicates that much higher voltage amplitudes should be applied to the system.

As shown in Figure 5.13 o, the soft robot showed slightly different beating frequency until day 7 after the application of electrical stimulation with different parameters, performed for 4–5 h compared with that of the soft robot without microelectrodes and electrical stimulation. However, the overall beating frequency until day 7 was found to be around 1 Hz with strong spontaneous beating.

Although our bioinspired actuators do not generate forward propulsion, the results obtained in the present work not only encourage further developments in the field of bioinspired actuators but also serve as an initial platform for new, cutting-edge studies on local electrical stimulation of cell-laden constructs with embedded microelectrodes for use as a wireless control system for the entire scaffold. Therefore, microfabricated cell-based hybrid actuators have the potential to greatly enhance the performance of biorobotics and potentially result in low-cost, fast, and easier-to-use analytical tools that are more portable and scalable for point-of-care sample analysis and real-time diagnostics. Furthermore, this proof of concept study even in absence of propulsion has potential applications in regenerative medicine, e.g., cardiac or muscle patches integrated electrical stimulators for tissue regeneration. [2]

5.4 Bioprinting of a Soft Actuator With Wireless Electrical Stimulation

The bio-mimetic soft-actuator presented in Section 5.3 represented the starting point for a preliminary study about an improved version of the soft-robot fabricated using bio-printing techniques, instead of UV-photolithography, and exploiting wireless stimulation, in place of embedded microelectrodes. Bioprinting techniques allow to highly improve the versatility of the design of the final structure, including easily also curved geometries (see Chapter 7). Moreover, as underlined also by Pati *et al.*, this process can be more straightforward of the photolithographic one, with no need of custom lithographic masks, computer-controlled fabrication is possible and complex 3D geometries are easily printed [207]. On the other side, a wireless electrical stimulation of the cardiomyocytes-based soft-actuator would introduce enormous advantages not only because all the issues related to the need of connecting metal wires (also immersed in the cell culture media) can be eliminated but, also, because proximity cable-free stimulation is possible at close distances which can

[2]Ending point of the verbatim quote from [1], see Appendix A for the complete copyright and permission file.

be extremely useful in case of the future application for *in vivo* implants. Due to the complexity and extensive multidisciplinary nature of the project, as well as to its early stage, the main focus during the present Ph.D. activity was devoted to the optimization of an effective bioprinting process of the hybrid actuator, with fish inspired design, that could act as biomimetic scaffold for freshly isolated neonatal rats cardiomyocytes. As anticipated in the chapter abstract, the development of the first prototype of the wireless stimulating electrodes was developed in the framework of the Ph.D. activity of L. Pirrami (University of Applied Sciences and Arts Western Switzerland, Fribourg and Politecnico di Torino, Italy). The biodegradation and the biocompatibility of the fabricated electrodes with cardiomyocytes culture was then assessed by the author at the Khademhosseini Laboratory.

In Section 5.4.1, a brief introduction and state of the art about bioprinting techniques for tissue engineering will be provided, while, the specific experimental bioprinting setup adopted in the present work will be presented in Section 5.4.2.

5.4.1 Introduction About Bioprinting Techniques for Tissue Engineering

Bioprinting techniques belong to the family of additive manufacturing technologies i.e., technologies in which 3D structures are created by the layer-by-layer deposition of precursor materials [208]. Recently this technique, originally used for electronic, aerospace and industrial applications [209], was translated to the field of tissue engineering by enabling the direct printing of biological materials [208]. Usually a computer aided design (CAD software is also present in order to guide the deposition process according to the desired geometry. By tuning the bioprinting parameter specific 2D or 3D geometries and complex architectures of tissues can be easily fabricated. One of the greatest potentialities of these 3D tissues architectures, as anticipated in Chapter chapter 2 is that they can be designed to mimic, as close as possible, the intricated *in vivo* organization of the tissues thus enormously increasing the potentialities of tissue engineering applications [192]. These adavantages are not only related to the fabrication of bioprinted implantable organs but also, to more reliable *in vitro* models for the study of new drugs and of fundamental biological processes. As depicted in the schematics of Figure 5.14, 3D bioprinting represents the natural step forward starting from 2D cell cultures and moving towards hydrogel-based 3D cell cultures that can promote the maturation of functional tissue that can potentially be successively implanted *in vivo* [192]. It is worth mentioning that, the high versatility of the bioprinting techniques allows also the bioprinting process to be performed directly on the patient him/her-self [210]. In fact, several preliminary studies are reported in the literature where bioactive hydrogels are directly printed on wounds or burns to favor the healing of the tissue [210].

Biocompatible hydrogels stand out as optimal candidates for the selection of suitable biological inks (also referred as bio-inks) [210]. Their extremely tunable mechanical and rheological properties as well as their biocompatibility, especially in case of natural hydrogels, allow the design and synthesis of countless possible bio-inks for different bioprinting processes.

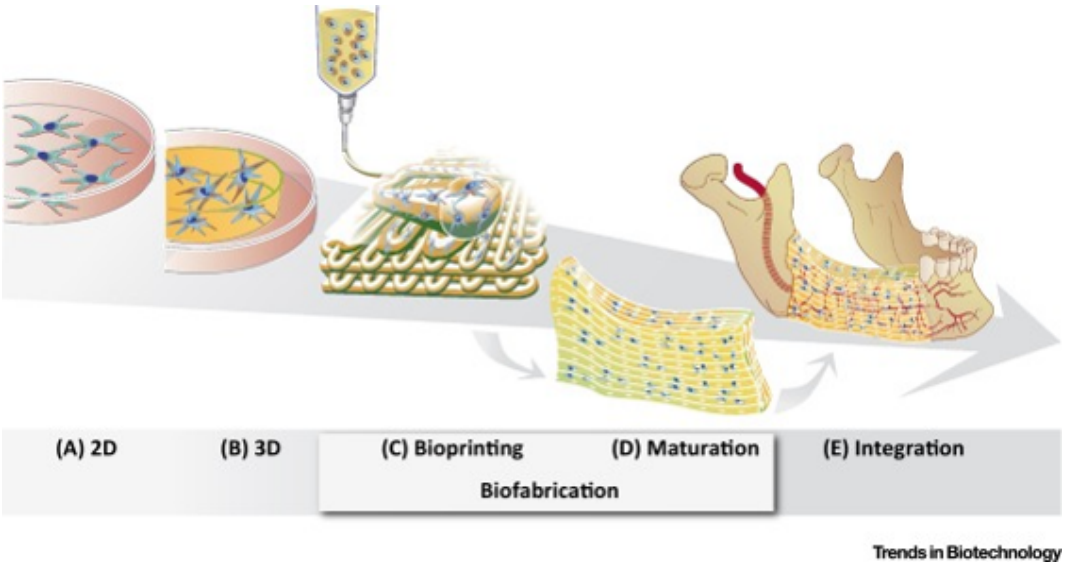

Fig. 5.14 Schematic diagram of the path from 2D (a) to 3D (b) cell cultures and their biofabrication procedures (c) inducing tissue maturation (d) and bio-integration in the body (e) (Reprinted from Trends in Biotechnology, Vol. 34, B. J. Klotz, D. Gawlitta, A. J.W.P. Rosenberg, J.Malda, F. P.W. Melchels, Gelatin-Methacryloyl Hydrogels: Towards Biofabrication-Based Tissue Repair, Pages No. 394-407, Copyright (2016), with permission from Elsevier [192]).

The shortage of tissues/organs for transplantations enormously encourages the scientific research on 3D bioprinting due to the exceptional impact of clinical applications [211]. These ambitions future perspectives are sustained by the fact that by combining multiple and/or different bioprinting processes as well as bio-inks and complex geometries the intricated architecture and infrastructure found in living organs and tissues, which is what guides and promote the cellar proliferation and functionality, can be artificially faithfully recreated [212]. Indeed, as outlined by Zhang *et al.*, the same physiological activities of organs in the human body are strongly dependent on their peculiar architectures like the capillaries in the nephron system or the alignment of myofibers in the hearth [212]. Therefore, it is not surprising how numerous bioprinted organs models can be found in the literature reproducing the ears [213], bones [209, 213] and heart's valves [212, 214].

For example, Mannoor *et al.*, fabricated a bionic ear, with the same anatomy of human ears, by 3D bioprinting of a cell-laden hydrogel [213]. Despite the

successful anatomy resemblance, cartilage tissue was successfully cultured around a an antenna embedded in the bionic ear enabling a cochlear-like signals exchange [213]. Differently, Duan *et al.*, bioprinted a hydrogel-based version of the aortic cardiac valve with laden human aortic vascular interstitial cells [214]. To tune the mechanical properties of the hydrogel for a correct valve displacement and stiffness, they optimized to different types of hydrogels: metahcrylated hyaluronic acid and GelMA [214]. Although high cell viabilities are obtained after several days of culture on bioprinted organs and tissues, e.g., Duan *et al.* reached more than 90% viability after 7 days of culture on their bionic heart valve [214], the problem of organ rejection once implanted *in vivo*. This problem can be overcome by directing the research efforts towards the use of autologous cells, i.e., cells directly collected from the target patient him/her-self or by a reprogramming step of him/her-stem cells [210]. This research can strongly impact also the field of personalized medicine, i.e., tailoring the therapy approach on each individual patient, which is a highly discussed topic in the current literature [215].

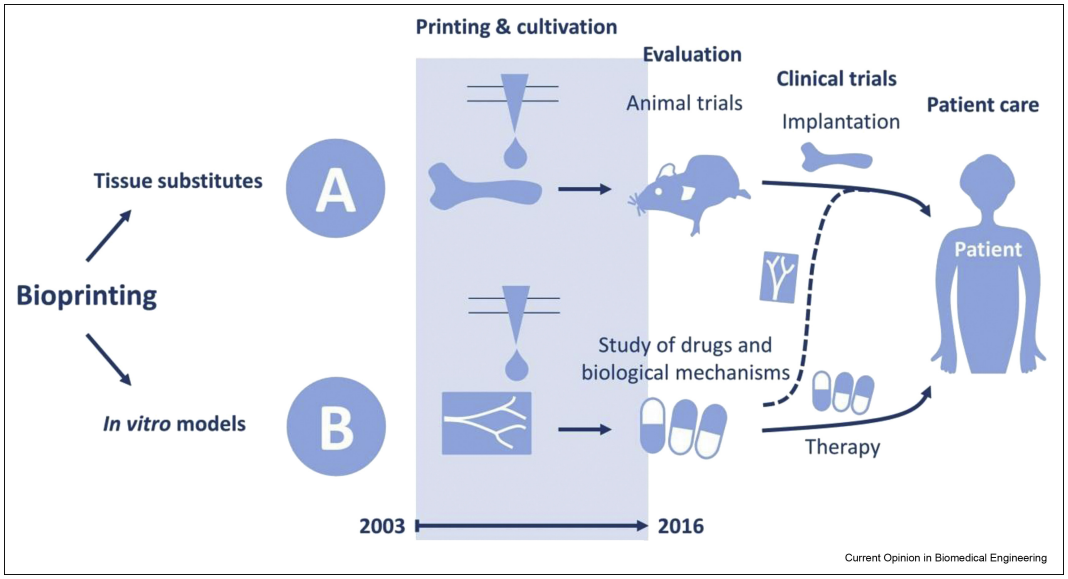

Fig. 5.15 Schematic diagram of the possible paths that lead bioprinting towards different patient care applications (Reprinted from Current Opinion in Biomedical Engineering, Vol. 2, A. Blaeser, D. F. D. Campos, H. Fischer, 3D bioprinting of cell-laden hydrogels for advanced tissue engineering, Pages No. 58-66, Copyright (2017), with permission from Elsevier [216]).

As pointed out by Blaeser *et al.*, the fabrication of artificial organs for *in vivo* implants is not the only target of bioprinting techniques [216]. Indeed, huge contribution can be provided also for *in vitro* tissues models for the study of new drugs or for the understanding of fundamental biological processes (not visible in standard 2D cell cultures, as anticipated in Chapter 2) [216]. Both the applications will contribute

to improve the patients health-care (as outlined in Figure 5.15), even if in different ways.

Nevertheless, still consistent improvements of the bio-inks physical and chemical properties, of the bio-printing techniques as well as of the necessary regulations and standardization for *in vivo* applications are necessary [208]. Therefore, part of the presented Ph.D. thesis work was aimed to optimized a tailored bioprinting technique for the creation of a hybrid cardiomyocytes-powered soft bioactuator, representing a first proof-of-concept for the use of this technique and material for the bio-printing of cardiac patches to be implanted in the heart and eventually, wireless stimulated. The physical properties and of the bio-active tissue, as well as the geometry, are fundamental to stimulate and induce the functional proliferation of the cardiac cells, both when implanted *in vivo* or for *in vitro* studies. This is particularly relevant since, up to now, injured cardiac cells cannot be recovered [212], therefore engineered bio-active tissues, capable to induce the proliferation of healthy cardiac cells are crucial for the fight against cardiac failures.

Due to the high relevance of bioprinting technologies, not only in the clinical field, several types of bioprinting processes have been developed in the years [216, 210, 209, 217]. Usually, they can be classified according to their working principle in laser-induced, inkjet printing and robotic dispensing, also referred as extrusion-based (see Figure 5.16) [207, 218].

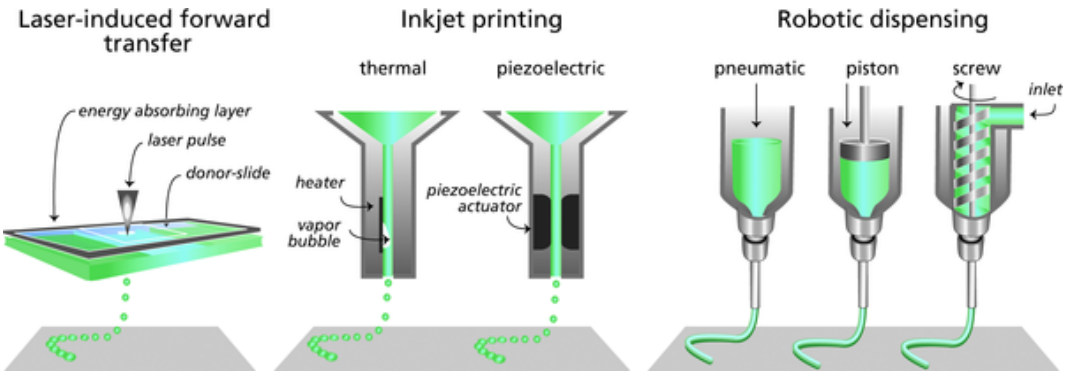

Fig. 5.16 Schematics of the different bioprinting methods present in the literature (reproduced with permission from [218], © 2013 WILEY-VCH Verlag GmbH & Co. KGaA, Weinheim).

Laser-induced bioprinting exploits laser pulses to induce the formation of high-pressure gas bubbles which, in turns, propels the dropping of the bio-ink on a given substrate even at the picoliter scale [210, 216]. The energy delivered by the laser per unit area is one of the main parameters affecting the final resolution obtainable along with the substrate wettability and the thickness and viscous properties of the bio-ink [210]. As envisioned, although high resolutions can be achieved, the technique is extremely time-consuming due to the low flow rate [210].

High-speed depositions are instead possible in case of inkjet bioprinting [210]. This technique originated from the commercial 2D inkjet printing technology commonly present in the industrial and domestic market. The ink cartridge was substituted by a bio-ink reservoir while, a x-, y- and z-axis controllable movable stage has replaced the place of the paper foil. Also in this case, as observable in Figure 5.16, the ink is deposited drop-wise. However, a different physical mechanism is exploited to generate the ink droplets. Usually thermal or piezoelectric-generated acoustic forces are the main responsible for the ink deposition [210]. In the thermal inkjet process, the printing nozzle is electrically heated so that pulses of propelling pressure are generated, with localized temperatures as high as 300°C(see Figure 5.16). A more precise control over the drop size and and directionality can be instead obtained by exploiting the acoustic wave generated by a piezoelectric material when a specific voltage is applied [210]. In this way, precise bio-ink droplets can be deposited at regular intervals [210]. The ink suitable for inkjet bio-printers need necessarily to be in the liquid form, hence imposing a strict constraint on the physical properties of the materials that can be used as bio-inks.

A more versatile family of bioprinting techniques is indeed represented by the robotic dispensing extrusion systems. The robotic dispensing system is usually controlled by a software interface so that specific CAD-designed layouts and 3D geometries can be printed [210]. These systems are based on the controlled robotic extrusion of the bio-ink from a reservoir to a stage movable on the x, y ans z directions. Differently from laser-induced and inkjet printing, micro-extrusion lead to the deposition of a continuous filament of material rather then to single droplets (see Figure5.16). By moving the stage in the z direction, multi-layered 3D geometries can be obtained. The bio-ink extrusion can be induced by different methods like the use of pneumatic or mechanical dispensers [210]. Despite their simpler architecture, pneumatic dispensing systems, in which the extruding force is generated by an air-pressure variation, can lead to delays in the dispensed materials due to the dynamic of the compressed gas [207]. On the contrary, mechanical dispensing systems, although requiring slightly more complex setups, allow for a more precise control over the bio-ink deposition as well as improved spatial control [210]. They are usually identified by piston- or screw-based systems [207]. If compared with the other 2 bioprinting approaches previously described, micro-extrusion allows a very wide range of different materials to be deposited. Bio-inks with viscosities ranging from 1 mPa (very low) to $96 \cdot 10^4$ mPa (extremely high) viscosities can be printed, and, according to the chosen viscosity a multitude of nozzles diameters and flow rates can be then selected [216].

Depending on the requirements of the target application, the optimal bioprinting technique can be selected accordingly. As a rule of thumb, laser-induced bioprinting can be optimal in case high resolution is required, inkjet bioprinting for high-speed low-cost depositions while, micro-extrusion represent the best candidate for quickly

depositing thicker constructs belonging to a wide range of materials [211]. Moreover, the dynamic and multifaceted nature or biomimetic tissues and organs, with their intricated architecture, often demands for the combination and customization of different bioprinting approaches in one. In fact, as pointed out by Pati *et al.*, often a single bioprinting approach is not suitable enough to satisfy all the constraints of a specific target project hence pushing the ongoing and future research to develop new hybrid systems [207].

In the present work, due to its high versatility, system simplicity and bio-ink versatility, the piston-base extrusion-dispensing approach was selected. In Section 5.4.2, preliminary details about the bioprinting experimental setup optimized in the present work will be presented, while, the bioprinting experimental results will be detailed in Chapter 7.

5.4.2 Bioprinting: Experimental Setup

In the present Ph.D. work, the NovoGen MMX Bioprinter^{TM} (Organovo, San Diego, USA) was selected as extrusion bioprinter for the cardiomyocytes-powered soft actuator (see Figure 5.17). This was the first worldwide 3D bioprinter developed for production [219]. A recent partnership of Organovo with the French company L'Oreal was also recently announced for the bioprinting of tissues for animal-free cosmetic tests [220], therefore underlying the interest of 3D bioprinting also in the commercial/industrial framework.

As visible in Figure 5.17 a, the bioprinter is designed with two different printing nozzles one for hydrogels and the other for cell dispensing through a thin glass capillary (200 μm - 500 μm diameter) [221]. Therefore the system allows for the simultaneous bioprinting of hybrid cells/hydrogel constructs. A computer-controlled electronic arm is responsible of moving the nozzles in x, y and z directions ($\pm$ 10 μm repeatability), while, a laser system is responsible for their precise calibration and alignment. The working principle of the Organovo bioprinter is based on the aspiration of the bio-ink, either cells or hydrogels, from a heated reservoir into the glass capillary and on its subsequent dispensing on the desired substrate. Complex 3D geometries can be designed using CAD softwares and then adapted for the Organovo bioprinter, as it will be described later in this section.

Despite the great potentialities of the system for the creation of cell-laden hydrogel constructs, the large diameter of the capillary strongly limit the final resolution achievable during the printing process. For this reason, in the present work, the system was modified in order to dispense the bio-ink through custom-modified needles with inner diameters down to 110 μm. Only a single nozzle was used for each experiments to print only hydrogel substrates. More precisely a PHD 2000 programmable syringe pump (Harvard Apparatus, Holliston, USA) was used to

dispense, in a controlled way, the bio-ink from a common laboratory syringe on the desired substrate, usually a glass slide (see Figure 5.17, a-1 and b).

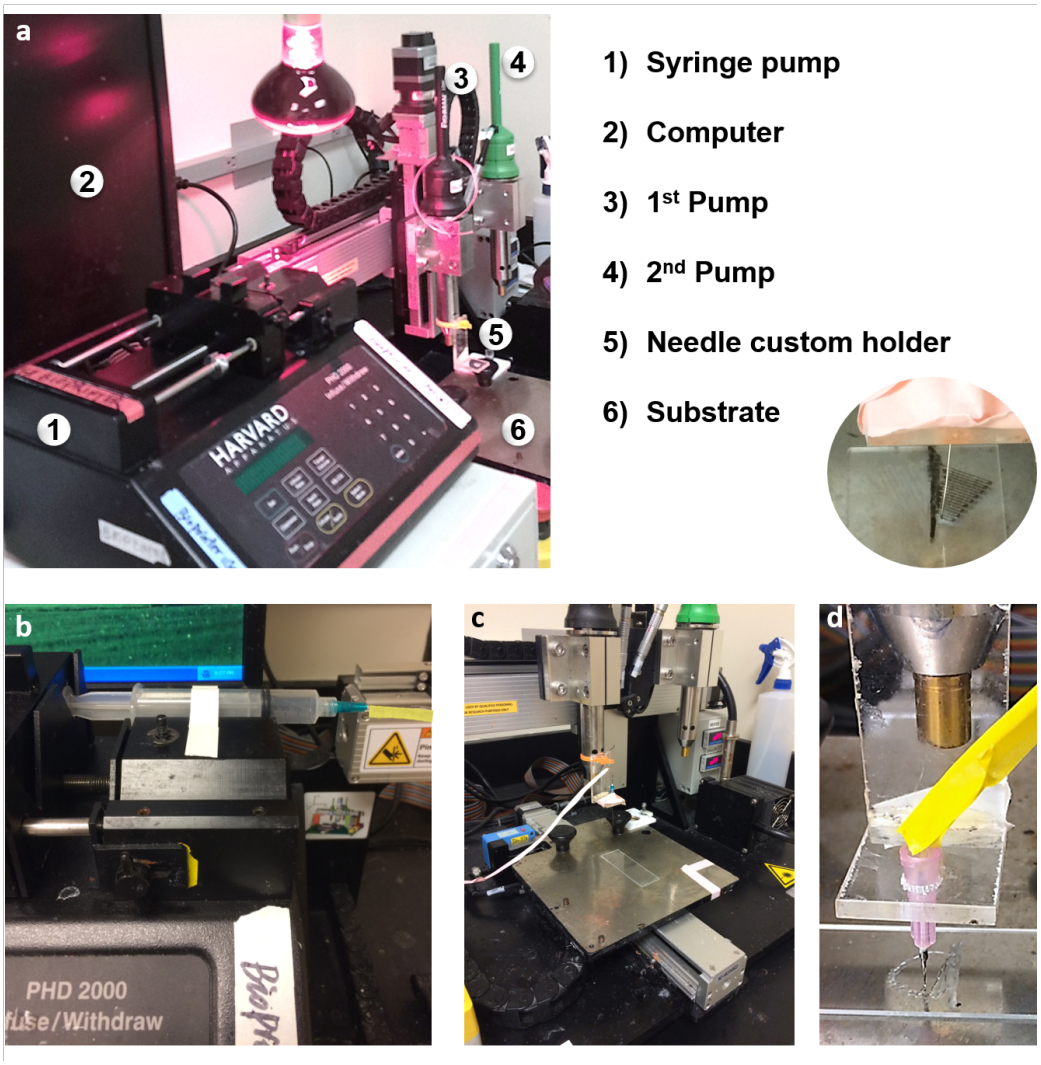

Fig. 5.17 Experimental setup for the bioprinting experiments. (a) The main components of the setup are: a syringe pump (1), a computer (2), 2 printing pumps with their relative nozzle (3 and 4), a customized needle holder where to position the custom adapted needle (5) and the holding substrate (6). (b) Detail of the syringe pump with mounted syringe acting as ink reservoir and flushing system. (c) Example of a bioprinting experiment where one pump (the black one) of the bioprinter is used for printing after mounting the custom dispensing needle on the modified holder (d).

As visible in Figure 5.17 b and c, the syringe was connected using a common Tygon® tubing to the custom-modified dispensing needle previously fixed on a custom-fabricated PMMA holder (Figure 5.17 a-5 and d) secured on the electronic

arm of the bioprinter holding the nozzle. The connection tubing was further wrapped with some opaque tape, in order to prevent any ambient light unwanted bio-ink cross-linking, even minimal, due to the presence of the photoinitiator. In this way, by correctly calibrating the bioprinter for the new customized dispenser it was possible to exploit the precise 3D motion capabilities of the Organovo bioprinter to print fine hydrogel structures thanks to the reduced diameter of the personalized dispensing needles.

The personalized dispensing needles are fabricated starting from four types of common laboratory syringe needles with different diameters (see Figure 5.18, a). The two bigger needles, gauge 18 (G18) and gauge 23 (G23), have inner diameters (ID) of 0.84 mm and 0.34 mm, respectively. They are principally used for the interconnection with the tubing system, G23, and as holders, G18. It is important to remember that increasing gauge numbers corresponds to needles with decreasing ID. The two smaller needles, instead, gauge 30 (G30) and gauge 32 (G32), have inner diameters (ID) of 0.16 mm and 0.11 mm, respectively, and are therefore used as dispensing needles. As visible from Figure 5.18, the metal needles tips where cut so that the ending part became blunt (if not already as in case of the G32 needles). This step, not only reduced the risk of creating holes, i.e., leakages, in the connecting tube during the insertion, but also, it improved the quality of the final bioprinted line, due to a more homogeneous ink dispensing, thanks to the planar (and not tilted) interface. In Figure 5.17 are reported two examples of the modified needles directly mounted on the bioprinter using either the G30 dispensing needle (longer needle tip, Figure 5.17, a inset) or the G32 (shorter needle tip, Figure 5.17, d).

As visible in Figure 5.18 b, in order to connect the dispensing needle to the tubing, the plastic connector of the G30 or G32 dispensing needles are fused together with the plastic connector of the G23 interconnecting needle using fire to achieve a leak-proof sealing. To further prevent any leakage, a small piece of parafilm was also wrapped around the connection. An example of this type of needles, where a G32 needles was selected for the dispensing part, can be seen in Figure 5.18 b (left, "old layout") and in Figure 5.17 a and c. Although this system worked correctly, often, the ink resulted blocked in the connecting chamber probably due to the partial cross-linking of the bio-ink or due to residues from previous bioprinting experiments that was not possible to completely remove during the final cleaning step (performed by flushing warm deionized water). For this reason, a new layout was developed (Figure 5.18, right, "new layout" and Figure 5.17 d) in which the interconnecting chamber was removed. In this case, a G18 needle was used as principal support (after being blunted) then, the tip of a G23 intermediate was not only blunted, but also cut from the plastic connector so to obtain only an hollow metal tube. This tube was glued to the connecting tube (using common super glue), on one side and, then inserted inside the G18 needle and glued to it (see the schematics of Figure 5.18 b, right). At last, the dispensing needle was also cut from the plastic connector

and glued inside the G23 intermediate needle. In this way, less obstructions of the ink during the printing process were observed.Moreover less ink was wasted due to the absence of the connection chamber that needed to be completely filled with ink before the bioprinting process could start and that was never completely cleaned after the bioprinting process due to the difficult accessibility.

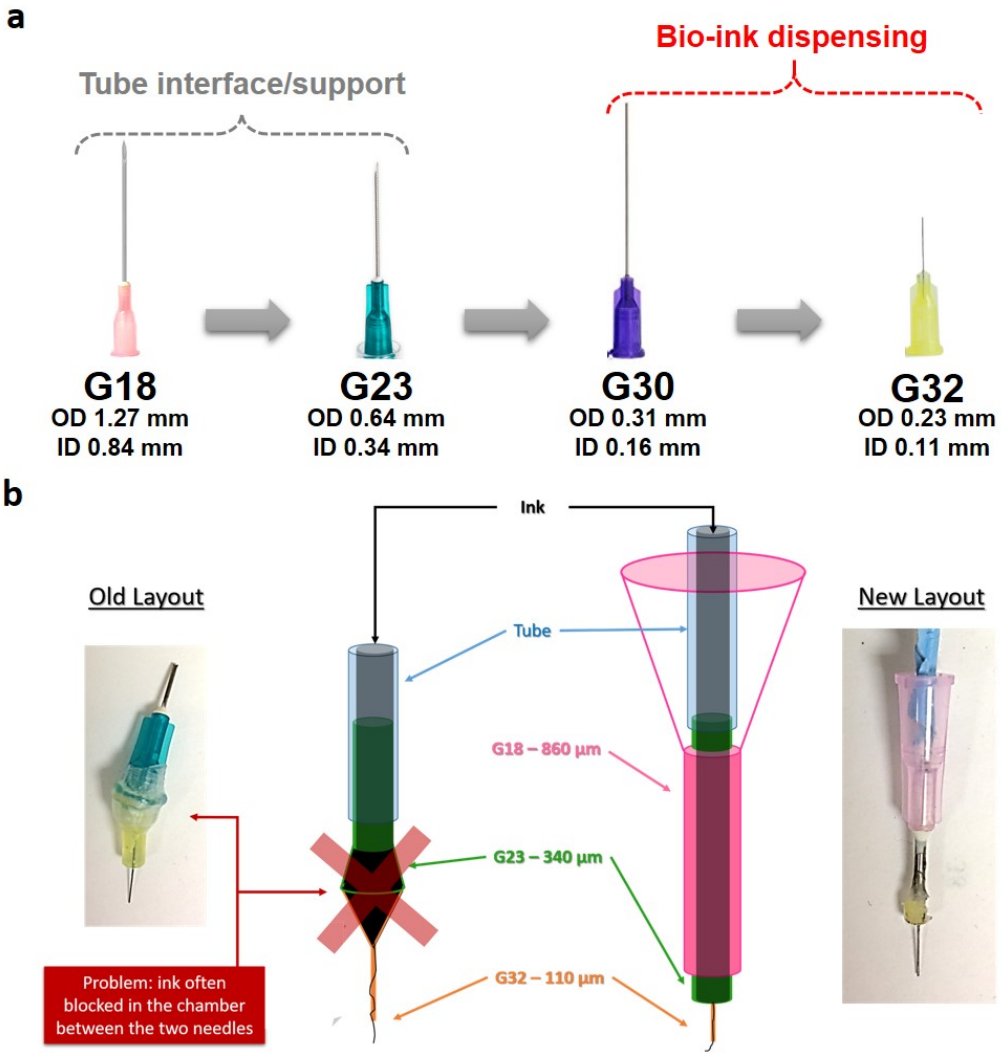

Fig. 5.18 (a) Different needles used during the bioprinting process with inner diameter randing from 0.84 mm to 0.11 mm. (b) Two different approaches used for the customization of the needles for the bioprinting process.

Before proceeding to the next section, where the design of the wireless stimulating system will be briefly presented (Section 5.4.3), a small introduction the implementation of the bioprinting code will be given. The software of the bioprinter requires text files as inputs, with the customized *.3DScpt* extension, where the instruc-

tions for each single nozzle movement are indicated step by step. Specifically, the software of the Organovo bioprinter requires a specific format in which successive movements of the nozzle, in the x, y or z directions, are mapped into distances from the previous point coordinates. One example of the bioprinting code instruction responsible for the nozzle movement is reported in:

$$Instrument.DispenseCellLine(v, \Delta x, \Delta y, \Delta z) \tag{5.1}$$

where v is the nozzle motion speed, and Δ x, Δ y and Δ z represent the distances to be covered in the x, y and z direction, respectively. Usually, in the present work, the speed and the distance in the z direction are kept constant, so that uniform hydrogel constructs can be deposited, layer by layer. According to the presented coding approach, an individual line of code must me specified for each single bioprinted line. This work can become extremely time-consuming in case of complex geometries with numerous points, especially in case of curved features, which require the successive printing of multiple straight segments. Therefore, a semi-automated approach has been developed in the present work in order to solve this problem. As outlined in the flow chart of Figure 5.19, at first, the desired geometry is designed using a CAD tool. In the present work, the open-source Blender software was chosen, but also other software like SolidWorks or AutoCAD can be selected.

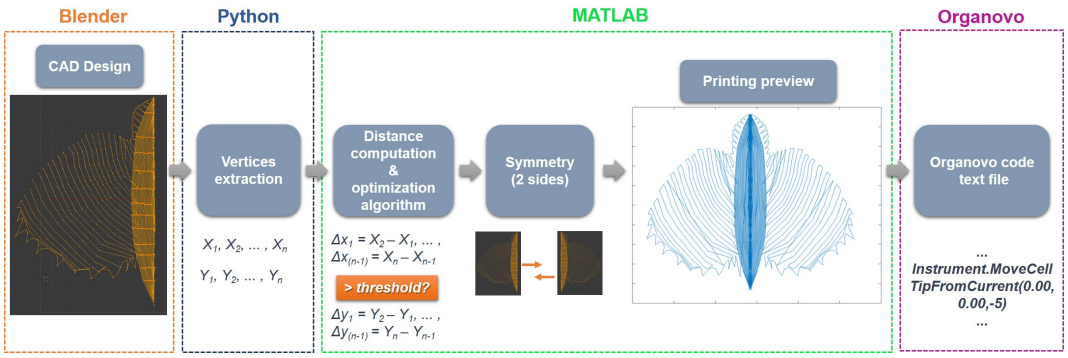

Fig. 5.19 Flow chart of the method developed to design, optimize and create the bioprinting code for the Organovo Bioprinter. At first, the desired geometry is designed with the Blender CAD software (only one side in case of symmetric layouts). Then, the vertices are extracted using a Python script and imported in MATLAB where the distances between successive points are computed and optimized. Then, after duplicating the computed distances along the vertical symmetry axes, a drawing simulating the bioprinting process is plotted. At last, the calculated distances are translated into Organovo code.

Usually, symmetric geometries were adopted in the present work, therefore allowing the CAD design of only half pf the desired structure. Afterwards, a text file with all the vertices forming the designed geometry was extracted by means of a customized Python script. It is important to consider that, since the Organovo

bioprinting process is based on the extrusion of a continuous ink filament, the extracted vertices must be in successive spatial order so that no unwanted jumps can create extra line connections during the bioprinting process, which would alter the final shape. This must be kept in mind at the very initial stage of the Blender geometry definition.

The generated text file was then imported in the MATLAB software where the distances between successive points were computed. During the numerous experiments performed, it was found out that if the distance between two successive points (connected by a oblique line and not just by a vertical/horizontal segment, with reference to the bioprinter axes) was ≤ 0.3 mm, a code error was generated by the bioprinter software during the bioprinting step. Therefore, a "code optimization" algorithm so that, if any segment was smaller than the critical distance, a small increment was sequentially added to the distance until the dimensional constraint was satisfied. Usually, the increment, being of the order of 10^{-2} mm was optically imperceptible, hence not affecting the final layout (usually in the cm scale). This was also possible thanks to the fact that 3 different increments where added depending on the mutual dimensional relationship between the Δ x and the Δ y, so that the correct proportionality of the geometry was maintained.

After this step, a single vector containing all the computed sequential distances in mm forming the final layout was obtained. By computing the symmetrical vector according to the x axis, and adjusting the offset, the missing symmetrical part of the geometry was computed and then, the final layout was graphically plotted in order to have a preview of the final printed construct, before starting the actual bioprinting experiments (see Figure 5.19). This step is fundamental not only to understand how the designed CAD geometry will be interpreted by the Organovo bioprinter but, also, to check if the distance optimization algorithm did introduced any unwanted geometrical modification. This step was essential in order to save time during the effective bioprinting experiments. In fact, when new geometries were printed for the first time, after connecting all the system components and preparing and loading all the necessary bio-inks (especially in case of complex fish-like shapes like the one reported as example in Figure 5.19), it was extremely easy to run up against distance errors or against a mistaken geometrical interpretation of the layout when moving from vertices to distances.

At last, all the optimized distances are inserted in a text file, directly printed by the MATLAB software, according to the syntax of the Organovo software. In Chapter 7 the experimental results obtained using the Organovo bioprinter will be presented in details. These results represent a preliminary proof-of-concept about the possibility of using bio-printing techniques to develop cm-scale soft-actuators, embedding also μm-scale functional features to enhance the bio-activity of cardiac cells cultured on their surface.

5.4.3 Towards Wireless Electrical Stimulation

In this section is presented the preliminary version of a custom wireless powering and controlling system that is able to provide to the muscle actuator the required excitation waveform using magnetic induction coupling. Since, as already anticipated in this Chapter, the electronic system was developed during Ph.D. activity of L. Pirrami (University of Applied Sciences and Arts Western Switzerland, Fribourg and Politecnico di Torino, Italy), the detailed description of the design and fabrication of the wireless-stimulating system is beyond the aim of this thesis. Instead, after a general high-level overview of the system, more focus will be given to the biodegradation and biocompatibility tests of the presented system, directly performed by the author at the Khademhosseini Laboratory in Boston.

A radio-frequency (RF) circuit was design in order to wireless transmit the voltage signal from a custom-designed excitation coil, connected to the waveform generator and directly printed on a Petri dish (see Figure 5.20, b), to the receiving coil directly embedded in the hydrogel-based actuator and capable to provide the required voltage to excite the soft robot through encapsulated microelectrodes. RF stimulation of living tissues, exploiting the phenomenon of electromagnetic induction, was already reported in the literature since early 1900s, to remotely modulate and control the stimulation not only of the heart but also of other organs like the bladder or nerves t[222]. The great advantages of this approach are not only related to the possibility of modulating the excitation of physiological electrical signals with a control external from the human body, but, also, to its simple operation as well as the possibility to modify/stop the excitation without any need of modifying the implant *in vivo* [222].

All the components of the wireless power and control system embedded in the muscle actuator were fabricated through ink-jet printing on a flexible polyethylene naphthalate (PEN) polymeric substrate in order not to impede the contraction of cardiomyocytes seeded on the surface i.e., the actuation dynamics. A conductive ink, formed by single-crystal silver nanoparticles dispersed in ethylene glycol, was chosen to fabricate the conductive components ($\sim$ 100 nm diameter, Sicrys^{TM} I30EG-1, Pvnanocell, Israel). More in details, the first prototype of the bio-actuator RF stimulating system was created by the superposition of three different functional layers on top of a flexible 50 μm PEN substrate (see Figure 5.20, a). The topmost layer was constituted by the excitation electrodes, which being in direct contact with the printed construct, are expected to be the main responsible for the transmission of the excitation signal to the bio-actuator (see Figure 5.20, a). The electrodes layout was designed to be compatible with the fish-like shape of the printed construct. A diagonal wider electrode was expected to be responsible for the excitation of the thicker fish body, while, serpentine-like thinner electrodes were associated with the stimulation of the fins of the bioprinted fish. The serpentine-like designed was

selected according to the improved dissipation of the physical stress of the metal electrodes during the beating actuation dynamics as previously studied in [1] and in [202].

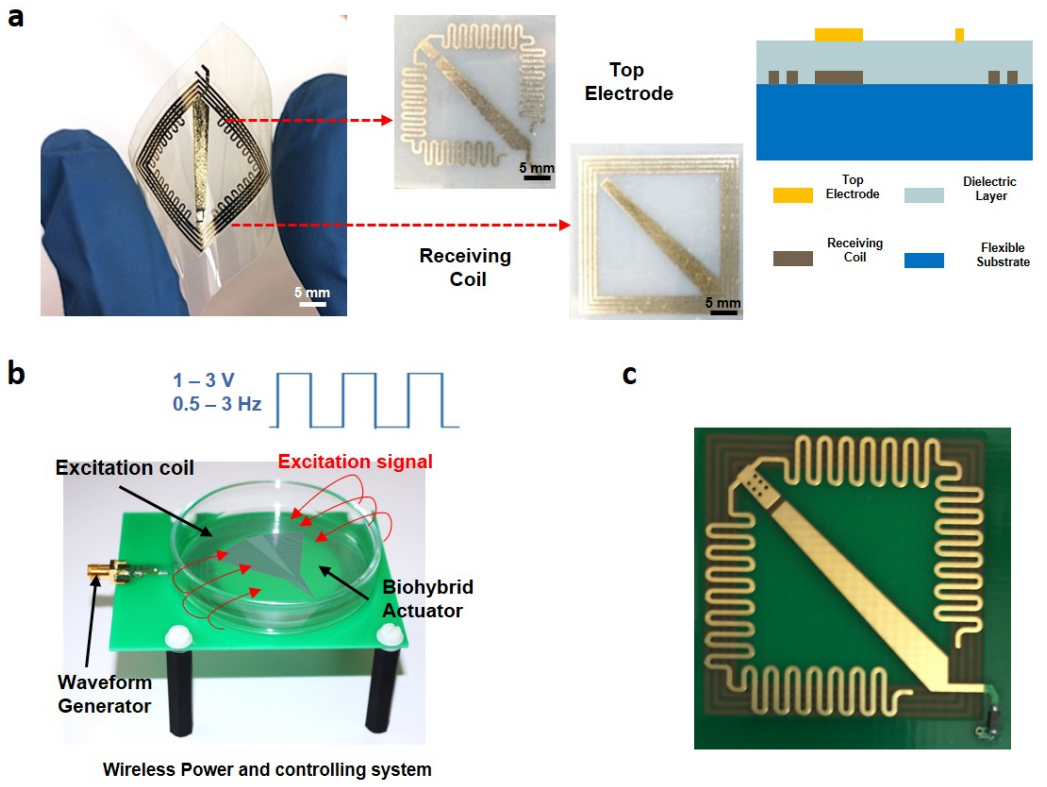

Fig. 5.20 Bio-hybrid actuator preliminary wireless stimulating system. (a) Complete electrodes system with the stimulating electrodes, receiving coil and dielectric layer on the PEN flexible substrate. (b) Schematics of the working principle of the wireless induction-based stimulation of the bioactuator. (c) Test structure of the complete wireless electrodes system on a standard PCB.

An intermediate dielectric layer was ink-jet printed using a dielectric SiO_2 nanoparticles-based ink (InkA-I220, Politronica, Italy) between the top electrode and the receiving coil. The receiving coil, ink-jet printed with the silver nanoparticle-based ink on the bottom conductive layer, was in charge of receiving the stimulation signal transmitted through the excitation coil. The overall concept of the wireless RF stimulating system is outlined in Figure 5.20, b. At first, a common laboratory waveform generator, needs to be connected to the PCB embedding the excitation coil. Then, thanks to inductive coupling between the excitation and receiving coils the excitation signal can be transmitted to the stimulating electrodes embedded in the bioprinted construct directly immersed in cell culture medium inside the Petri dish (see outline in Figure 5.20, b).

During the present work, the very first prototypes of the described wireless stimulating system were tested for biodegradation in cell culture conditions and for cellular biocompatibility. Due to the fixed amount of time spent at the Khademhosseini laboratory, where this work was performed by the author, and due to technical delays of the ink-jet printing electrodes, it was not possible to test the complete wireless stimulating system on the flexible electrodes (see also Chapter 7 for further discussion). Nevertheless, a brief verification of the correct RF transmission of the electrical signals was performed on a test system, with exactly the same layout of the flexible one, but, fabricated on a standard PCB (Figure 5.20 c).

In Chapter 7, the preliminary results obtained by the author regarding the biocompatibility and cytotoxicity of the presented wireless stimulating system will be presented.

Part II

Experimental Results and Data Analysis

Chapter 6

Electronic Sensing Platforms for Micro-Structures Electrical Characterization

Chapter Abstract *In Chapter 6 are presented the experimental results, obtained during the Ph.D. activity, about the integration of synthetic microstructures on electronic platforms for different sensing applications. The selected synthetic microstructures, and their fundamental physical/chemical properties were presented in Chapter 2, while, the passive and active electronic platformed in Chapter 3 and Chapter 4, respectively. The majority of this work was also published by the author in [2], [3] and in [4]. Specifically, the UV-Visible light sensing properties of ZnO microwires measured on passive electric platforms (Section 6.1) were published by the author in [2], while, the sensing of UV-visible light with also temperature and pH variations (Section 6.2) were published in [3]. At last, the sensing measurements, always of ZnO microwires, but on the active M4N chips (Section 6.4) were previously published in [4]. Therefore, different parts of the cited articles are verbatim quoted in this chapter with permission of the copyright holders (a starting and an ending footnote will be present at the beginning and at the end of the quoted sections, see Appendix A for the complete copyright rights and permissions).*

6.1 ZnO Microwires UV-Visible Light Sensing on Nanogap Chips

Part of the content of this sections was previously published by the author in: B. Miccoli, A. Bonanno, V. Cauda, A. Sanginario, D. Demarchi: "Interface of a single ZnO-Nanowire assembled onto custom-fabricated nanogap device for UV sensing applications", 2015 38th International Spring Seminar on Electronics Technology (ISSE), Eger (Hungary), pp. 431-435. ©2015 IEEE (see Appendix A for the copyright and permission).

In Chapter 2, the physical and chemical properties of ZnO microwires were presented. Focusing on the variation of the electrical properties of these microstructures, in response to a variation of an environmental parameter, such as UV-visible light, a UV-visible light sensor was fabricated using the nanogap chips and fabrication flow, exploiting the advantages of electromigration and dielectrophoresis, described in Chapter 3. [1] Thanks to the widespread sensing properties of ZnO microwires, the fabricated device can be used to monitor in real-time the UV-visible light. DC measurements have shown a Schottky-like I-V characteristic which varies depending on the UV light intensity. The AC analysis of the ZnO microwires electrical properties has also shown impedance variations proportional to the UV irradiance. In particular, the reported measurements show high sensitivity to low UV irradiance (below 1 mW/cm^2) translated to both resistive and capacitive variations. ZnO microwires have attracted high interest for sensing thanks to their capability to respond to a wide range of external stimuli such as variations of UV light [104, 106, 105], pH [59] or different gases [107, 223]. Considering especially their application as UV photodetectors, several approaches were used in the literature in order to study and characterize different aspects of the nanostructure toward the UV sensitivity [104, 106, 105, 224]. The junction created between ZnO microwires and the underling electrodes also plays a crucial role for the final sensor performances. Indeed, a Schottky contact is preferable to an Ohmic one with respect to the sensitivity, the reset time [225] and the response time [226].

In the present chapter we developed a low-cost, easy-to-fabricate and low noise electronic interface able to read-out the signal of a single ZnO microwire aligned through dielectrophoretic (DEP) force between two micrometric-spaced gold electrodes. This technique can be easily performed using a common waveform generator to apply the required AC signal which, once it reaches the electrodes, generates an alternate and non-uniform electric field able to attract the ZnO microwires to-

[1] Starting point of the verbatim quote from [2], see Appendix A for the complete copyright and permission file.

wards the integration area. This approach does not require additional metal contacts, hence leaving all the nanostructure surface available for sensing and preserving the Schottky behavior of the ZnO-microwires/gold junction. The ultimate goal is to exploit the UV sensing properties of a single ZnO microwire since that, thanks to a better crystal purity and higher surface-to-volume ratio, if compared to bulk materials, it can reduce carriers recombination problems leading to better sensor performances [227]. The electrical properties of the nanosensor under different UV light irradiances (from 0.14 mW/cm^2 to 2.63 W/cm^2) are studied both in the DC and the AC domains.[2]

6.1.1 Sensor Fabrication Process

In order to deposit the ZnO microwires, synthesized according to the procedure described in Chapter 2, across the nano/micro-metric spaced gap of the nanogap chips (see Chapter 3), 0.8 mg of ZnO powder were at first dispersed in 1 ml of isopropyl alcohol. Then, 10 μl of the prepared solution were dropped on the surface of the nanogap chips while applying the dielectrophoretic signal. The process can be easily monitored with a common reflection optical microscope (see Figure 3.7 and Figure 6.1 a).

[3]Positive DEP is obtained by applying a sinusoidal waveform at 1 MHz and 3 $V_{peak-peak}$ with zero offset.

6.1.2 Electrical Characterization

This section presents both DC and AC (from -1 V to 1 V and from 500 Hz to 10 kHz) characterization of the fabricated sensor performed employing respectively an Agilent B2912A femptoampere-meter and an Agilent 4294A Impedance Analyzer. The UV-visible illumination is instead tuned using a mercury-xenon lamp (Hamamatsu) whose optical fiber is set such that the radiation hits the chip surface perpendicularly. DC characterization of the single ZnO-NW UV sensor is carried out applying a DC voltage in the range from -1 V to 1 V and measuring the corresponding current flowing in the ZnO microwire/Gold junction. As it can be observed from Figure 6.1 b, a nonlinear I-V characteristic is obtained with a current in the range of hundreds of nA. Although the ZnO-NW is just deposited across the gold electrodes by DEP without any further anchoring or contact improvement, a definite Schottky junction is observed, in accordance from what expected from theory [228].

[2]Ending point of the verbatim quote from [2], see Appendix A for the complete copyright and permission file.

[3]Starting point of the verbatim quote from [2], see Appendix A for the complete copyright and permission file.

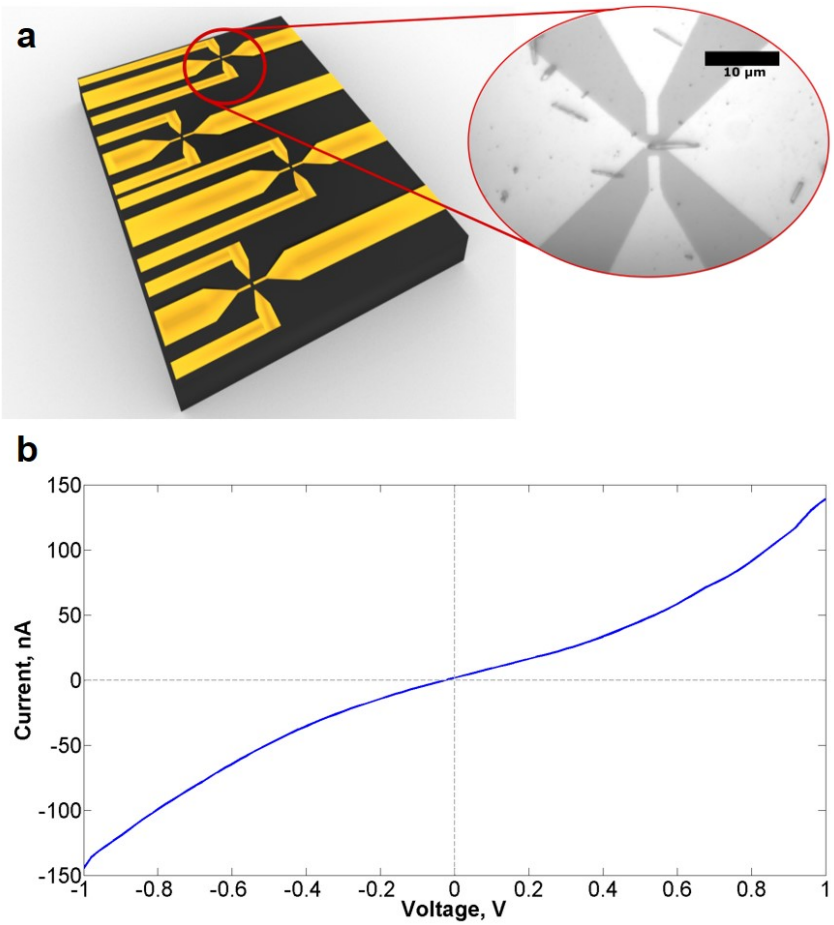

Fig. 6.1 (a) Schematic of the ZnO microwires-based UV photodetector on the nanogap chips. In the inset, a phase contrast image of a successful dielectrophoresis experiment is shown. (b) Example of a I-V curve measured on a single ZnO microwire/gold electrodes junction by a femptoampere-meter from -1 V to 1 V. (adapted with permission from [2], ©2015 IEEE).

When the chip is exposed to UV radiation of different intensities (from 0 up to 2.6 W/cm^2) a current increase is observed 6.2, a. The UV lamp radiation is composed by different wavelengths, with a Gaussian distribution peaking around 365 nm, which is close to the typical excitation wavelength range (325-350 nm) of ZnO [106]. The obtained results are in accordance with the literature [104]: the ZnO photosensitivity is attributed to the generation of electron-hole pairs due to incident photons. Negatively charged oxygen ions (O_2^-) are spontaneously adsorbed on the ZnO microwire surface and form a narrow depletion layer. Therefore the formed holes are trapped near the surface leading to a reduction of the depletion layer and to an increase of the number of electrons available for conduction. The higher is the UV radiation intensity and the more electron/hole pairs are generated leading to a current increase. A percentage increase up to 180% is observed for UV radiation of 2.63 W/cm^2, resulting in a maximum current of 377 nA.

AC analysis is performed studying the impedance variation, measured with an impedance analyzer, depending on the UV light irradiation. The chosen configuration on the instrument consists of a parallel between a resistor and a capacitor. This assumption is justified by the fact that a current is flowing in the DC regime and also that a frequency dependence is observed in the AC domain.

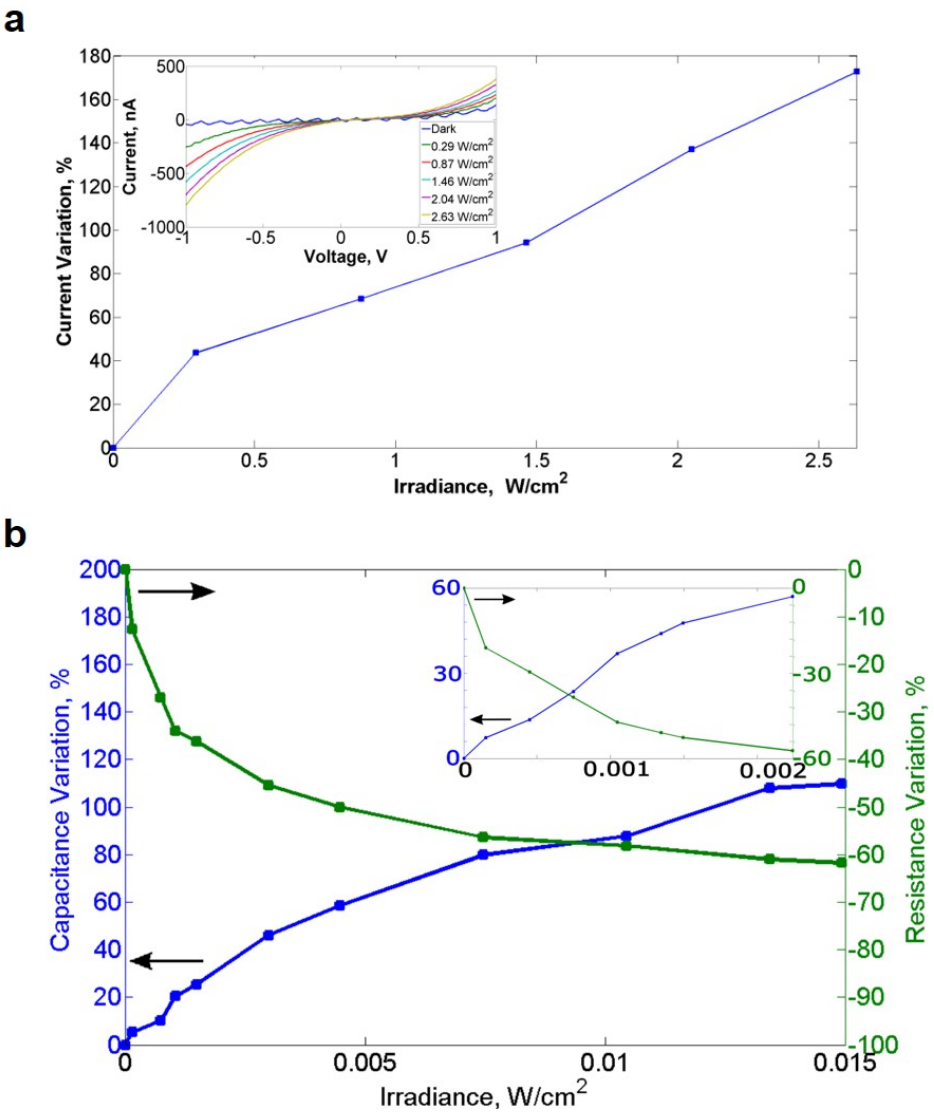

Fig. 6.2 (a) Microsensor current variation at 1V and I-V curves modification (inset) under UV light illumination from 0 to 2.5 W/cm^2. Current values are reported as a percentage variation from the starting one measured in dark condition. (b) Nanosensor capacitance and resistance percentage variations under different UV light intensities. The measurements are done at a fixed frequency of 1 KHz. The inset reports the same analysis on a different sample.(adapted with permission from [2], ©2015 IEEE).

According with the DC case, the measurements performed at fixed frequency of 1 kHz show a decrease of resistance correspondent to the increase of the UV light irradiance. At the same time, the percentage increase of capacitance is about 120 % (see Figure 6.2, b). Indeed, by varying the UV light irradiance from 0 to 0.015 W/cm^2, the measured resistance spans from 5 to 1.9 MΩ while the capacitance from 28.0 to 58.7 pF.

The AC analysis is performed in a lower irradiance range with respect to the DC measurements and it shows that the single ZnO microwire sensor is able to detect UV light radiation also for irradiance of 0.14 mW/cm^2. This UV irradiance range can be explored thanks to the choice of performing AC measurements at frequencies higher than 500 Hz, avoiding the influence of flicker noise (i.e., 1/f noise) present in the DC analysis. More in details, at 0.14 mW/cm^2 a resistance of 4.7 MΩ is detected, which corresponds to a resistance decrease of 12.6 % from the dark value. Similarly, at the same irradiance value, a capacitance of 29.46 pF is measured which corresponds to a 5 % increase. Comparing the results with the ones obtained from another chip, hence another NW-gold junction (inset of Figure 6.1, b), it can be noticed that under 2 mW/cm^2 both devices show a resistance decrease around 60%. This is highly relevant for measurement reproducibility since the same percentage variation is obtained for the same illumination condition onto two different devices. Monitoring the resistance and capacitance variations with time under different UV-visible light irradiances, it is possible to observe the nanosensor dynamics. It can be noticed that each irradiation condition is clearly recognizable being characterized by a step in the measured curves (Figure 6.3). The lower the frequency, the higher the capacitance difference between two subsequent illumination steps, suggesting better sensing performances at lower frequencies. The resistance/capacitance value on the way back is almost the same to the forward one validating the sensing capability of the ZnO-NW to measure the same quantity in two different times giving back the same result. The sharp capacitance changes between two different illumination conditions suggest that the response time of the nanosensor is less than 1 s. It can be noticed that, in contrast to what happens for capacitance measurements, the resistance drastically changes between dark and 1.5 mW/cm^2 irradiance whereas, at higher irradiance conditions, it is easier to resolve capacitance variations than resistance ones. All the measurements collected using different ZnO microwires are useful to characterize the UV nanosensor as much independent as possible from fabrication process variations. Indeed, all the synthesized ZnO microwires cannot have exactly the same size, leading to slightly different resistance and capacitance values. In addition, since each microwire deposited through DEP forms a peculiar contact with the underlying electrodes, an eventual tilting or rotation should not interfere with the sensing measurements. Interestingly, we have demonstrated in this work that sensing measurements acquired from different chips and from different ZnO-gold interfaces produce similar variations of electrical parameters.

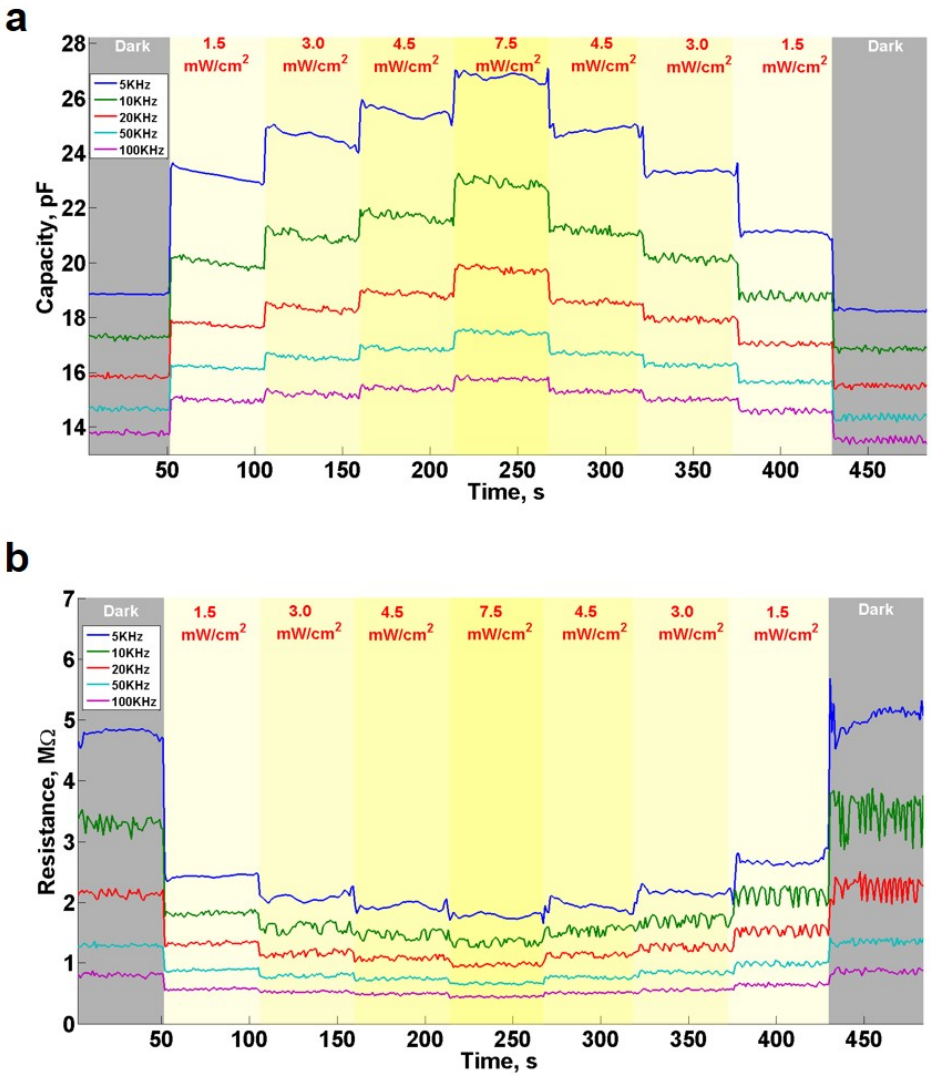

Fig. 6.3 (a) Capacitance behavior versus time at five different AC frequencies under different UV-light irradiations from 1.5 mW/cm^2 to 7.5 mW/cm^2.(b) Resistance behavior versus time at five different AC frequencies under different UV-light irradiations from 1.5 mW/cm^2 to 7.5 mW/cm^2. (adapted with permission from [2], ©2015 IEEE).

6.1.3 Conclusions

The presented work proposes the fabrication and electrical characterization, both in AC and DC domains, of a single ZnO-NW deposited between a pair of gold electrodes under varying UV-light irradiation. Thanks to EIBJ and DEP approaches, a low-cost and easy-to-fabricate nanosensor is obtained with UV response time of less than 1 s and UV sensitivity up to 0.14 mW/cm^2.

The DC characterization is performed at higher UV irradiance values to avoid measurement noise due to flicker effect (i.e., 1/f noise). The AC measurements are thus performed at frequencies higher than 500 Hz enabling higher accuracy at lower UV irradiance. The reported results based on different samples show high measurements reproducibility, which is a key-point in NW-based sensors. Moreover, thanks to the absence of additional metal contacts at ZnO microwires ends, the supporting electrodes can be easily reused for successive analysis since that the deposited ZnO microwires can be efficiently removed by an isopropanol ultrasonic bath. Thanks to the low-cost assembly process, the proposed nanowire-on-nanogap-based UV sensor can be considered as a preliminary step to characterize nanomaterials before assembling them onto CMOS technology (see Section 6.4) not only for noise and interference reduction but also for performing more complex types of analysis. [4] Therefore, in the next Section (Section 6.2), not only a mathematical model of the ZnO microwire/gold junction sensing capabilities will be developed, but, also, the simultaneous sensing of UV-visible light, pH and temperature will be discussed.

6.2 ZnO Microwires Multi-Parametric Sensing of UV-Visible Light, Temperature and pH on Nanogap Chips

Part of the content of this sections was previously published by the author in: B. Miccoli, V. Cauda, A. Bonanno, A. Sanginario, K. Bejtka, F. Bella, M. Fontana: "One-Dimensional ZnO/Gold junction for Simultaneous and Versatile Multisensing Measurements", Scientific Reports, vol. 6, Pages 29763, 2016. Licensed under a CC-BY 4.0 license (see Appendix A for the copyright and permission).

As demonstrated in Section 6.1, the Schottky junction formed between the ZnO microwires and the gold microelectrodes of the nanogap chip can be used as an effective photodetector for UV-visible light variations. In this section, after recalling and presenting further details about the basic chip structure and UV-visible light sensing, the multi-parameter sensing of UV-visible light combined with also pH and temperature measurements will be deeply discussed. Specifically, [5] The sensing capabilities of zinc oxide nano/micro-structures have been widely investigated

[4] Ending point of the verbatim quote from [2], see Appendix A for the complete copyright and permission file.

[5] Starting point of the verbatim quote from [3], see Appendix A for the complete copyright and permission file.

and these structures are frequently used in the fabrication of cutting-edge sensors. However, to date, little attention has been paid to the multi-sensing abilities of this material. In this work, we present an efficient multisensor based on a single zinc oxide microwire/gold junction. The device is able to detect in real time three different stimuli, UV-VIS light, temperature and pH variations. This is thanks to three properties of zinc oxide its photoconductive response, pyroelectricity and surface functionalization with amino-propyl groups, respectively. The three stimuli can be detected either simultaneously or in a sequence/random order (see Figure 6.4). A specific mathematical tool was also developed, together with a design of experiments (DoE), to predict the performances of the sensor. Our micro-device allows reliable and versatile real-time measurements of UV-VIS light, temperature and pH variations. Therefore, it shows great potential for use in the field of sensing for living cell cultures.

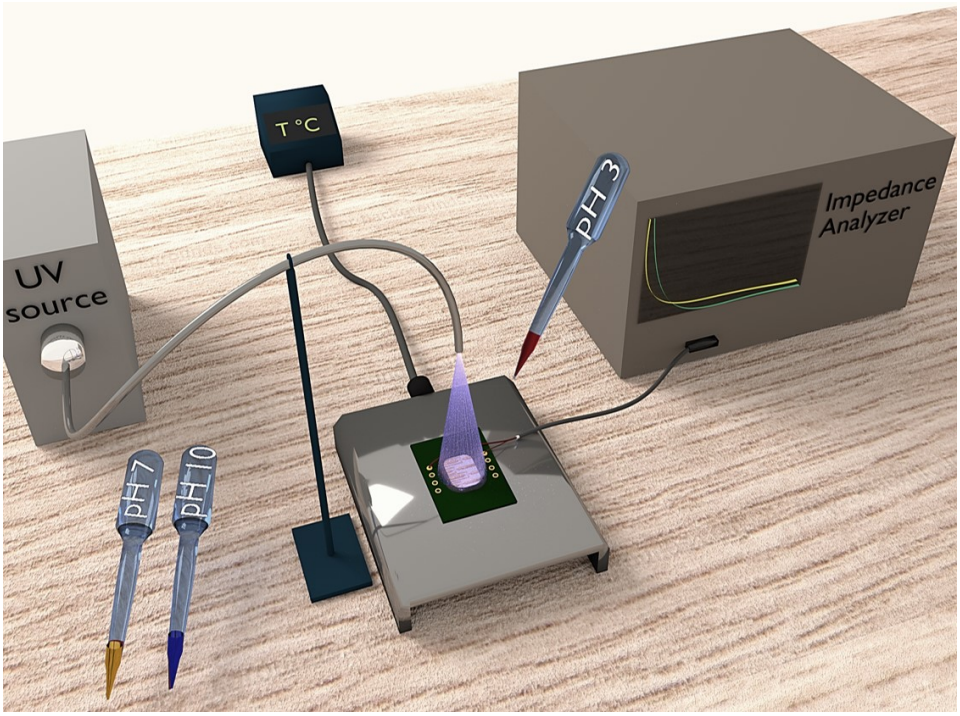

Fig. 6.4 Schematic overview of the experimental setup used for the multi-parametric sensing on the ZnO microwire/gold junction. (Reproduced from [3],licensed under a CC-BY 4.0 license).

Currently, most of the literature focuses on arrays of ZnO nanostructures and it reports mainly on their light and gas sensing properties [229, 230]. Although few papers present the electrical dependence of ZnO on pH and temperature [61, 224], Menzel et al. [231] showed the measurement of UV, pH and temperature stimuli using arrays of vertically aligned nanowires. These measurements were not carried out

simultaneously in one single experiment. By contrast, our innovative work focused on exploiting the multisensing behavior of a single ZnO μ-wire under ultraviolet-visible (UV-VIS) light, and at specific temperatures and pH values, within the same experiment. In particular, the stimuli-responsive measurements of these three parameters were taken both simultaneously and in a random sequence on the same chip. Embedding this multisensor in living cell culture microenvironments could allow the precise monitoring of the three aforementioned parameters, which are crucial for cell life. Variations in pH are strongly related to enzyme activity and localization, as well as taking part in the process of ATP synthesis [232].Temperature directly affects the molecular architecture and mechanical properties of cells. Moreover, the cellular membrane permeability strongly depends on temperature, making this parameter of crucial importance for the study of intra/extra-cellular therapeutic treatments [233]. Finally, the tuning and monitoring of UV radiation directly impact on cell survival and they are of extreme importance in different processes of microorganism disinfection [234].

6.2.1 Multi-parametric Sensor Assembling and Electrical Characterization

One drop of amino-functionalized ZnO μ-wires in isopropyl alcohol (0.8 $mg \cdot mL^{-1}$) was dispensed on the chip. Dielectrophoresis was carried out at 1 MHz AC signal and 3 $V_{peak-peak}$(sinusoidal waveform, offset 0 V) until the complete evaporation of the solvent. Once the individual ZnO μ-wires were aligned on each gold-electrode pair, forming a ZnO/gold junction, the electrical characterization in DC returned in all cases a non-linear I-V characteristic (Figure 6.1, b), i.e. a Schottky behavior with currents of hundreds of nA or few μA, as previously reported [59] (further details about the created Schottky junction will be given in Section 6.2.3).

The multisensing measurements under UV-VIS light, pH and temperature variations on the chip containing the ZnO/gold junctions were carried out using a custom-assembled setup in order to vary, individually or simultaneously, each stimulus (i.e. UV-VIS light, pH and T, see Figure 6.4). An opaque cage sheltered the assembled sensing device from environmental light. A medium-pressure mercury lamp (LC8 Lightingcure^{TM} by Hamamatsu supplied with 8 mm light guide) tuned the UV-VIS illumination. The chip responsivity to different pH values was tested by spilling distinct drops (10 μl each) on the chip surface, then drying under nitrogen flux after few tenths of seconds. Hydrochloric acid (HCl) with molarities in the range 10 μM - 10 mM was used for acidic pH experiments (from pH 2 to 5), while sodium hydroxide (NaOH) with molarities between 10 μM - 100 mM was chosen for the alkaline ones (from pH 9 to 13). The device was furthermore positioned on an heating plate and connected to a thermocouple with instantDAQ technology (National Instruments USB-TC01) to perform real-time temperature analysis. The

DC electrical characterization was performed through a precision source/meter unit (B2912A by Keysight Technologies) in the voltage range between -1 and +1 V. A precision impedance analyzer (4294a by Keysight Technologies) was instead used for the AC characterization in the frequency range 5 kHz - 100 kHz. Both the instruments were interfaced with a computer using LabVIEW software for customized measurements acquisition.

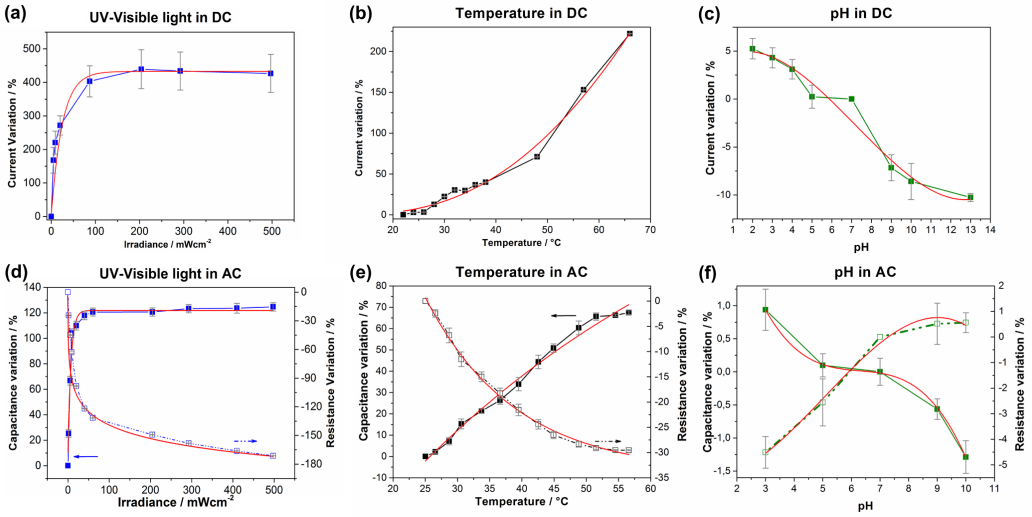

Fig. 6.5 DC and AC electrical characterization of individual stimuli. The electrical behavior of the ZnO/gold junction measured under (a,d) UV-VIS irradiation, (b,e) temperature and (c,f) pH variations. Top graphs are obtained in DC domain, measuring the current % variation with respect to the starting conditions at 1 V. Bottom graphs are AC measurements with capacitance (left y-axis) and resistance (right y-axis) % variations obtained at a fixed frequency of 5 kHz. Standard deviation bars are also reported for each data set. The experimental data (lines with symbol) are fitted by the red curves. (Reproduced from [3],licensed under a CC-BY 4.0 license).

AC measurements were performed with a precision impedance analyzer (4294a by Keysight Technologies, USA) from 5 to 100 kHz and assuming that each ZnO/gold junction had a capacitor and a resistor in parallel [224]. To properly interpret the sensing measurement results, the influence of three different parameters (UV-VIS light, temperature and pH) were initially evaluated separately on single ZnO/gold junctions, both with DC and AC analyses (Figure 6.5).

Control experiments, for each external stimulus, when no ZnO μ-wire was bridging the gold electrodes, are reported in Figure 6.6. For an effective comparison of the results and further modeling, the electrical values in Figure 6.5 are reported as a percentage of the initial value (i.e., dark condition, 25 °C and pH 7).

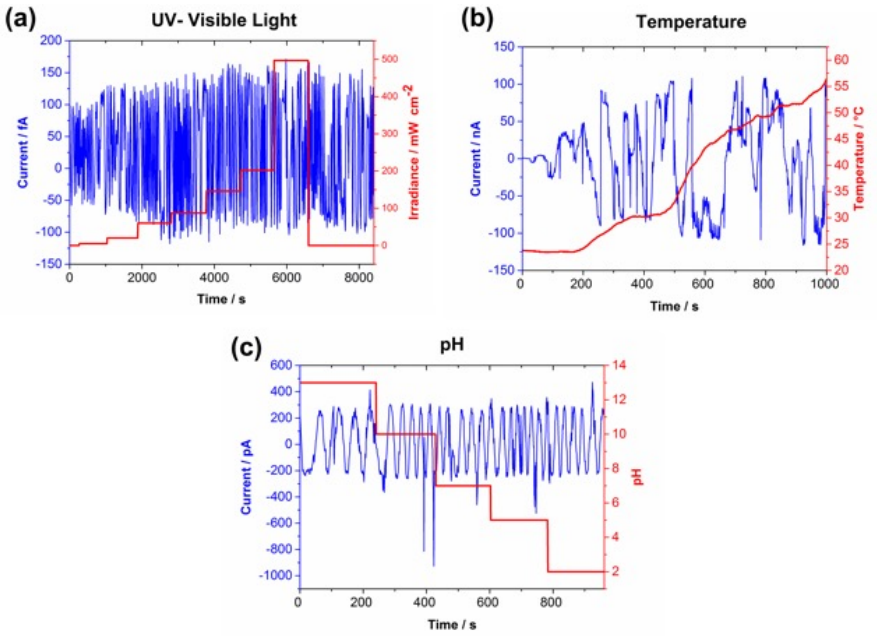

Fig. 6.6 Control Measurements. One couple of gold electrodes, with no ZnO μ-wire bridging them, is electrically characterized upon external variations of UV-Visible light, temperature and pH (red curves). The applied voltage is 1 V. As expected, just noise is measured (blue curves), since an open circuit condition is present, and no fluctuations correlated to the variation of the external stimuli are registered.(Reproduced from [3],licensed under a CC-BY 4.0 license).

The absolute values of current, capacitance and resistance are shown in Figures 6.7, 6.8, 6.9 and 6.10. Specifically, the DC electrical behavior of the ZnO/gold junctions measured under UV-visible light irradiation (Figure 6.7, a), temperature (Figure 6.7, b), and pH variations (Figure 6.7, c). The three graphs are obtained in DC domain, measuring the current at 1 V. The sensor sensitivities, for each of the three stimuli considered independently, are extracted from the slope of the line tangent to the experimental curves in specific ranges. For UV-visible light, temperature and pH external variations, the sensitivity exhibits a non linear characteristic identifying preferred experimental ranges of higher sensitivity. For UV-Visible light external variations (Figure 6.7, a), the sensitivity shows higher values for lower irradiance ($0.03\ \mu A \cdot mW^{-1} \cdot cm^2$ in the range 0-50 $mW \cdot cm^{-2}$ and $0.01\ \mu A \cdot mW^{-1} \cdot cm^2$ in the range 50-200 $mW \cdot cm^{-2}$), while it strongly decreases (up to $1.70 \cdot 10^{-4}\ \mu A \cdot mW^{-1} \cdot cm^2$) above $\sim$200 $mW \cdot cm^{-2}$. Temperature variations (Figure 6.7, b), instead, point out a sensitivity increase (from 0.10 $\mu A/°C$ to 0.33 $\mu A/°C$) for temperatures above $\sim$ 48 °C. Interestingly, pH changes, (Figure 6.7, c), show almost the same sensitivity, 4.50 $nA \cdot pH^{-1}$ and 4.17 $nA \cdot pH^{-1}$ in absolute value, for strong acid and basic pH, respectively.

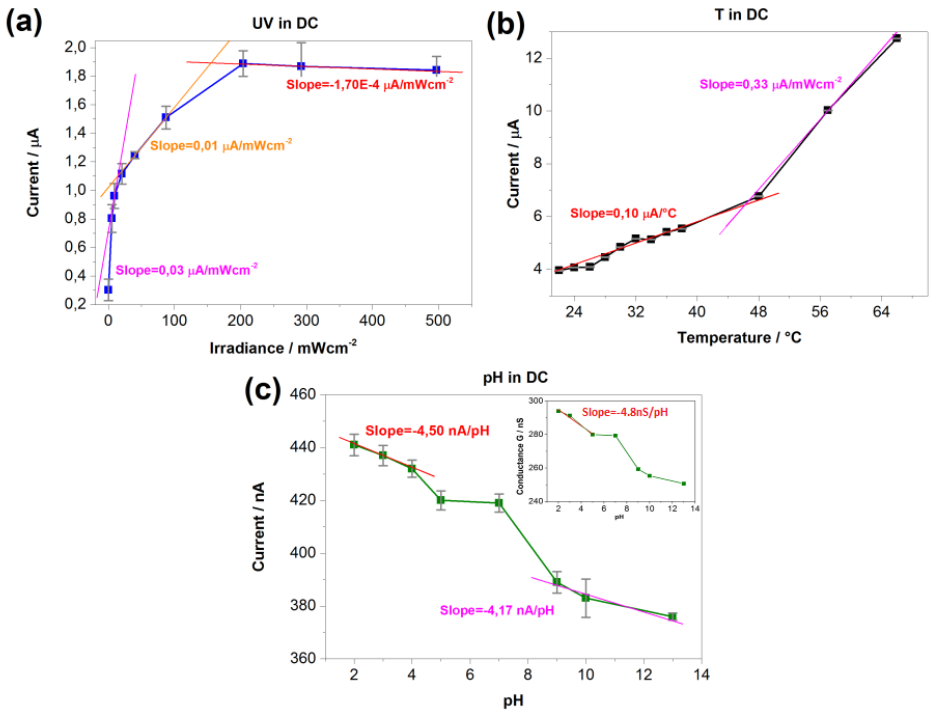

Fig. 6.7 The DC electrical behavior of the ZnO/gold junctions measured under (a) UV-visible light irradiation, (b) temperature, and (c) pH variations. The three graphs are obtained in DC domain, measuring the current at 1 V. The sensor sensitivities, for each of the three stimuli considered independently, are extracted from the slope of the line tangent to the experimental curves in specific ranges (Reproduced from [3],licensed under a CC-BY 4.0 license).

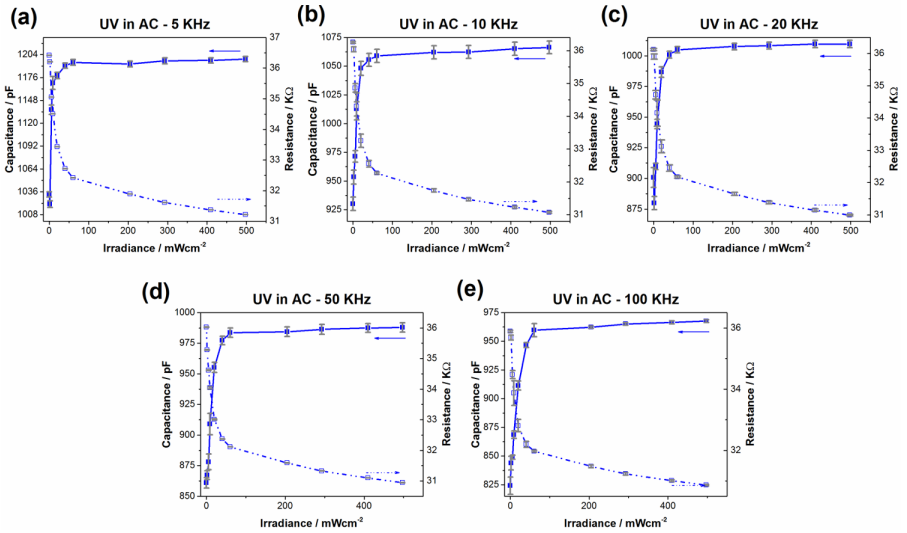

Fig. 6.8 AC electrical characterization varying UV-visible irradiation. The AC electrical behavior of ZnO/gold junctions measured under UV-visible light irradiation variation (capacitance is on the left y-axis and resistance on the right y-axis) obtained at frequencies of (a) 5 kHz, (b) 10 kHz, (c) 20 kHz, (d) 50 kHz and (e) 100 kHz (Reproduced from [3],licensed under a CC-BY 4.0 license).

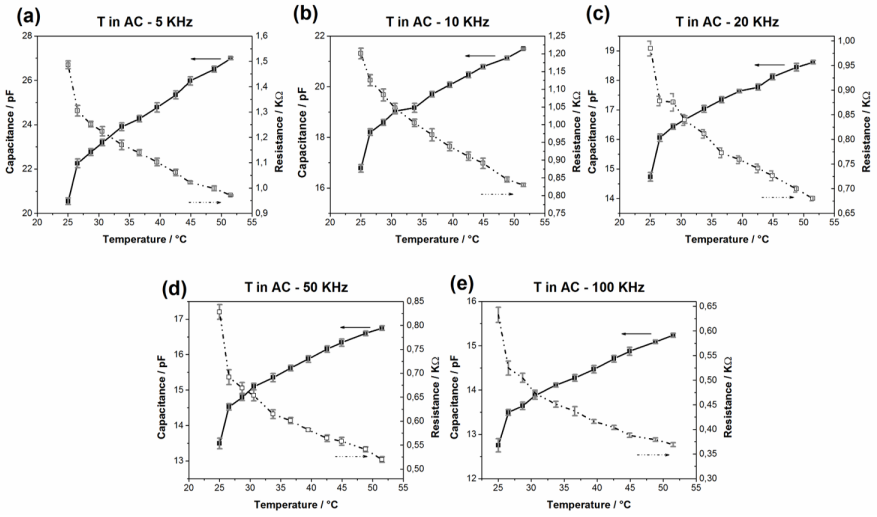

Fig. 6.9 AC electrical characterization varying UV-visible irradiation. The AC electrical behavior of the ZnO/gold junction measured under temperature variation. The graphs are AC measurements with capacitance (y-axis on the left) and resistance (y-axis on the right) values obtained at different frequencies of (a) 5 kHz, (b) 10 kHz, (c) 20 kHz, (d) 50 kHz and (e) 100 kHz (Reproduced from [3],licensed under a CC-BY 4.0 license).

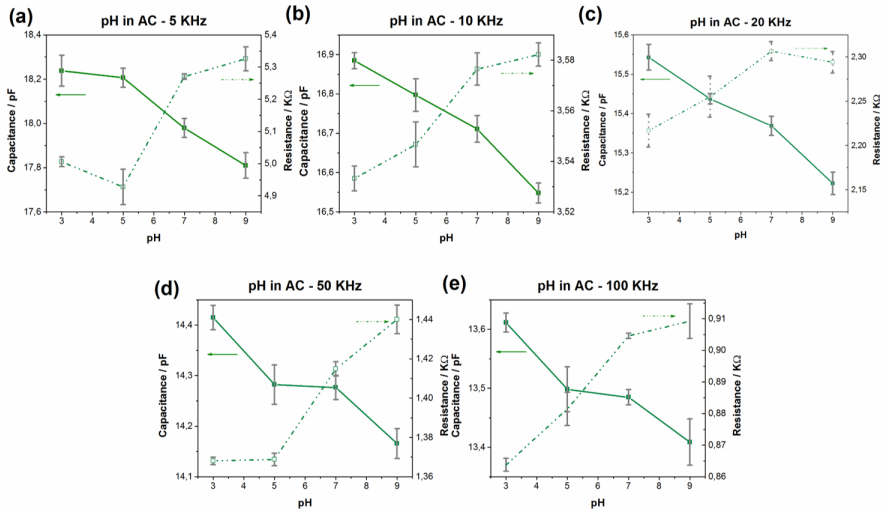

Fig. 6.10 The electrical behavior of the ZnO/gold junction measured under pH variation (capacitance is on the left y-axis and resistance on the right y-axis) at different frequencies (a) 5 kHz, (b) 10 kHz, (c) 20 kHz, (d) 50 kHz and (e) 100 kHz (Reproduced from [3],licensed under a CC-BY 4.0 license).

6.2.2 UV-VIS Light Characterization

The UV-VIS light incident perpendicularly on a single ZnO/gold junction abruptly increased the measured current from dark to light conditions. By varying the UV-VIS irradiation from 0 up to 450 $\text{mW} \cdot \text{cm}^{-2}$, at a fixed voltage of 1 V, the DC current increased to 450% of the reference value measured in the dark (Figure 6.5 a). A similar behavior was observed for the AC measurements under UV-VIS irradiation, in the frequency range 5-100 kHz. Specifically, the capacitance increased and the resistance decreased as outlined in Figure 6.5 d, which shows measurements at 5 kHz (the measurements at the remaining frequencies are reported in Figure 6.8). Small values of UV-VIS irradiance can be discerned (down to 0.1 $\text{mW} \cdot \text{cm}^{-2}$) thanks to the selected frequency range within which the measurements are not affected by Flicker noise (1/f noise). Flicker noise afflicts electronic devices and materials at low frequencies, but it can be significantly reduced by performing measurements at high frequencies. In contrast, DC measurements are at low frequency and hence suffer from higher noise and are only reliable for higher irradiance values. UV-VIS light on/off cycles were carried out to further assess the photo-response of a single ZnO μ-wire (see Figure 6.11). The response was extremely fast and it was possible to clearly distinguish between the "on" and "off" states. The photosensitivity of ZnO nanostructures is attributed to electron-hole pairs generation due to the incident photons [2, 230, 105]. At increasing irradiance values, more electron-hole pairs are generated. Holes are trapped by the negatively-charged oxygen ions (O^{2-}) adsorbed

on the ZnO surface, whereas the electrons are available in the conduction band, contributing to a current increase.

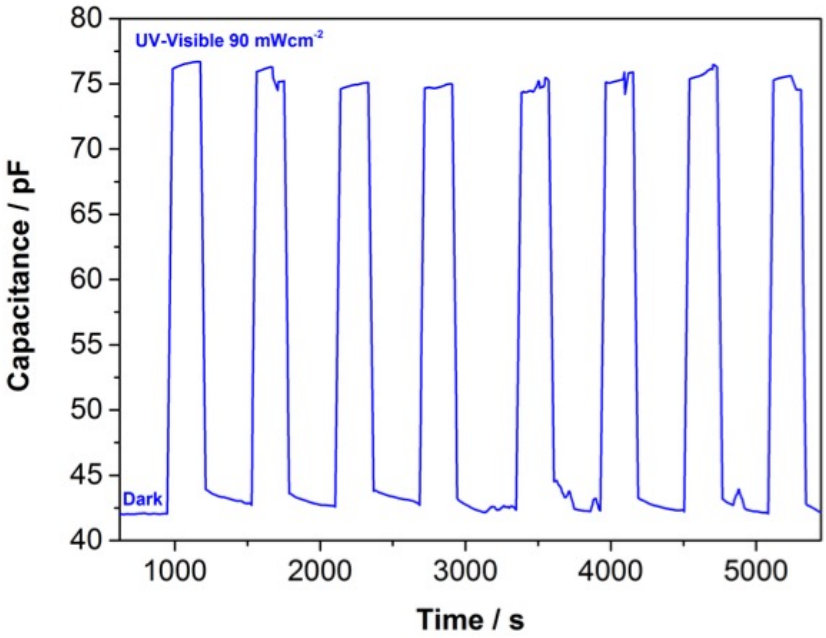

Fig. 6.11 UV-Visible on/off cycles. The UV-visible on/off cycles performed on a single ZnO μ-wire/gold junction are shown. The results represent the capacitance variation, at 100 kHz, when the UV-visible light, at 90 $mW \cdot cm^{-2}$, is switched on and off for eight times (Reproduced from [3],licensed under a CC-BY 4.0 license).

The current plateau observed in Figure 6.5 a and d, at higher light irradiance, may be attributed to the limited number of O^{2-} adsorption sites on the ZnO surface, being saturated by the trapped holes. This leads to a higher recombination rate of electron-hole pairs and thus to a reduction of carriers available for conduction. This behavior highlights the greater sensitivity of ZnO at low irradiance values than at higher ones. Between 0 and 50 $mW \cdot cm^{-2}$ a sensitivity of 0.03 $\mu A \cdot mW^{-1} \cdot cm^2$ was estimated for the ZnO/ gold junction, whereas it fell to $1.70 \cdot 10^{-4}$ $\mu A \cdot mW^{-1} \cdot cm^2$ approximately at 150 $mW \cdot cm^{-2}$ (further details about the sensitivity computation are reported in Supplementary Figure 6.7 a). The presence of amine-functionalizing groups on the surface is not believed to interact with the electron-hole pair formation and, at worst, it can slightly decrease the photoresponse with respect to a pristine ZnO material. In addition, the current increase due to local heating provided by the UV-VIS source (about 0.5–1 °C) can be neglected during irradiation experiments. In fact, no further current increase was observed by maintaining a constant irradiation over time on the ZnO/gold junction (see Figure 6.12), meaning that the dominant effect, reported in 6.5 a and d, is the photoelectric one.

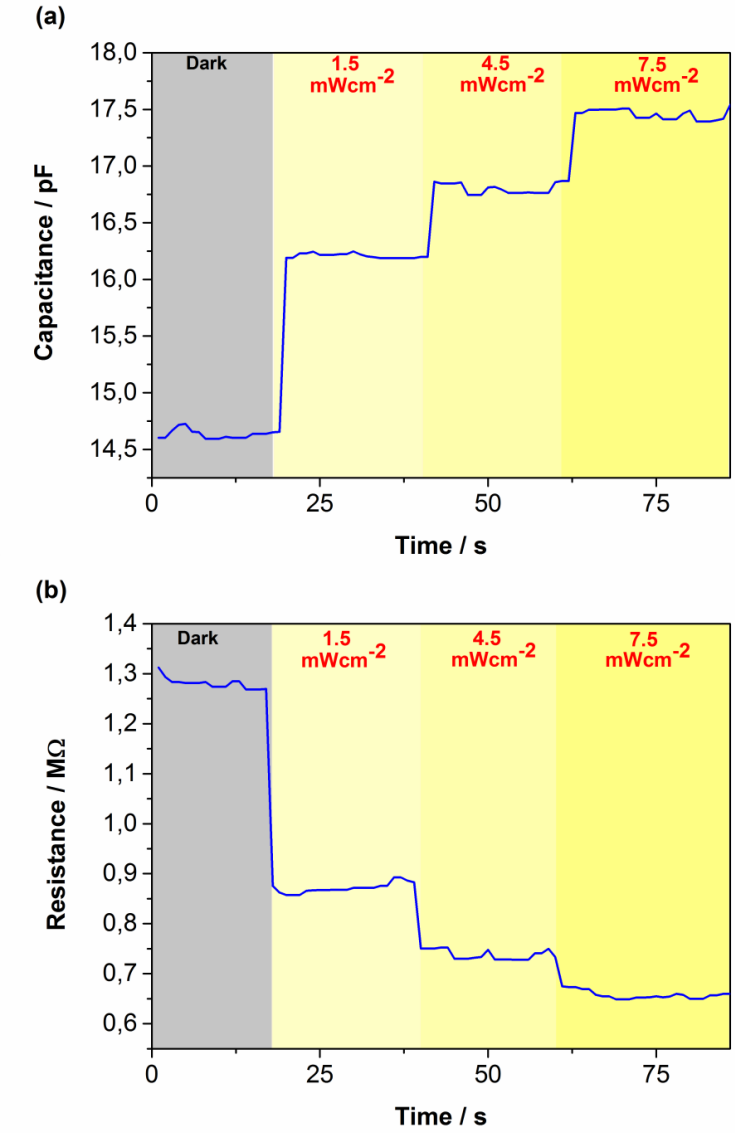

Fig. 6.12 Time dependent AC behavior varying UV-visible light. The time-dependent AC behavior of the ZnO/gold junction at increasing UV-visible light irradiation: (a) capacitance and (b) resistance obtained at 50 kHz (Reproduced from [3],licensed under a CC-BY 4.0 license).

6.2.3 Temperature Sensing

Concerning the temperature variation, an exponential increase in both the current in DC and the capacitance in AC (with a concomitant decrease in resistance) was observed (Figure 6.5 b and e). These variations, at increasing temperature, are attributed to the coupling of the semiconducting and pyroelectric properties of ZnO

material. Specifically, a polarization electric field is created along the μ-wire length as a result of the temperature variation over time [224, 235]. Due to the Schottky barriers between the ZnO and Au-electrodes, and to the temperature increase, an electric potential is established between the two ends of the ZnO μ-wire, resulting in a positively and a negatively charged end. The negative electric potential (V^-) can raise the local conduction band of ZnO and the Fermi level of one gold electrode by $\Delta E = e(V^+ - V^-)$. This drives electrons to flow from one gold electrode to the other through the external electric circuit (i.e., the PCB board and the connecting wires) thus leading to the current measurement. As it is a pyroelectric material, currents are only generated by ZnO during the temperature variation, whereas when the equilibrium is reached at the new temperature no current output is observed [235].

The conduction mechanism of ZnO/gold Schottky junctions is currently under study. However, as a first approximation, the experimental I-V curves are compared with the behavior of an ideal Schottky diode at different temperatures, considering the thermionic emission model (see Figure 6.13). The ZnO/gold junction ideality factor and barrier height are extracted from the experimental IV curves in order to qualitatively analyze the goodness of the Schottky behavior. At first, the experimental I-V curves are fitted with the ideal Schottky diode equation (see Equation 6.1) [236] in the voltage range 0 V – 1 V.

$$I = I_S \left[e^{\frac{qV}{nk_BT}} - 1 \right] \tag{6.1}$$

where q is the electron charge, V is the bias voltage, n is the ideality factor, k_B is the Boltzmann constant and T is the temperature expressed in K.

The value of the saturation current and of the ideality factor can then be extracted from fitting parameters, as shown in Figure 6.13 a and b, for the I-V measurements performed at 22 °C. To estimate the value of the barrier height, ϕ_B, the Arrhenius plot of the saturation current equation (Equation 6.2) is exploited [237].

$$I_S = A^{**} S T^2 e^{\left(\frac{-q\phi_B}{k_BT}\right)} \rightarrow ln\left(\frac{I_S}{T^2}\right) = ln\left(A^{**}S\right) - \frac{q\phi_B}{k_BT} \tag{6.2}$$

Where A^{**} is the effective Richardson constant and S is the diode area. The behavior of the ideality factor and of the barrier height extracted from the I-V curves for different temperatures are reported in Figure 6.13 c. The obtained ideality factor is higher than 1, which is the reference value for an ideal diode according to the thermionic emission model. This indicates that an important deviation from the

theoretical model occurs in the experimental I-V curves. Nevertheless, the curve trends are in accordance with what reported in literature: as the temperature increases, the effective barrier height increases, since more electrons acquire enough energy to overcome the potential barrier, along with a decrease of the ideality factor [236].

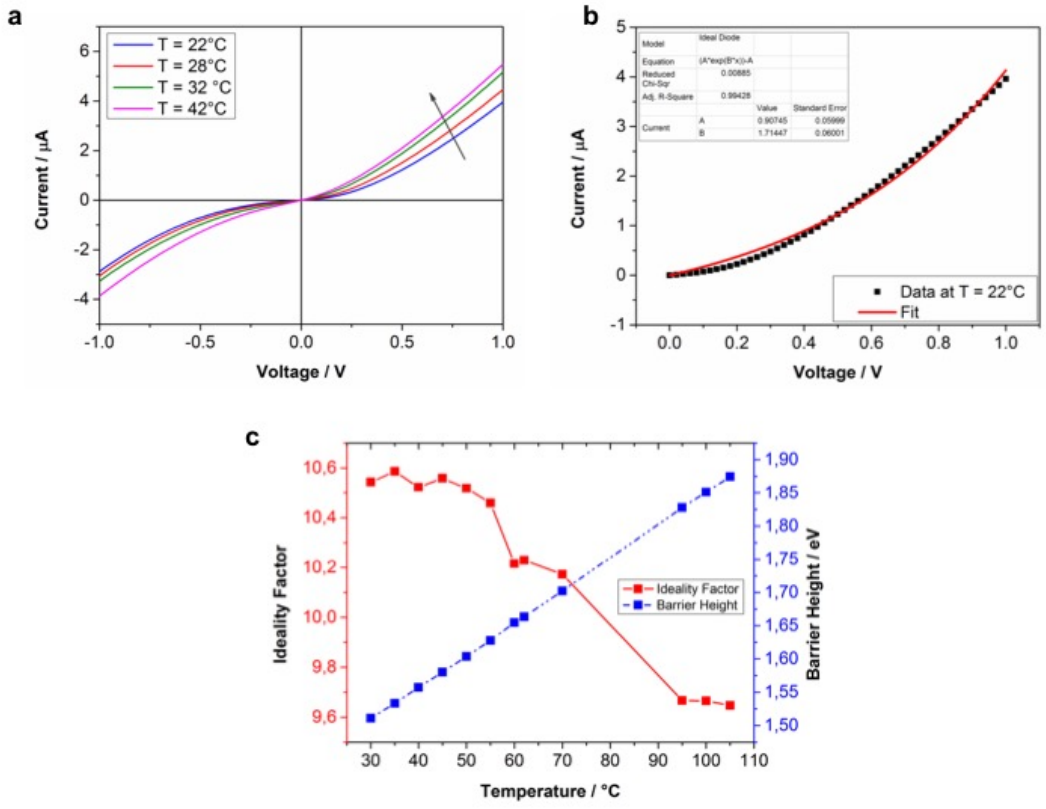

Fig. 6.13 ZnO/gold junction IV curves and fit with the ideal diode law. (a) The I-V characteristics the ZnO/gold junction measured at varying temperatures between -1 V and +1 V. Fit of the experimental curve at T = 22 °C with the ideal diode equation (b). The value of the saturation current and of the ideality factor of the Zn-gold Schottky junction are obtained from fitting parameters A ($I_S = A$) and B ($n = q/Bk_BTn$=q/BKBT), respectively. (c) Behavior of the ZnO/gold junction ideality factor (y-axis on the left) and the barrier height (y-axis on the right) under temperature variation. Both the data are extrapolated from the fit of the experimental I-V curves at different temperatures with the ideal diode equation (Reproduced from [3],licensed under a CC-BY 4.0 license).

Specifically, the obtained ideality factor is 10.54 - 9.65 in the temperature range 30–105 °C. Furthermore, the temperature dependence of the barrier height (1.5 - 1.8 V at 30 - 105 °C) highlights a strong influence of additional mechanisms that are not considered in the thermionic model, such as the field emission and the thermionic-field emission ones. Both these effects could be connected to quantum mechanical tunneling through the potential barrier between the metal and the semiconductor

[238, 236]. The observed deviation from the ideal Schottky diode model may be attributed to several factors, i.e. surface-localized states due to the high number of defects present on the μ-wire surface, barrier height inhomogeneities, Fermi level pinning, and tunneling effects [236].

6.2.4 pH Detection

pH-dependent DC measurements, on a single ZnO/gold junction, showed a current decrease when the pH was increased from 2 to 13 (Figure 6.5 c). The conductance of the ZnO μ-wire varied almost linearly when the pH was varied from 2 to 5 and the sensitivity extracted from the curve slope is -4.5 $nA \cdot pH^{-1}$ (or -4.8 $nS \cdot pH^{-1}$ as depicted in Figure 6.7 and according to the literature) [239]. Similarly, during the AC measurements the capacitance decreased and the resistance increased as the pH was increased from 3 to 10 (Figure 6.5 f). The prominent role in pH sensing is here played by the aminopropyl-group (NH_2) functionalization on the ZnO surface. This is because the aminopropyl-group is protonated from $-NH_2$ to $-NH_3^+$ in acidic media and it is, instead, deprotonated when in contact with basic media [59]. Besides, also the ZnO surface undergoes protonation and deprotonation mechanisms, which e.g., leads to the formation of hydroxyl groups at acidic pH values. However, the large amount of amine-functionalizing groups was responsible for the majority of the conductance variation of the ZnO/gold junction as also quantitatively demonstrated by Cauda *et al.* [59]. In details, the pH-dependent net surface charge changes the voltage at the ZnO/liquid interface and this modifies both the DC current and the impedance in the AC model [59, 239]. It is noteworthy that no evidence of degradation was observed on the ZnO μ-wires after pH-related experiments. This was due to the protective role of the aminopropyl-groups, grafting in large amount the surface of ZnO (around 1.78 molecules·nm^{-2}) [59].

6.2.5 Multiparametric Sensor Characterization

The results obtained when the UV-VIS light, temperature and pH were varied one by one were observed on distinct amine-functionalized ZnO/gold junctions (see Table 6.1), thus strengthening the repeatability of the proposed sensing mechanism. In addition, a mathematical modeling of the experimental trends was also performed. This mathematical modeling was able to properly fit the measured data with reproducible exponential or polynomial curves, as it will be discussed later in this Section (red lines in Figure 6.5).

Studied Range	**Sensitivity**	**Resolution**
	UV-VIS Light	
0 - 450 mW $\cdot$ cm^{-2}	0.03 μA $\cdot$ mW^{-1} $\cdot$ cm^2 between 0 - 50 mW $\cdot$ cm^{-2}	0.14 mW $\cdot$ cm^{-2}
	0.01 μA $\cdot$ mW^{-1} $\cdot$ cm^2 between 50 - 200 mW $\cdot$ cm^{-2}	
	$1.70 \cdot 10^{-4}$ μA $\cdot$ mW^{-1} $\cdot$ cm^2 above 200 mW $\cdot$ cm^{-2}	
	Temperature	
0 - 66 °C	0.10 μA $\cdot$ °C^{-1} between 22 - 40 °C	1 °C
	0.33 μA $\cdot$ °C^{-1} between 40 - 66 °C	
	pH	
2 - 13	-4.50 nA $\cdot$ pH^{-1} between pH 2 - pH 5	1 unit
	-4.17 nA $\cdot$ pH^{-1} between pH 9 - pH 13	

Table 6.1 Multifunctional sensor specifications. Sensitivity, resolution and analyzed UV-VIS light, temperature and pH ranges for the developed multiparametric sensor based on single ZnO μ-wire.

These results allow to use the ZnO μ-wire/gold junction as a multisensing device. In light of this, the UV-VIS light, temperature and pH stimuli were applied in sequence or simultaneously on various ZnO/gold junctions. DC and AC real-time outputs (Figure 6.14), measured on two different junctions respectively, were acquired starting from room temperature, neutral pH and dark conditions. Successively, the three stimuli were varied independently, resulting in a sum of effects when two or three parameters were changed simultaneously. The colored bars underneath the graphs in Figure 6.14 show in which order the three stimuli were applied and modified. The DC and AC outputs of the ZnO/gold junction acquired during the multisensing experiments were then analytically reconstructed. The analytical reconstruction was achieved by a linear combination of the fitting equations which regulate the electrical output when the external stimuli are varied one by one (see Equations 6.3-6.5). Thus, the output trends of the multisensor, both in DC and AC, was analytically created as depicted Figure 6.14 (red lines).

$$I_{DC} = f(x_{UV}) + g(x_T) + h(x_{pH}) \tag{6.3}$$

$$C_{AC} = A(f'(x_{UV}) + g'(x_T) + h'(x_{pH})) \tag{6.4}$$

$$R_{AC} = f"(x_{UV}) + g"(x_T) + h"(x_{pH}) \tag{6.5}$$

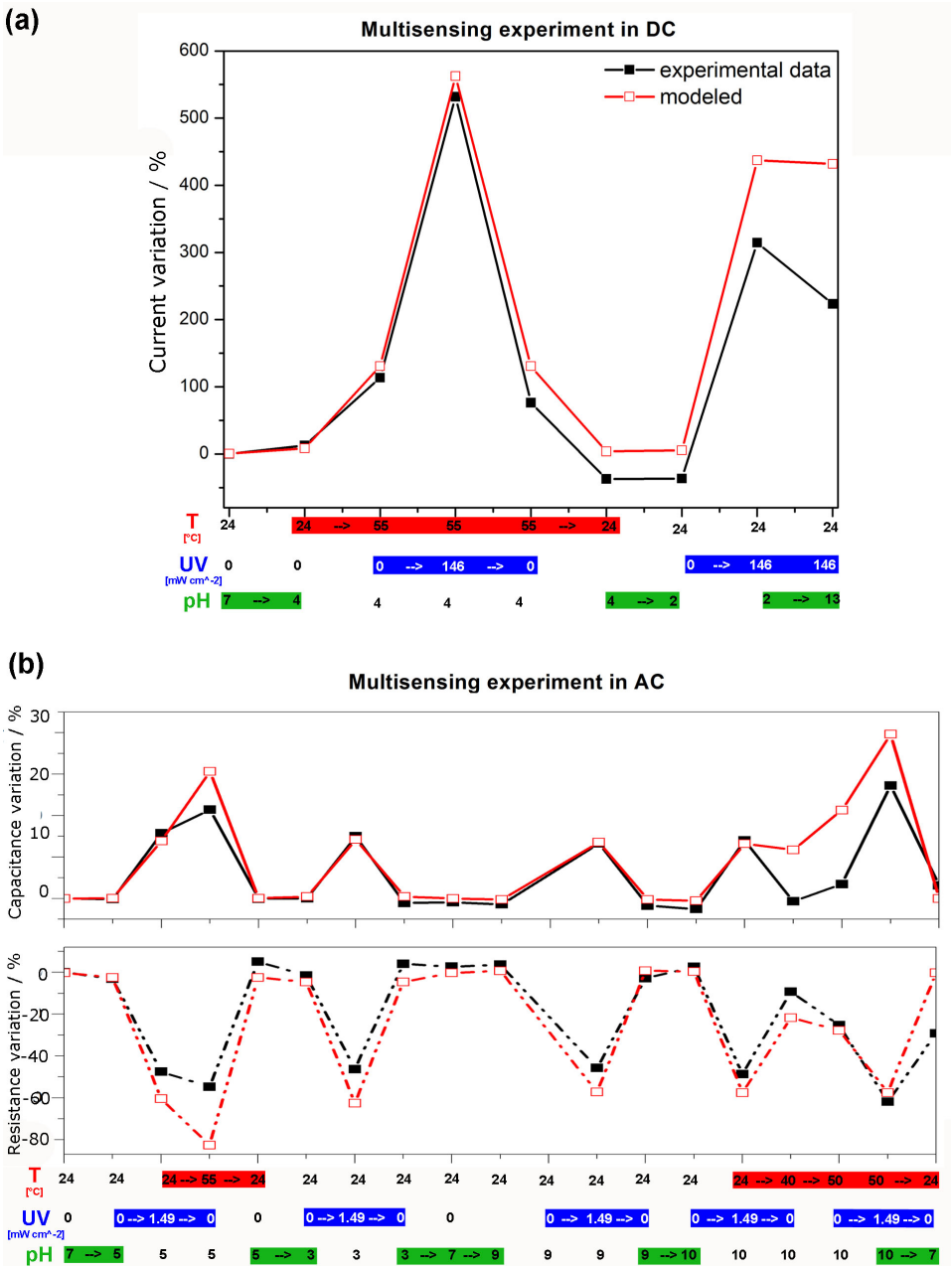

Fig. 6.14 DC and AC characterization of the multifunctional sensor. Multisensing measurements on ZnO/gold junctions by varying UV-VIS irradiance, temperature and pH simultaneously and in a random order within different ranges in both (a) DC domain at 1 V and (b) AC one at 5 kHz (Reproduced from [3],licensed under a CC-BY 4.0 license).

In Equations 6.3-6.5, f, f', f", g, g', g", h, h', h" are the modeling equations when the three external stimuli are varied one by one (see Table 6.2). Therefore they predict the electrical output as a function of UV-VIS irradiance (x_{UV}), temperature (x_T) and pH (x_{pH}). The coefficient A is a corrective factor (calculated to be 0.28)

ascribing the influence of other capacitance variations, external to the ZnO/gold junction, on the experimental behavior upon the stimuli application. These external contributions are instead negligible on the resistance (and thus on the current) value of the multisensor.

Modeling Function	***Adj. R-Square***
Current Modeling Functions	
$f(x_{UV}) = -429.220 \cdot e^{-x_{UV} \cdot 0.041} + 432.824$	0.963
$g(x_T) = 18.370 \cdot e^{x_T \cdot 0.0407} - 44.419$	0.989
$h(x_{pH}) = 3.714 + 1.512 \cdot x_{pH} - 0.501 \cdot x_{pH}^2 + 0.023 \cdot x_{pH}^3$	0.954
Capacitance Modeling Functions	
$f'(x_{UV}) = -111.367 \cdot e^{-x_{UV} \cdot 0.134} + 121.883$	0.999
$g'(x_T) = -267.410 \cdot e^{-x_T \cdot 0.018} + 170.135$	0.988
$h'(x_{pH}) = 5.866 - 2.723 \cdot x_{pH} + 0.428 \cdot x_{pH}^2 - 0.022 \cdot x_{pH}^3$	0.998
Resistance Modeling Functions	
$f''(x_{UV}) = -45.000 - 20.414 \cdot \ln(x_{UV} + 0.400)$	0.997
$g''(x_T) = 270.748 \cdot e^{-x_T \cdot 0.07159} - 34.006$	0.996
$h''(x_{pH}) = -5.052 - 0.744 \cdot x_{pH} + 0.380 \cdot x_{pH}^2 - 0.025 \cdot x_{pH}^3$	0.969

Table 6.2 Multiparametric sensor modeling equations. Equations of the functions reported in Figure 6.5 (red lines) fitting the experimental data collected for the current % variation (f, g, h), the capacitance % variation (f', g', h'), and the resistance % variation (f", g", h").

Since the modeling of multisensors is a challenging task, considering a linear combination of Equations 6.3-6.5 as all-inclusive model is a simplification. Nonetheless, the multisensing fitting curves, I_{DC}, R_{AC} and C_{AC}, reasonably predicts the experimental behaviors considering that the modeling equations were obtained from different junctions and with a simplified global model. Only slight deviations appear when the three stimuli are combined together due to the propagation of the fitting errors. To prove the reconstruction capability of the presented multisensing module, an additional investigation of the proposed mathematical model was carried out. At first, two stimuli among UV-visible irradiation, temperature and pH are fixed, e.g. UV-visible and pH, and will be then addressed as boundary conditions. The remaining one, e.g. the temperature, is varied in the range 20 - 80 °C and its behavior is reconstructed according to the multisensor model in order to predict the sensor output at different temperatures. Thus the temperature is considered as independent variable, x_T, in the multiparametric sensor equations (Equation 6.5) and - as a representative example - we calculated the resistance output (R_{AC}) in the multisensory

model as reported in Equation 6.6 (the procedure is the same for all DC and AC outputs).

$$\begin{cases} x_{pH} = 7 \\ x_{UV} = 0 \\ R_{AC} = f"(x_{UV}) + g"(x_T) + h"(x_{pH}),\ x_T = [20, ..., 80] \end{cases} \tag{6.6}$$

where x_{pH} corresponds to the fixed pH value, x_{UV} is the fixed UV irradiance expressed in $\text{mW} \cdot \text{cm}^{-2}$, x_T is the variable temperature expressed in °C.

Equations f", g", h" are the fitting functions reported in Table 6.2. The output predicted by the multiparametric sensor model is thus shown in Figure 6.15 a by the red dot curve. The obtained behavior is in line with the experimental one (blue square curve) since the applied boundary conditions bring to zero the values of $f"(0)$ and $h"(7)$, thus making the R_{AC} function equal to the temperature fitting function, $g"(x_T)$, as also reported in Figure 6.5 e, when only the temperature varies.

This first preliminary step is fundamental for the validation of the constructed mathematical model with respect experimental data. The same procedure can be repeated for any other multiparametric sensor equations I_{DC}, C_{AC} or R_{AC} or boundary conditions. For instance, the capacitance response of the sensor to a variable pH stimulus at fixed temperature (x_T = 24 °C) and UV-irradiation (x_{UV} = 1.49 $\text{mW} \cdot \text{cm}^{-2}$) is reported in Figure 6.15 b. Another prediction, in DC domain, is depicted in Figure 6.15 c, considering a variable UV irradiation and fixed pH (x_{pH} = 10) and temperature (x_T = 55 °C). In Figure 6.15 b and c, it can be appreciated that the trend of both curves are in complete accordance with the expected ones (see Figure 6.5 f and c). This fact underlines the robust predictive potentialities of the multiparametric sensor model in different experimental conditions.

Therefore, both the predicted and the experimental curves can be generalized for all our chips, despite different μ-wire shapes, dimensions or contact area with the underlying gold electrodes. This is not a trivial effort considering that the synthesized ZnO 1*mu*-wires cannot have all the same size, hence leading to slightly different values of resistance and capacitance. Moreover, the obtained multiparametric equations (Equations 6.3 - 6.5) can reconstruct back the sensing behavior in both AC and DC domains under a specific external stimulus by fixing two boundary conditions. We can thus predict the behavior of the sensor output, both in AC and in DC, without performing any experiment.

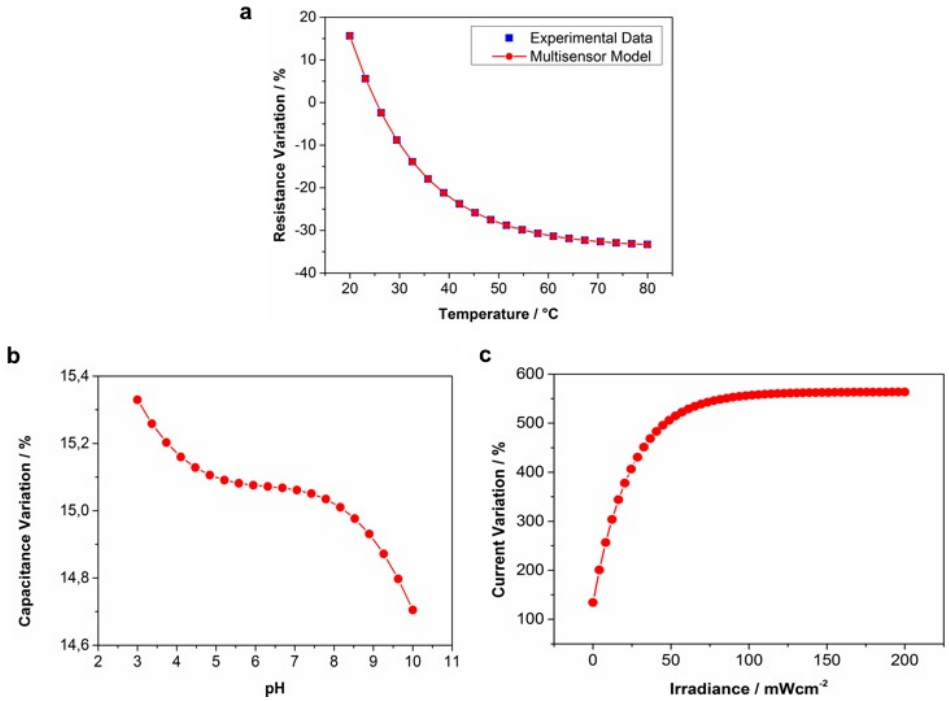

Fig. 6.15 (a) Fit of the resistance variation upon temperature with the multiparametric sensor model. Resistance percentage variation as function of temperature at 5 kHz. The behavior predicted by the multiparametric sensor model (red curve) is compared with the experimental data (blue squares). The boundary conditions are pH = 7 and UV-visible irradiance = 0 $mW \cdot cm^{-2}$. (b) Capacitance percentage variation as a function of pH predicted by the multisensory model (red curve) at 5 kHz. The value of UV-visible irradiance is fixed at 1.49 $mW \cdot cm^{-2}$ while the temperature at 24 °C. (c) Current percentage variation as a function of UV-visible irradiance predicted by the multisensor model (red curve). The value of pH is fixed at 4 while the temperature at 55 °C (Reproduced from [3],licensed under a CC-BY 4.0 license).

6.2.6 Conclusions

We demonstrated a powerful method to understand and then predict the behavior of a semiconductor/metal junction in a multisensing approach. This work is also a clear proof-of-concept about the fabrication of a real-time measurement device based on single ZnO μ-wire/gold junction, which allows multifunctional sensing.

Furthermore, the ease of the multisensor assembly, based on EIBJ and dielectrophoresis techniques, ensures the reproducibility and the re-use of the final device. These features, along with the capability of testing and predicting the device in a wide range of experimental conditions, are all key features for sensors development. Specifically, a quick prediction of the sensor output, in different experimental scenarios (i.e., the behavior of the ZnO/gold junction under different stimuli), can be

obtained without the need of testing all of them. By changing the mathematical boundary conditions, plenty of distinct experimental situations can be modeled prior to or alternatively to experimental measurements.

It is noteworthy that modeling the behavior of this multisensing device is a complex multidisciplinary task. Nevertheless, our simplified model, with its assumptions and approximations, is capable to faithfully and accurately reproduce the experimental curves. This fact underlines the robust predictive potentialities of our multiparametric sensor model in different experimental conditions. Moreover, a multivariate chemometric investigation further confirmed the model and it was also useful for the formulation of the three equations that correlate the measured responses with the individual external stimuli. These results will underpin future studies about additional ZnO sensing capabilities, e.g. molecules or mechanical pressure detection. These studies can be well identified and predicted, thus being completely incorporated in our multisensing approach. Broadening the potentialities of our multisensor can lead to a leading edge and resourceful device that, if embedded in a living cell culture or organ-on-a-chip, can help to reveal and understand the complex mechanisms occurring in the cellular microenvironment. Even further, the high versatility of ZnO material applied in energy storage [40], photo-conversion [102], and nanogenerator [30] together with multi-parameters sensitivity can become a base for highly multifunctional and smart self-powered nanosensors.[6]

6.3 $Mo_6S_4I_6$ Microwires Electrical Characterization on *Nanogap* Chips

Part of the data presented in this section were obtained in collaboration with the Master Thesis work of F. Capua [100]

In order to validate the potentialities of the nanogap chips, not only for advanced sensors fabrication, but, also as tool for studying the electronic properties of materials, the $Mo_6S_4I_6$ microwires, described in Chapter 2, were deposited on the chip.

As already mentioned in Section 3.4.2, successful dielectrophoresis experiments came out in case of $Mo_6S_4I_6$ microwires (see Figure 6.16 a and c). The electrical characterization of the microwire/gold junction revealed also in this case a Schottky junction (Figure 6.16 b). In order to try to study different electro-physical properties of $Mo_6S_4I_6$, due to the scarce literature available regarding this specific material,

[6]Ending point of the verbatim quote from [3], see Appendix A for the complete copyright and permission file.

reinforcements platinum (Pt) contacts were deposited at the extremes of the junctions between the microwire and the gold contacts, using the FIB microscope. One example is shown in Figure 6.16 c.

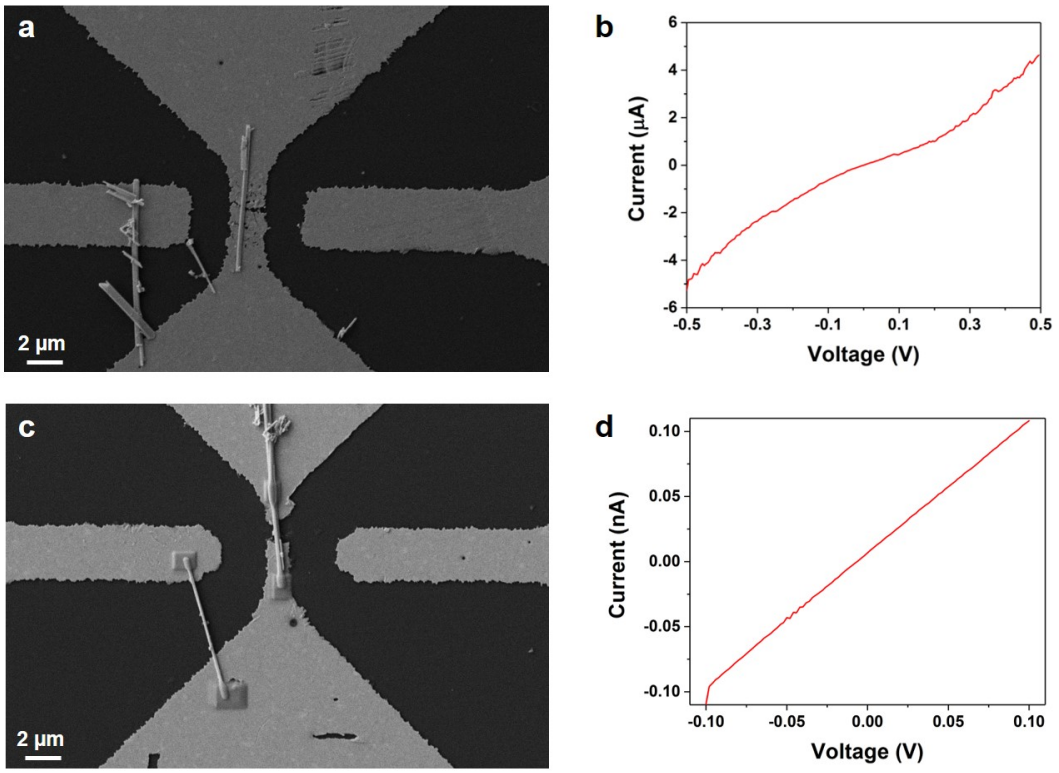

Fig. 6.16 FESEM images of the $Mo_6S_4I_6$ microwires deposited on the nanogap chip, without (a) or with (b) Pt reinforcement contacts. The presence of the Pt contacts modifies the measured IV curve from Schottky (b) to ohmic (d).

It is interesting to notice how, after the addition of the Pt metal contacts, the nature of the microwire/metal junction strongly changed from Schottky to ohmic (Figure 6.16 d). This behavior was attributed to the modification of the work functions difference between the pristine $Mo_6S_4I_6$/gold junction and the new $Mo_6S_4I_6$/gold/platinum one. Despite the work function of platinum (5.12 – 5.93 eV) is highly similar to the one of gold (5.10 – 5.47 eV), the Pt metallorganic precursor used in the FIB microscope presented also some traces of carbon, which, together with the cloud contamination issue generally present during ion beam lithography, can be the main responsibles of the intense modification of the junction nature.

As already mentioned in Section 6.2 and in [3], Schottky-like characteristics are usually better than ohmic ones for sensing applications due to the higher variation of the measured quantity for smaller variations of the sensed parameter, hence increasing the final sensitivity of the sensor. Nevertheless, additional Pt contacts

may help to increase the stability of the junction hence being more suitable for deeper, time-consuming and different sensing experiments to characterize the nature of unknown or less studied materials.

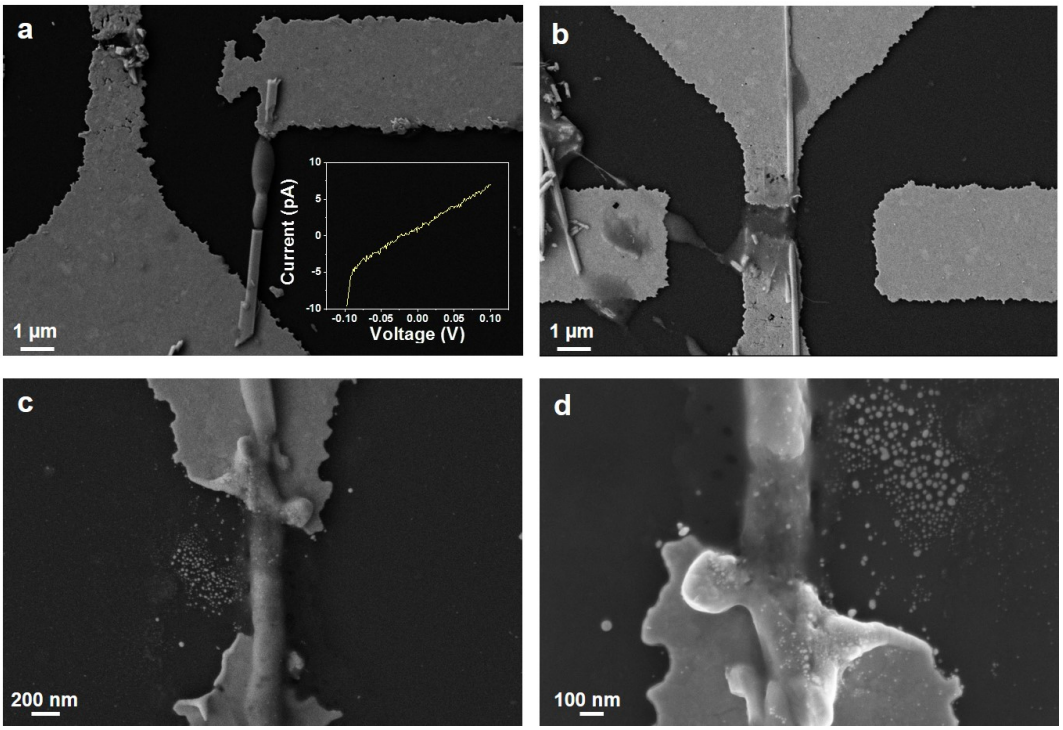

Fig. 6.17 Examples of $Mo_6S_4I_6$ microwires rupture due to IV measurements. Also reported in [100].

Unfortunately, after the application of voltages in the same range of the once used in case of the ZnO microwires, the rupture of the $Mo_6S_4I_6$ microwires was observed after the electrical measurements (see Figure 6.17). This phenomenon, appearing similar to a melting process, could be associated to a too high current density flowing in the material through the microwire/gold junction. This was also noticed during the initial electrical measurements since the IV curve resulted in much smaller currents, in the order of few pA (inset of Figure 6.17 a), hence not relevant for the electrical characterization of the material. For this reason, a maximum voltage of 0.5 V was applied to the $Mo_6S_4I_6$ microwires/gold junction in presence of the Pt contact enforcements.

At last, as initial characterization of the electro-physical properties of the material, its potentialities to be used as photodetector were investigated. This choice was supported by observing the absorption spectrum of the $Mo_6S_4I_6$ microwires in presence of UV light radiation as reported in [74]. By repeating the measurement of the UV-VIS absorption spectrum of $Mo_6S_4I_6$ microwires, results in accordance with the one reported in [74] were obtained (Figure 6.18 a). Nevertheless, to date, no

UV-VIS light sensing experiments are reported in the literature. To start to fill this gap, preliminary characterizations of the electrical properties of $Mo_6S_4I_6$ microwires deposited on the nanogap chips and illuminated with UV-VIS light were performed. The experimental setup was the same as the one used in case of ZnO microwires described in Section 6.1 and 6.2.

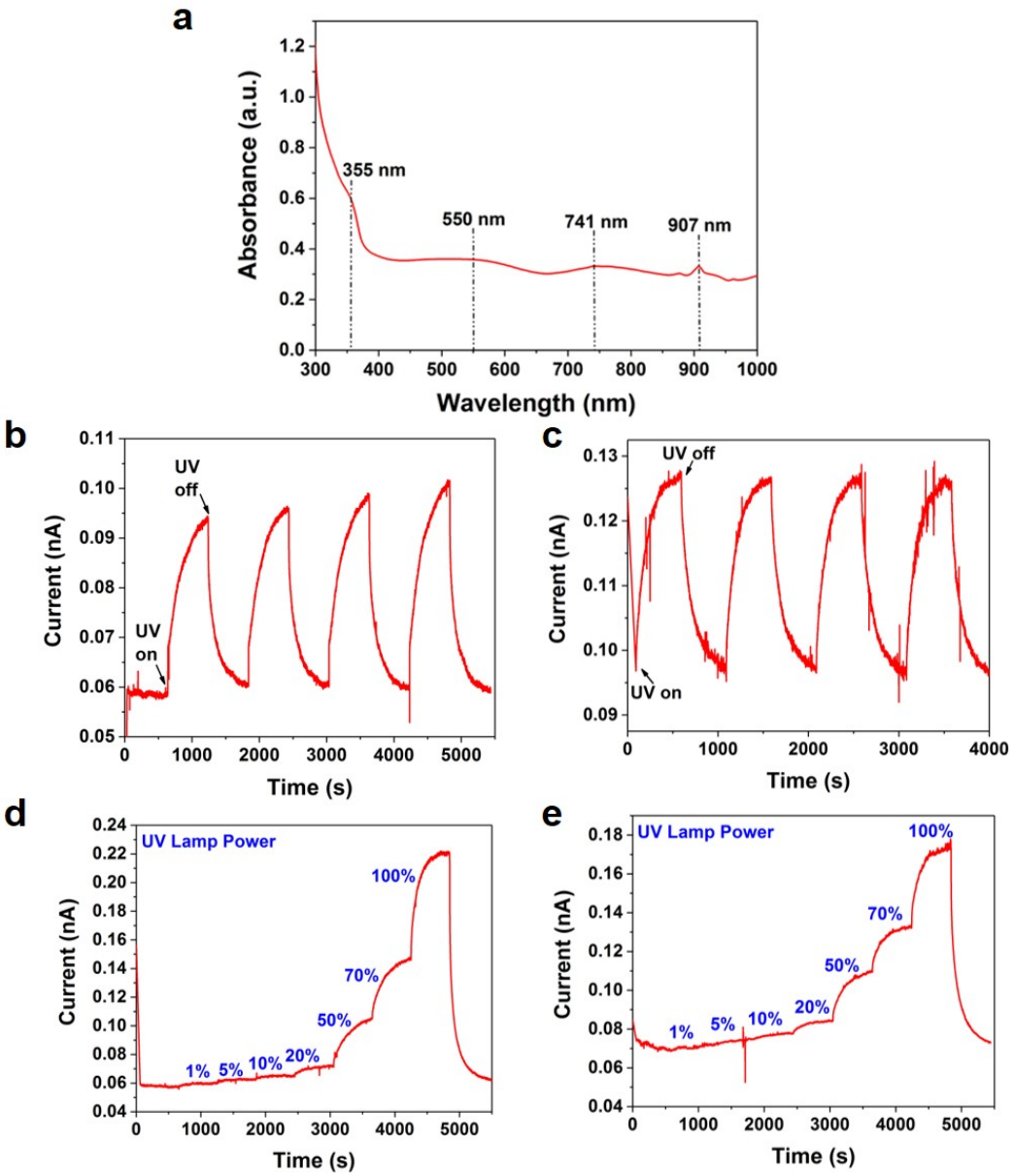

Fig. 6.18 (a) UV-VIS absorption spectrum of $Mo_6S_4I_6$ microwires. Also reported in [100]

At first, the current flowing the microwire/gold junction was monitored during sequential cycles of illumination and dark conditions (Figure 6.18 b and c). The

current at the junction was fixed at 1 V while, the power of the UV lamp was fixed at 50% at a distance of 2.1 cm. As expected, an increase of the current flowing in the junction was observed when the junction was illuminated with UV-VIS light, due to the contribution of the photo-generated current. A clear on/off pattern can be recognized in Figure 6.18 b and Figure 6.18 c. Nevertheless, the response time of the material resulted of the order of $\sim$ 500 seconds, hence suggesting the presence of extended transients of time in which the structure stabilizes. Similar transient effects, attributed to non-equilibrium dynamics in the microstructure itself, were also reported in the literature in case of other semi-insulators materials, like mesoporous silicon [240].

Then, the power of the UV lamp was varied in order to observe the relationship between the intensity of the UV-VIS radiation and the current increase (Figure 6.18 d and e). The power range was varied between 1% and 100% of the lamp range, that, at a distance of 2.1 cm, corresponds to an irradiance between 6.63 mW/cm^2 and 670 mW/cm^2 (see Section 6.4 for a detailed description of the conversion between the UV-VIS lamp power % and the irradiance).

As expected, by increasing the UV-VIS light irradiance, a correspondent current increase was observed (Figure 6.18 d and e). Nevertheless, for UV lamp powers smaller than 20%, the current increase resulted too limited to be able to clearly observe a significantly relevant difference hence suggesting that the limit of detection of the sensor could be in this range of powers. Nevertheless, additional tests are necessary in order to be able to concretely characterize the performances of the sensor like the response time, the sensitivity and the limit of detection.

6.4 ZnO Microwires UV-Visible Light Sensing on M4N Chip

In order to improve the performances of the ZnO/gold junction sensor presented in the Section 6.1 and 6.2, the same approach was transposed on the active M4N chips (described in Chapter 4). The presence of the integrated circuits to measure the variation of the electrical properties of the microstructure directly underneath the electrodes strongly reduces the noise and parasitics influences [4]. Moreover,

the embedded dielectrophoresis circuits further improves the system portability and integration.

The procedure for deposition of the ZnO microwire between the metal electrodes is the same as in the case of the nanogap chips: 10 μL of isopropyl alcohol solution with dispersed ZnO microwires with a concentration of 0.8 mg/mL was dropped on the chip while the dielectrophoretic signal generators are enabled. Five different frequencies can be chosen, as anticipated in the range between 50 kHz and 1MHz, for the dielectrophoretic triangle-wave signal. Specifically 370 kHz, 480 kHz, 700 kHz, 850 kHz and 1 MHz. In the present work, no significant difference was observed between the different frequencies in terms of successful dielectrophoresis of ZnO microwires. Therefore, in the presented experiments, the frequency was kept constant at 370 kHz. The dielectrophoresis process can be easily monitored using a standard phase contrast microscope (see Figure 6.19), as in the case of the nanogap chips, with the advantage that no external voltage generator is needed.

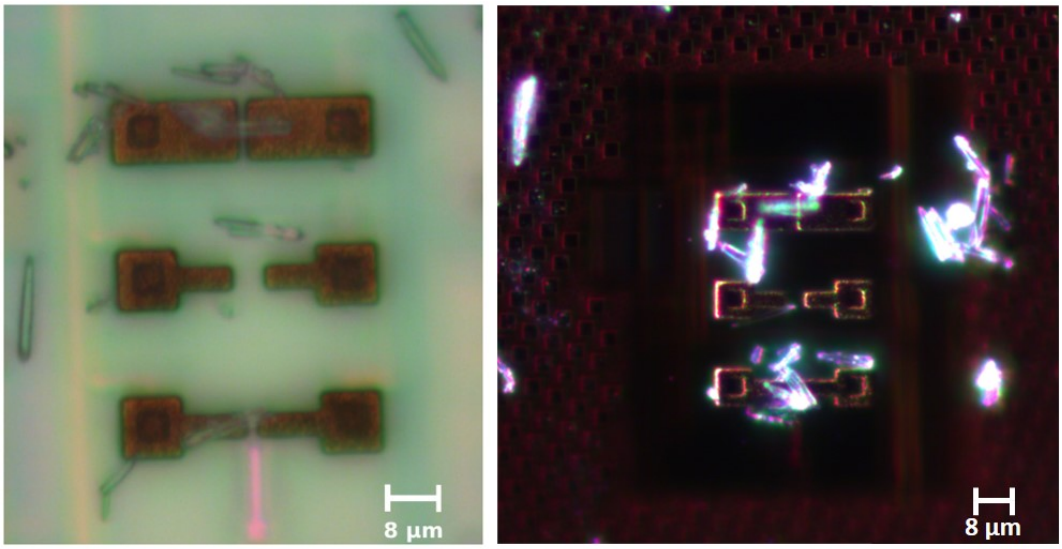

Fig. 6.19 (a) Optical microscope images, both in bright (a) or dark (b) fields configurations, of a single ZnO microwire deposited between the M4N facing electrodes. Image (a) is reproduced from [4],licensed under a CC-BY 4.0 license.

As visible from Figure 6.19 b, in some cases the dark field modality can be more advantageous for the correct identification of the deposited microstructures on the chip. A more in depth characterization of the junction topography can be obtained by FESEM characterization (see Figure 6.20 and 6.21). During the dielectrophoresis process the microwires will disperse on the whole M4N chip surface with a preferential attraction force towards the electrodes gaps, where the electric field will be of higher intensity. Therefore, as visible from Figure 6.20 a, at the end of the process the microwires will be present on the overall chip surface.

Nevertheless, the microwires deposited on the SiO_2 chip surface will not have any influence on the overall device operation.

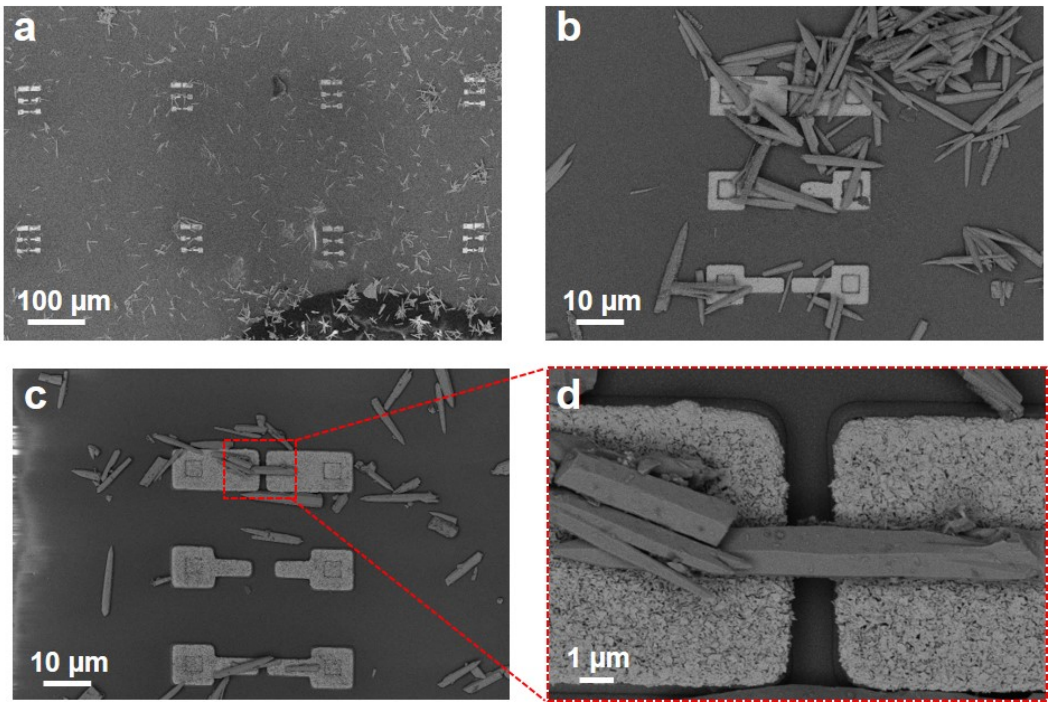

Fig. 6.20 FESEM images of ZnO deposited on the M4N chips with the embedded dielectrophoretic circuits.

Indeed, it is extremely important to correctly tune the concentration of the microwires solution in order to avoid microwires accumulation at the electrodes junctions (see Figure 6.20, b). With the optimized concentration of the ZnO microwires solution, 0.8 mg/mL, we achieved the correct alignment of a single ZnO microwire across the couples of facing electrodes where the dielectrophoretic signal was applied (see Figure 6.20 c and d).

It is worth noting that even fragments of ZnO microwires where successfully attracted between the electrodes, forming a functional ZnO/gold junction, as shown in Figures 6.21 a and b. In these pictures the typical pencil-like ending of ZnO microwires can be also appreciated. At last, the effectiveness of the dielectrophoresis process was further validated with the deposition of $Mo_6S_4I_6$ microwires on a test chip, where also ZnO microwires where previously deposited. As visible from Figure 6.21 c, a single $Mo_6S_4I_6$ microwire was correctly deposited between the facing gold electrodes. On the electrode sides, the ZnO microwires can be also be appreciated and identified thanks to their different morphology and bigger dimensions. This test, was a first proof of concept about the possibility of depositing multiple materials on a single chip in order to achieve high-throughput multisensing on-chip. Specifically,

each of the 8 cells present on a single chip, each one formed by three couples of facing electrodes, can be independently enabled or disabled so that different micro-materials can be deposited on each cell in multiple dielectrophoresis experiments.

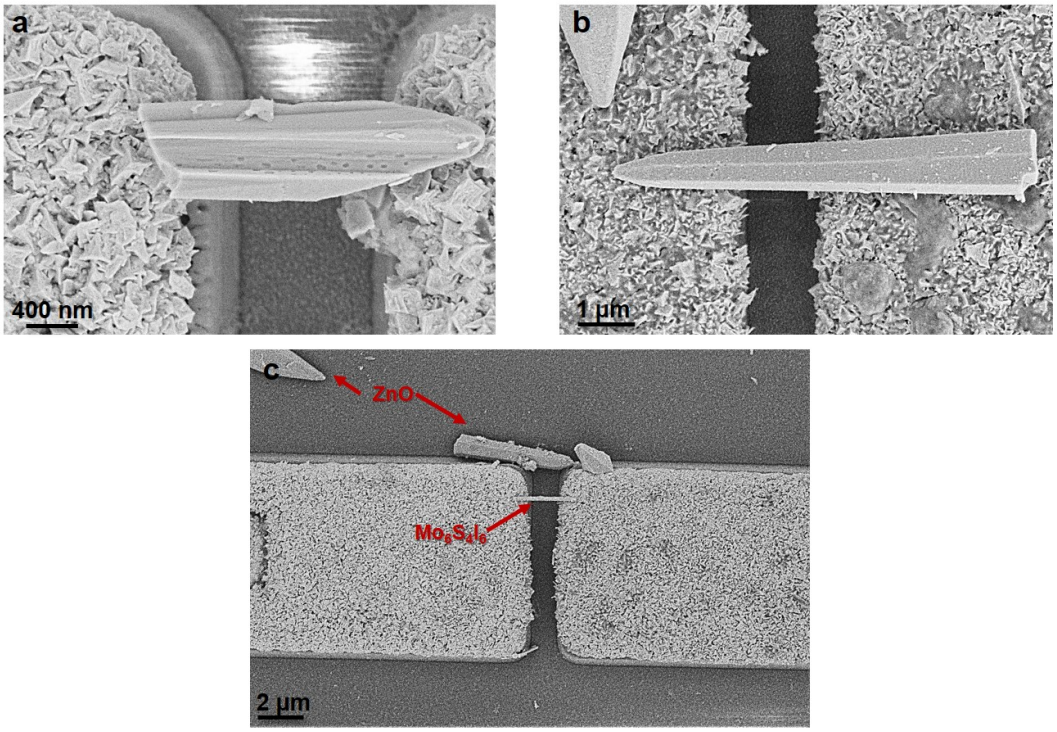

Fig. 6.21 FESEM images of fragments of ZnO ((a) and (b)) or of $Mo_6S_4I_6$ (b) microwires deposited on the M4N chips with the embedded dielectrophoretic circuits.

At last, the UV-VIS sensing potentialities of ZnO microwires deposited on the M4N chips were assessed. [7] Successful electrical connections were created between the ZnO microwires and several couples of aluminum top electrodes (AlTEs) of the M4N array like the one showed in Figure 6.19-a in which one ZnO microwire has been successfully integrated between the upper and bottom pairs of electrodes. We chose two to make further discussion and we identify them as ZnO microwire A (ZnO_A) and ZnO microwire B (ZnO_B). Under dark conditions, the resistance of ZnO_B is about 330 MΩ, whereas the microwire resistance measured for ZnO_A is about 700 MΩ. A LightningCure LC8 UV lamp (Hamamatsu, Japan), with adjustable power irradiance and emission wavelength peaked at 365 nm, was used to evaluate the sensitivity of a single ZnO microwire and to validate the M4N approach.

As described in the UV lamp data-sheet, by considering a sample placed at distance d = 1 cm, the emitted radiant flux is focused by a specific light guide on a

[7] Starting point of the verbatim quote from [4]

restricted area of about 1 cm^2 with a measured maximum irradiance of about 4500 mW/cm^2. The enlightened area slightly increases if the sample is placed at a higher distance, whereas the irradiance decreases as $1/d^2$. Assuming that the irradiance is constant on the whole enlightened area and considering a single ZnO microwire with size of about 5 μm x 500nm assembled on the M4N chip, the incident radiant flux (IRF-UV) on the ZnO microwire is only a small part of the emitted UV light flux and proportional to its surface (i.e., 7.85 m^2). In particular, since the power of the UV lamp can be adjusted from 1% to 100% of the nominal power, the estimated IRF-UV varies from 2.29 nW to 229 nW for a ZnO microwire placed at 1 cm. The results of the On/Off experiment are shown in Figure 9, where the UV light source is alternatively switched off and on at 20%, 30% and 50% of the maximum irradiance power. Once the UV lamp is switched on, the R_{NW} decreases due to the contribution of photo-generated current. The reported data have been already weighted by considering the influence of the UV irradiation on the CMOS circuit.

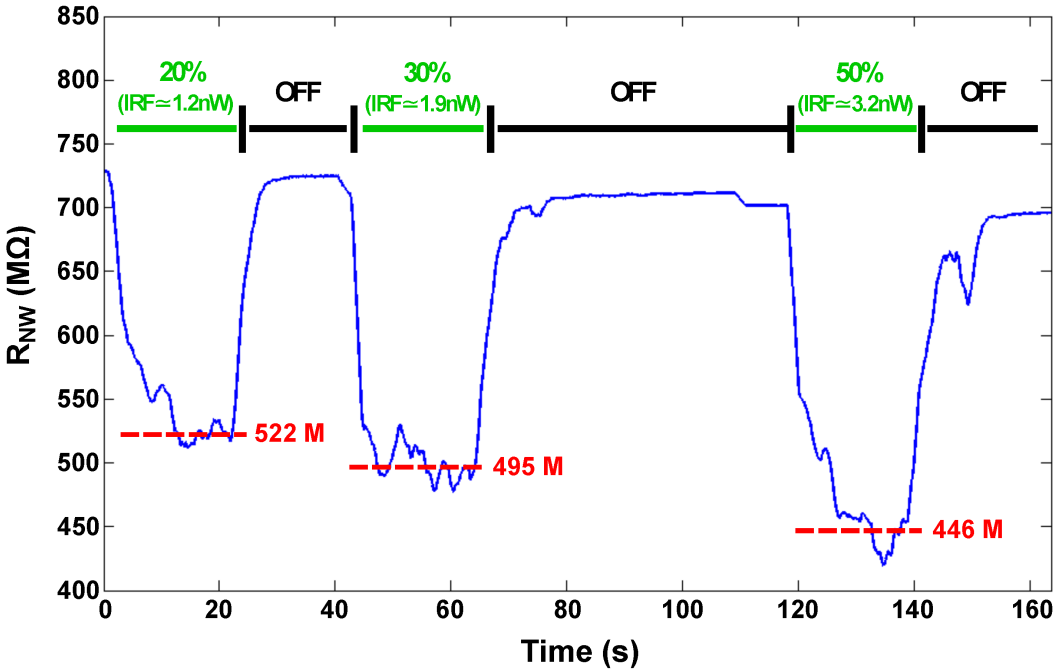

Fig. 6.22 Real-time behaviour of the resistance of ZnO microwire A when it is exposed to the UV source placed at 6 cm and working at 20%, 30% and 50% of the maximum irradiance power. The IRF-UV corresponds to about 1.2 nW, 1.9 nW, 3.2 nW, respectively. Reproduced from [4],licensed under a CC-BY 4.0 license.

Specifically, the ZnO microwires are assembled onto gold-metalized microelectrodes placed just on top of the CMOS read-out circuit. As reported in the literature [241, 242], P-N junction of doped silicon is also sensitive to light in a large wavelength range (e.g., CMOS photodiode). During real-time experiments at different UV

irradiance powers, the whole chip is exposed to an intense UV light flux and a small variation of the ROC output has been also detected even where the microwires were not connected. Indeed, the ROC circuit, exposed to UV light flux even if attenuated by thick silicon oxide layer, can be affected by leakage current variation.

As explained in [124], the leakage current estimation during characterization steps is fundamental for accurate calculation of the microwire resistance. The designed ROC reads-out an equivalent resistance and capacitance at the input and encodes these values on time delays T_1 and T_0 of a square-wave generated at the ROC output. Small variations on T_1 have been noticed, corresponding to a reduction of the maximum measurable resistance as proved by the behavior of the black curve in Figure 6.23. Hence, considering a standard upper limit resistance (RMAX) of about 1 GΩ without any assembled microwire on top of the ROC, the corresponding average leakage current (I_{leak}) is about 700 pA (i.e., $I_{leak} = V_{ROC}$, stim/R_{max}).

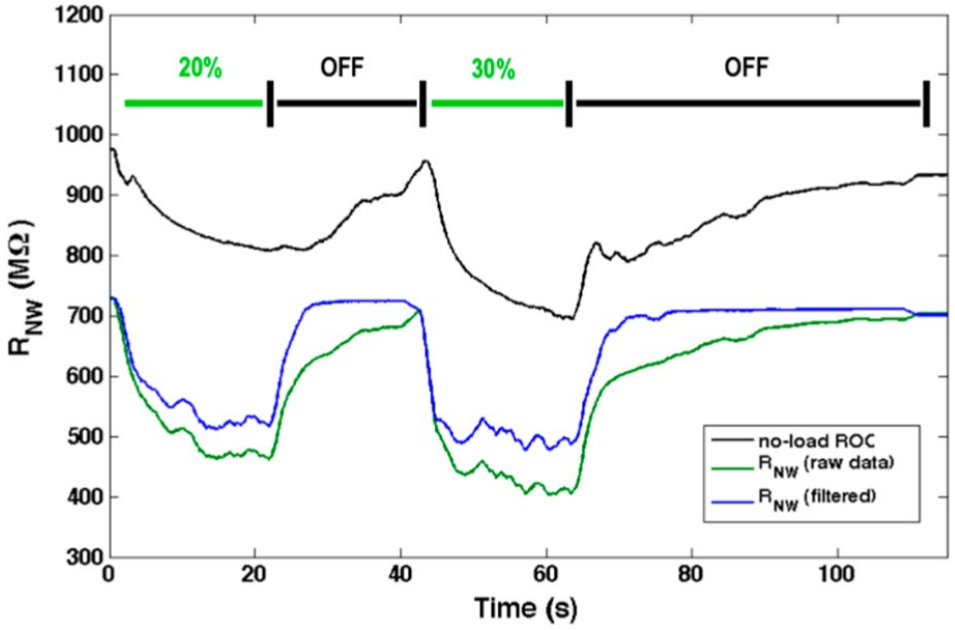

Fig. 6.23 Estimated resistance under UV-light exposure: the maximum measurable microwire resistance (black curve), the raw data (green curve) and the filtered data (blue curve) of the microwire resistance.

The decrease of R_{max} observed during experiments suggests an increase of about 175 pA of I_{leak} in case of 1.2 nW of UV irradiation power. Under dark conditions, the equivalent microwire current is about 1 nA considering that the applied stimulation voltage, AC applied by ROC is 100 mV peak-to-peak with a DC value of about 700 mV. Under IRF-UV $\sim$ 1.2 nW, the microwire resistance decreases from 700 MΩ to 460 MΩ (i.e., $I_{NW} \sim 1.521$ nA) that corresponds to an increase of 521 pA. Actually, if considering leakage current as a constant value, there would be an overestimation

of about 175 pA. Subtracting this value, we obtain to $I_{NW} \sim 1.346$ nA and, thus, to $R_{NW} \sim 520M\Omega$.

For this reason, a single ROC in the array has been considered as reference, disconnecting the couple of AlTEs from the underlying circuit and estimating the increase of I_{leack} due to UV light. In real-time data processing, such contribute has been subtracted from the measurement results obtained by the assembled ZnO microwires used as UV sensors. The normalized blue curve is reported in Figure 6.23. This effect is almost negligible for more conductive ZnO microwire (e.g., ZnO microwire B). In [124], such compensation was not required because the microwires were placed on an external passive device (i.e., a gold electrode nano-gap) and not directly assembled on the silicon M4N chip. The excitation and relaxation time corresponding to the switching on and off of the UV source are now few seconds and the drift under constant irradiation is completely removed. This correction of the estimated microwire resistance is needed only for experiments including UV light and large temperature variations, since these factors can induce small variation on leakage of ROCs. The characterization of the designed ROC under temperature variations is reported in [124]. Indeed, chemical or bio-sensing on M4N chip would not influence the ROC behavior.

The higher the UV light incident the more electron-hole pairs will be generated in the material, i.e., the higher will be the total current. Specifically, the oxygen ions (O_2^-) naturally adsorbed on the ZnO microwire surface will attract the photogenerated holes, while the electrons will contribute to the current in the conduction band [230, 105]. Although the assembled microwires (shown in Figure 6.22) have different electrical characteristics, they are both sensitive to the UV light with similar trend. The sensitivity has been calculated with a piecewise linear approximation of the experimental curves within two regions delimited by an ideal knee point at 20 nW. Both microwires show best sensitivity for an estimated IRF-UV lower than 20nW. Several experimental data for the ZnO microwire A are reported in Figure 6.24 a, and the linear approximation of the nanosensor sensitivity to UV-light is about 10.21 MW/nW for IRF-UV < 20 nW and about 1.08 MW/nW for IRF-UV > 20 nW. Similarly, the other ZnO microwires assembled on the same M4N chip, whose experimental data are plotted in Figure 6.24 b, shows a sensitivity to UV-light of about 8.04 MW/nW for IRF-UV < 20 nW,whereas it decreases to about 2.23 MW/nW for higher UV intensity.

The UV experiment is only reported as proof of concept for the M4N system validation, since the designed platform has to be considered as an essential support for implementing nanowire-based sensing in different field (e.g., chemical or biomedical). Indeed, the electronics integrated on the M4N chip has been already used for real-time biosensing, as described in detail in [32], where the measurement on capacitance reveals the adhesion of BSA protein on single functionalized ZnO microwires assembled on external gold nanogap device. Performing the same experiment on

the M4N surface will increase the sensitivity due to an evident and expected noise reduction.

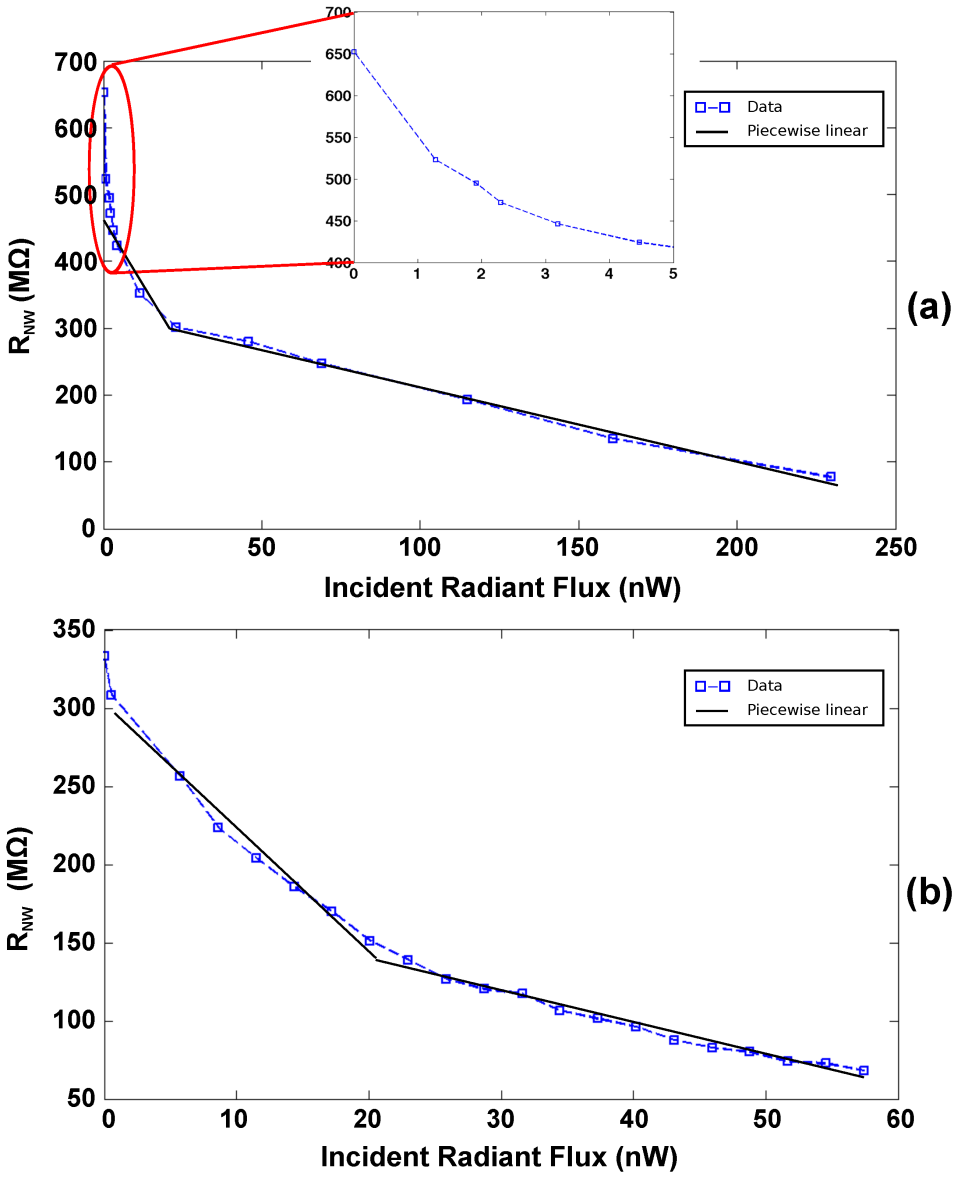

Fig. 6.24 Variation of the microwire resistance depending on the IRF-UV for ZnO microwire A (a) and ZnO microwire B (b) in the same M4N array. During experiments reported in (a), the M4N chip has been placed at 1 cm and 6 cm from the UV source, whereas in (b) the M4N chip has been fixed at 2 cm.

6.4.1 Conclusions

A complete system for nanomaterial-based sensing platform was described in detail. The system was composed of both hardware and software building blocks. The hardware core was represented by the 130nm CMOS technology silicon chip with the microcontroller-based low-cost platform to interface the M4N IC. While, an easy configurable GUI was developed for real time data visualization. The ZnO microwires were then successfully integrated across the AlTEs using the on-chip DEP generators, creating the electrical connections with the gold microelectrodes. Two integrated ZnO microwires were then used as UV-light sensors. The results of these experiments showed large variation of the RNW up to 80% of the nominal value, if the single ZnO microwire is exposed to different incident UV light radiant flux in the nW range. The average sensitivity of the two microwires to UV light can be calculated in two IRF-UV range separately. Indeed, the UV sensitivity for ZnO microwire A and ZnO microwire B was about 10.21 MW/nW and 8.04 MW/nW for IRF-UV < 20nW, whereas it was about 1.08 MW/nW and 2.23 MW/nW for IRF-UV > 20nW, respectively. The slight difference of resistance and UV sensitivity probably depended on the size of microwires or on the electrical connection with AlTEs.

The proposed system is not only conceived of for experiments on light exposure, but also suits for experiments in different fields (e.g., chemical or biomedical), depending on the material and on the chemical functionalization of nanowires assembled onto the M4N chip. Thus the described M4N system represents a step forward for an ease-to-use nanowire-based sensing platform with integrated electronic circuits.[8]

6.5 Preliminary Biodegradation Tests

In order to investigate the possible use of the presented passive (nanogap) and active (M4N) electrodes platforms for biological, and specifically cell-compatible, experiments, the two systems have been tests in a biologically relevant environment formed by simulated body fluid (SBF) and cell culture medium. SBF is a water-based solution whose ion concentration and pH is extremely similar to the one in the human blood plasma [243].

The SBF solution was custom-made by the author following the protocol published by Kobuko *et al.* in [244]. The solution is formed by sequentially adding all the compounds listed in Table 6.3 to 500 mL of distilled water under stirring at room temperature. The complete dissolution of each compound was waited before adding the next one. The pH was then adjusted to 7.4 using HCl.

[8]Ending point of the verbatim quote from [4], see Appendix A for the complete copyright and permission file.

Priority	Compound	Quantity
1	NaCl	7.996 g
2	$NaHCO_3$	0.350 g
3	KCl	0.224 g
4	$K_2HPO_4 \cdot 3H_2O$	0.228 g
5	$MgCl_2 \cdot 6H_2O$	0.305 g
6	HCl (1M)	40 ml
7	$CaCl_2$	0.278 g
8	Na_2SO_4	0.071 g
9	$(CH_2OH)_3CNH_2$	6.057 g

Table 6.3 Protocol for the SBF preparation.

In order to perform measurements in liquid, both the nanogap and the M4N chips were modified by gluing, around the active area of the chip, either a truncated 1.5 mL Eppendorf tube (Figure 6.25 a) or a truncated 5 mL Falcon tube (Figure 6.25 b). The container is then sealed using the same epoxy used for the bonding pads protection.

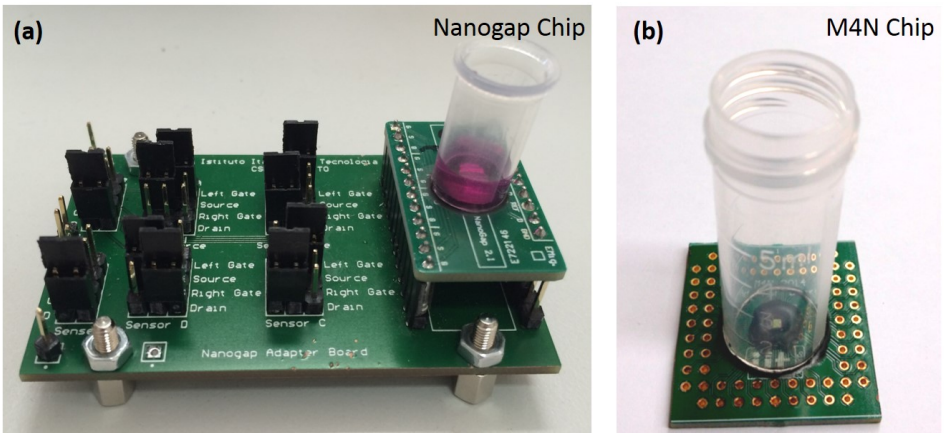

Fig. 6.25 Setup used for the measurements on nanogap (a) and M4N (b) chips in liquid. Image (b) is reproduced from the Supporting Informations of [4], licensed under a CC-BY 4.0 license.

Considering the nanogap chips, at first, the IV curve of a ZnO microwire deposited across one couple of electrodes was characterized, between 0 V and 3 V, before starting the biodegradation experiments (see the blue curve in Figure 6.26 a). Then, the IV measurement was repeated after the addition of the cell culture

medium (Figure 6.26 b). Interestingly, despite an increase of the measured current was expected, due to the contribution of the ions present in the solution, a strong decrease of the current amplitude was observed (red curve in Figure 6.26, b).

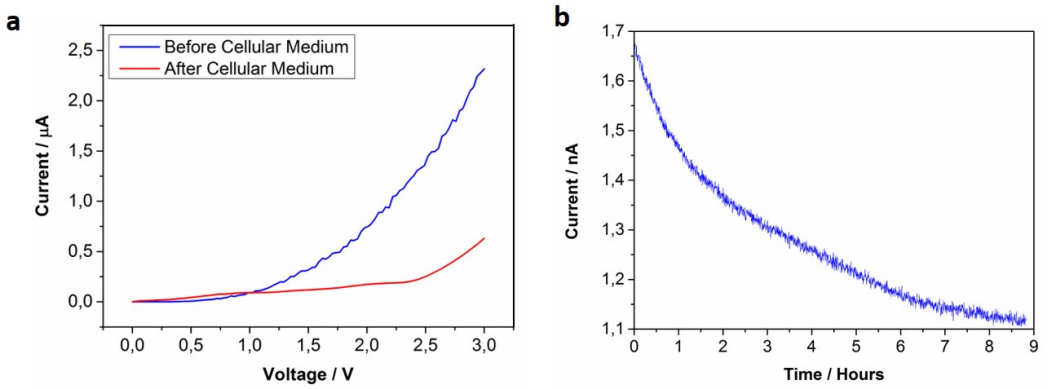

Fig. 6.26 (a) IV curve before (black) and after (red) the addition of cell culture medium to the ZnO/gold junction on the nanogap chip. (b) Current measurements in time, at 1 V, of the ZnO microwire/ gold junction with cell culture medium.

Moreover, after fixing the potential at the ZnO microwire/gold junction at 1 V, the current at the junction was monitored in real-time for 9 hours (Figure 6.26 b). As visible from Figure 6.26 b, an exponential decrease of the current is observed during time. Although further investigation is needed, this behavior can be associated to the biodegradation and corrosion of the ZnO/gold junction during the measurements in the conductive cell culture medium solution. This hypothesis was motivated by the characterization of the chip with the FESEM technique. In fact, as reported in Figure 6.27, a significant degradation of the junction happened during the biodegradation experiments. Specifically, looking at Figure 6.27 a, one of the two gold microelectrodes forming the junction was completely corroded (top), while, the other one (bottom), revealed the presence of additional material on its surface.

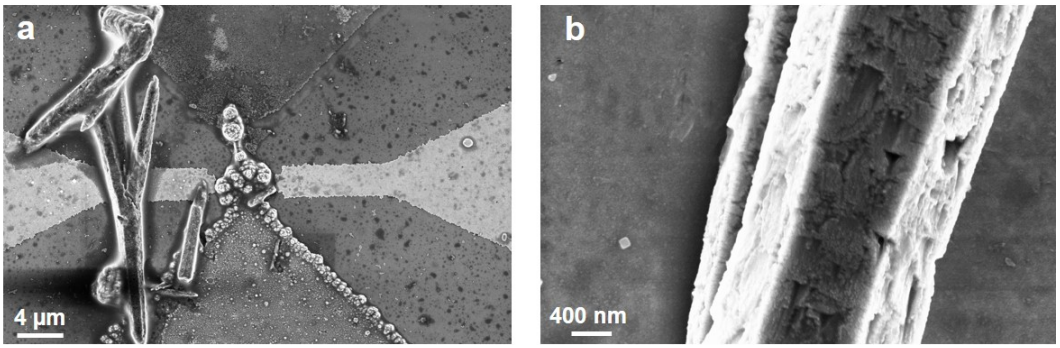

Fig. 6.27 FESEM imaging of the ZnO microwire/gold junction after the biodegradation experiments on the nanogap chip (a) with detail of the surface of a single ZnO microwire (b).

Moreover, observing, with higher magnification, the surface of a ZnO microwire, some degradation of its surface can be hypothesized, if the picture is compared with the ones reported in Chapter 2, where the surface of the microstructure was appearing completely smooth. In order to validate the stated hypotheses, and to understand the chemical nature of the modification of the ZnO microwire/gold junction, additional EDX analysis was performed. As shown in Figure 6.28 a, the upper electrode resulted completely corroded so that the underneath SiO_2 surface was detected (spectrum 2).

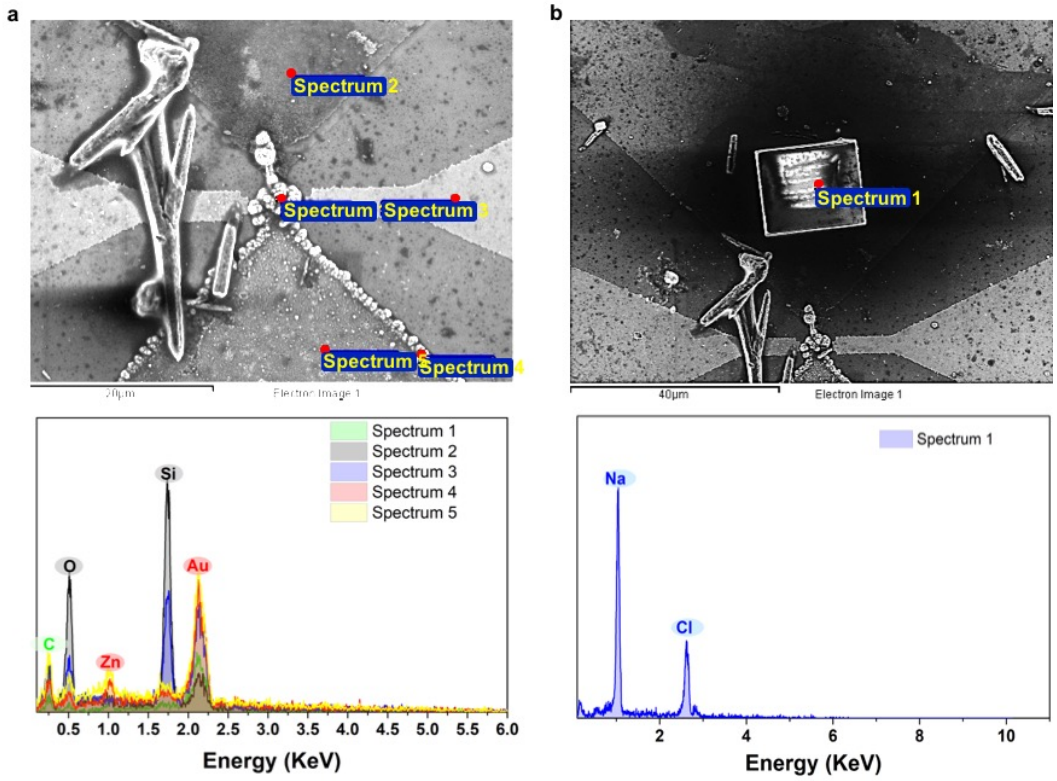

Fig. 6.28 EDX analysis of the chemical elements present on the surface of the nanogap chip after the biodegradation experiments

The spectra on the bottom electrode, instead (spectrum 4 and 5), evidenced the presence of significant amounts of gold. The spectrum acquires at one of the extremes of the ZnO microwire, showed instead the presence of both gold and zinc atoms (spectrum 1). According to the obtained results, it can be hypothesized that, due to the high voltages present, comparable to the value also of the water splitting voltage 1.23 V [245], a corrosion phenomenon occurs on the electrodes by which the metal atoms are removed from the grounded electrode and transported in the conductive solution, probably towards the biased electrode. Nevertheless, due to the complex electro-chemistry involved, these assumptions need further and deeper

verifications. At last, it is interesting to notice the formation of a NaCl cubic crystal close to the junction region (Figure 6.28 b), confirmed then by the EDX analysis.

The same experiment was then repeated on a M4N chip with SBF solution. The obtained results are very similar to the ones obtained in the case of the nanogap chips. The electrical measurement of the resistance and capacitance of the ZnO microwire during the biodegradation experiments was stopped few minutes after the introduction of the SBF in the falcon tube. Therefore, it was not possible for the system to correctly completing the acquisition and saving of the data. Nevertheless, the characterization of the chip surface with the FESEM, reveled that it is highly probable that a process similar to the one happened on the nanogap chips occurred. Specifically, not only on some electrodes the growth of extra-material is present (Figure 6.29, a), probably related to the precipitation of different salts in the solution, but, also, the corrosion of specific electrodes was observed (Figure 6.29, b, c and d). Also in this case, these assumptions were verified by the EDX analysis (Figure 6.30).

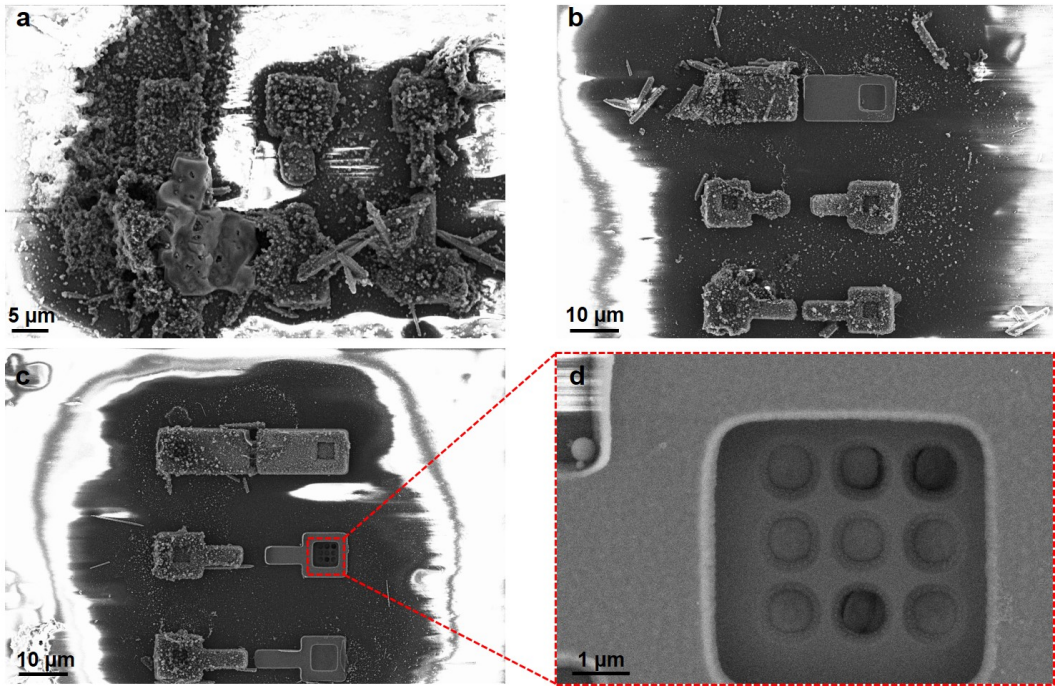

Fig. 6.29 FESEM imaging of the ZnO microwire/gold junction after the biodegradation experiments on the M4N chip with a detail about the electrodes corrosion (d).

Different elements contained in the SBF solution are present on the electrodes surface (spectrum 1, 2 and 3 of Figure 6.30 a), like P, Mg, Ca and again NaCl. In addition, on the corroded electrodes (right column of electrodes in Figure 6.30 b) the corrosion was so intense that the copper metal lines underneath the vias, now exposed and visible (see also Figure 6.29, d), are detected. This result is extremely

significant in order to understand the power of the corrosion phenomena of the gold electrodes in biologically relevant solutions.

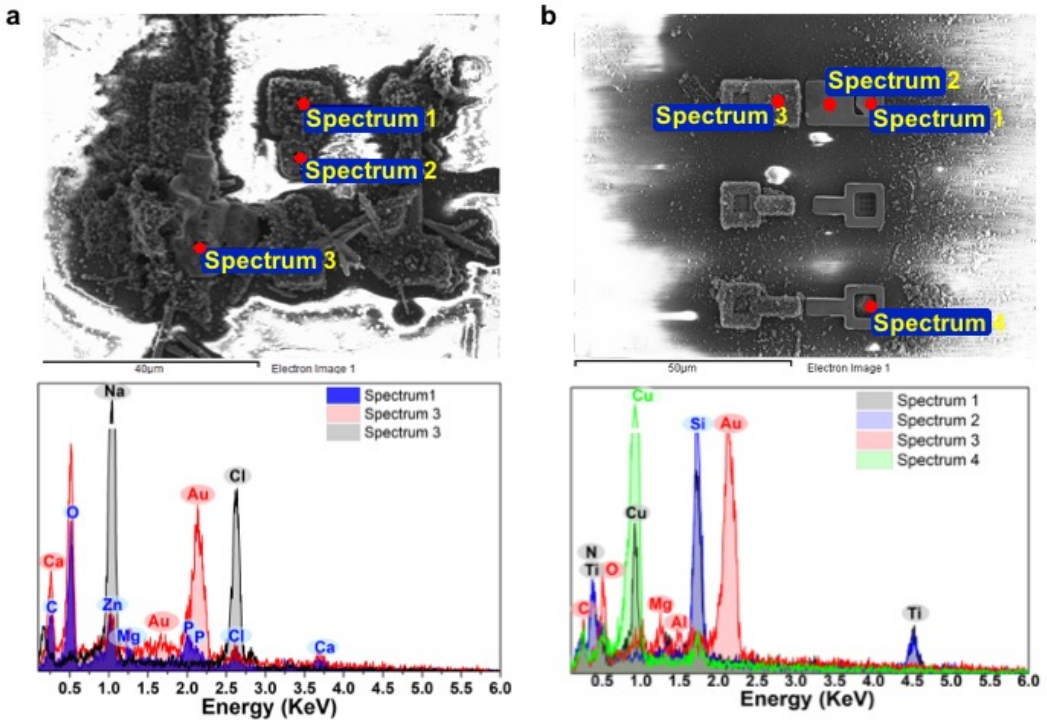

Fig. 6.30 EDX analysis of the chemical elements present on the surface of the M4N chip after the biodegradation experiments.

Although the results presented in this section are only preliminary, they still underline the importance of tuning and optimizing all the different aspects of the experiment not only on the biological side but also on the electrical one. As the sensing environment must be adapted and made as much as biocompatible as possible, in order to favor the proliferation of cells, at the same time, the electrical apparatus must be protected from the extremely aggressive biological/physiological wet environment. This implies that, in case of biologically relevant experiments, the electrical signals involved must be carefully designed and optimized, not only not to damage the living organisms, but, also, to protect the electrodes themselves from unwanted electrochemical reactions that may undermine the electrodes integrity and stability.

Chapter 7

Electrical Modulation of Cardiomyocytes-Based Soft Actuator

Chapter Abstract *In the present chapter the results of the bioprinting experiments of the bioactuator scaffold will be presented. At first, the preliminary printing tests with simple test patterns will be shown (7.1), then the bioprinting of two different layouts for the fish-like constructs will be introduced in Section 7.1.1. Afterwards, the culture of primary neonatal rats cardiac fibroblast and cardiomyocytes on the bioprinted scaffolds will be discussed in Section 7.2 with also detailed analysis of the beating behavior. At last, the electrical stimulation of the cardiomyocytes on the scaffold and the preliminary biocompatibility tests of the flexible electrodes for the wireless actuation will be presented (Section 7.3).*

7.1 Bioprinting Tests

As presented in Section 5.4.3 of Chapter 5, part of the present work involved the bioprinting of biocompatible hydrogels acting both as an actuator and as scaffold for the growth of cardiac cells. The starting point was therefore the optimization of a reliable bioprinting process, with the experimental apparatus described in Section 5.4.3.

Two specific inks were the ones predominantly used: CNT-GelMA hydrogel and poly(ethylene glycol) diacrylate (PEDGA) mixed with pristine GelMA hydrogel (PEGDA-GelMA). The CNT-GelMA hydrogel was selected as principal scaffold for the cardiac cells growth and proliferation, thanks to its favorable biophysical properties, as deeply discussed in Section 5.2.2. The ink was constituted by mixing 8% bare GelMA hydrogel, 1.6 mg/mL of CNTs stock solution (see Section 5.2.2)

and 1% of Irgacure D-2959 photoinitiator (PI) in a solution of DPBS (no calcium, no magnesium, Gibco, USA).

A second hydrogel, PEGDA-GelMA, was also used as support layer, following the same design concept reported in Section 5.3. In fact, as published in [1], the PEGDA hydrogel is stiffer than the bare GelMA one (about 2 orders of magnitude), due to the increased Young's modulus (see also Figure 5.12). These properties make it suitable to act as support for the whole structure, without impeding the actuation movement induced by the contracting cardiac cells especially since the supporting PEGDA-GelMA structure was not completely filled with hydrogel but a line pattern was present (as in the case of the work presented in Section 5.4.3). The PEGDA-GelMA hydrogel was usually obtained by dissolving in DPBS 8% GelMA hydrogel, 20% PEGDA (molecular weight 1000 Da) and 1% PI. Usually both the inks where freshly prepared in a volume of 3 ml in order to avoid the bleaching and degradation of the PI due to the aging of the solution. Moreover, after mixing, both the solution were heated at 80 °C for 30 minutes to allow the complete dissolution of the components.

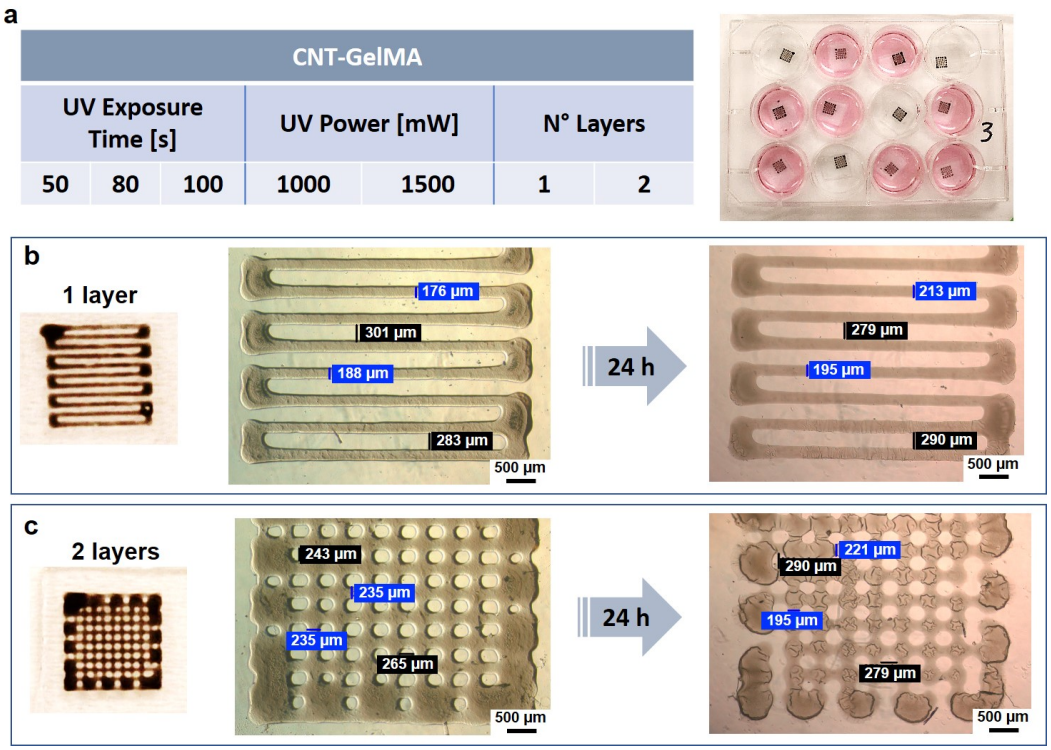

Fig. 7.1 Optimization of the crosslinking parameters of the CNT-GelMA hydrogel (UV exposure time, UV lamp power, number of layers) when immersed in cell culture medium.

The ink was usually printed on a custom-functionalized 3-(Trimethoxysilyl)propyl methacrylate (TMSPMA, Sigma Aldrich, USA) coated glass slide. This coating have

been widely used in order to covalently link hydrogel to the glass slides, in order to improve their adhesion and stability during experiments as well as for the adhesion of cells or, also, entire organs [246]. After printing, the sample was then transferred in a opaque PMMA box where the fiber of a OmniCure S2000 mercury UV lamp (Excelitas Technologies, USA).

The first parameters to be optimized were the UV exposure time and the power of the UV lamp. For these tests CNT-GelMA hydrogel was used as sample, bioprinted with serpentine test structures with a G30 needle. As reported in Figure 7.1, three different UV exposure times where selected (50 s, 80 s and 100 s), and two different values of power for the UV lamp (1000 mW and 1500 mW while the sample was placed at 8 cm from the optical fiber output of the lamp).

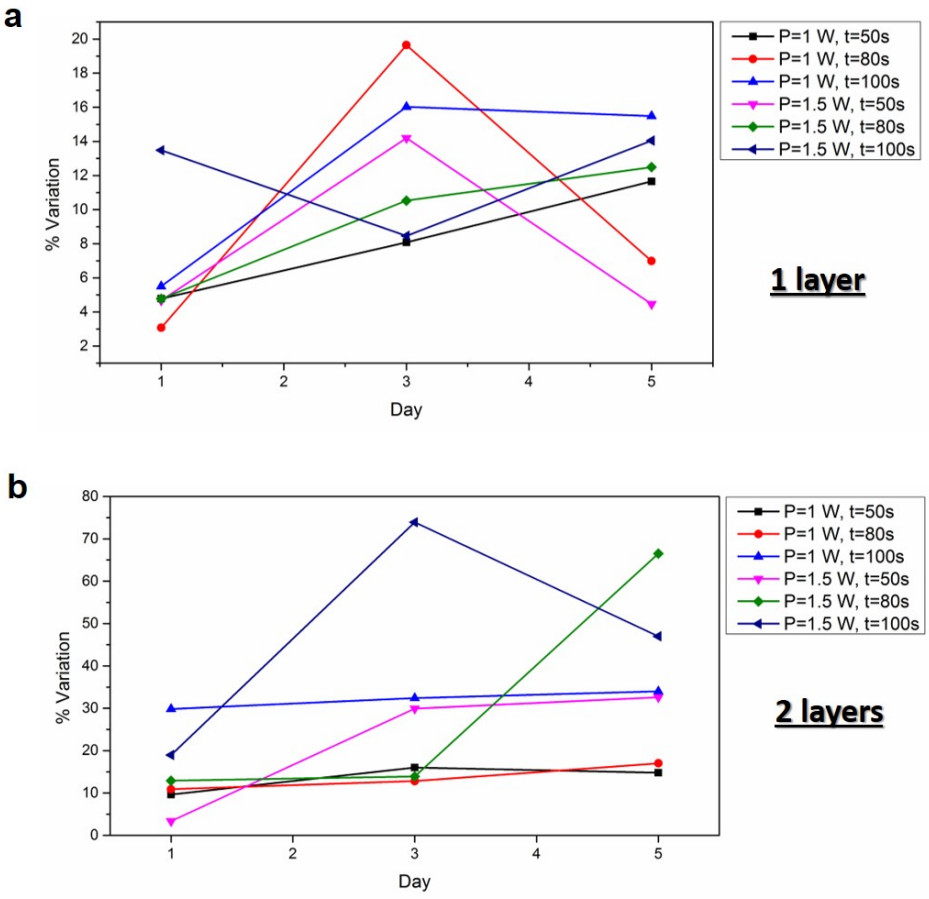

Fig. 7.2 Results of the optimization of the crosslinking parameters of the CNT-GelMA hydrogel during 5 days immersed in cell culture medium.

Moreover, preliminary tests of the bioprinting of multiple layers (1 or 2 layers) were also performed. Specifically, the second layer was printed after the crosslinking

of the first layer was completed, and, after rotating the sample of 90° in order to obtain a grid-like pattern (see Figure 7.1 c). A total of 36 samples was tested in the different experimental conditions. After the bioprinting process was completed, the samples were immersed in cell culture medium at 37 °C for 5 days (Figure 7.1 b).

Each day, an optical microscope was used to measure the distance of the line pattern, always in the same specific points, in order to observe the variation of the hydrogel structure during time in physiological conditions, i.e., its biodegradation. Two examples for a single and a double layer are reported in Figure 7.1 b and c, respectively. The percentage variation of the hydrogel structure and dimensions with respect to the one measured on the first day was then plotted in order to understand if an optimal cross-linking condition could be identified (see Figure 7.2). The obtained results revealed a high variability of the UV crosslinking process. A higher modification of the printed structure was observed in case of the bioprinting of the double layer for higher power (1500 mW) and longer UV exposure time (80 s and 100 s)(see Figure 7.2, b), while, in case of a single layer these same conditions resulted as some of the best ones in terms of smaller % variation in time. After numerous bioprinting tests, the standard UV crosslinking condition, suitable for both single and double layer, was chosen to be 100 seconds of UV exposure time with a UV power lamp of 1000 mW. This condition resulted extremely good in case of double layer, while, in case of a single printed layer, an initial significant variation of 16% is observed up to day 3, but then the processes tended to reach a stabilization condition.

After the preliminary UV crosslinking optimization, several inks composition were tested in order to identify the optimal bio-ink for the selected application. As already mentioned at the beginning of this section, the two selected hydrogels were mainly CNT-GelMA and PEGDA-GelMA. Despite the CNT-GelMA hydrogel and the PEGDA polymer where kept as constants, different composition of the inks varying e.g. the amount of CNTs or the hydrogel mixed to PEGDA polymer where tried. Due to the significant amount of trials performed it has been chosen to summarize all the results in a table structure. Some additional details will then be given for the most relevant trials throughout the section. In Table 7.1, are reported all the different ink compositions tested, the used needle and the main considerations regarding the final outcome of the bioprinting. the two optimal conditions selected are shown in blue. No significant difference was observed in the CNT-GelMA hydrogel by modifying the CNTs concentration from the initial 1.6 mg/mL to 1.0 mg/mL. The same happened by varying the GelMA quantity from 8% to 5%. The 8% GelMA composition was at last select only due to a slight increase of the solution viscosity which allowed an easier bioprinting process. As if will be discussed in the next paragraphs, it was possible to print the CNT-GelMA ink also using the G32 needle (inner diameter 110 μm). In this case, the resolution was increased but

multiple layers where necessary in order to have a strong and robust constructs (see the discussion of Figure 7.4).

Ink	Needle	Comments
CNT-GelMA (CNT 1.6 mg/mL, 8% GelMA, 1% PI)	**G30, G32**	**Good printability, higher resolution with G32 needles but more layers were necessary in order to have a good hydrogel layer.**
CNT-GelMA (CNT 1 mg/mL, 8% GelMA, 1% PI)	G30, G32	Good printability, higher resolution with G32 needles but more layers were necessary in order to have a good hydrogel layer.
CNT-GelMA (CNT 1.6 mg/mL, 5% GelMA, 1% PI)	G30, G32	Good printability, higher resolution with G32 needles but more layers were necessary in order to have a good hydrogel layer.
CNT-GelMA (CNT 1 mg/mL, 5% GelMA, 1% PI)	G30, G32	Good printability, higher resolution with G32 needles but more layers were necessary in order to have a good hydrogel layer.
PEGDA-GelMA (20% PEGDA, 8% GelMA, 1% PI)	**G30**	**Good Printability. Sometimes the needle was blocked.**
PEGDA (20% PEGDA, 1% PI)	G30	The ink was very liquid, easily dissolved in DPBS.
PEGDA (10% PEGDA, 1% PI)	G30	Too liquid to be printed.
PEGDA (30% PEGDA, 1% PI)	G30	The ink was very liquid, easily dissolved in DPBS.
PEGDA (40% PEGDA, 1% PI)	G30	The ink was very liquid, easily dissolved in DPBS.
PEGDA-Gelzan (gellan gum) (20% PEGDA, 0.1% Gelzan, 1% PI)	G30 (often blocked), G23	Too liquid to be printed.
PEGDA-Gelzan (gellan gum) (20% PEGDA, 0.5% Gelzan, 1% PI)	G30 (often blocked), G23	Ink more viscous but 0.8% gellan gum was better.
PEGDA-Gelzan (gellan gum) (20% PEGDA, 0.8% Gelzan, 1% PI)	G30 (often blocked), G23	Best PEGDA ink printability, extremely good behavior during culture (almost no degradation even after 5 days of culture). Cells were not spreading on it. Line too thick with G30.
PEGDA-Gelzan (gellan gum) (20% PEGDA, 1% Gelzan, 1% PI)	G30 (often blocked), G23	Too viscous to be printed.
CNT-Gelzan (CNT 1 mg/mL, 0.8% Gelzan 1% PI)	G30, G23	Good printability, extremely good degradation but cells are not spreading to its surface at all.

Table 7.1 Summary table with the most relevant inks/needles combination used during the bioprinting process.

Several trials were also performed in order to print PEGDA-only hydrogel, in different concentrations (10 %, 20 %, 30 % and 40 %). This trial was designed to understand if it was possible to remove the GelMA hydrogel from the PEGDA

solution in order to further reduce the amount of cardiac cells adhering on the PEGDA supporting layer. Nevertheless, the PEGDA-only solution resulted always too liquid in order to be printed. The main issue related to the excessive fluidity of the solution was related to the effectiveness of the crosslinking process. In fact, the presence of water is essential for the correct photo-crosslinking activity of the PI. If the printed construct dries out too quickly, hence before the sample is placed under the UV lamp, no crosslinking will occur when it will be exposed to UV light, resulting in the dissolution of the printed construct in few minutes when immersed e.g., in DPBS or in cell culture medium. Due to the thinness of the printed lines, ink drying was often observed before the UV step in case of too fluid solutions. Despite the concentration of the PEGDA polymer was increased up to 40%, no significant increase of the solution viscosity was observed. Therefore the bioprinting of PEGDA-only hydrogels was stopped. Several trials where then performed by mixing the PEGDA polymer with gellan gum, a biocompatible material, approved by the FDA [247], recently gaining always more interest for tissue engineering applications [248].

Different concentration of gellan gum, also commercially known as Gelzan (Sigma Aldrich, USA), were tested: 0.1 %, 0.5 %, 0.8% and 1%. The solution containing 1% gellan gum resulted too viscous to be printed with the presented system and the selected needles while the 0.1 % one still was too liquid when mixed to 20 % PEGDA. The optimal concentration for the bioprinting process was found to be 0.8 % and some results of both bioprinting constructs and cell culture on the scaffold will be shown in the next sections (Section 7.1.1 and 7.2). Due to the observed superior resistance against biodegradability of the PEGDA-Gellan Gum hydrogel, which showed no apparent signs of biodegradation during 5 days of culture of cardiomyocytes (see Section 7.2), 0.8 % of gellan gum was also added to the CNT-GelMA solution. Nevertheless, to the absence of any anchoring sites for cell on gellan gum [248], no cardiac cell proliferated on the created material (see section 7.2). Therefore, the original solutions of CNT-GelMA and PEGDA-GelMA hydrogel solutions (in blue in Table 7.1) where used afterwards to continue the bioprinting experiments.

After these preliminary results, some tests were performed to understand, instead, the variability between the dimensions of the structure designed with the CAD software and the final bioprinted construct (Figure 7.3). A test serpentine structure with a line spacing of 500 μm was chosen as sample (see Figure 7.3 a). Due to the physical width of the printed ink line, which resulted to be of the order of 200 μm in case of CNT-GelMA printed with a G30 needle, the final spacing between the pattern lines resulted to be $\sim$ 300 μm. This is an important detail to consider when designing the code for the bioprinter in order to avoid the unwanted connections of the different lines of the design. As shown in Figure 7.3 b, for higher line distances a more significant difference between the expected and the obtained line spacing was

observed. This gap was then observed to decrease as the spacing between the lines was reduced.

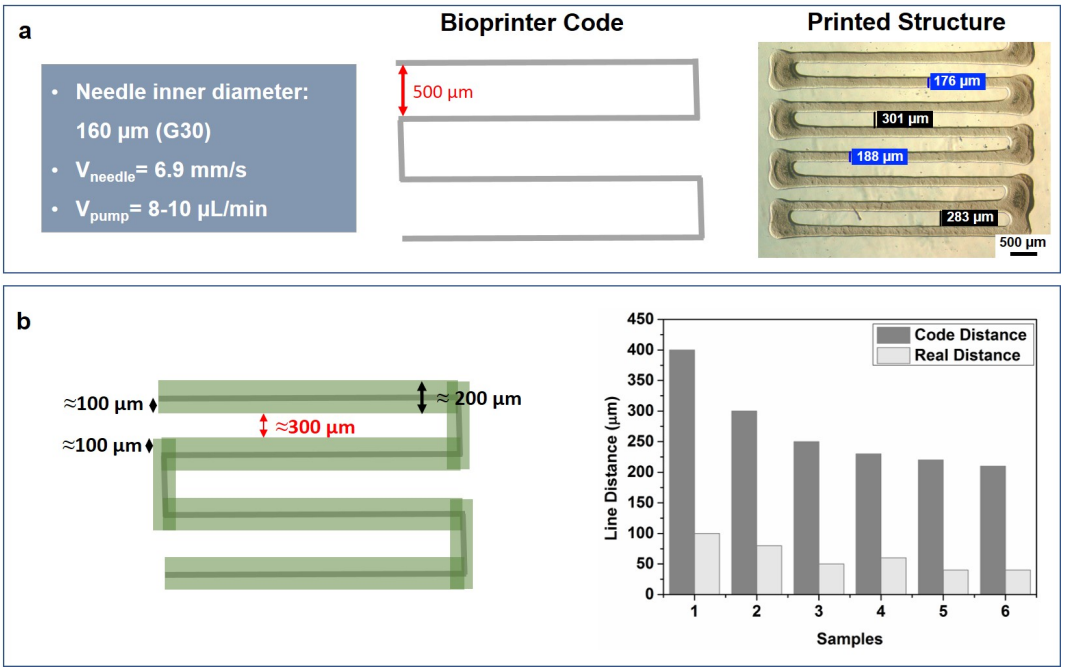

Fig. 7.3 Comparison of the target distance of the printed pattern, as set on the bioprinting software instructions (a), with the actual distance obtained after the bioprinting process. The actual distance between the bioprinted lines was measured on 6 different CNT-GelMA test samples, with different line spacing codes between 400 um and 200 um (b).

An additional optimization of the bioprinted process performed was related to the maximum achievable resolution of the final printed constructs. This optimization was mainly related to the CNT-GelMA ink. In fact, in case of the PEGDA-GelMA one, it was not possible to use needles smaller than G30 due to the obstruction of the needle caused by the solution viscosity. Nevertheless, due to the support nature of the PEGDA-GelMA hydrogel and to the necessity to have a spaced pattern to decrease the final stiffness of the PEGDA layer, no further optimizations were performed in order to decrease the final resolution of the PEGDA-GelMA layer. Instead, to improve the final resolution of the CNT-GelMA layer, more relevant for the cells functional growth, the needle was changed from the G30 (inner diameter 160 μm) to the G32 (inner diameter 110 μm. A significant difference in the bioprinting results was observed (see Figure 7.4). At first, it can be observed by comparing Figure 7.4 b and Figure 7.1 b, that a single layer printed with the smaller G32 needle resulted extremely thin, almost not visible, i.e., not robust enough to sustain a beating cardiac cell culture on its surface. Therefore, the bioprinting of multiple layers was necessary in order to strengthen the final printed construct. Differently from the initial double layer biodegradation experiments, in this case the crosslinking of the hydrogel was

performed at the end of the bioprinting of the multiple layers, instead that after the individual crosslinking of each individual layer, resulting, experimentally, in a more reliable crosslinking of the final hydrogel. In Figure 7.4 c, the superimposition of 10 different bioprinted layers can be observed. As visible from the magnifications of Figure 7.4 c and d, the 10 layers are perfectly superimposed one on top of the other forming a sharp structure with a final resolution of about 150 μm.

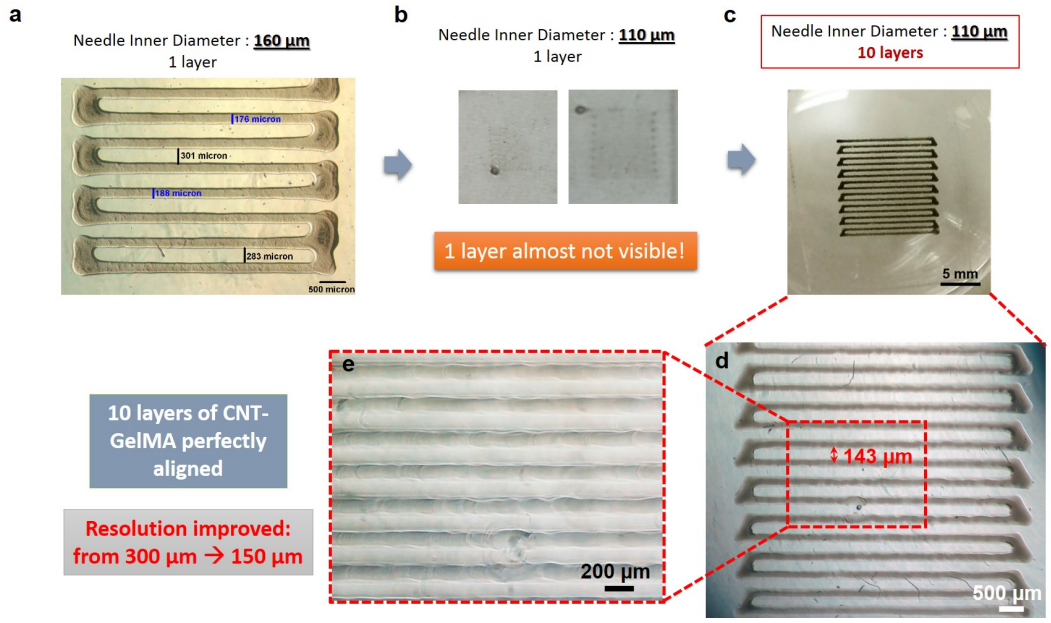

Fig. 7.4 Improvement of the bioprinting process resolution by reducing the diameter of the used needle and by increasing the number of printed layers.

By comparing these results with the ones obtained using the G30 needle, Figure 7.4 a, it can be noticed that the final resolution was improved from 300 μm to 150 μm, i.e. the final achievable resolution was doubled. Additional tests where performed with also different numbers of layers, e.g., 7 as shown in Figure7.5 a. This is linked to the fact that, in case of the bioprinting of test serpentine structures, the bioprinting process is extremely quick (less than 1 minutes) also in case of multiple layers but, the printing of the complete fish-like structure may take up to 2 minutes for a single layer. Therefore, a trade-off must be found in order to have a sufficient number of layers for the construct robustness and a bioprinting time not too high so that the bioprinted layers will not dry out before the UV crosslinking step.

In Figure 7.5 also one example of PEGDA-GelMA hydrogel pattern can be observed (Figure 7.5 b). In this case, a commercially available fluorescent paint was added to the transparent PEGDA-GelMA ink in order to be able to perform the imaging of the printed samples. At last, the superposition of the PEGDA-GelMA hydrogel on the CNT-GelMA printed constructs is also reported in Figure 7.5 c.

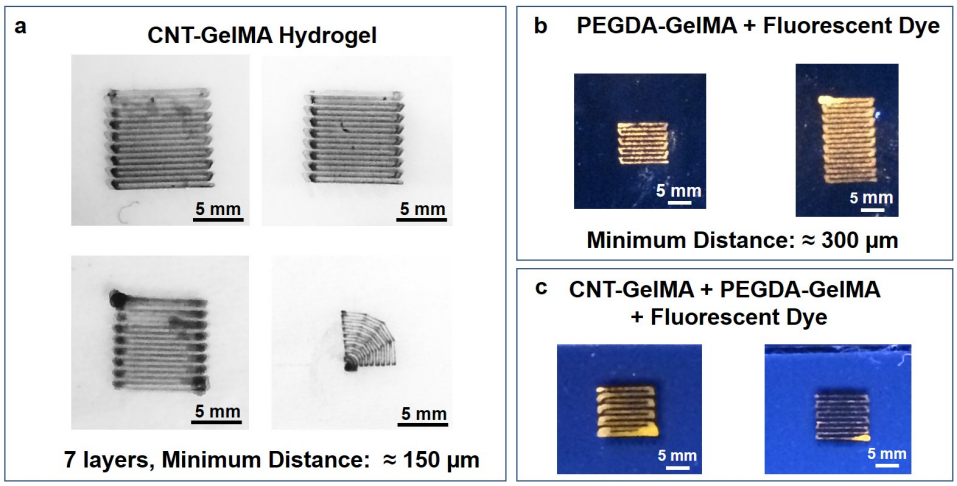

Fig. 7.5 Bioprinting optimization of both CNT-GelMA and PEGDA-GelMA hydrogels. A commercial fluorescent dye was embedded in the PEGDA hydrogel for imaging purposes.

At last, a final additional optimization of the UV crosslinking process was performed by trying to crosslink the printed sample while immersed in a thin layer of DPBS. This trial was supported by the fact that in this way, plenty of water molecules can be available for the crosslinking of the PI and, the sample drying can be further avoided. Therefore, three serpentine test patterns of CNT-GelMA GelMA hydrogel were printed and crosslinked in standard dry conditions for 100 s, in DPBS for 100 s or in DPBS for 200 s (Figure 7.6). The sample was then kept in DPBS for 4 days and the imaged again. As visible from the results (Figure 7.6), higher degradation and wrinkles formation can be observed on the samples printed in the dry or 100s DPBS conditions. The sample crosslinked 200 s in DPBS, instead, despite starting to detach from the glass slide, revealed a less wrinkled and more stable structure if compared with the others.

Due to the initial stage of the bioprinting process of the project developed at the Khademhosseini Laboratory in Boston, numerous fundamental and time consuming steps were necessary in order to establish a reliable bioprinting protocol suitable then also for the bioprinting of more complex fish-like structures. After this preliminary work was concluded, despite continuously updating, different fish-like structures where bioprinted as it will be discussed in Section 7.1.1.

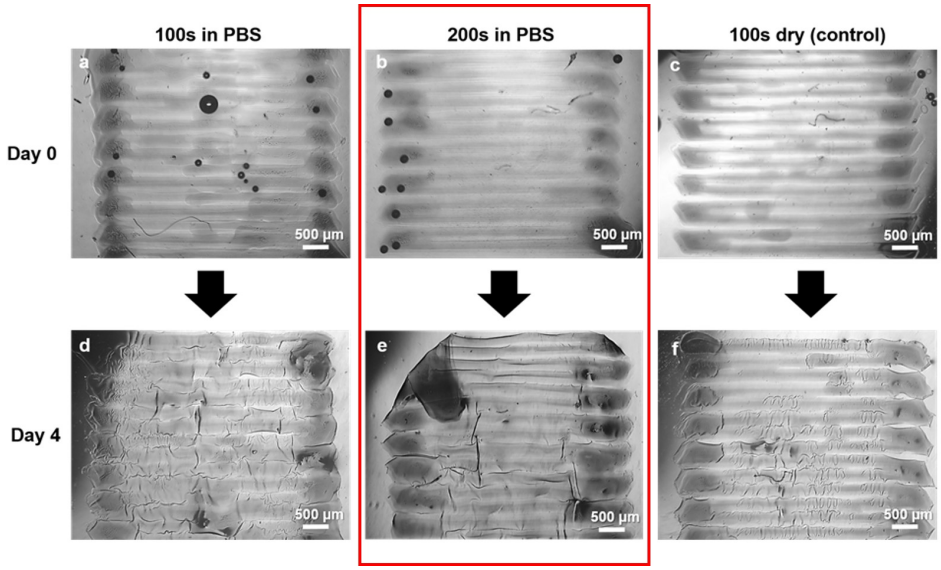

Fig. 7.6 Optimization of the UV cross-linking procedure by performing it when the construct is immersed in DPBS. Pictures where acquired both after the crosslinking (Day 0) and after 4 days that the samples were immersed in DPBS (Day 4).

7.1.1 Bioactuator Geometrical Design and Bioprinting

One of the main reasons while the bioactuator fabrication technique was modified from UV photolithography to bioprinting is related to the higher flexibility of the latter to easily fabricate curved complex geometries. Despite, as it will be seen during the following discussion, the final resolution of the bioprinted constructs cannot yet achieve the same values of the UV-photolithography ones ($\sim 50\ \mu$m), a more flexible layout was obtained that can better mimic the muscle structure of the manta batoid ray. Therefore, one of the first steps performed in parallel with the bioprinting optimization was the design of a new layout for the manta-like actuator capable to more reliably mimicking the physiognomy of the muscular structure of the manta batoid ray. The new Blender layouts for both the PEGDA-GelMA layer (mimicking the cartilage joints as explained in Chapter 5) and the CNT-GelMA one (associated instead to the muscle fibers of the manta ray fins) are shown in Figure 7.7. After simulating, testing and optimizing the bioprinting code as described in Chapter 5, the bioprinted constructs reported in Figure 7.8 were obtained. As previously discussed, both a single (Figure 7.8 a) and a double layer (Figure 7.8 b) were tested. Also in this case, the double layer resulted more robust in view of the next cardiac cell culture (as it will be shown in Section 7.2).

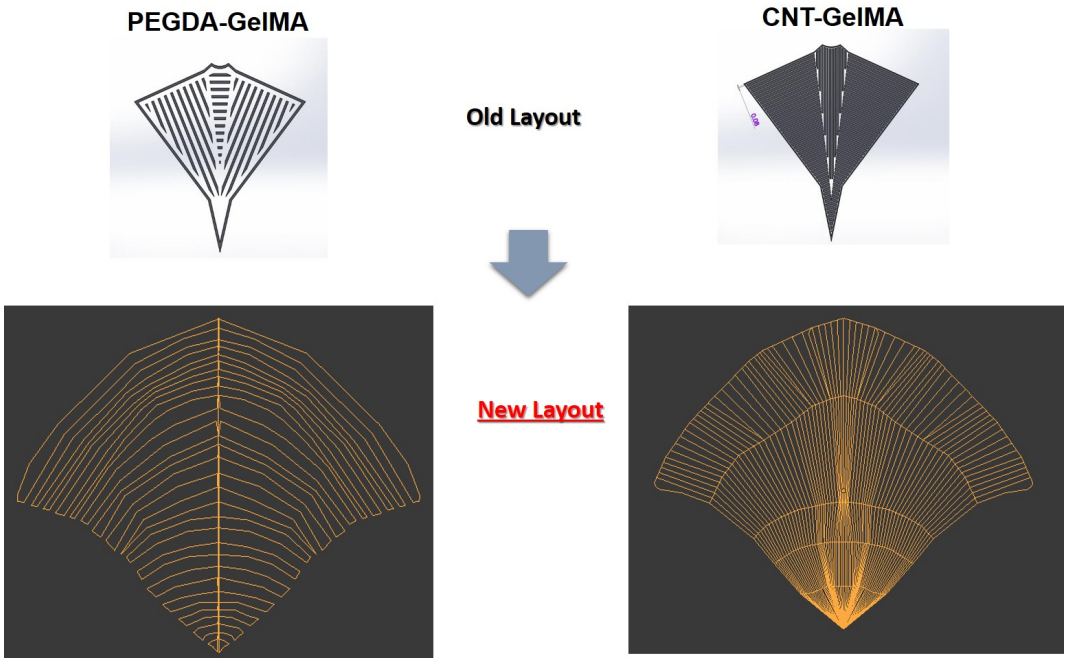

Fig. 7.7 Comparison between the previous straight fish layout (top) and the new curve one (bottom) for both the PEGDA-GelMA and the CNT-GelMA hydrogels. Also reported in [161].

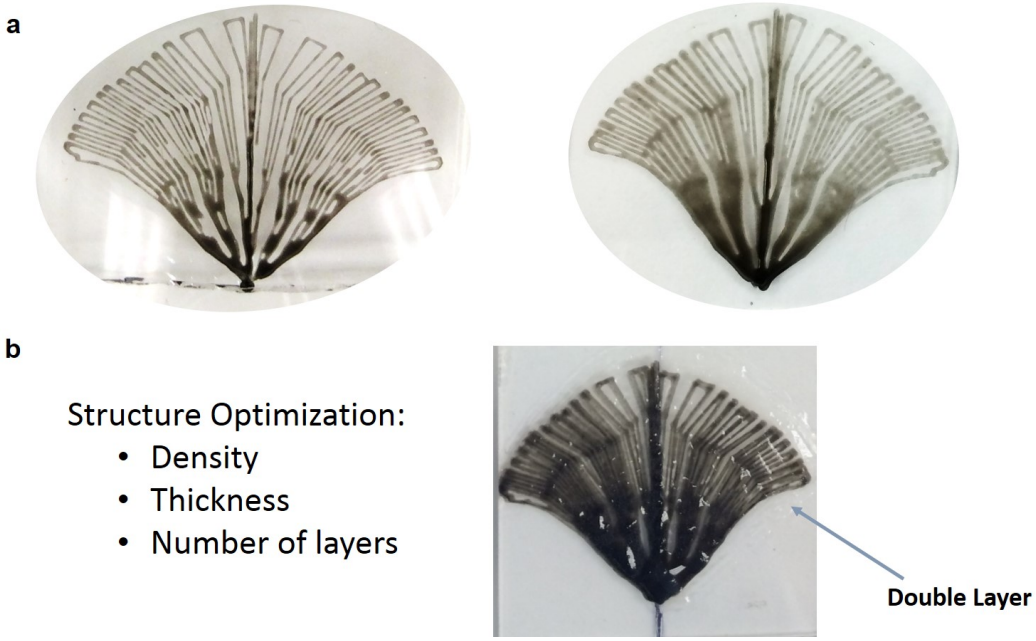

Fig. 7.8 Examples of CNT-GelMA manta-like constructs printed with the curve layout both with a single (a) or a double (b) layer.

In Figure 7.9 are instead reported different results of the bioprinting of the PEGDA-GelMA layer. At first, a sample structure with mm-spacing between the different lines was printed on top of a CNT-GelMA layer (Figure 7.9 a) in order to test the superposition and alignment of the layers. Then, a denser layout was also printed, with embedded fluorescent dies (Figure 7.9 b and c). As visible from Figures 7.9 b and c, a slight variability between different bio-printed constructs was present, for the same design, probably due to different environmental/experimental conditions like, e.g., the temperature, the needle wearing or the ink stability. All these parameters should need a further investigation in order to improve the repeatability of the printed constructs, especially in view of the extremely low resolution wanted.

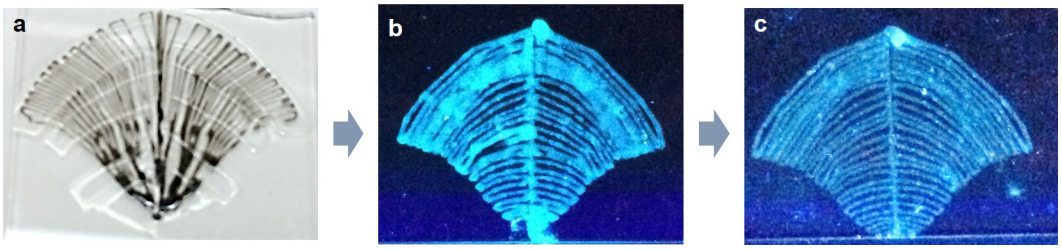

Fig. 7.9 Examples of PEGDA-GelMA manta-like constructs printed with the curve layout both on top of the CNT-GelMA layer (a) or stand-alone with embedded fluorescent dye for improved imaging contrast (b).

After printing, the support glass of the bioprinted constructs was cut to fit a common laboratory 6 wells plate and immersed in DPBS until ready for the cardiac cells culture. The day preceding the culture the samples where then sterilized in order to limit the risk of bacterial contamination during the cardiac culture. Specifically, at first the samples were transferred in a new, sterile 6 wells plate under a biological laminar flow hood, then 4 consecutive washing steps, each one 15 minutes long, with sterile DPBS with 1% Penicillin-Streptomycin (P/S) antibiotics were performed. After these, additional 4 washing in the cardiac cell culture medium (also containing 1% P/S) for 30 minutes each were performed. The numerous washing steps are necessary in order to be sure to have removed any trace of contaminants for the 3D-like structure of the hydrogels. Standard sterilizations methods usually involve the washing with 70 % ethanol and UV light sterilization. Nevertheless, in the present work, the porosity of the used materials make not advisable the use of ethanol, since some residues may still remain and provoke the death of the cell culture, while, UV sterilization may cause over-crosslinking resulting in cracks formation along the printed structures. Nevertheless, the presented protocol was optimized during numerous trials and lead to successful sterilization of the bioprinted samples before the culture. Before proceeding to the next section, where the culture of cardiac cells on the bioprinted constructs will be presented, a second fish-like layout tested will be presented. Specifically, in order to fully investigate the potentialities of the selected

approach, another fish-like structure, favorable for the actuation dynamic of the actuator was tested. Therefore, the physical structure of the *Dactyloptena Orientalys* fish, often known also as flying fish, was mimicked. The fish presents a complex geometry with a central body and extended lateral fins, similar to wings, that allow the fish to perform remarkable jumps above the surface of the water like if they were flying (see Figure 7.10 a).

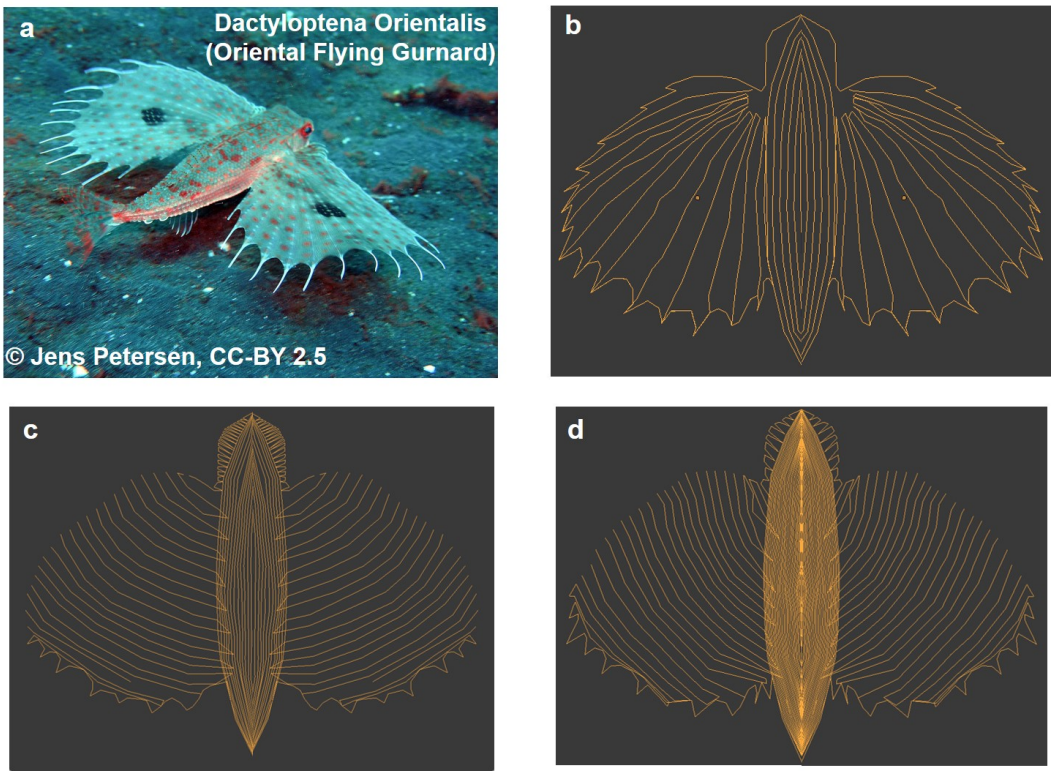

Fig. 7.10 New fish-like actuator designed mimicking the *Dactyloptena Orientalis* (a). (b) PEGDA-GelMA layer design. (c) and (d) two different CNT-GelMA layer designs with slightly different pattern orientation. Image (a) was reproduced from Wikipedia, ©Jens Petersen, licensed under a CC-BY 2.5 license.

At first, the fish structure was designed using the Blender software, as previously done also in the case of the manta ray fish. The PEGDA-GelMA layout, Figure 7.10 b, was designed according to the main bone structure of the fish, again, acting as principal support. The CNT-GelMA layer, instead, was designed with a denser line spacing in the central body and with a perpendicular orientation with respect to the PEGDA-GelMA one. Specifically, two different orientations of the patterned line, more or less tilted with respect to the PEGDA-GelMA lines orientation, were tested (Figure 7.10 c and d). The motivation was to see if it was possible to achieve a different actuation dynamics, once the actuator was seeded with beating cardiomyocytes,

according to different geometries. Unfortunately, due to the limited time spent at the Khademhosseini laboratory, it was not possible to further verify this assumption.

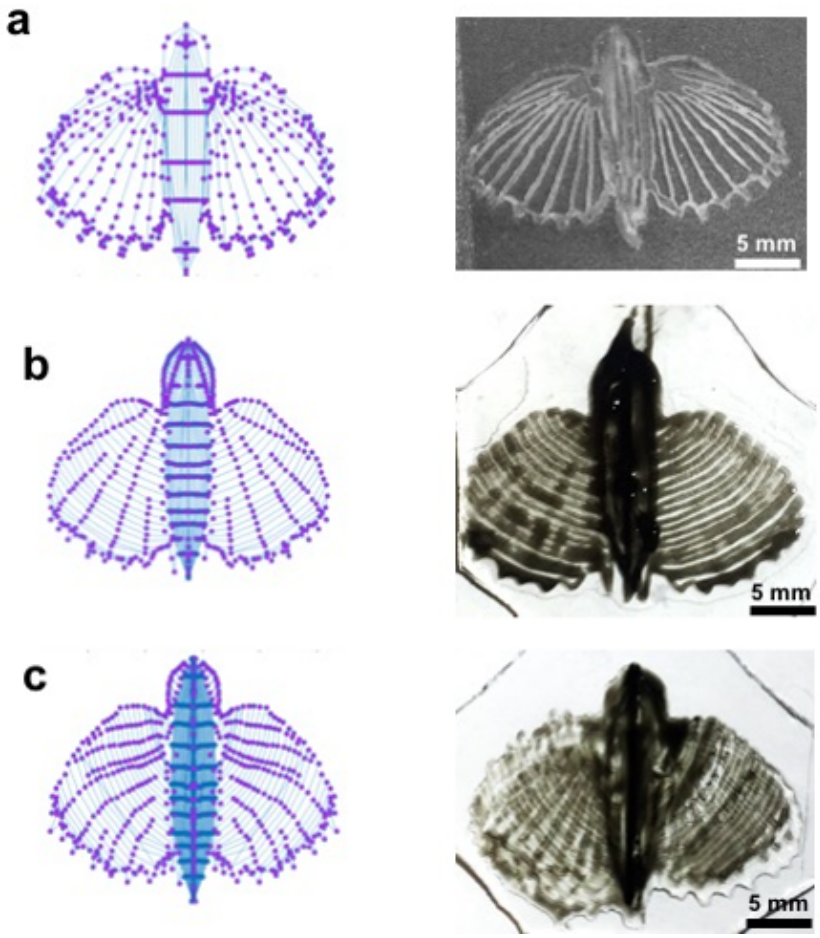

Fig. 7.11 Examples of the Matlab simulations of the printed construct final structure and the actual printed structure mimicking the *Dactyloptena Orientalis* for both PEGDA-GelMA (a) and CNY-GelMA (b,c) hydrogels.

In Figure 7.11 are reported different simulations of the bioprinted structures, with the corresponding bioprinted construct (all the samples were printed using a G30 needle). As previously anticipated, due to the different ink viscosity, the PEGDA-GelMA pattern results always with a larger spacing than the CNT-GelMA one, fact also related to the impossibility to use the G32 needle with that hydrogel. In the specific samples reported in Figures 7.11 b and c, the CNT-GelMA layer was printed on top of the PEGDA-GelMA one, although difficult to see with naked eye.

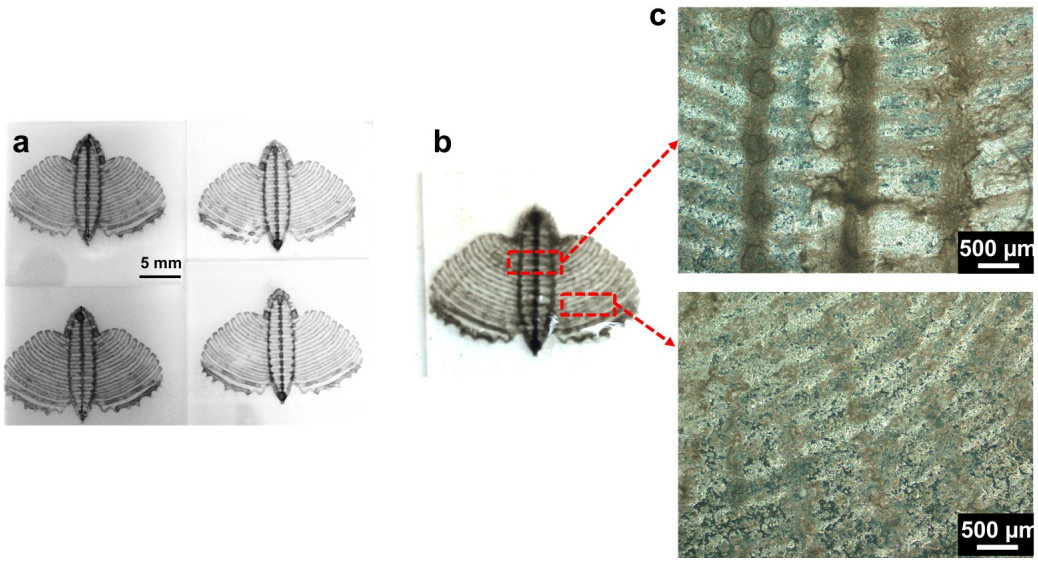

Fig. 7.12 Examples of the CNT-GelMA bioprinted constructs mimicking the muscle structure of the *Dactyloptena Orientalis*.

In Figure 7.12 are reported some additional examples of printed CNT-GelMA constructs, printed on top of the PEGDA-GelMA layer, using the smaller G32 needle. As expected, the final printed construct layout resulted more defined than in case of the G30 needle although additional printed layers would be necessary in order to improve the robustness of the construct during culture.

At last, as anticipated in Section 7.1, the experimental results obtained in case of bioprinting with PEGDA-Gellan gum ink are shown. At first, a summary of the different inks compositions tried, with the corresponding printability results are reported in Figure 7.13 a. The addition of 0.8 % of gellan gum to both 10 %, 20 % and 30 % PEGDA hydrogel resulted in all the cases in a correctly printable structure with good crosslinking. Nevertheless, the addition of gellan gum above this limit produced, in any case, a not printable, too viscous ink. One example of PEGDA-Gellan Gum construct with embedded fluorescent dies is shown in Figure 7.13 b. The addition of gellan gum to the PEGDA hydrogel resulted in a increased resistance to biodegradation of the scaffold during the cardiac cell culture. This was proven by the fact that, after 5 days of culture, while in the normal CNT-GelMA/PEGDA-GelMA samples some degradation of the structure was always present (see Section 7.2), in case of gellan gum addition, the sample completely maintained its structural integrity, as shown in Figure 7.13 c, so that it was even possible to pick the sample up using tweezers without damaging or breaking it.

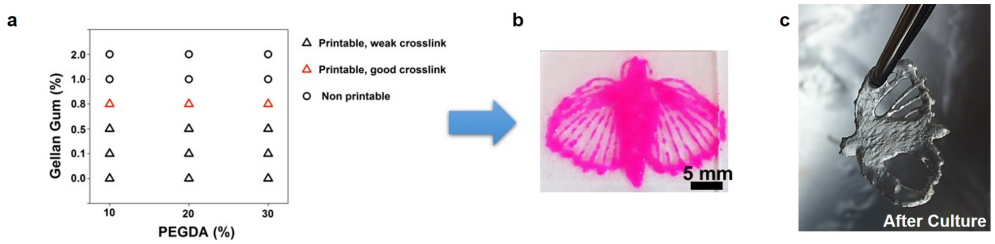

Fig. 7.13 Bioprinting results with the PEGDA-Gellan gum hydrogel. (a) Summary table with all the tested inks compositions. (b) Example of PEGDA-Gellan gum printed fish-like construct with embedded fluorescent dies. (c) PEGDA-Gellan Gum printed construct after 5 days of culture with cardiac fibroblasts.

7.2 Cell Culture on Bioprinted Constructs

In Figure 7.14 the standard 6 wells plates used for the culture of cardiac cells on the bioprinted constructs are shown. The sample still present the supporting TMSPMA-coated glass underneath, properly cut to fit the wells. Due to the large area of the bioprinted construct ($\sim$ 2 cm x 2 cm) a high amount of cardiac cells, around 2 million cells per well, is necessary in order to obtain a good coverage of the surface. Therefore, a custom-made ring, done using standard hot glue, was added around the bioprinted structure (see Figure 7.14 a). This was done in order to confine the cells on the scaffold area as much as possible. The hot glue rings are then sterilized together with the sample and they are then detached at the end of the culture. No signs of cellular death were observed by employing this material in the cell culture. In Figure 7.14 b, is shown a typical well plate at the end of the cell culture. The thicker samples showed less structural damages, while, the thinner ones, were considerably degraded during the culture. This is the reason why the robustness of the printed structure is a key factor for the successful outcome of the experiment.

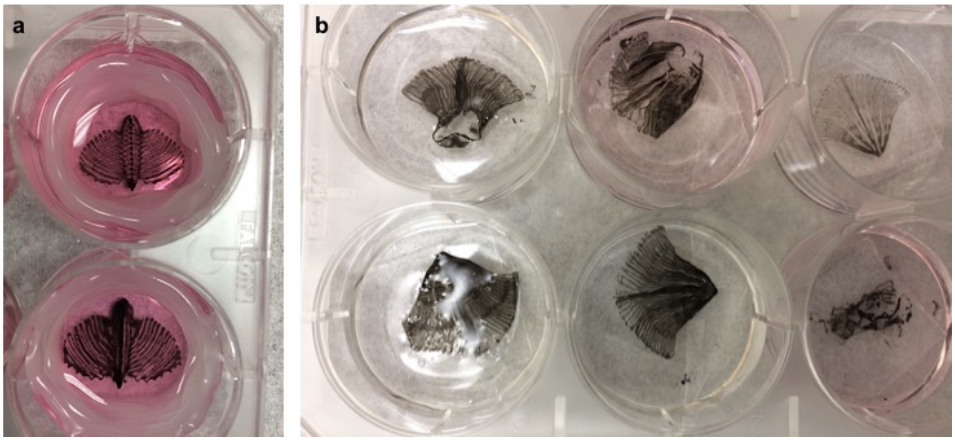

Fig. 7.14 Examples of bioprinted constructs cultured in standard 6 wells plates before (a) and after (b) culture.

At first, the culture of cardiomyocytes was tested on the sample CNT-GelMA serpentine patterns. In Figure 7.15 are reported some among the optimal phase contrast images of different sample patters after that cardiomyocytes were cultured on their surface for 2 days. As visible from the results, a substantial cellular growth is observed also in between the deposited CNT-GelMA lines. As already discussed in [1], a preferential orientation of the cardiomyocytes along the CNT-GelMA pattern is observed on the bottom cells layers while, as the culture grows and expands, additional layers of cells fill in all the available surface. This behavior contributes to create a uniform cardiac tissue, with a good synchronization of the beating activity. Nevertheless, the actuation dynamics is mainly guided by the bottom cellular layers,

with improved adhesion to the scaffold and superior sarcomere alignment (as also confirmed by the fluorescent images of Figure 7.19.

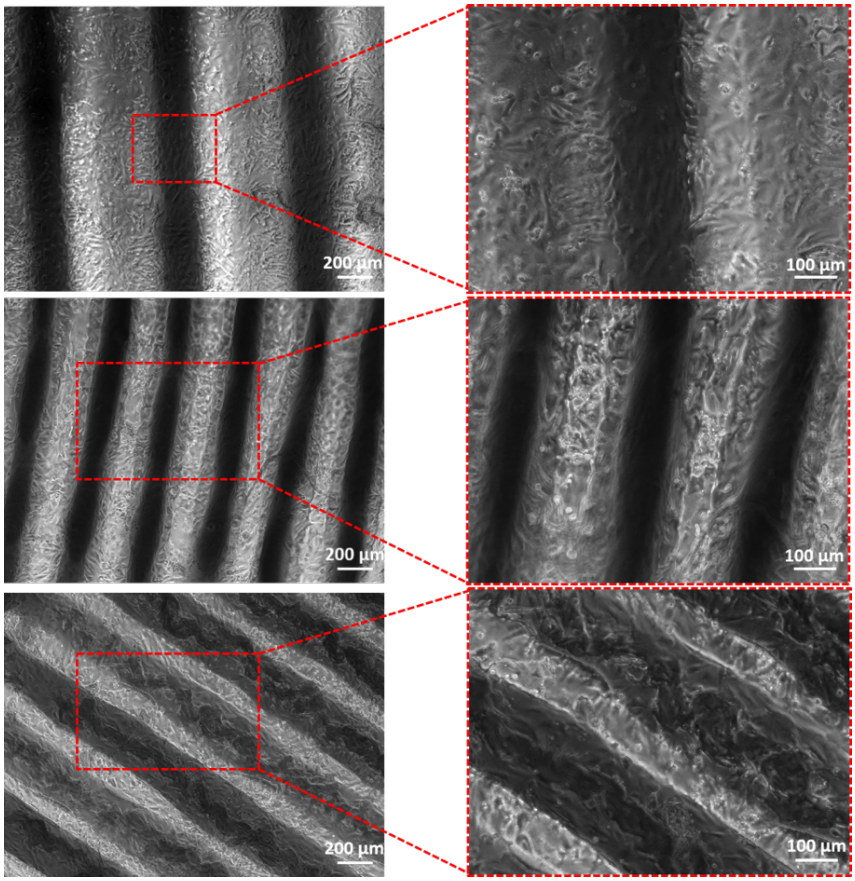

Fig. 7.15 Phase contrast imaging of different bioprinted patterns with cultured cardiomyocytes.

During the phase contrast imaging, the video of the beating activity of the cells were also recorded. Despite some good beating is clearly visible from the phase contrast video, the pixel intensity variation (PIV), can further help to improve the actual visualization and measurement of the beating activity. The PIV method analyzes the variation of the total pixel intensity in time of the stacked images composing the frames of the beating video [249]. This method is widely used in electrophysiology to monitor non invasive the beating activity of cardiac cells as well as the motility of other types of cells [249]. This method can be easily integrated in the open source software ImageJ, commonly used for the quantification of the data obtained from microscopy characterizations. The first step involves the computation of the average intensity picture, averaged on the total acquired frames. Then, this picture is sequentially subtracted to each frame image. In this way, after considering the absolute value and adjusting the brightness/contrast, pictures as the ones reported

in Figures 7.16-b and 7.17-b, can be obtained in which, for each frame, i.e. at each time, the differences of the pixels from the average frame are highlighted. This gives clear evidence of the actual movement of the cardiac cells due to their beating activity. The PIV image processing script already embedded in the software can extract the rhythmic intensity variation in time, over the sequence of frames, obtaining graphs similar to the one reported in Figure 7.16 c. The rhythmic oscillation in PIV values correlates with cardiac contractions, which can then be associated to the beating frequency of the cardiac cells.

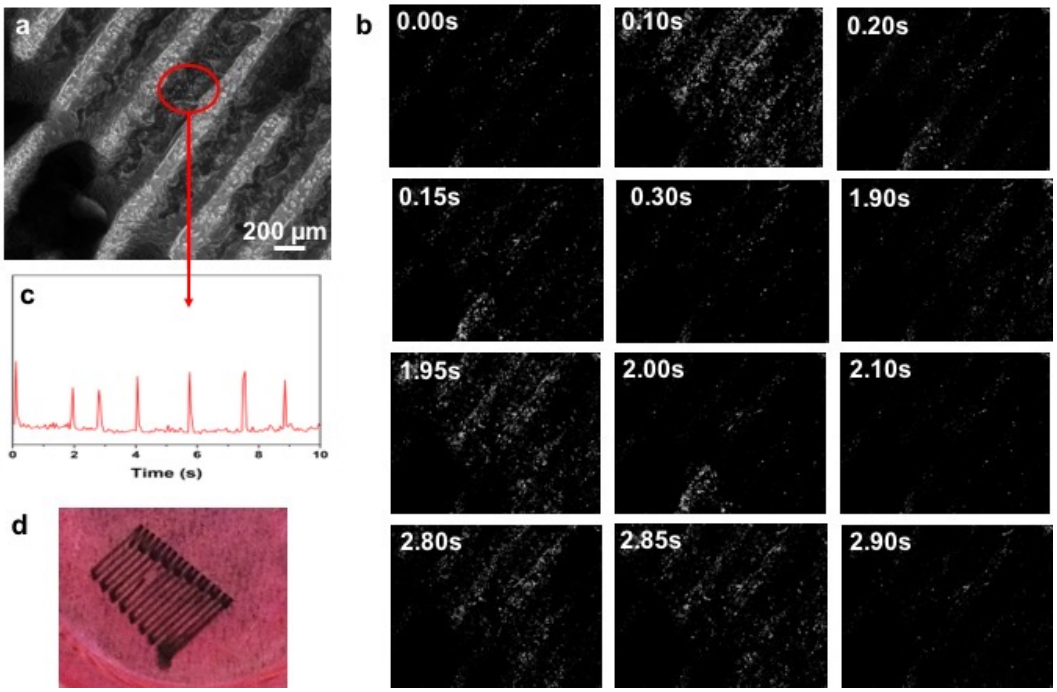

Fig. 7.16 Analysis of the beating behavior of cardiomyocytes on a bioprinted pattern after 1 DIV (a). Pixel Intensity Variation analysis (b) and extracted beating profile (c). (d) Example of the detachment of the sample from the glass slide after the cell culture.

The results of PIV on a beating sample after 1 day in vitro (DIV) are shown in Figure 7.16 a and b. As visible from the different frames, a beating wave propagated across the sample starting from the top right corner and proceeding along the diagonal towards the bottom left one. The PIV z-profile extracted using the ImageJ software revealed the presence of a periodic beating activity, still not completely stable and uniform, with frequency between 0.5 Hz and 1 Hz (Figure 7.16, c).

The intense beating activity of cardiac cells leads to the detachment of the scaffold from the supporting glass slide. In Figure 7.16 d, is reported one example of a printed construct that was starting to detach from the supporting glass due to the cardiac cell culture.

The same measurements were then repeated after 4 DIV (Figure 7.17). During this time usually the increase in the intensity of the beating activity of cells is observed together with a higher synchronization. This is mainly related to the fact that the cells grow and expand (but, as already mentioned in Chapter 2 they do not divide) slowly forming an organized tissue with interconnected gap junctions. As visible from the PIV shown in Figure 7.17 b, a much intense beating activity, with also a wider spatial spreading of the beating wave, is observed if the data are compared withe ones of 1 DIV shown in Figure 7.16 b. Looking at the PIV z-profile (Figure 7.17 c), more defined and uniform peaks are observed with respect to the ones of 1 DIV. Due to the high synchronization of the cardiac tissue the PIV z-profile was also acquired from the whole image, instead than only on a area showing more intense beating in order to reduce the noise introduced by the non-beating regions, as in case of Figure 7.16.

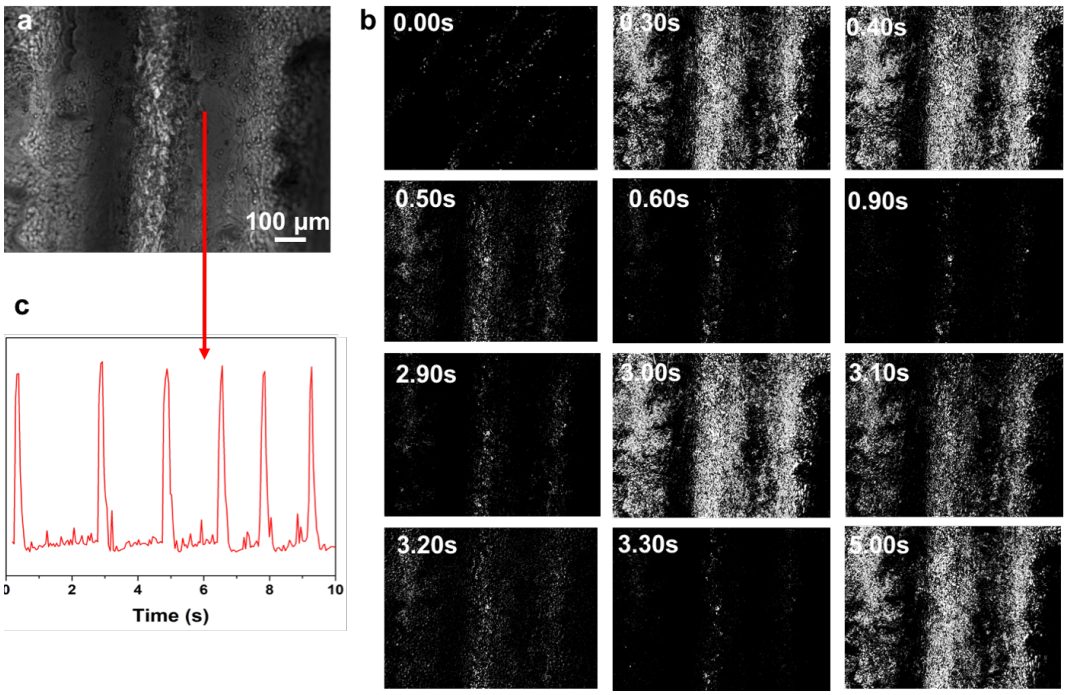

Fig. 7.17 Analysis of the beating behavior of cardiomyocytes on a bioprinted pattern after 4 DIV (a). Pixel Intensity Variation analysis (b) and extracted beating profile (c).

In order to have a better understanding of the structural organization of the cardiac tissue, fluorescent staining of the F-actin filaments and of the nuclei were performed (see Figure 7.18, 7.19 and 7.20). Usually this staining was performed after 5 DIV since at this time a complete tissue organization was observed and, usually from day 5-7 the beating activity of cells started to diminish. For the F-actin staining the anti-actin antibody, already conjugated with the fluorescent label Alexa Fluor®488 (Sigma Aldrich, USA) was used (absorption 495 nm, emission 518 nm).

The nuclei, instead, were stained using the already mentioned DAPI nucleic acid staining (absorption 358 nm, emission 461 nm).

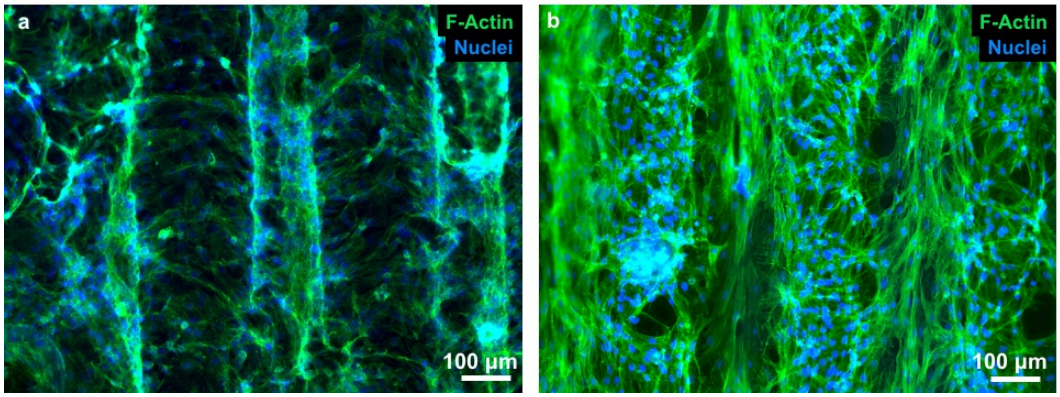

Fig. 7.18 Fluorescent staining of the cardiomyocytes on the bioprinted construct, after 5 DIV, to observe th F-actin and nuclei organization.

As already mentioned in this section and in [1], a preferential alignment of cardiomyocytes along the CNT-GelMA hydrogel structures happens at the very bottom cellular layers, then, the cells keep growing also in between the patterned lines, linking together and forming a complete synchronized tissue layer. This assumptions, despite being published in [1], were also observed in the higher-spaced bioprinted patterns. In Figure 7.18 a, it can be clearly recognized a preferential elongation of the cells along the CNT-GelMA hydrogel. Nevertheless, network-like connections can be observed in between the different hydrogel lines. In this way, the preferential elongation of the muscle structure on the CNT-GelMA hydrogel will lead the direction of the actuation dynamics, while, the interconnection of the different line patterns will contribute to have a good synchronization of the electrical signals transmitted in the cell culture, hence contributing to an efficient beating dynamics. The same staining repeated on a different sample in the same experimental conditions Figure 7.18 b, revealed even a higher cells interconnection between the different layers so that the hydrogel pattern lines can be barely recognized only for the presence of the nuclei on the top-most level. In some cases, the 3-dimensionality nature of the bioprinted construct was increasing the complexity of performing good fluorescent microscope imaging due to the different focal planes present in different parts of the structure. One example is reported in Figure 7.19 where at first the image was focused on the CNT-GelMA pattern, then on the holding substrate and, at last the two focused images were merged together to have simultaneous focus of both the different layers. This result was reported since it can be interesting to notice the different spreading of the cardiomyocytes on the CNT-GelMA hydrogel and on the substrate.

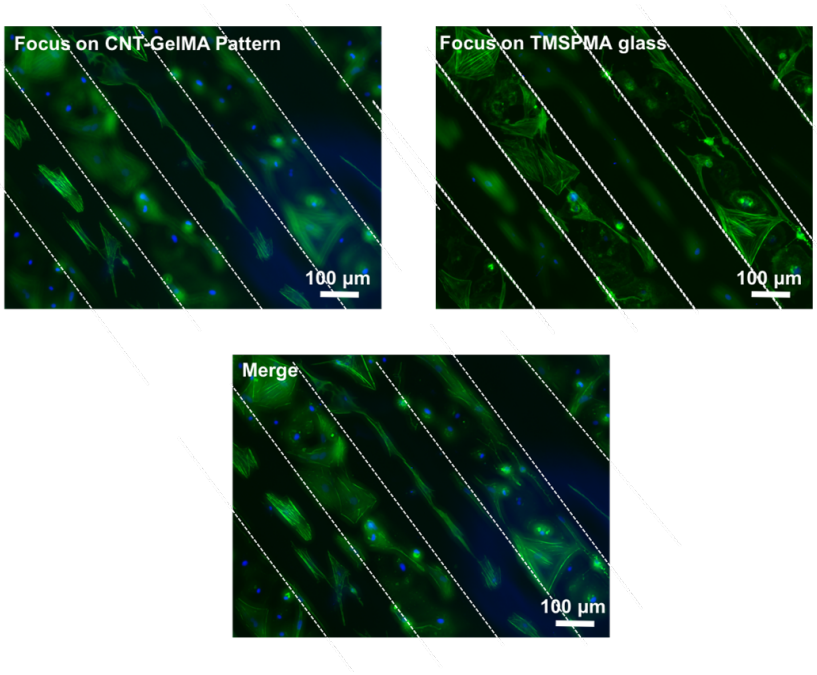

Fig. 7.19 Fluorescent staining of F-actin and nuclei of the cardiomyocytes on the bioprinted samples, after 5 DIV, with details about the three dimensionality of the construct.

A more elongated structure of the cells can be appreciated on the CNT-GelMA hydrogel, which promotes a longitudinal fiber-like cell organization, which is more similar to the myofibrils present in the living organisms. On the supporting substrate, instead, a more rounded and spatially spread cell conformation was noticed, which is less physiologically relevant and, also, not optimal for an effective interconnection of the gap junctions for having a highly-synchronized final tissue.

In Figure 7.20, another F-actin/DAPI staining is shown, with lower magnification, so that a wider portion of the patterned scaffold can be observed. Nevertheless, in order to have a better insight of the different layers forming the tissue construct, confocal microscopy usually is considered a better approach thanks to the possibility to acquire stacks of images at different depths. One example is reported in Figure 7.21, where the immunostaining for the sarcomeric-α-actinin and Cx-43 antibodies was performed, as well as always also the nuclei. As already mentioned in Chapter 2, the sarcomeric-α-actinin staining unveil the structural organization of sarcomeres, the fundamental contractile units of the cardiac cells, while, connexin-43 is one of the most relevant gap junctions protein.

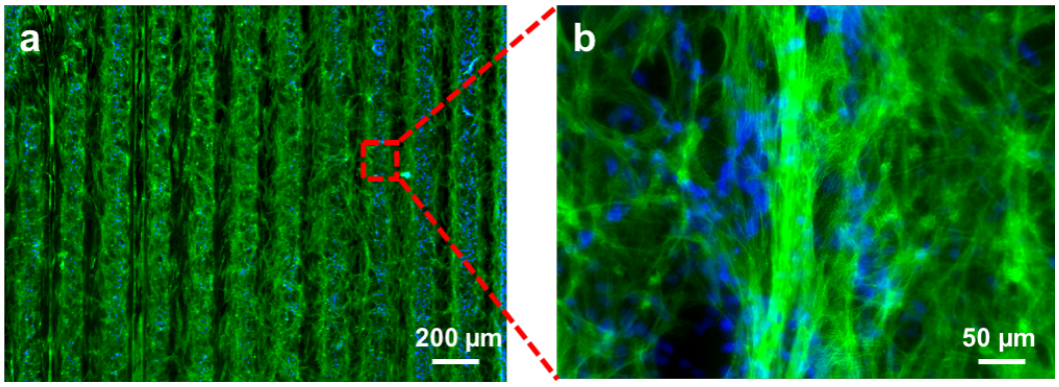

Fig. 7.20 Fluorescent staining of the cardiomyocytes on the bioprinted construct, after 5 DIV, to observe th F-actin and nuclei organization.

The confocal images shown in Figure 7.21, were performed after 5 DIV on the samples that showed higher beating activity (i.e. higher Cx-43 activity). Moreover, the images were acquired at a depth corresponding to the surface of the CNT-GelMA hydrogel line.

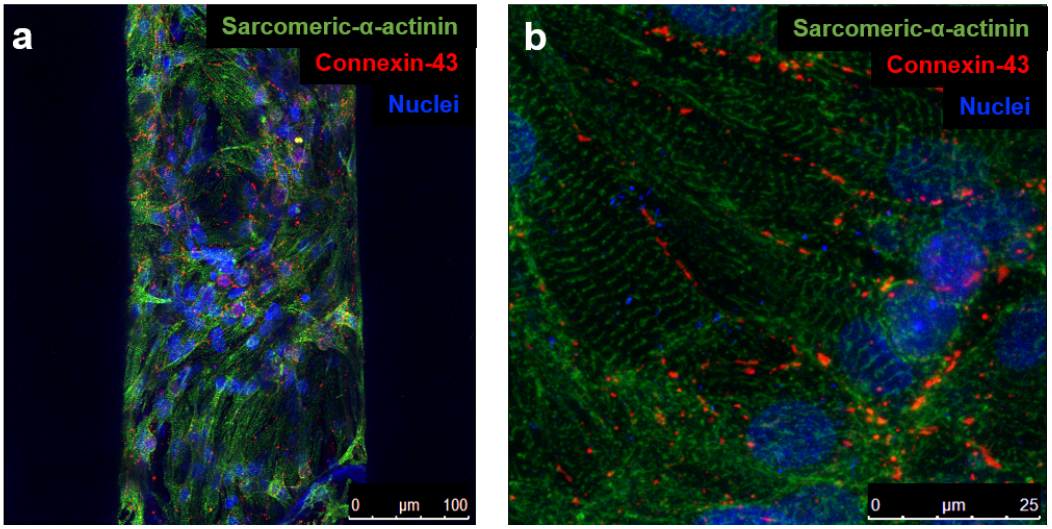

Fig. 7.21 Immunostaining of Sarcomeric-α-Actinin and Connexin-43 on the bioprinted sampled after 5 DIV.

Although a perfect vertical alignment of the fibers, parallel to the hydrogel line was not observed, a general longitudinal trend of cellular growth can be recognized in a S-like shape (Figure 7.21 a). A higher Cx-43 expression can be also recognized in the regions with higher beating activity, due to the more efficient electrical coupling between the cells as also visible from the higher magnification in Figure 7.21 b. In Figure 7.21 b it is also possible to clearly recognize the individual sarcomere

structures, in parallel stacked one after the other, with the red dots corresponding to the individual Cx43 gap junctions.

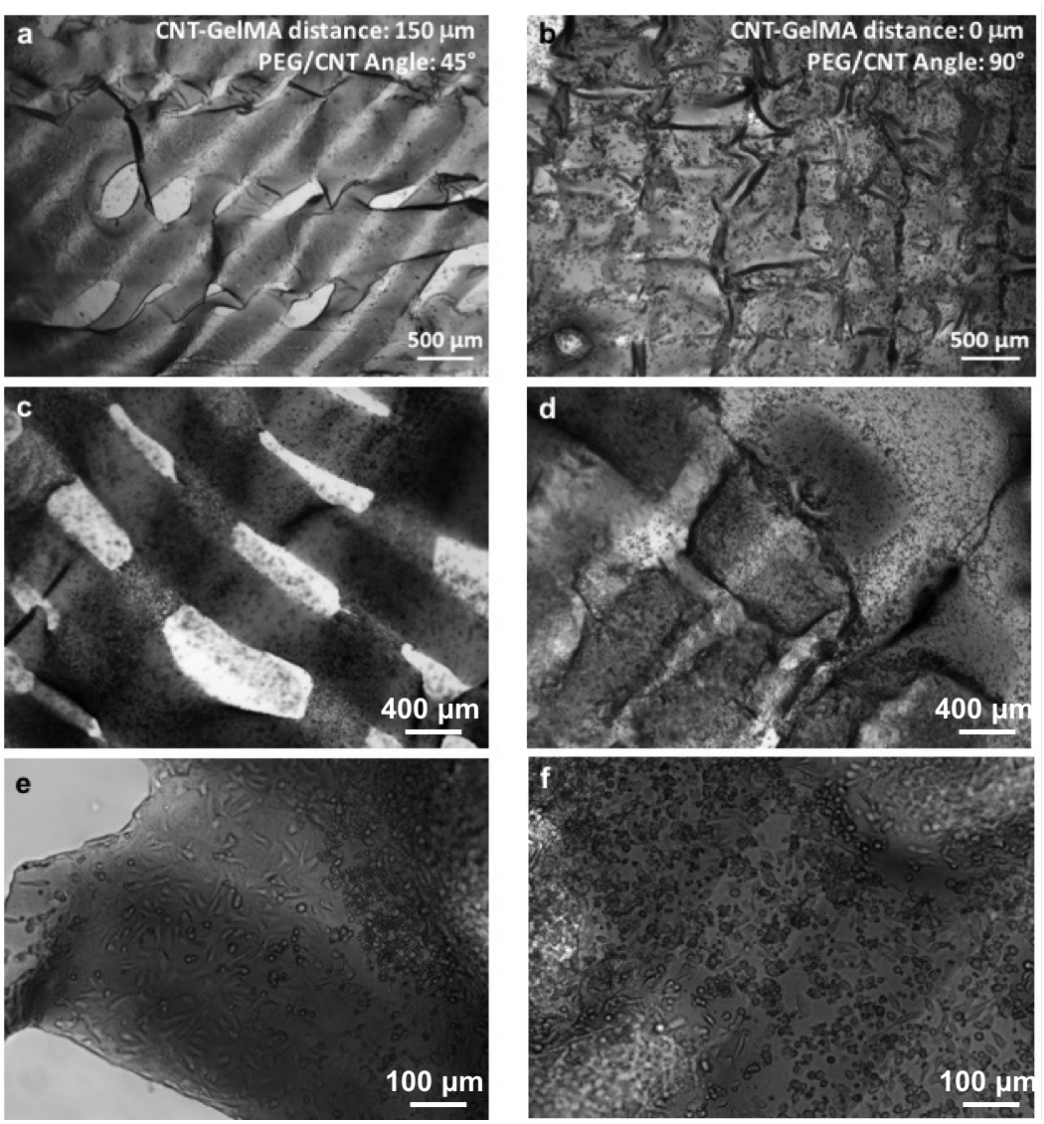

Fig. 7.22 Cardiomyocytes culture on the *Dactyloptena Orientalis* fish structure. The culture resulted unsuccessful leading to cellular death after 1 DIV, as anticipated by the presence of a high number of dead cells.

At last, the same seeding tests of cardiac cells on the whole bioprinted fish-like structures were performed (Figure 7.22). Unfortunately, the cardiomyocytes culture started to die after 1 DIV, due probably to unpredictable issues during the cell isolation procedure. Therefore, only phase contrast images were acquired after 1 DIV and no further imaging of staining was then performed. In the shown examples, the CNT-GelMA layer was printed on top of the PEGDA-GelMA one with different line

spacing. One test was also performed by printing a whole CNT-GelMA layer with to pattern (Figure 7.22 b). The original idea was to observe if a stronger actuation dynamics was observed due to the assumed higher interconnection between the cardiac cells. As visible from the magnifications in Figure 7.22 e and f, ah high number of dead cells is present on the surface (characterized by the typical rounded shape), while, some healthy cardiomyocytes/cardiac fibroblasts, still were starting to spread on the scaffold. Unfortunately, due to the limited period of time spent at the Khademhosseini laboratory it was not possible to personally conclude the analysis of the complete actuation dynamics of cardiomyocytes on the whole fish structure.

7.3 Electrical Stimulation

At last, the electrical stimulation of the bioprinted constructs immersed in the cell culture medium was performed. Due to the impossibility to receive some complete wireless stimulating systems during the 6 months spent at the Khademhosseini laboratory, preliminary excitation/modulation tests where performed on the printed construct exploiting the conductivity of the cell culture medium solution. Specifically, a custom-fabricated PDMS structure was inserted in a 10 cm x 15 cm common laboratory polystyrene Petri dish (see Figure 7.23 a).

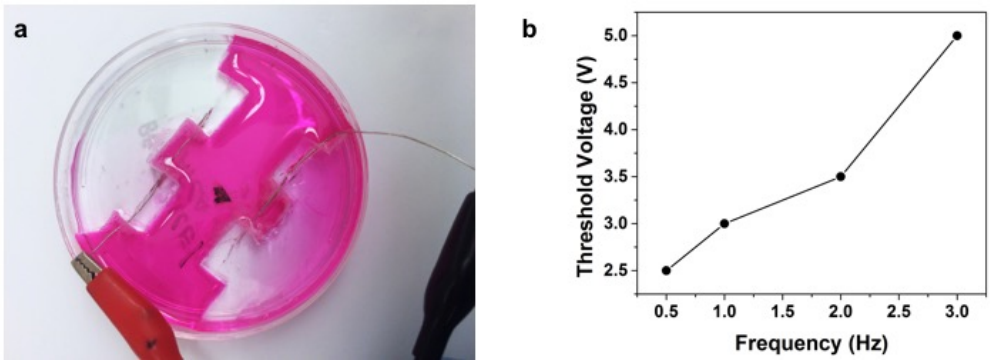

Fig. 7.23 Electrical stimulation of a bioprinted test structure with Pt electrodes immersed in the cell culture medium (a). The beating frequency of the scaffold was successfully modulated between 0.5 Hz and 3 Hz according to the frequency of the external signal applied.

This structure acted as a holder for two platinum wires, directly immersed in the cell culture medium, and separated by 3 cm. The platinum wires were then connected to a common laboratory waveform generator through crocodile connections. A square waveform was selected as excitation signal, and its frequency was varied between 0.5 Hz and 3 Hz, since these conditions are similar to the physiological ones, according

to previously published results [1]. Then, the beating construct, a sample serpentine pattern in Figure 7.23 a, was carefully transferred in the central region of the dish, checking that the structure was completely covered by the culture medium. For each frequency, the starting amplitude of the waveform was fixed at 1 $V_{peak-peak}$. Then, if no synchronization of the beating frequency of the printed construct with the frequency of the external square waveform applied was observed, the amplitude was was increased, with steps of 1 $V_{peak-peak}$, up to a maximum value of 5 $V_{peak-peak}$.

As observable from the results plotted in Figure 7.23 b, increasing the modulation frequency, higher amplitudes were necessary in order to be able to synchronize the tissue to the external frequency applied. Despite amplitudes between 3 $V_{peak-peak}$ and 5 $V_{peak-peak}$ may result too high to avid damages to the living tissue, the obtained results represent a successful proof-of-concept about the possibility of modulating the beating frequency of the bioprinted actuator with external electrical signals.

Despite it has not been possible to test the complete wireless stimulation system, preliminary biodegradation and cytotoxicity results were performed on the separate components forming the stimulating system stack, i.e., the receiving coil and the stimulating electrodes. The first biodegradation test performed, started with the sample sterilization, with sequential washing steps in DPBS and cell culture medium, both with 1 % P/S antibiotics. As observable from the results shown in Figure 7.24 a, since from the very first DPBS washing step, some damages were observed on the ink-jet printed electrodes, especially on the one of the receiving coil (left). The damages slightly increased already with the next washing step in cell culture medium (Figure 7.24 b). Finally, after 5 days immersed in cell culture medium at 37 °C, a complete electrodes biodegradation was observed (see Figure 7.24 c). The obtained results suggest that a protective coating layer, for both improving the electrodes biocompatibility and to protect the electrodes themselves from the harsh biological environment is necessary.

For this reason, before proceeding with the successive experiments with living cells, the surface of the electrodes was covered by a uniform layer of 1% pristine gelatin (Sigma Aldrich, USA). The coating was performed by immersing the samples in a sterile DPBS solution with 1 % gelatin for minimum 2 hours. After the coating, cardiac fibroblast were seeded on the surface of the electrodes with a seeding density of $1 \cdot 10^5$ cells/mL. Cardiac fibroblasts were often used in the present work as preliminary testing system before proceeding to the cardiomyocytes one. This was mainly motivated by the fact that the excess cardiac fibroblast collected during the primary cardiac cells isolation can be easily passaged in common laboratory cell culture flasks (since they can duplicate) as well as they can be frozen and stored for successive use. In this way, it is possible to perform the preliminary tests, with a high probability of failure, on unknown substrates or experimental conditions using previously stored cardiac fibroblasts, instead of sacrificing new animals.

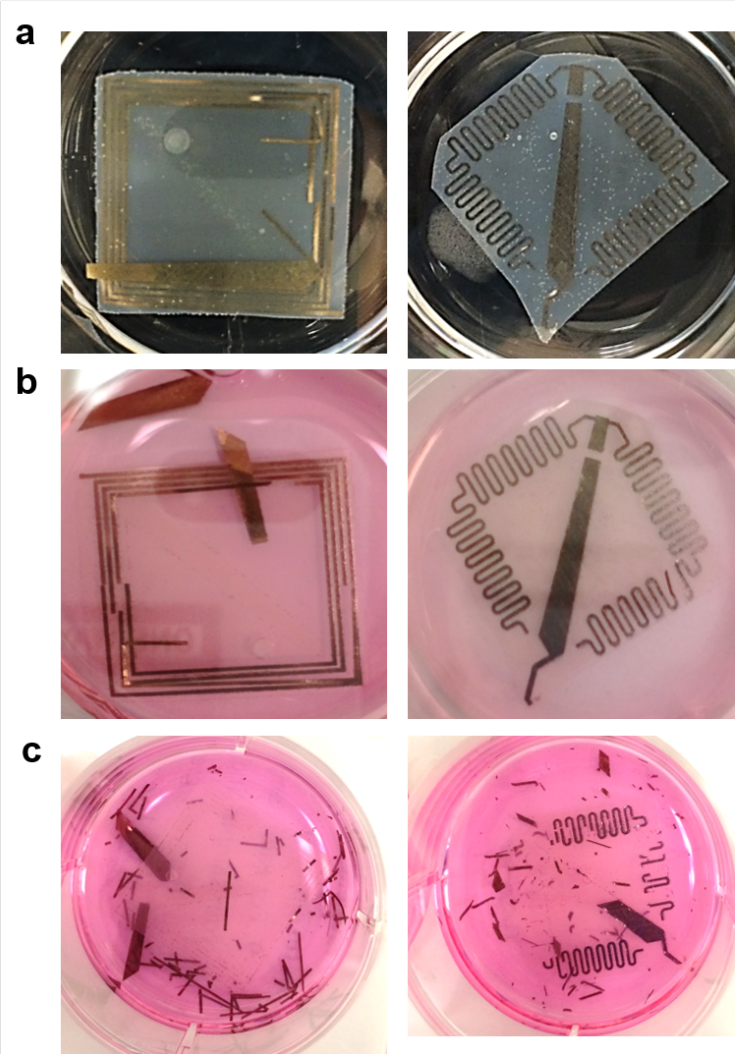

Fig. 7.24 Biodegradation of the wireless electrodes in physiological solutions. Electrodes degradation was visible since the preliminary sterilization step (a) and the first immersion in cell culture medium (b). After 5 days in cell culture medium at 37 °C the electrodes resulted completed degraded.

It is important to notice that usually, for cardiac fibroblast a seeding density one order of magnitude smaller than the one adopted for cardiomyocytes is used, due to their larger dimensions. Therefore, cardiac fibroblast obtained from precedent primary cell isolation were seeded on different samples of the receiving coil/top electrodes coated with 1 % gelatin, in standard 6 wells plates. Different samples were then extracted after 1 and 5 DIV in order to performed a live & dead assay, to asses the cell viability. Specifically, the Live/Dead^{TM} Viability/cytotoxicity kit from Invitrogen^{TM} (USA), was adopted. The kit includes green-fluorescent calcein, a fluorescent dye that can permeate through the cellular membrane (absorption 495

nm, emission 515 nm), marking alive cells. Moreover, also red-fluorescent ethidium homodimer-1 is present, a fluorescent dye that, instead, cannot permeate through the cellular membrane of living cells, but only through bigger ruptures along it, usually present were the cells are in apoptotic or dead state.

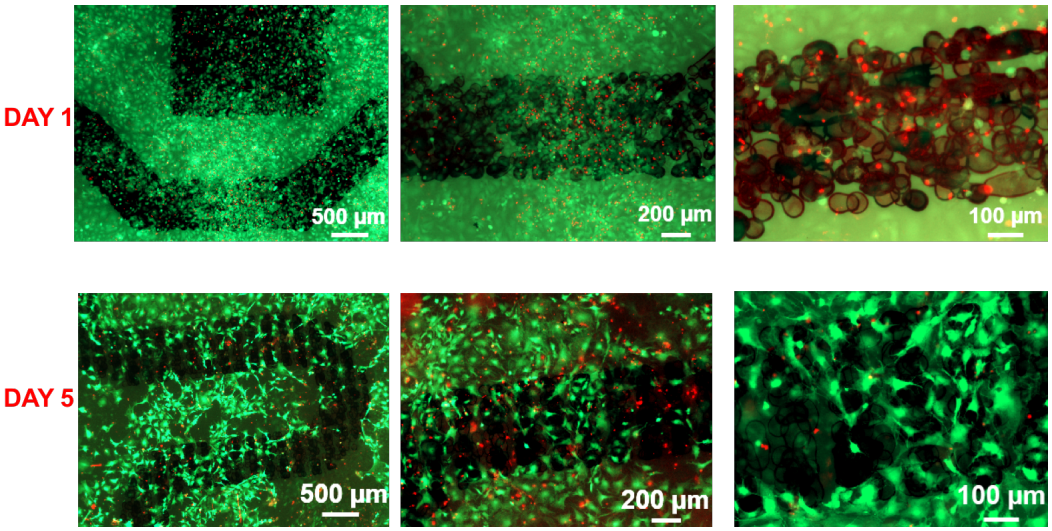

Fig. 7.25 Cytotoxicity tests of cardiac fibroblasts cultured on the wireless electrodes deposited on the PEN substrate. The living cells are marked in green, while, the dead ones are marked in red.

As observable from the results shown in Figure7.25, an extremely good cell viability was obtained, with the majority of the cells being alive both on the substrate and on the electrodes. The cell viability was also maintained after 5 days of culture. In order to quantify the obtained data, ImageJ software was used in order to count the number of living (green) and dead (red) cells. The summary graph is shown in Figure 7.26). A slightly higher cell viability was observed outside the electrodes surface, but of not significant difference. At day one, the dell viability was between 80% and 90%, for the cells on and outside the electrodes surface, respectively. These values then decrease to 70% and 80% during the 5 days of culture, hence confirming that no cytotoxic components are released in the culture due to the electrodes presence.

Nevertheless, one important consideration must be done about the auto-fluorescence of the PEN substrate. In fact, as visible from Figure 7.27, the PEN substrates emits in the blue region of the electromagnetic spectrum. This emission was associated to the blue background present in the acquired images, especially considering that in Figure 7.27 no fluorescent dye emitting in the blue region was added to the solution.

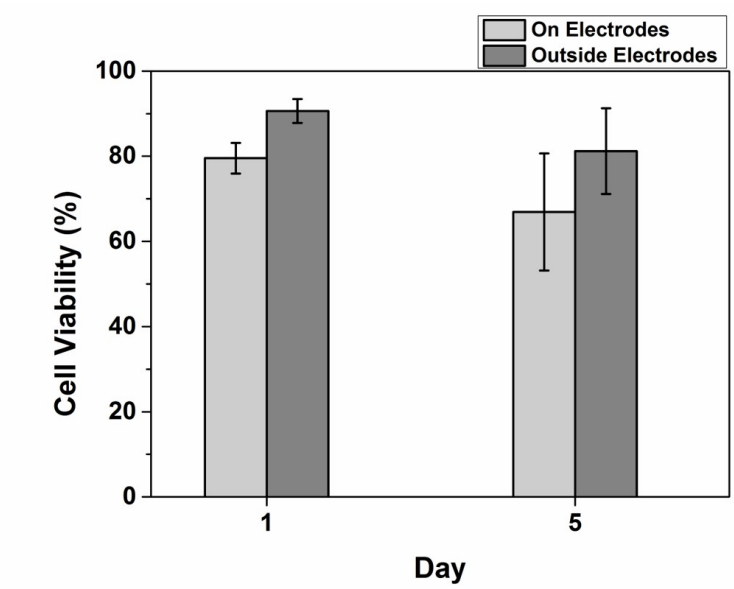

Fig. 7.26 Summary of the cytotoxicity tests of cardiac fibroblasts cultured on the wireless electrodes deposited on the PEN substrate.

As published by Ouchi *et al.*, the PEN substrate presents two emission peaks in the blue region of the electromagnetic spectrum, one centered at 425 nm, and the other one at 455 nm [250]. The emission wavelengths may overlap with the one of the DAPI usually used for the staining procedure. Moreover, the green background visible also in Figure 7.25, suggest that an additional overlap also in the green region of the spectrum is present.

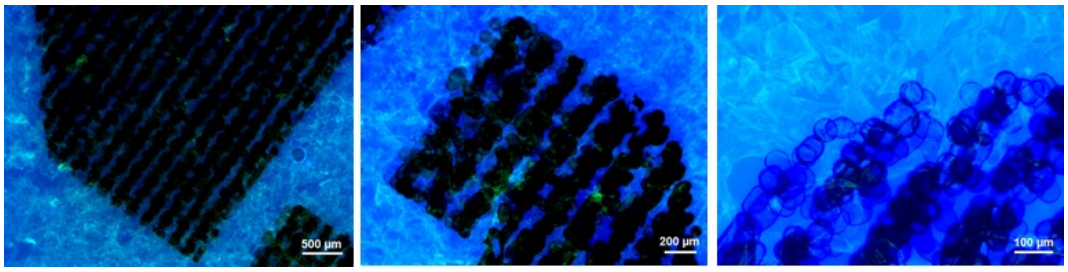

Fig. 7.27 Autofluorescence of the PEN substrate (emission 450 nm, excitation 330 nm).

For these reason, it would be advisable, for future developments of the project to select a different substrate whose emission spectrum is not overlapping with the usual wavelength used for the fluorescent imaging of the cells cultured on its surface.

At last the cytotoxicity tests were repeated also on the PCB version of the wireless stimulating system presented at the end of Chapter 5. Nevertheless, the resulted obtained in this case revealed that some cytotoxic substances may be released during

5 days of cell culture, probably by the PCB sample despite the gelatin coating. Although there are some alive cardiac fibroblasts (Figure 7.28 a), the morphology does not resemble the correct one, shown e.g., in Figure 7.25. Moreover, the majority of the cells directly on the electrodes surface result dead. Moreover, the scarce number of cells visible, in general, on the surface of the electrodes, suggest that the majority of the cells started to die at the beginning of the culture, therefore being washed away during the routine changes of the cell culture medium.

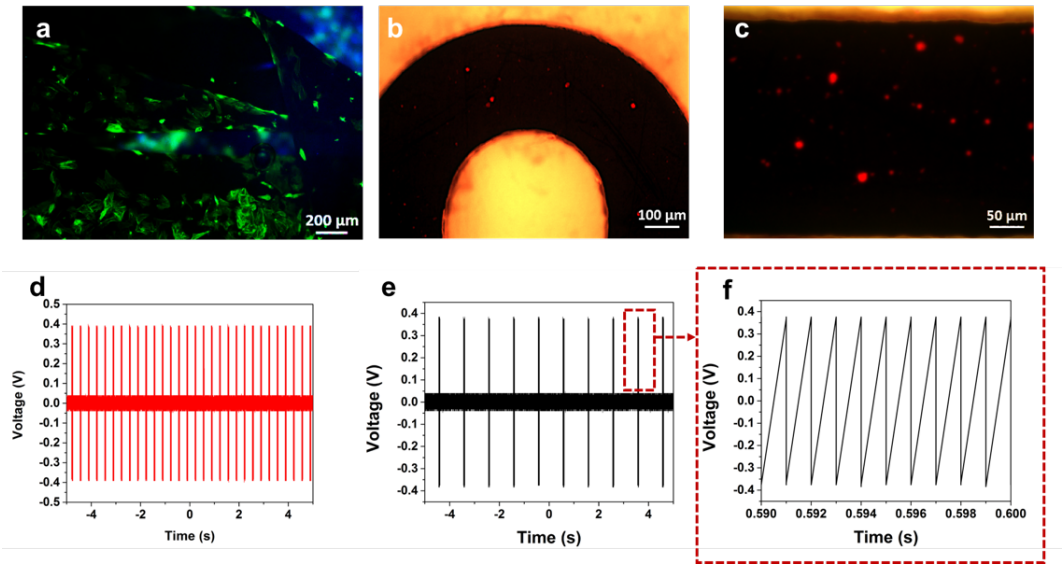

Fig. 7.28 Preliminary viability results on the PCB version of the wireless stimulation system and measurements of the signal transmitted to the electrodes surface for both 3 Hz (d) and 0.5 Hz (e).

Despite the PCB version of the wireless stimulating system did not represent a good substrate for the culture of cardiac cells, unless some thicker coating is performed on its surface to prevent any release of toxic components, it electrical functionality was tested.

In Figure 7.28 the signals read at the electrodes surface when a frequency of 3 Hz (Figure 7.28 d) or of 0.5 Hz (Figure 7.28 e) was set on the excitation signal are shown. In both the cases the measured amplitude of the signal is ~ 0.35 $V_{peak-peak}$. As visible from the magnification of Figure 7.28 f, the measured signals are still constituted by a square wave which is modulating a sawtooth wave baseline signal.

As already mentioned, due to the fixed and limited amount of time spent at the Khademhosseini laboratory, it was not possible to entirely complete the optimization and fabrication of the wireless bio-hybrid actuator. Nevertheless, the numerous expeirments done in order to optimize both the bioprinting process (inks, designs, layers), the cardiac cells isolation and culture on the printed construct, as well as

the preliminary wireless system electrodes characterization represented fundamental steps for the future development of the wireless-stimulated bioactuator. In addition, the perfomerd tests were extremely useful in order to understand the requirements and conditions necessary to grow functional cardiac tissue on artificial electrical stimulated substrates.

Chapter 8

Cardiac Cells Meet Electronic Sensing and Stimulating Platforms: Preliminary CMOS Multi Electrodes Arrays for Electrophysiology Studies

Chapter Abstract *In the present Chapter, the preliminary results obtained by interfacing cardiac cells, hydrogels and multi electrodes arrays will be presented. This activity was performed at the Italian Institute of Technology of Genova, in collaboration with the Microtechnology for Neuroelectronics group, lead by Dr. L. Berdondini. At first, the experimental procedures followed to prepare the 3Brain chips for the culture of cardiomyocytes will be described in Section 8.1. Then, the experimental results obtained during the recording and the stimulation of the cardiac tissue on the CMOS-MEA will be presented in Section 8.2. Although the obtained results are only preliminary, the constitute a fundamental starting point for future developments at the frontiers between biology, electronics and material science.*

8.1 3Brain Chip Sterilization and Coating

The culture of living cells on CMOS-MEA chips, requires preliminary sterilization and functionalization steps in order to favor the optimal growth and functional proliferation of the cells on the chip surface. At first, it is fundamental to clean and sterilize the chips in order to prevent any possible contamination, due e.g., to the bacteria commonly living in our body, that may lead to the death of the culture. To achieve this goal at first, the PCB and glass ring glued around the active area of the chip, to confine the cell culture medium, are wiped with sterilized 70 % ethanol. Then, also the chip surface is rinsed multiple times with sterile 70% ethanol by

continuously filling and drying the glass ring. After leaving the last ethanol solution in the chip well for 20 minutes, to ensure the complete death of all the possible contaminants, the same procedure is repeated with sterilized distilled water. This step is necessary in order to ensure that no residues of ethanol are present in the area of the chip that will be in contact with the cells since this can also result in potential cellular death. At last, the chips are incubated in cell culture media overnight in order to increase the surface hydrophilicity for the next coating step.

Up to this point, no treatment is done in order to promote the cellular adhesion on the silicon chip surface. As it was deeply discussed in Chapter 1 and 2, the creation of an environment as biocompatible and physiological as possible is a key requirement in order to guarantee the functional growth of the cardiac cells on the surface. For this reason, two different biocompatible coatings where tested in the performed experiments. The first one was done using poly-dl-ornithine (PDLO, 50 μg/mL, P0671 Sigma Aldrich, USA) polycationic molecule with also the aid of laminin, one of the numerous constituents of the extracellular matrix helping to promote cellular adhesion [160]. For the second type of coating, the GelMA hydrogel presented in Chapter 5 was crosslinked on the chips surface. In order not to decrease the quality of the electrical coupling between the cardiac cells and the recording electrodes, it was necessary to pattern an extremely thin layer of material on the chip surface. To achieve this goal, at first the chip surface was completely sterilized according to the described procedure. Then, before the surface hydrophylization in cell culture medium, the hydrogel was at first spin-coated on the chip surface and, then, crosslinked with UV light, before the pre-polymer solution was completely dry. Afterwards, different washing steps with DPBS with 1 % P/S antibiotics were performed as in the case of the hydrogel-based biohybrid actuator described in Chapter 5.

In Figure 8.1 it is possible to observe the difference of the chip surface appearance before (Figure 8.1 a) and after (Figure 8.1 b and c) the GelMA coating. Although not easily recognizable using a phase contrast microscope, a different contrast can be observed at the edges of the chips, where the spin-coated hydrogel shows a higher thickness (Figure 8.1 b). Using a profilometer, the hydrogel thickness was approximately measured to be $\sim$ 700 nm. A second optical inspection of the chip surface was also performed at the end of the sterilization, after filling the glass ring with cell culture medium. As visible from Figure 8.1 c, the GelMA hydrogel border on the bottom part of the chip can be clearly recognized. This inspection revealed that the deposited hydrogel did not detach from the chip surface after the different sterilization washing steps, hence suggesting the possibility to further proceed with the cardiomyocytes culture on chip.

During the overall cell culture experiments the chip was positioned in a 10 cm x 15 cm Petri dish, commonly used during cell culture experiments. An additional smaller Petri dish, filled with sterilized deionized water, was further added inside the

Petri dish to improve the humidity inside the Petri dish (see Figure 8.2 a). In fact, due to the small dimensions of the active area of the chips and of the surrounding glass ring only a small amount of cell culture medium (1/2 mL) can be added (see Figure 8.2 b)), which can easily evaporate if the surrounding environment is too dry.

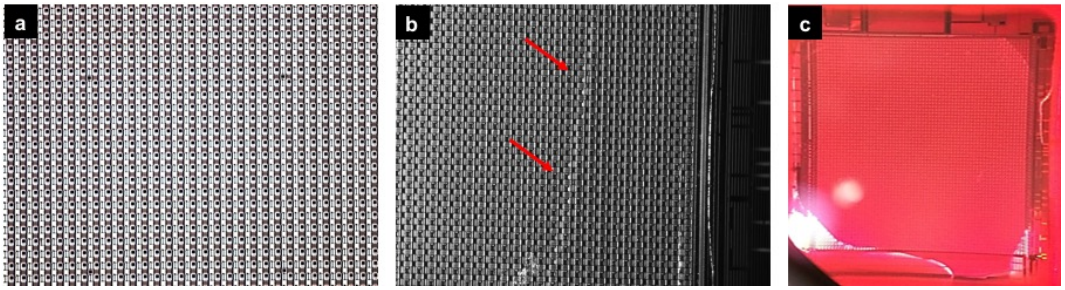

Fig. 8.1 Phase contrast images of the surface of the 3Brain chips before (a) and after (b) the spin coating with GelMA hydrogel. (c) GelMA coating check after the sterilization procedure.

At last, in order to preserve the culture sterility during the electrical measurements, which require to place the chip on the custom acquisition system described in Chapter 4, ad-hoc PDMS caps were fabricated (Figure 8.2c), with embedded the external reference electrode needed for the electrical measurements. The caps were only used during the chip transport and electrical measurements but not during the waiting time in the incubator in order to allow a sufficient gas exchange (with the 5% CO_2 present in the incubator environment) necessary for the cell culture grow and proliferation.

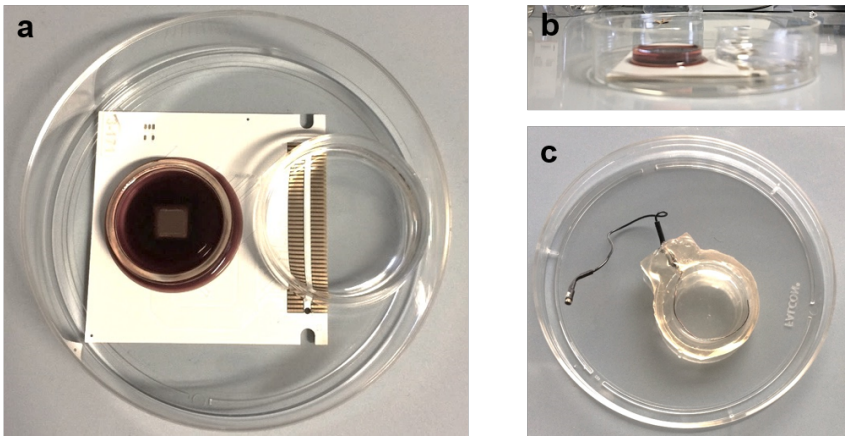

Fig. 8.2 (a)-(b) Example of one 3Brain chip during the cell culture experiments, a small Petri dish with sterilized distilled water is also added in order to increase the humidity. (c) PDMS cap used to keep the sterility of the system during the electrical measurements.

8.2 Electrical Recording and Stimulation of Cardiomyocytes on CMOS-MEA

After the overnight wetting of the chip surface in cell culture medium, the chip resulted ready for the seeding of embryonic cardiomyocytes. The PDLO-coated chips, still required a preliminary incubation for 2 hours in the solution containing the PDLO functionalizing agent. Due to the chip area, a seeding density of 1000 cells/μL was optimized experimentally.

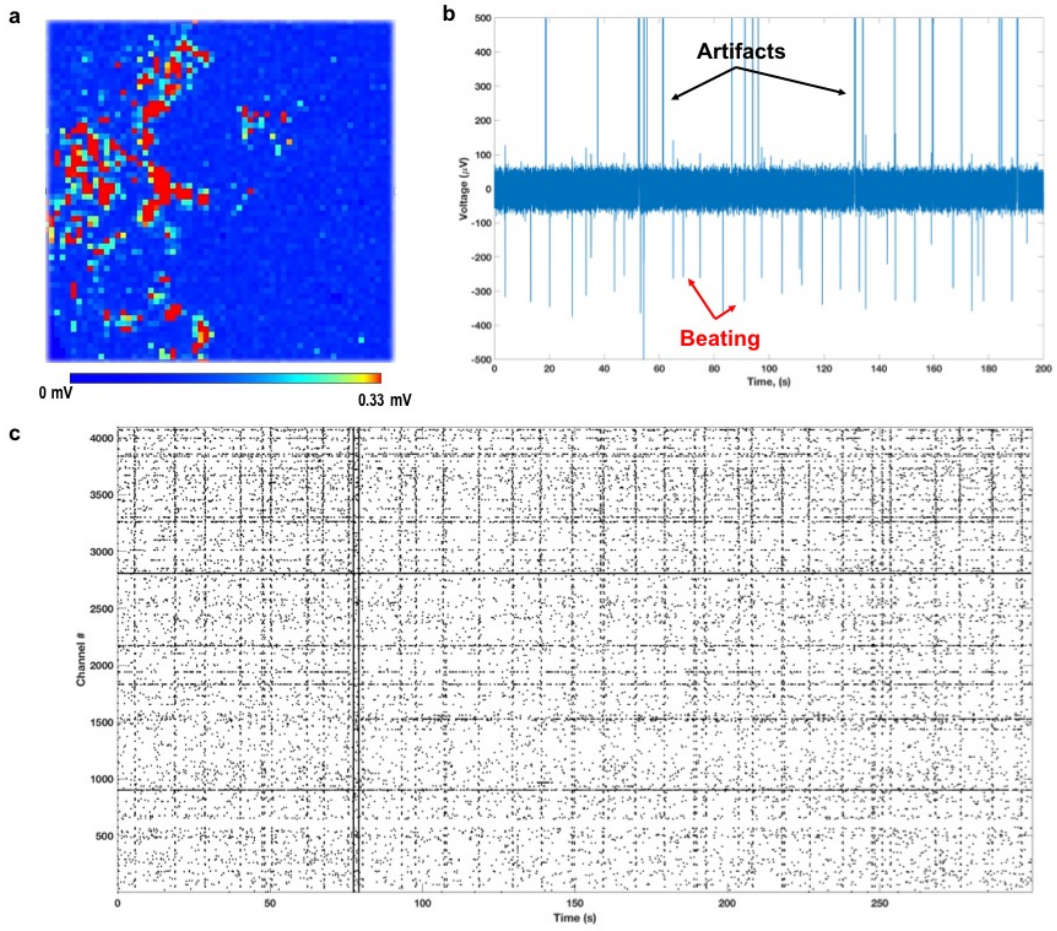

Fig. 8.3 Electrical recording from PDLO-coated chips. (a) heat map showing one instant of the electrical recording from the chip surface (b) Raw data acquired from a single channel. (c) Raster plot showing the overall beating events per single electrode in time.

After the cell seeding was completed, by just dropping the cell-containing solution on the chip surface, usually the electrical measurements were performed after 5 to 10 DIV, depending on the quality of the culture and of the coating procedure. In

Figure 8.3, the preliminary results obtained on the PDLO-coated chip after 13 DIV are shown.

In Figure 8.3 a, the heat map of the electrical activity on the chip surface during one recording experiment is shown. As visible from the result, the cell electrical coupling of the cell culture resulted extremely sparse and clustered revealing a non optimal adhesion and proliferation of the cells on the chip surface. Nevertheless, as visible from the raw data extracted from a single channel, Figure 8.3 b, rhythmic beating activity was achieved, with few artifacts related to saturated channels, probably related to damaged electrodes.

The acquired raw data were then at first preprocessed in the Brain Wave software, already embedded in the 3Brain system. The software, in addition to numerous additional functions, includes a peaks identification algorithm capable to extract the time-stamp of the spiking events for the data recorded from each single electrodes. The pre-processed data were then analyzed using the Matlab software.

An overall view of the beating spikes registered on each of the 4096 electrodes, is visible in the raster plot of Figure 8.3 c. The raster plot shows the time on the x-axis, while, on the y-axis the index of the 4096 electrodes is reported. Each time a spike event was identified on the signal of a specific electrode, a point is present in the raster plot. A certain periodicity of the beating activity of the cells can be recognized from the periodic vertical lines recognizable in Figure 8.3 c, meaning that, at that instant, numerous channels simultaneously recorded a spike event.

Interesting results were also obtained in case of the GelMA-coated chips (Figure8.4). At first, it can be observed how, in this case, a uniform cardiac tissue layer was formed on the overall surface (Figure 8.4 a). This can be assumed from the uniform distribution of the recorded signal on the voltage heat map shown. Specifically, in Figure 8.4 a, the wave-like propagation of the cardiac tissue action potential can be recognized, starting from the top left corner and propagating towards th bottom right one. The improved electrical coupling of the cardiac tissue can also be recognized from the increased amplitude of the recorded extra-cellular electrical signal (Figure 8.4 b) and from the higher frequency of the natural beating activity of the cells.

All the data reported up to now do not include any electrical stimulation. In order to investigate how an electrical stimulation can affect the beating activity of the cells, similarly as what shown for the modulation of the beating activity of the bio-hybrid actuator in Chapter 5, the 16 stimulated electrodes were connected to a 16 channels electrical stimulator, as anticipated in Chapter 4. The main goal was to investigate the possibility of evoking the propagation of an action potential by applying externally electrical signals. The stimulating signal was selected to be as similar as possible to the one successful for the modulation of the beating activity of the hydrogel-based bioactuator. Therefore, a low frequency biphasic square wave waveform, with the anodic phase first, was selected (600 $\mu A_{peak-peak}$, frequency

between 0.5 Hz and 3 Hz). In order to standardize the experiments, at first 1 minute of baseline signal was recorded, then the stimulation was activated for 4 minutes, at last, further 3 minutes of recording post-stimulation were acquired.

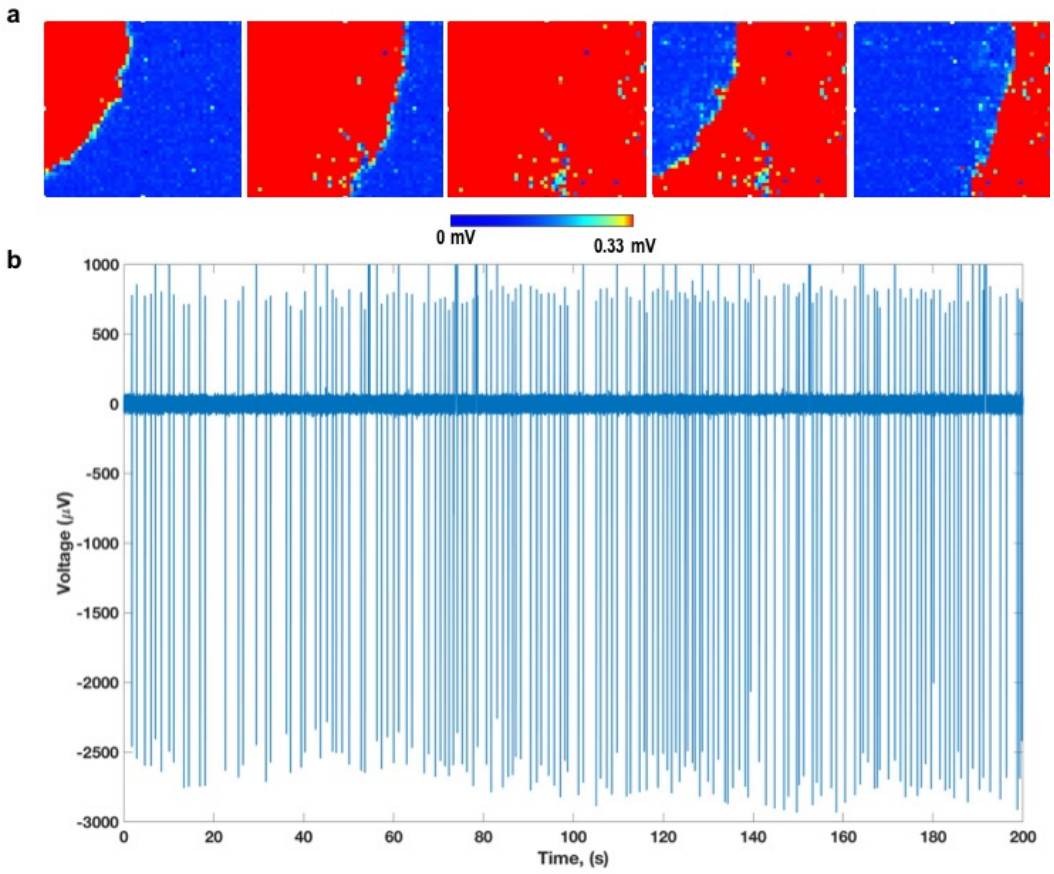

Fig. 8.4 Electrical recording from GelMA-coated chips. (a) heat maps at different time instants and raw data acquired from a single channel (b).

The preliminary stimulation results of the PDLO coated sample are reported in Figure 8.5. The culture was stimulated using only one stimulation electrode, at a frequency of 0.5 Hz (since the natural beating frequency was around 0.3 Hz. A successful modulation of the beating activity of the cells was observed with a beating frequency switch up to 0.5 Hz. This is particularly evident on the raw data measurements (Figure 8.5) where, a peak of smaller amplitude is observable just after the stimulation signals. The stimulation artifacts can be easily recognized since they usually saturate the corresponding electrode.

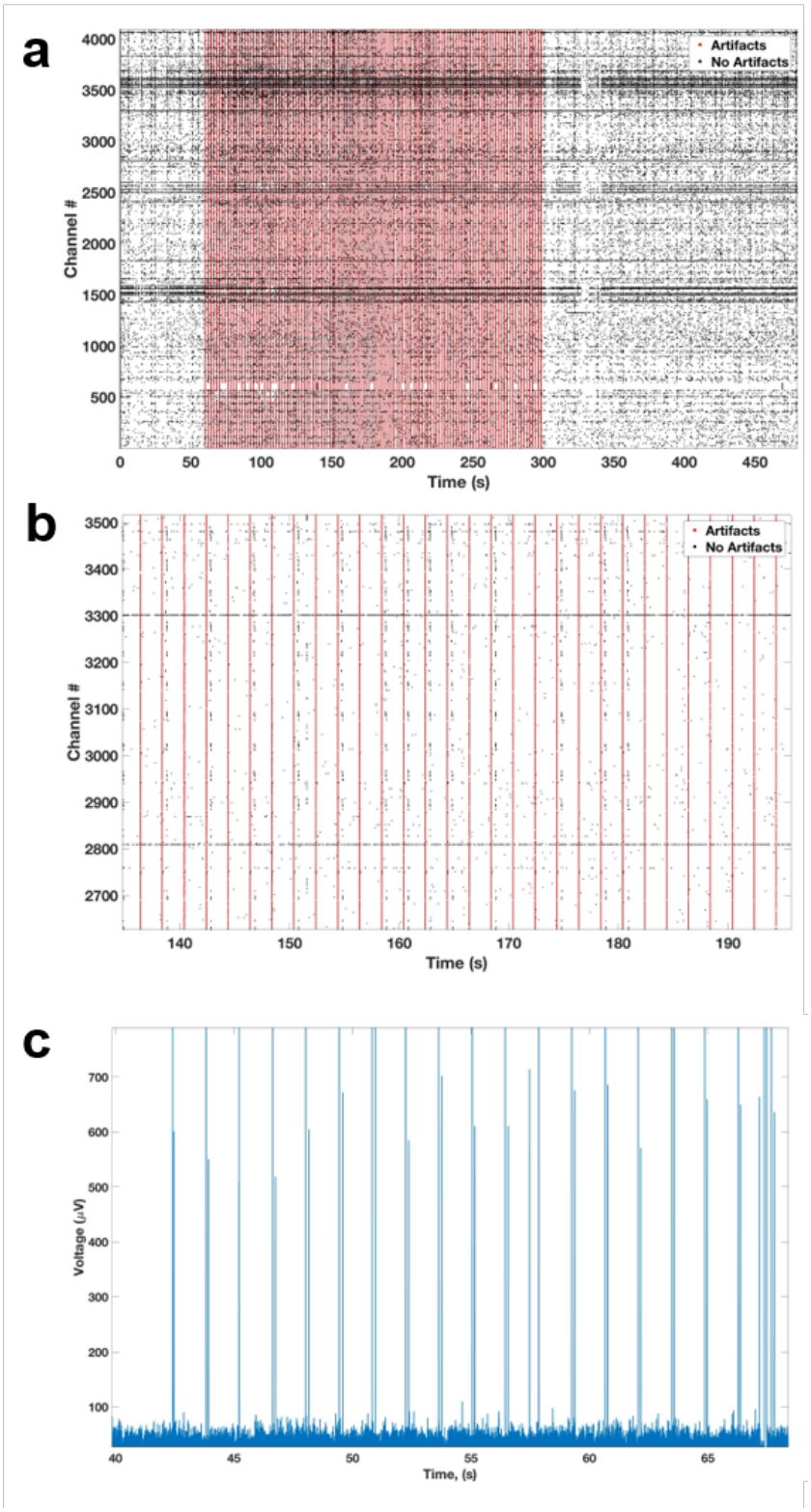

Fig. 8.5 Electrical recording and stimulation of the PDLO-coated chip. (a) Raster plot showing in red the stimulation artifacts, with zoom of the evocation of the cardiac potential (b). The evoked cardiac potentials are also visible from the raw data (c).

Singular results were obtained, instead, in the case of the GelMA coated chips (Figure 8.6). Despite the increase electrical activity and coupling of the cells, the evoked action potentials show a dynamic quite different from the PDLO-coated chips.

More precisely, the raw data and/or raster plots of the PDLO-coated chips showed the appearance of a series of evoked cardiac potentials on different electrodes less than 1 second after the stimulation signal. In case of the GelMA-coated chips, instead, despite an increase of the beating frequency was observed from the raster plot although although further tests would be necessary in order to verify if the increase in the beating frequency was actually related to the activation of the external stimulating signal.

In fact, as visible from the zoomed pictures of the raster plot before (Figure 8.6 a), during (Figure 8.6 b) and after (Figure 8.6 c) the stimulation the number of spikes in time is almost doubled when the stimulating signal is active. It could be hypothesized that, the presence of the hydrogel may introduce a delay in the propagation of the stimulating signal from the electrode to the culture, and therefore, this is why the evoked signal is slightly shifted. Additional tests should be anyway necessary in order to verify this assumption as well as the effect of the hydrogel thickness on the overall electrical performances of the chip.

Another interesting observation is related to the fact that, in both the PDLO- and the GelMA-coated chips, as soon as the electrical stimulating signal is turned off, the beating activity of the cells goes back to its original dynamics. This results suggests that, probably, more effective electrical signals, perhaps with higher amplitudes, could be optimized to significantly influence the behavior of the beating activity of cardiomyocytes.

Nevertheless, the preliminary results obtained pointed out the effective possibility of integrating extremely biocompatible hydrogels on top of CMOS chips for improving the quality of the cardiac cell culture on the top of the chip surface. As already mentioned, improving the quality of the cell culture on chip can unlock the investigation of new biological cues that were not detectable with previous system due to the impossibility to reach the optimal and completely functional proliferation of the cell culture *in vitro*.

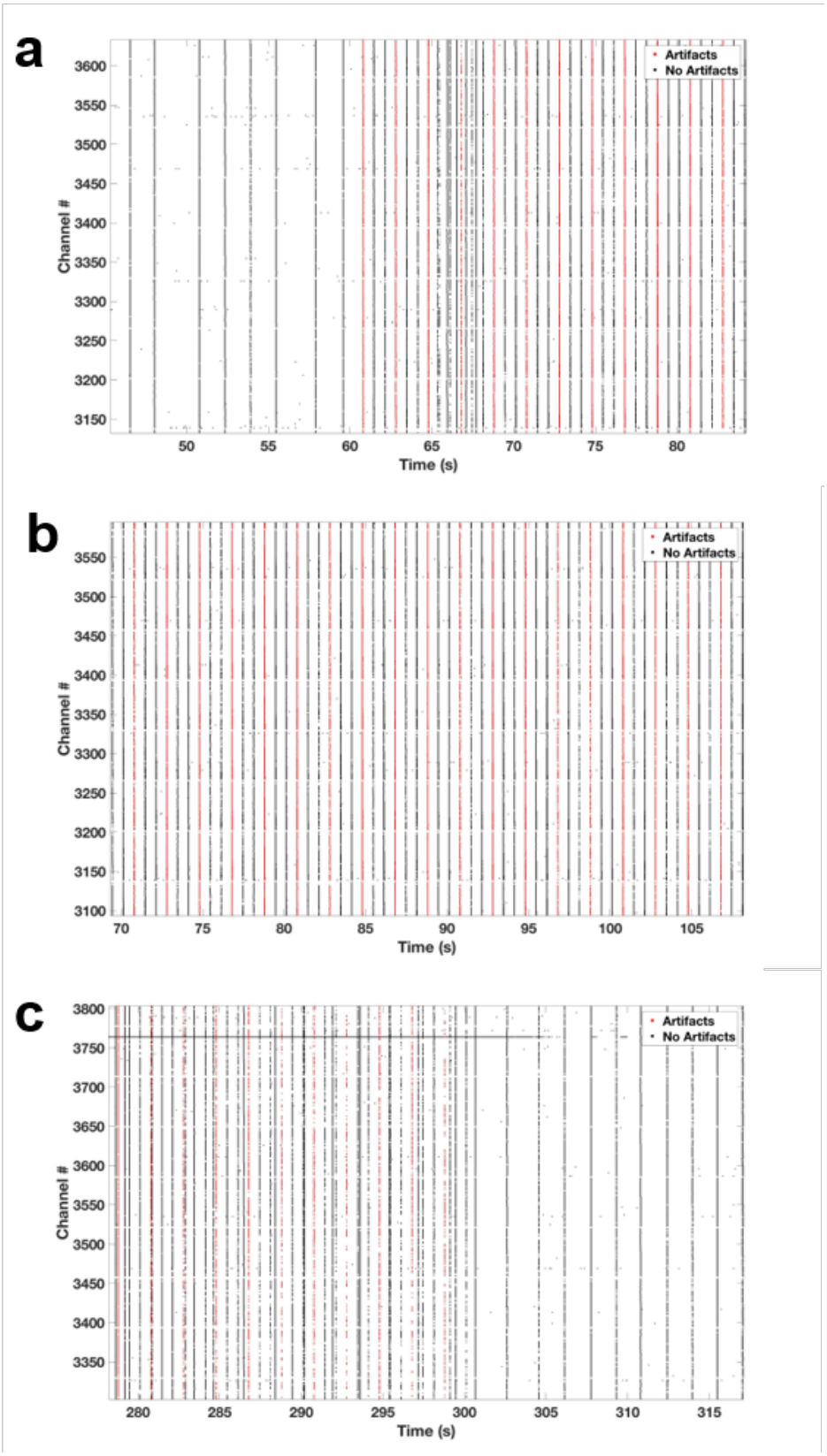

Fig. 8.6 Electrical recording and stimulation of the GelMA-coated chip. Magnification of the raster plot before (a), during (b) and after (c) the electrical stimulation.

Chapter 9

Conclusions and Future Perspectives

The present work was focused on the understanding of how effectively integrate both synthetic and living microstructures on electronic platforms for implementing electronically controlled organs-on-chip devices, integrating sensing and actuation functionalities. The presented activities demonstrated the feasibility of implementing bio-electrical devices for giving innovative solutions in the design of organs-on-chip devices. At first, two microelectrodes electronic platforms were optimized for the sensing of the electrical properties of microstructured materials. The first one, the nanogap chips, were formed by an array of four butterfly-like micrometer gold electrodes. The central metal line was then broken, in a controlled way, exploiting electromigration, to create a nano/micro-metric spaced gap in an easy and portable way accessible to numerous electronic laboratories. ZnO microwires were then deposited between the formed couples of metal electrodes through dielectrophoresis. Thanks to the Schottky junction formed between the ZnO microwires and the metal lines, it was possible to measure the electrical properties of the microstructure, specifically current, resistance and capacitance variations. Numerous external stimuli like UV-Visible light, pH and temperature can affect the electrical properties of the ZnO microwires. For this reasons, a multisensor, capable to detect simultaneously UV-visible, pH and temperature variations was developed exploiting the ZnO microwires/gold junctions on the nanogap chips. A mathematical multi-sensor model was also developed to be able to predict the behavior of the sensor.

Due to the small amplitudes of the measured electrical signals, in the order of nano- or micro- ampere/volts, the electrical noise and parasitic effects affecting the measurements must be reduced as much as possible. For this reason, an improved electrical platform was optimized, the micro-for-nano (M4N) chips, in which, CMOS circuits were embedded directly underneath couples of metal electrodes present on the chip surface. Specifically, the top aluminum metal lines of the M4N CMOS chips, previously designed to present 24 couples of micrometric electrodes, were exposed to the external environment using a reactive ion etching technique. Specifically,

two types of integrated circuits were present in the M4N chips. The first one, were responsible to apply the dielectrophoretic signal, to attract the microstructure between the electrodes couples present on the chip surface. The second one, instead, allowed the read-out of the impedance of the microstructure. In this way, it was possible to have an integrated platform, with no need of additional external instrumentation to perform the electrical measurements. Moreover, since the impedance read-out was done directly underneath the electrodes surface, without the needs of cables connected to external instrumentation, the noise and parasitic affects can be strongly reduced. In order to have a good electrical contact between the target microstructure and the metal electrodes, an electroless nickel gold immersion (ENIG) CMOS post-processing was developed to modify the metal surface from aluminum to gold, less prone to oxidation. The chip was then tested using ZnO microwires as target sensing element to fabricate an integrated and real-time UV-visible light detector.

In order to understand how to exploit microelectrodes array platforms for the electrical sensing of living microstructures, like cardiac cells, a biohybrid hydrogel-based actuator, actuated by the beating of cardiac cells growing on its surface, with potential electrical stimulation, was studied. This activity was performed during a 6 months visiting period at the Khademhosseini laboratory (Boston, Massachusetts). The main focus of the work was the optimization of a bioprinting process to fabricate a multi-layered hydrogel construct acting as a scaffold for cardiac cells growth and proliferation. The GelMA hydrogel was selected as cell substrate material, due to its structure and composition made of the same constituents of the extracellular matrix, while PEGDA-GelMA hydrogel was selected as support layer for the structure due to its higher stiffness. The structure was then electrically stimulated using, as preliminary test, platinum electrodes directly embedded in the cell culture medium. A square wave signal was then applied using an external waveform generator to modulate the beating frequency of the cardiac cells to the frequency of the applied electrical signal. The final aim was to print this construct on a wireless stimulating system, exploiting magnetic induction, in order to eliminate the cable contacts with the cell culture medium. Although this final goal was not possible to achieve in the 6 months, preliminary biodegradation and cytotoxicity tests were also performed on the induction stimulating system.

At last, preliminary results about the recording and stimulation of the electrical activity of cardiac cells on CMOS multi-electrodes arrays (MEA) was also performed. This activity was done during 2 months visiting the Microtechnologies for Neuro-electronics laboratory of the Italian Institute of Technology of Genova. Here, CMOS MEA chips, with 4096 electrodes, previously designed by the 3Brain company, were used to study the evocation of cardiac potential due to *in situ* electrical stimulation. Two types of experiments were performed, the first one using standard polypeptides coating to functionalize the electrodes surface before the cell culture, and the second one using the GelMA hydrogel optimized for the bio-hybrid actuator. The electrical

stimulation was performed using the 16 stimulating electrodes already integrated in the chip using a square waveform similar to the one used for the stimulation of the bio-hybrid actuator. The results evidenced the possibility to actually evoke cardiac action potential by applying electrical signals to the culture as well as an improved and more interconnected cardiac tissue when the GelMA hydrogel was used to functionalize the surface of the chip.

The presented activity represents the starting point for future developments in which CMOS MEA chips can be effectively integrated with smart materials and living cells. The final goal is the creation of state-of-the-art devices not only allowing direct recording/stimulation of the electrical properties of the cells but also, recreating an environment more similar to the *in vivo* one so that the cells can express their complete functionalities also *in vitro*, hence strongly impacting the current medical diagnostic paradigm.

References

[1] S. R. Shin, B. Migliori, B. Miccoli, Y.-C. Li, P. Mostafalu, J. Seo, et al. Electrically driven microengineered bio-inspired soft robots. *Advanced Materials*, page 1704189, 2018.

[2] B. Miccoli, A. Bonanno, V. Cauda, A. Sanginario, and D. Demarchi. Interface of a single ZnO-nanowire assembled onto custom-fabricated nanogap device for UV sensing applications. In *International Spring Seminar on Electronics Technology*, pages 431–435, Eger, Hungary, 2015.

[3] B. Miccoli, V. Cauda, A. Bonanno, A. Sanginario, K. Bejtka, F. Bella, et al. One-dimensional ZnO/gold junction for simultaneous and versatile multisensing measurements. *Scientific Reports*, 6:29763, 2016.

[4] A. Bonanno, A. Sanginario, S. Marasso, B. Miccoli, K. Bejtka, S. Benetto, et al. A multipurpose CMOS platform for nanosensing. *Sensors*, 16(12):2034, 2016.

[5] S. R. Shin, C. Shin, A Memic, S. Shadmehr, M. Miscuglio, H. Y. Jung, et al. Aligned carbon nanotube-based flexible gel substrates for engineering biohybrid tissue actuators. *Advanced Functional Materials*, 25(28):4486–4495, 2015.

[6] J. C. Nawroth, H. Lee, A. W. Feinberg, C. M. Ripplinger, M. L. Mccain, A. Grosberg, et al. A tissue-engineered jellyfish with biomimetic propulsion. *Nature Biotechnology*, 30(8):792–797, 2012.

[7] M. Zhang, S. Feng, L. Wang, and Y. Zheng. Biotribology lotus effect in wetting and self-cleaning. *Biotribology*, pages 31–43.

[8] S. R. Higgins, C. Lau, P. Atanassov, S. D. Minteer, and M. J. Cooney. Hybrid biofuel cell : Microbial fuel cell with an enzymatic. *ACS Catalysis*, 1:994–997, 2011.

[9] R. C. Webb, A. P. Bonifas, A. Behnaz, Y. Zhang, K. J. Yu, H. Cheng, et al. Ultrathin conformal devices for precise and continuous thermal characterization of humanskin. *Nature materials*, 12(10):938–44, 2013.

[10] N. M. Van Hemel and E. E. Van Der Wall. 8 october 1958, d day for the implantable pacemaker. *Netherlands Heart Journal*, 16:S3–S4, 2008.

[11] N. A. Wasio, R. C. Quardokus, R. P. Forrest, C. S. Lent, S. A. Corcelli, J. A. Christie, et al. Self-assembly of hydrogen-bonded two-dimensional quasicrystals. *Nature*, 507(7490):86–89, 2014.

[12] X. Zhang, L. Zhang, H. Tong, B. Peng, M. J. Rames, and S. Zhang. 3D structural fluctuation of IgG1 antibody revealed by individual particle electron tomography. *Scientific Reports*, 5:09803, 2015.

[13] M. C. H. Sørensen, Y. E. Gencay, T. Birk, S. B. Baldvinsson, C. Jäckel, J. A. Hammerl, et al. Primary isolation strain determines both phage type and receptors recognised by campylobacter jejuni bacteriophages. *Plos One*, 10(1):e0116287, 2015.

[14] W. L. Rice, A. N. Van Hoek, T. G. Păunescu, C. Huynh, B. Goetze, B. Singh, et al. High resolution helium ion scanning microscopy of the rat kidney. *Plos One*, 8(3):e57051, 2013.

[15] C. G. Golding, L. L. Lamboo, D. R. Beniac, and T. F. Booth. The scanning electron microscope in microbiology and diagnosis of infectious disease. *Scientific Reports*, 6:26516, 2016.

[16] F. Pierigè, S. Serafini, L. Rossi, and M. Magnani. Cell-based drug delivery. *Advanced Drug Delivery Reviews*, 60:286–295, 2008.

[17] M. Călin, D. Constantinescu-Aruxandei, E. Alexandrescu, R. Iuliana, M. B. Doni, M.-l. Arsene, et al. Degradation of keratin substrates by keratinolytic fungi. *Electronic Journal of Biotechnology*, 28:101–112, 2017. DOI: 10.1016/j.ejbt.2017.05.007, https://creativecommons.org/licenses/by-nc-nd/4.0/.

[18] A. M. Percebom, J. J. Giner-Casares, N. Claes, S. Bals, W. Loh, and L. M. Liz-marzán. Janus gold nanoparticles obtained via spontaneous binary polymer shell segregation. *Chemical communications*, 52(23):4245–4396, 2016.

[19] S. Gómez-Graña, B. Goris, T. Altantzis, C. Fernández-López, E. Carbó-Argibay, A. Guerrero-Martínez, et al. Au@Ag manoparticles: halides stabilize {100} Facets. *The Journal of Physical Chemistry Letters*, 4:2209–2216, 2013.

[20] C.-H. Ke, N. Pugno, B. Peng, and H. D. Espinosa. Experiments and modeling of carbon nanotube-based NEMS devices. *Journal of the Mechanics and Physics of solids*, 53:1314–1333, 2005.

[21] P. Xu, H. Yu, and X. Li. Functionalized mesoporous silica for microgravimetric sensing of trace chemical vapors. *Analyical Chemistry*, 83:3448–3454, 2011.

[22] H. Zhang, D. Xu, X. Zhang, Q. Chen, H. Xie, and S. Li. Model-Based Angular Scan Error Correction of an Electrothermally-Actuated MEMS Mirror. *Sensors*, 15:30991–31004, 2015.

[23] F. Viela, D. Granados, A. Ayuso-Sacido, and I. Rodríguez. Biomechanical cell regulation by high aspect ratio nanoimprinted pillars. *Advanced Functional Materials*, 26:5599–5609, 2016.

[24] G. Plascencia-Villa, C. R. Starr, L. S. Armstrong, A. Ponce, and Miguel José-yacamán. Imaging interactions of metal oxide nanoparticles with macrophage cells by ultra-high resolution scanning electron microscopy techniques. *Integrative Biology*, 4(11):1358–1366, 2012. http://dx.doi.org/10.1039/C2IB20172K.

[25] H. Morkoç and Ü. Özgür. *Zinc Oxide: Fundamentals, Materials and Device Technology*. Wiley-VCH, 2009.

[26] C. Ottone, S. Stassi, P. Motto, M. Laurenti, D. Demarchi, and V. Cauda. ZnO nanowires: synthesis approaches and electrical properties. In L. J. Wilson, editor, *Nanowires: Synthesis, Electrical Properties and Uses in Biological Systems*, chapter 1, pages 1–57. Nova Science Publishers, New York, 2014.

[27] W. I. Park, J. S. Kim, G.-C. Yi, M. H. Bae, and H.-J. Lee. Fabrication and electrical characteristics of high-performance ZnO nanorod field-effect transistors. *Applied Physics Letters*, 85(21):5052–5054, 2004.

[28] D. Weissenberger, D. Gerthsen, A. Reiser, G. M. Prinz, M. Feneberg, K. Thonke, et al. Influence of the measurement procedure on the field-effect dependent conductivity of ZnO nanorods. *Applied Physics Letters*, 94(4):042107, 2009.

[29] S. Stassi, V. Cauda, C. Ottone, A. Chiodoni, C. F. Pirri, and G. Canavese. Flexible piezoelectric energy nanogenerator based on ZnO nanotubes hosted in a polycarbonate membrane. *Nano Energy*, 13:474–481, 2015.

[30] M. Laurenti, G. Canavese, A. Sacco, M. Fontana, K. Bejtka, M. Castellino, et al. Nanobranched ZnO structure: p-type doping induces piezoelectric voltage generation and ferroelectric-photovoltaic effect. *Advanced Materials*, 27(28):4218–4223, 2015.

[31] J. Maçaira, L. Andrade, and A. Mendes. Review on nanostructured photoelectrodes for next generation dye-sensitized solar cells. *Renewable and Sustainable Energy Reviews*, 27:334 – 349, 2013.

[32] A. Sanginario, V. A. Cauda, A. Bonanno, K. Bejtka, S. Sapienza, and D. Demarchi. An electronic platform for real-time detection of bovine serum albumin by means of amine-functionalized zinc oxide microwires. *RSC Advances*, 6(2):891–897, 2016.

[33] Q. Yang, X. Guo, W. Wang, Y. Zhang, S. Xu, D. H. Lien, et al. Enhancing sensitivity of a single ZnO micro-/nanowire photodetector by piezo-phototronic effect. *ACS Nano*, 4(10):6285–6291, 2010.

[34] Y. He, W. Zhang, S. Zhang, X. Kang, W. Peng, and Y. Xu. Study of the photoconductive ZnO UV detector based on the electrically floated nanowire array. *Sensors and Actuators A: Physical*, 181:6–12, 2012.

[35] Y. Xie, Y. He, P. L. Irwin, T. Jin, and X. Shi. Antibacterial activity and mechanism of action of zinc oxide nanoparticles against campylobacter jejuni. *Applied and Environmental Microbiology*, 77(7):2325–2331, 2011.

[36] P. X. Gao, W. Mai, and Z. L. Wang. Superelasticity and nanofracture mechanics of ZnO nanohelices. *Nano Letters*, 6(11):2536–2543, 2006.

[37] X. Gao, X. Li, and W. Yu. Flowerlike ZnO nanostructures via hexamethylenetetramine-assisted thermolysis of zinc-ethylenediamine complex. *The Journal of Physical Chemistry B*, 109(3):1155–1161, 2005.

[38] S. Cho, S. Kim, H.-J. Kim, B. R. Lee, and K.-H. Lee. Facile and fast synthesis of single-crystalline fractal zinc structures through a solution phase reaction and their conversion to zinc oxide. 25(17):10223–10229, 2009.

[39] L. Xu, Qing L., Jianping Z., Xicheng A., and D. Xu. Single-crystalline ZnO nanotube arrays on conductive glass substrates by selective disolution of electrodeposited ZnO nanorods. *The Journal of Physical Chemistry C*, 111(12):4549–4552, 2007.

[40] V. Cauda, R. Gazia, S. Porro, S. Stassi, G. Canavese, I. Roppolo, et al. Nanostructured ZnO materials: synthesis, properties and applications. In S. Zauscher B. Bhushan, D. Luo, S. R. Schricker, W. Sigmund, editor, *Handbook of Nanomaterials Properties*, chapter 5. Springer Verlag, 2014.

[41] S. M. Sze and K. K. Ng. *Physics of Semiconductor Devices*. Wiley-Interscience, New York, 1969.

[42] F. H. Pough. *A field guide to rocks and minerals*. Houghton Mifflin Company, Boston, 1960.

[43] Ü Özgür, Y. I. Alivov, C. Liu, A. Teke, M. A. Reshchikov, S. Doğan, et al. A comprehensive review of ZnO materials and devices. *Journal of Applied Physics*, 98(4):1–103, 2005.

[44] G.-H. He, M.-M. Jiang, L. Dong, Z.-Z. Zhang, B.-H. Li, C.-X. Shan, et al. Near-infrared light-emitting devices from individual heavily Ga-doped ZnO microwires. *Journal of Materials Chemistry C*, 5:2542–2551, 2017. http://dx.doi.org/10.1039/C6TC05568K.

[45] I. Rago, R. Chandraiahgari, M. P. Bracciale, G. De Bellis, E. Zanni, M. C. Guidi, et al. Zinc oxide microrods and nanorods: different antibacterial activity and their mode of action against Gram-positive bacteria. *RSC Advances*, 4:56031–56040, 2014. http://dx.doi.org/10.1039/C4RA08462D.

[46] D. Yu, T. Trad, J. T. McLeskeyJr, V. Craciun, and C. R. Taylor. ZnO nanowires synthesized by vapor phase transport deposition on transparent oxide substrates. *Nanoscale Research Letters*, 5:1–12, 2010.

[47] R. S. Wagner and W. C. Ellis. Vapor-liquid-solid mechanism of single crystal growth. *Applied Physics Letters*, 5, 1964.

[48] M. H. Huang, S. Mao, H. Feick, H. Yan, Y. Wu, H. Kind, et al. Room-temperature ultraviolet nanowire nanolasers. *Science*, 292:1897–1900, 2001. http://science.sciencemag.org/content/292/5523/1897.

[49] Y.-J. Zeng, Z.-Z. Ye, W.-Z. Xu, L.-P. Zhu, and B.-H. Zhao. Well-aligned ZnO nanowires grown on Si substrate via metal – organic chemical vapor deposition. *Applied Surface Science*, 250:280–283, 2005.

[50] Y. Zhang, M. K Ram, Elias K. S., and D. Y. Goswami. Synthesis , characterization , and applications of ZnO nanowires. *Journal of Nanomaterials*, 2012:1–22, 2012.

[51] A. E. Danks, S. R. Hall, and Z. Schnepp. The evolution of 'sol-gel' chemistry as a technique for materials synthesis. *Materials Horizons*, 3:91–112, 2016.

[52] B. L. Cushing, V. L. Kolesnichenko, and C. J. O. Connor. Recent advances in the liquid-phase syntheses of inorganic nanoparticles. *Chemical Reviews*, 104:3893–3946, 2004.

[53] N.B. Ibrahim, S.M. AL-Shomar, and S. Hj. Ahmad. Effect of aging time on the optical, structural and photoluminescence properties of nanocrystalline ZnO films prepared by a sol–gel method. *Applied Surface Science*, 283:599 – 602, 2013.

[54] G. Zhu, A. C. Wang, Y. Liu, Y. Zhou, and Z. L. Wang. Functional electrical stimulation by nanogenerator with 58 V output voltage. *Nano Letters*, 12(6):3086–3090, 2012.

[55] C. Xu, P. Shin, L. Cao, and D. Gao. Preferential growth of long ZnO nanowire array and its application in dye-sensitized solar cells. *Journal of Physical Chemistry C*, 114(1):125–129, 2010.

[56] Y. Quin, X. Wang, and Z. L. Wang. Microfibre–nanowire hybrid structure for energy scavenging. *Nature*, 451:809–813, 2008.

[57] M. Laurenti, V. Cauda, R. Gazia, M. Fontana, F. Rivera, S. Bianco, et al. Wettability control on ZnO nanowires driven by seed layer properties. *European Journal of Inorganic Chemistry*, 2013(14):2520–2527, 2013.

[58] V. Cauda, S. Stassi, A. Lamberti, M. Morello, F. C. Pirri, and G. Canavese. Leveraging ZnO morphologies in piezoelectric composites for mechanical energy harvesting. *Nano Energy*, 18:212–221, 2015.

[59] V. Cauda, P. Motto, D. Perrone, G. Piccinini, and D. Demarchi. pH-triggered conduction of amine-functionalized single ZnO wire integrated on a customized nanogap electronic platform. *Nanoscale research letters*, 9(1):53, 2014.

[60] A. Fulati, Syed M. Usman A., M. Riaz, G. Amin, O. Nur, et al. Miniaturized pH sensors based on zinc oxide nanotubes/nanorods. *Sensors*, 9(11):8911–8923, 2009.

[61] B. Saravanakumar, S. Soyoon, and S.-J. Kim. Self-powered pH sensor based on a flexible organic-inorganic hybrid composite nanogenerator. *ACS Applied Materials and Interfaces*, 6(16):13716–13723, 2014.

[62] A. Hassanien, G. Leintschnig, A. Mrzel, M. Tokumoto, and H. Kataura. Electronic and mechanical properties of $MoS_2 - I_x$ nanotubes and $Mo_6S_xI_y$ nanowires. *Surface and Interface Analysis*, 38:1380–1385, 2006.

[63] M. Chhowalla and G. A. J. Amaratunga. Thin films of fullerene-like MoS_2 nanoparticles with ultra-low friction and wear. *Nature*, 407(6801):164–167, 2000.

[64] J. V. Lauritsen, J. Kibsgaard, S. Helveg, H. Topsoe, B.S. Clausen, E. Laegsgaard, et al. Size-dependent structure of MoS_2 nanocrystals. *Nature Nanotechnology*, 2(1):53–58, 2007.

[65] A. Kovič, D. Vengust, M. Vilfan, and A. Mrzel. Controlled self-decoration of $Mo_6S_yI_z$ ($8.2 \leqslant y+z \leqslant 10$) nanowires and their transformation to MoS_2 nanotubes with gold nanoparticles. *Journal of Nanoparticle Research*, 15(7):1791, 2013.

[66] A. Kis, G. Csanyi, D. Vrbanic, A. Mrzel, D. Mihailovic, A. Kulik, et al. Nanomechanical investigation of $Mo_6S_{9-x}I_x$ nanowire bundles. *Small*, 3(9):1544–1548, 2007.

[67] D. Vrbanic, M. Remskar, A. Jesih, A. Mrzel, P. Umek, M. Ponikvar, et al. Air-stable monodispersed $Mo_6S_3I_6$ nanowires. *Nanotechnology*, 15:635–638, 2004.

[68] S. J. Chin, P. Hornsby, D. Vengust, D. Mihailović, J. Mitra, P. Dawson, et al. Composites of poly(ε-caprolactone) and Mo6S3I6 nanowires. *Polymers for Advanced Technologies*, 23:149–160, 2012.

[69] F. Dassenoy, L. Joly-Pottuz, J.M. Martin, D. Vrbanic, A. Mrzel, D. Mihailovic, et al. Tribological performances of $Mo_6S_3I_6$ nanowires. *Journal of the European Ceramic Society*, 27(2):915 – 919, 2007.

[70] V. Nicolosi, Z. Aslam, K. Sader, G. M. Hughes, D. Vengust, N. P. Young, et al. A facile route to self-assembled Hg//MoSI nanowire networks. *New Journal of Chemistry*, 34:2241–2246, 2010.

[71] D. Vrbanic, S. Pejovnik, D. Mihailovic, and Z. Kutnjak. Electrical conductivity of $Mo_6S_3I_6$ and $Mo_6S_{4.5}I_{4.5}$ nanowires. *Journal of the European Ceramic Society*, 27:975–977, 2007.

[72] M. Remškar. Inorganic nanotubes. *Advanced Materials*, 16(17):1497–1504, 2004.

[73] M. T. Swihart. Vapor-phase synthesis of nanoparticles. *Current Opinion in Colloid and Interface Science*, 8:127–133, 2003.

[74] M. Remskar, A. Mrzel, M. Virsek, M. Godec, M. Krause, A. Kolitsch, et al. The MoS_2 nanotubes with defect-controlled electric properties. *Nanoscale Research Letters*, 6(1):1–6, 2011.

[75] M. Radisic and K. L. Christman. Materials science and tissue engineering: Repairing the heart. *Mayor Clinical Proceedings*, 88(8):884–898, 2014.

[76] P. Abiri, A. Abiri, R. R. S. Packard, Y. Ding, A. Yousefi, J. Ma, M. Bersohn, et al. Inductively powered wireless pacing via a miniature pacemaker and remote stimulation control system. *Scientific Reports*, 7:1–10, 2017.

[77] L. Mao, J. Chen, X. Zhang, M. Kwak, Y. Wu, and R. Fan. A promising biodegradable magnesium alloy suitable for clinical vascular stent application. *Scientific Reports*, 7:1–12, 2017.

[78] L. Xu, S. R. Gutbrod, A. P. Bonifas, Y. Su, M. S. Sulkin, N. Lu, et al. 3D multifunctional integumentary membranes for spatiotemporal cardiac measurements and stimulation across the entire epicardium. *Nature communications*, 5:3329, 2014.

[79] C. Laborde, F. Pittino, H. A. Verhoeven, S. G. Lemay, L. Selmi, M. A. Jongsma, et al. Real-time imaging of microparticles and living cells with CMOS nanocapacitor arrays. *Nature Nanotechnology*, 10(9):791–5, 2015.

[80] R. Huys, D. Braeken, D. Jans, A. Stassen, N. Collaert, J. Wouters, et al. Single-cell recording and stimulation with a 16k micro-nail electrode array integrated on a 0.18 μm CMOS chip. *Lab on a Chip*, 12(7):1274, 2012.

[81] K. Imfeld, S. Neukom, A. Maccione, Y. Bornat, S. Martinoia, P. A. Farine, et al. Large-scale, high-resolution data acquisition system for extracellular recording of electrophysiological activity. *IEEE Transactions on Biomedical Engineering*, 55(8):2064–2073, 2008.

[82] Nicholas J. Severs. The cardiac muscle cell. *BioEssays*, 22:188–199, 2000.

[83] OpenStax College. *Anathomy and Physiology*. OpenStax, Rice University, 2017. Downloaded for free at: https://openstax.org/details/books/anatomy-and-physiology.

[84] C. A. Walker and F. G. Spinale. Basic science review the structure and function of the cardiac myocyte : A review of fundamental concepts. *The Journal of Thoracic and Cardiovascular Surgery*, 118(2):375–382, 1999.

[85] A. Vydyanath, C. A. Gurnett, S. Marston, and P. K. Luther. Axial distribution of myosin binding protein-C is unaffected by mutations in human cardiac and skeletal muscle. *Journal of Muscle Research and Cell Motility*, 33:61–74, 2012.

[86] B. Emde, A. Heinen, A. Gödecke, and K. Bottermann. Wheat germ agglutinin staining as a suitable method for detection and quantification of fibrosis in cardiac tissue after myocardial infarction. *European Journal of Histochemistry*, 58:315–319, 2014.

[87] S. R. Shin, S. M. Jung, M. Zalabany, K. Kim, P. Zorlutuna, S. B. Kim, et al. Carbon-nanotube-embedded hydrogel sheets for engineering cardiac constructs and bioactuators. *ACS Nano*, 7(3):2369–2380, 2013.

[88] K. M. Broughton, J. Li, E. Sarmah, C. M. Warren, Y. Lin, M. P. Henze, et al. A myosin activator improves actin assembly and sarcomere function of human-induced pluripotent stem cell-derived cardiomyocytes with a troponin T point mutation. *American journal of physiology. Heart and circulatory physiology*, 311:107–117, 2016.

[89] M.-J. Goumans, T. P. de Boer, A. M. Smits, L. W. Van Laake, P. Van Vliet, et al. TGF-β 1 induces efficient differentiation of human cardiomyocyte progenitor cells into functional cardiomyocytes in vitro. *Stem Cells Research*, 1:138–149, 2008.

[90] M. Pluess and E. Ehler. Cardiac cytoarchitecture in health and disease. In Elisabeth Ehler, editor, *Cardiac Cytoarchitecture: How to Maintain a Working Heart*, chapter 1. Springer International Publishing, 2015.

[91] W. E. Louch, K. A. Sheehan, and B. M. Wolska. Methods in cardiomyocytes isolation, culture and gene transfer. *Journal of Molecular and Cellular Cardiology*, 51(3):288–298, 2011.

[92] E. A. Woodcock and S. J. Matkovich. Cardiomyocytes structure, function and associated pathologies. *The International Journal of Biochemistry and Cell Biology*, 37:1746–1751, 2005.

[93] C. Altomare, E. Pianezzi, E. Cervio, S. Bolis, V. Biemmi, P. Benzoni, et al. Human-induced pluripotent stem cell-derived cardiomyocytes from cardiac progenitor cells: effects of selective ion channel blockade. *Europace*, 18:67–66, 2016.

[94] A. Nikolskaya and V. Sharma. Cell culture models and methods. In D. C. Sigg, P. A. Iaizzo, Y.-F. Xiao, and B. He, editors, *Cardiac Electrophysiology Methods and Models*, chapter 10. Springer Science & Business Media, 2010.

[95] L. Li, I. Vorobyov, and T. W. Allen. The different interactions of lysine and arginine side chains with lipid membranes. *The Journal of Physical Chemistry B*, 117(40):11906–11920, 2013.

[96] B. Lauzier, F. Vaillant, C. Merlen, R. Gélinas, B. Bouchard, M.-E. Rivard, et al. Metabolic effects of glutamine on the heart. anaplerosis versus the hexosamine biosynthetic pathway. *Journal of molecular and cellular cardiology*, 55:92–100, 2013.

[97] J. Baum and H. S. Duffy. Fibroblasts and myofibroblasts : What are we talking about ? *Journal of Cardiovascular Pharmacology*, 57(4):376–379, 2011.

[98] A. Spanu, S. Lai, P. Cosseddu, M. Tedesco, S. Martinoia, and A. Bonfiglio. An organic transistor-based system for reference-less electrophysiological monitoring of excitable cells. *Scientific Reports*, 5:1–7, 2015.

[99] Beatrice Miccoli. Multi-sensor platform for pH and temperature measurements in organs-on-a-chip devices. Master's thesis, Politecnico di Torino, 2014.

[100] F. Capua. Caratterizzazione elettrica, termica ed optoelettronica di microstrutture di ZnO e $Mo_6S_4I_6$ per la realizzazione di micro-sensori integrati. Master's thesis, Politecnico di Torino, 2016.

[101] J. Yoon, W. K. Hong, M. Jo, G. Jo, M. Choe, W. Park, et al. Nonvolatile memory functionality of ZnO nanowire transistors controlled by mobile protons. *ACS Nano*, 5(1):558–564, 2011.

[102] V. F. Rivera, F. Auras, P. Motto, S.o Stassi, G. Canavese, E. Celasco, et al. Length-dependent charge generation from vertical arrays of high-aspect-ratio ZnO nanowires. *Chemistry – A European Journal*, 19(43):14665–14674, 2013.

[103] L. Liao, Z. Zhang, B. Yan, Z. Zheng, Q. L. Bao, T. Wu, et al. Multifunctional CuO nanowire devices: p-type field effect transistors and CO gas sensors. *Nanotechnology*, 20(8):085203, 2009.

[104] O. Lupan, G. Chai, L. Chow, G. a. Emelchenko, H. Heinrich, V. V. Ursaki, et al. Ultraviolet photoconductive sensor based on single ZnO nanowire. *Physica Status Solidi (A) Applications and Materials Science*, 207(7):1735–1740, 2010.

[105] H. Kind, H. Yan, B. Messer, M. Law, and P. Yang. Nanowire ultraviolet photodetectors and optical switches. *Advanced Materials*, 14(2):158–160, 2002.

[106] Q. Humayun, M. Kashif, U. Hashim, and A. Qurashi. Selective growth of ZnO nanorods on microgap electrodes and their applications in UV sensors. *Nanoscale research letters*, 9(1):29, 2014.

[107] S. N. Das, J. P. Kar, J.-H. Choi, T. I. Lee, K.-J. Moon, and J.-M. Myoung. Fabrication and characterization of ZnO single nanowire-based hydrogen sensor. *The Journal of Physical Chemistry C*, (3):1689–1693.

[108] S. Carrara, D. J. Riley, V. Bavastrello, E. Stura, and C. Nicolini. Methods to fabricate nanocontacts for electrical addressing of single molecules. *Sensors and Actuators B: Chemical*, 105:542–548, 2005.

[109] W. Chen, H. Ahmed, and K. Nakazoto. Coulomb blockade at 77 K in nanoscale metallic islands in a lateral nanostructure. *Applied Physics Letters*, 66(24):3383–3384, 1995.

[110] T. Nagase, T. Kubota, and S. Mashiko. Fabrication of nano-gap electrodes for measuring electrical properties of organic molecules using a focused ion beam. *Thin Solid Films*, 438:374 – 377, 2003.

[111] A. Notargiacomo, V. Foglietti, E. Cianci, G. Capellini, M. Adami, P. Faraci, et al. Atomic force microscopy lithography as a nanodevice development technique. *Nanotechnology*, 10(4):458, 1999.

[112] A. F. Morpurgo, C. M. Marcus, and D. B. Robinson. Controlled fabrication of metallic electrodes with atomic separation. *Applied Physics Letters*, 74(14):2084–2086, 1999.

[113] M. A. Reed, C. Zhou, C. J. Muller, T. P. Burgin, and J. M. Tour. Conductance of a molecular junction. *Science*, 278(5336):252–254, 1997.

[114] P. Pourhossein and R. C. Chiechi. Fabricating nanogaps by nanoskiving. *Journal of Visualized Experiments*, 75:1–7, 2013.

[115] D. Demarchi, P. Civera, G. Piccinini, M. Cocuzza, and D. Perrone. Electrothermal modeling for EIBJ nanogap fabrication. *Electrochimica Acta*, 54(25):6003–6009, 2009.

[116] A. Dimonte. *Nanogap structures for Molecular Electronics and BioSensing*. PhD thesis, Politecnico di Torino, 2012.

[117] P. Motto, M. Crepaldi, G. Piccinini, and D. Demarchi. NanoCube: A low-cost, modular, and high-performance embedded system for adaptive fabrication and characterization of nanogaps. *IEEE Transactions on Nanotechnology*, 13(2):322–334, 2014.

[118] D. R. Strachan, D. E. Smith, D. E. Johnston, T. H. Park, M. J. Therien, et al. Controlled fabrication of nanogaps in ambient environment for molecular electronics. *Applied Physics Letters*, 86(4):043109, 2005.

[119] R. Pethig. Review Article — Dielectrophoresis: Status of the theory, technology, and applications. 4:022811, 2010.

[120] T. Schnelle, R. Hagedorn, G. Fuhr, S. Fiedler, and T. Müller. Three-dimensional electric field traps for manipulation of cells–calculation and experimental verification. *Biochimica et biophysica acta*, 1157(2):127—140, 1993.

[121] J. Voldman, M. L. Gray, M. Toner, and M. A. Schmidt. A microfabrication-based dynamic array cytometer. 74:3984–3990, 2002.

[122] B. Miccoli, A. Bonanno, A. Sanginario, V. Cauda, and D. Demarchi. A customized nanowire-based sensing array on programmable CMOS chip. In *NanoIsrael*, page Poster, Tel Aviv, 2016.

[123] V. Allegra. Technologies and Circuits for Integrated Nanosensors. Master's thesis, Politecnico di Torino, 2015.

[124] A. Bonanno, M. Morello, M. Crepaldi, A. Sanginario, S. Benetto, V. Cauda, et al. A low-power 0.13μm CMOS IC for ZnO-nanowire assembly and aanowire-based UV sensor interface. *IEEE Sensors*, 15(8):4203 – 4212, 2015.

[125] P. Motto Ros, B. Miccoli, A. Sanginario, and D. Demarchi. Low-Power Architecture for Integrated CMOS Bio-Sensing. In *IEEE Biomedical Circuits and Systems Conference (BioCAS)*, Torino, 2017, status: accepted.

[126] H. Xie, L. Erdmann, X. Zhu, K. J. Gabriel, and G.K. Fedder. Post-CMOS processing for high-aspect-ratio integrated silicon microstructures. *Journal of Microelectromechanical Systems*, 11(2):93–101, 2002.

[127] H. Qu. CMOS MEMS fabrication technologies and devices. *Micromachines*, 7(14):1–21, 2016.

[128] S. Sedky, A. Witvrouw, and K. Baert. Poly SiGe, a promising material for MEMS post-processing on top of standard CMOS wafers. In E. Obermeier, editor, *Transducers '01 Eurosensors XV*, pages 988–989. Springer, Berlin, Heidelberg, 2001.

[129] J. Schmitz. Adding functionality to microchips by wafer post-processing. *Nuclear Instruments and Methods in Physics Research A*, 576(1):142–149, 2007.

[130] P. F. Van Kessel, L. J. Hornbeck, R. E. Meier, and M. R. Douglass. A mems-based projection display. *Proceedings of the IEEE*, 86(8):1687–1704, 1998.

[131] S. R. Chang, C. H. Chang, J. S. Lin, S. C. Lu, Y. T. Lee, S. R. Yeh, et al. Die-level, post-CMOS processes for fabricating open-gate, field-effect biosensor arrays with on-chip circuitry. *Journal of Micromechanics and Microengineering*, 18:115032, 2008.

[132] Y. Xu. Post-CMOS and post-MEMS compatible flexible skin technologies : a review. *IEEE Sensors Journal*, 13(10):3962–3975, 2013.

[133] P. W. Barth, S. L. Bernard, and J. B. Angell. Flexible circuit and sensor arrays fabricated by monolithic silicon technology. *IEEE Transactions on Electron Devices*, 32(7):1202–1205, 1985.

[134] Y. Xu, Y.-C. Tai, A. Huang, and C.-M. Ho. IC-integrated flexible shear-stress sensor skin. *Journal of Microelectromechanical Systems*, 12(5):740–747, 2003.

[135] R. B. Katragadda and Y. Xu. A novel intelligent textile technology based on silicon flexible skins. In *Ninth IEEE International Symposium on Wearable Computers (ISWC'05)*, pages 78–81, 2005.

[136] J. John, Y. Li, J. Zhang, J. A. Loeb, and Y. Xu. Microfabrication of 3D neural probes with combined electrical and chemical interfaces. *Journal of Micromechanics and Microengineering*, 21(10):105011, 2011.

[137] J. K. John, E. Kim, H. Tu, J. Zhang, J. A. Loeb, and Xu Y. Multifunctional chronic 3D electrode arrays based on a simple folding process. In *2013 Transducers Eurosensors XXVII: The 17th International Conference on Solid-State Sensors, Actuators and Microsystems (TRANSDUCERS EUROSENSORS XXVII)*, pages 1476–1479, 2013.

[138] A. H. D. Graham, J. Robbins, C. R. Bowen, and J. Taylor. Commercialization of CMOS integrated circuit technology in multi-electrode arrays for neuroscience and cell-based biosensors. *Sensors*, 11:4943–4971, 2011.

[139] A. Ravaglioli and A. Krajewski. *Bioceramics*. Springer Netherlands, 1 edition, 1992.

[140] M. Kawahara, M. Kato, and Y. Kuroda. Effects of aluminum on the neurotoxicity of primary cultured neurons and on the aggregation of β-amyloid protein. *Brain Research Bulletin*, 55(2):211 – 217, 2001.

[141] L. H. A. Silva, J. R. da Silva, G. A. Ferreira, R. C. Silva, E. C. D. Lima, R. B. Azevedo, et al. Labeling mesenchymal cells with dmsa-coated gold and iron oxide nanoparticles: assessment of biocompatibility and potential applications. *Journal of Nanobiotechnology*, 14:59, 2016.

[142] J. W. Ko, H. C. Koo, D. W. Kim, S. M. Seo, T. J. Kang, Y. Kwon, et al. Electroless gold plating on aluminum patterned chips for CMOS-based sensor applications. *Journal of The Electrochemical Society*, 157(1):46–49, 2010.

[143] O. Sadiku-Agboola, E. R. Sadiku, and O. F. Biotidara. The properties and the effect of operating parameters on nickel plating (review). *International Journal of the Physical Sciences*, 7(3):349–360, 2012.

[144] S. Kundu, S. D. Kalyan, and P. Sahoo. Properties of electroless nickel at elevated temperature-a review. *Procedia Engineering*, 97:1698–1706, 2014.

[145] M. K. Arshad, I. Ahmad, A. Jalar, and G. Omar. The effects of zincation process on aluminum bond pad surfaces for electroless nickel immersion gold (ENIG) deposition. In *IEEE International Conference on Software Engineering (ICSE)*, pages 656–662, 2004.

[146] S. G. Robertson and I. M. Ritchie. A kinetic and electrochemical study of the zincate immersion process for aluminum. *Journal of Applied Electrochemistry*, 25:659–660, 1995.

[147] J. Zhang, I. Hsu, and C. Li. New immersion gold technology for uniform Au thickness distribution (IMPACT-IAAC 2016). *IEEE International Microsystems Packaging Assembly and Circuits Technology Conference (IMPACT)*, pages 191–194, 2016.

[148] R. Huys, D. Braeken, D. Jans, A. Stassen, N. Collaert, J. Wouters, et al. Single-cell recording and stimulation with a 16k micro-nail electrode array integrated on a 0.18 μm CMOS chip. *Lab on a Chip*, 12:1274–1280.

[149] M. E. Spira and A. Hai. Multi-electrode array technologies for neuroscience and cardiology. *Nature Nanotechnology*, 8(2):83–94, 2013.

[150] Flavio Heer. *CMOS-based microelectrode array for communication with electrogenic cells*. PhD Thesis, Swiss Federak Institute Of Technology, 2005.

[151] A. L. Hodgkin and A. F. Huxley. Currents carried by sodium and potassium ions through the membrane of the giant axon of loligo. *The Journal of Physiology*, 116(4):449–472, 1952.

[152] J. O. Bockris, A. K. Reddy, and M. E. Gamboa-Adelco. The Electrified Interface. In *Modern Electrochemistry 2A*, pages 623–846. Springer, USA, 2002.

[153] Rashmi R Shah. The significance of QT interval in drug development. *British Journal of Clinical Pharmacology*, 54(2):188–202, 2002.

[154] J. Abbott, T. Ye, L. Qin, M. Jorgolli, R. S. Gertner, D. Ham, et al. CMOS nanoelectrode array for all-electrical intracellular electrophysiological imaging. *Nature Nanotechnology*, 12(5):460–466, 2017.

[155] D. Braeken, D. Jans, R. Huys, A. Stassen, N. Collaert, L. Hoffman, et al. Open-cell recording of action potentials using active electrode arrays. *Lab on a Chip*, 12(21):4397, 2012.

[156] L. Berdondini, P.D. Van der Wal, O. Guenat, N.F. de Rooij, M. Koudelka-Hep, P. Seitz, et al. High-density electrode array for imaging in vitro electrophysiological activity. *Biosensors and Bioelectronics*, 21(1):167–174, 2005.

[157] 3Brain, 2018. Date of access: 16/01/2018, https://www.3brain.com.

[158] Multichannel Systems. Innovations in electrophysiology, 2018. Date of access: 16/01/2018, https://www.multichannelsystems.com/products.

[159] Alpha MED Scientific Inc., 2018. Date of access: 16/01/2018.

[160] H. Amin, A. Maccione, F. Marinaro, S. Zordan, and L. Nieus, T.and Berdondini. Electrical responses and spontaneous activity of human iPS-derived neuronal networks characterized for 3-month culture with 4096-electrode arrays. *Frontiers in Neuroscience*, 10, 2016.

[161] A. Defeudis. Bio-Hybrid Actuator using a 3D printing approach with embedded gold microelectrodes for Engineering Cardiac Tissue Regeneration. Master's thesis, Politecnico di Torino, 2016.

[162] D. Rus and M. T. Tolley. Design, fabrication and control of soft robots. *Nature*, 521:467–475, 2015.

[163] M. Pawlaczyk, M. Lelonkiewicz, and M. Wieczorowski. Age-dependent biomechanical properties of the skin. *Advances in Dermatology and Allergology*, 30(5):302–306, 2013.

[164] A. W. Feinberg, A. Feigel, S. S. Shevkoplyas, S. Sheehy, G. M. Whitesides, et al. Muscular thin films for building actuators and powering devices. *Science*, 317(5843):1366–1370, 2007.

[165] R. F Taylor and J. S. Schultz. *Handbook of Chemical and Biological Sciences*. CRC Press, Boca Raton, Florida (USA), 1996.

[166] H.-T. Lin, G. G. Leisk, and B. Trimmer. Goqbot: a caterpillar-inspired soft-bodied rolling robot. *Bioinspiration and Biomimetics*, 6(2):026007, 2011.

[167] M. Calisti, M. Giorelli, G. Levy, B. Mazzolai, B. Hochner, C. Laschi, and P. Dario. An octopus-bioinspired solution to movement and manipulation for soft robots. *Bioinspiration and Biomimetics*, 6(3):036002, 2011.

[168] I. Ieropoulos, I. A. Anderson, T. Gisby, C.-H. Wang, and J. Rossiter. Microbial-powered artificial muscles for autonomous robots. In *Proceeding Volume 7287: SPIE Smart Structures and Materials*, volume 7287, pages 728708 – 728712, San Diego, California, 2009.

[169] K. Suzumori, S. Endo, T. Kanda, N. Kato, and H. Suzuki. A bending pneumatic rubber actuator realizing soft-bodied manta swimming robot. In *Robotics and Automation, 2007 IEEE International Conference on*, pages 4975–4980. IEEE, 2007.

[170] S. Seok, C. D. Onal, K.-J. Cho, R. J. Wood, D. Rus, and S. Kim. Meshworm: A peristaltic soft robot with antagonistic nickel titanium coil actuators. *IEEE/ASME Transactions on Mechatronics*, 18(5):1485–1497, 2013.

[171] T. Li, G. Li, Y. Liang, T. Cheng, J. Dai, X. Yang, et al. Fast-moving soft electronic fish. *Science Advances*, 3(4):e1602045, 2017.

[172] S.-J. Park, M. Gazzola, K. S. Park, S. Park, V. Di Santo, E. L. Blevins, et al. Phototactic guidance of a tissue-engineered soft-robotic ray. *Science*, 353(6295):158–162, 2016.

[173] M. T. Holley, N. Nagarajan, C. Danielson, P. Zorlutuna, and K. Park. Development and characterization of muscle-based actuators for self-stabilizing swimming biorobots. *Lab on a Chip*, 16(18):3473–3484.

[174] C. Cvetkovic, R. Raman, V. Chan, B. J. Williams, M. Tolish, P. Bajaj, et al. Three-dimensionally printed biological machines powered by skeletal muscle. *Proceedings of the National Academy of Sciences*, 111(28):10125–10130, 2014.

[175] K. Deisseroth, G. Feng, A. K. Majewska, G. Miesenböck, A. Ting, and M. J. Schnitzer. Next-generation optical technologies for illuminating genetically targeted brain circuits. *The Journal of neuroscience: the official journal of the Society for Neuroscience*, 26(41):10380, 2006.

[176] K. M. Tye and K. Deisseroth. Optogenetic investigation of neural circuits underlying brain disease in animal models. *Nature Reviews Neuroscience*, 13(4):251, 2012.

[177] G. Camci-Unal, N. Annabi, M. R. Dokmeci, R. Liao, and A. Khademhosseini. Hydrogels for cardiac tissue engineering. *NPG Asia Materials*, 6(5):e99, 2014.

[178] Z. Z. Khaing, R. C. Thomas, S. A. Geissler, and C. E. Schmidt. Advanced biomaterials for repairing the nervous system: what can hydrogels do for the brain? *Materials Today*, 17(7):332–340, 2014.

[179] R. Scharf, T. Tsunematsu, N. McAlinden, M. D. Dawson, S. Sakata, and K. Mathieson. Depth-specific optogenetic control in vivo with a scalable, high-density μLED neural probe. *Scientific Reports*, 6, 2016.

[180] E. M. Ahmed. Hydrogel: Preparation, characterization, and applications: A review. *Journal of Advanced Research*, 6(2):105–121, 2015.

[181] E. Caló and V. V. Khutoryanskiy. Biomedical applications of hydrogels: A review of patents and commercial products. *European Polymer Journal*, 65:252–267, 2015.

[182] N. Annabi, S. M. Mithieux, A. S. Weiss, and F. Dehghani. The fabrication of elastin-based hydrogels using high pressure CO_2. *Biomaterials*, 30(1):1–7, 2009.

[183] KIKGEL. Neoheal ®. Sterile hydrogel dressings for moist wound management, 2017. Date of access: 29/12/2017, https://kikgel.com.pl/produkty/neoheal/.

[184] Elsevier Scopus. Database search "hydrogels" + "tissue engineering", 2017. Date of access: 02/01/2018, https://www.scopus.com.

[185] E. S. Place, J. H. George, C. K. Williams, and M. M. Stevens. Synthetic polymer scaffolds for tissue engineering. *Chemical Society Reviews*, 38(4):1139, 2009.

[186] Ibrahim M. El-Sherbiny and Magdi H. Yacoub. Hydrogel scaffolds for tissue engineering: Progress and challenges. *Global Cardiology Science & Practice*, 2013(3):316–342, 2013.

[187] F. Rossi, G. Perale, G. Storti, and M. Masi. A library of tunable agarose carbomer-based hydrogels for tissue engineering applications: The role of cross-linkers. *Journal of Applied Polymer Science*, 123(4):2211–2221, 2011.

[188] J. Wang, S. Hao, T. Luo, Z. Cheng, W. Li, F. Gao, et al. Feather keratin hydrogel for wound repair: Preparation, healing effect and biocompatibility evaluation. *Colloids and Surfaces B: Biointerfaces*, 149:341 – 350, 2017.

[189] A. D. Augst, H. J. Kong, and D. J. Mooney. Alginate hydrogels as biomaterials. *Macromolecular Bioscience*, 6(8):623–633, 2006.

[190] P.-H. G. Chao, S. Yodmuang, X. Wang, L. Sun, D. L. Kaplan, and G. Vunjak-Novakovic. Silk hydrogel for cartilage tissue engineering. *Journal of biomedical materials research. Part B, Applied biomaterials*, 95(1):84, 2010.

[191] K. Yue, G. Trujillo-de Santiago, M. M. Alvarez, A. Tamayol, N. Annabi, and A. Khademhosseini. Synthesis, properties, and biomedical applications of gelatin methacryloyl (GelMA) hydrogels. *Biomaterials*, 73:254–271, 2015.

[192] B. J. Klotz, D. Gawlitta, A. J. W. P. Rosenberg, J. Malda, and F. P.W. Melchels. Gelatin-methacryloyl hydrogels: Towards biofabrication-based tissue repair. *Trends in Biotechnology*, 34(5):394–407, 2016.

[193] An I. Van Den Bulcke, B. Bogdanov, N. De Rooze, E. H. Schacht, M. Cornelissen, and H. Berghmans. Structural and rheological properties of methacrylamide modified gelatin hydrogels. *Biomacromolecules*, 1(1):31–38, 2000.

[194] Y.-C. Chen, R.-Z. Lin, H. Qi, Y. Yang, H. Bae, Juan M. M.-M., et al. Functional human vascular network generated in photocrosslinkable gelatin methacrylate hydrogels. *Advanced Functional Materials*, 22(10):2027–2039, 2012.

[195] K. Zhu, S. R. Shin, T. Van Kempen, Y.-C. Li, V. Ponraj, A. Nasajpour, et al. Gold nanocomposite bioink for printing 3d cardiac constructs. *Advanced Functional Materials*, 27(12), 2017.

[196] S. R. Shin, B. Aghaei-Ghareh-Bolagh, T. T. Dang, S. N. Topkaya, X. Gao, S. Y. Yang, et al. Cell-laden microengineered and mechanically tunable hybrid hydrogels of gelatin and graphene oxide. *Advanced Materials*, 25(44):6385–6391, 2013.

[197] S. R. Shin, H. Bae, J. M. Cha, J. Y. Mun, Y.-C. Chen, H. Tekin, et al. Carbon nanotube reinforced hybrid microgels as scaffold materials for cell encapsulation. *ACS Nano*, 6(1):362–372, 2012.

[198] A. Sanginario, B. Miccoli, and D. Demarchi. Carbon nanotubes as an effective opportunity for cancer diagnosis and treatment. *Biosensors*, 7(1):9, 2017.

[199] R. S. Russo, S. S. Blemker, F. E. Fish, and H. Bart-Smith. Biomechanical model of batoid (skates and rays) pectoral fins predicts the influence of skeletal structure on fin kinematics: implications for bio-inspired design. 10(4):046002.

[200] Y. Wang, R. Yang, Z. Shi, L. Zhang, D. Shi, E. Wang, and G. Zhang. Super-elastic graphene ripples for flexible strain sensors. *ACS Nano*, 5(5):3645–3650, 2011.

[201] S. Sharifi, S. B. G. Blanquer, T. G. van Kooten, and D. W. Grijpma. Biodegradable nanocomposite hydrogel structures with enhanced mechanical properties prepared by photo-crosslinking solutions of poly(trimethylene carbonate)–poly(ethylene glycol)–poly(trimethylene carbonate) macromonomers and nanoclay particles. *Acta Biomaterialia*, 8(12):4233–4243, 2012.

[202] P. Gutruf, E. Zeller, S. Walia, S. Sriram, and M. Bhaskaran. Mechanically tunable high refractive-index contrast TiO_2–PDMS gratings. *Advanced Optical Materials*, 3(11):1565–1569, 2015.

[203] Y.-C. Li, M.-W. Lin, M.-H. Yen, S. M.-Y. Fan, J.-T. Wu, T.-H. Young, J.-Y. Cheng, and S.-J. Lin. Programmable laser-assisted surface microfabrication on a Poly(Vinyl Alcohol)-coated glass chip with self-changing cell adhesivity for heterotypic cell patterning. *ACS Applied Materials & Interfaces*, 7(40):22322–22332, 2015.

[204] J. U. Lind, T. A. Busbee, A. D. Valentine, F. S. Pasqualini, H. Yuan, M. Yadid, et al. Instrumented cardiac microphysiological devices via multimaterial three-dimensional printing. *Nature Materials*, 16(3):303–308, 2017.

[205] Essential role of the zinc finger transcription factor casz1 for mammalian.

[206] J. Tchao, L. Han, B. Lin, L. Yang, and K. Tobita. Combined biophysical and soluble factor modulation induces cardiomyocyte differentiation from human muscle derived stem cells. *Scientific Reports*, 4, 2014.

[207] F. Pati, J. Jang, J. W. Lee, and D.-W. Cho. Extrusion Bioprinting. pages 123–152. Elsevier, 2015.

[208] J. Li, M. Chen, X. Fan, and H. Zhou. Recent advances in bioprinting techniques: approaches, applications and future prospects. *Journal of Translational Medicine*, 14, 2016.

[209] Y. He, F. Yang, H. Zhao, Q. Gao, B. Xia, and J. Fu. Research on the printability of hydrogels in 3d bioprinting. *Scientific Reports*, 6(1), 2016.

[210] S. V. Murphy and A. Atala. 3D bioprinting of tissues and organs. *Nature Biotechnology*, 32(8):773–785, 2014.

[211] H.-W. Kang, S. J. Lee, I. K. Ko, C. Kengla, J. J. Yoo, and A. Atala. A 3D bioprinting system to produce human-scale tissue constructs with structural integrity. *Nature Biotechnology*, 34(3):312–319, 2016.

[212] Y. S. Zhang, K. Yue, J. Aleman, K. Mollazadeh-Moghaddam, S. M. Bakht, J. Yang, et al. 3D bioprinting for tissue and organ fabrication. *Annals of Biomedical Engineering*, 45(1):148–163, 2017.

[213] M. S. Mannoor, Z. Jiang, T. James, Y. L. Kong, K. A. Malatesta, W. O. Soboyejo, et al. 3D printed bionic ears. *Nano Letters*, 13(6):2634–2639, 2013.

[214] B. Duan, E. Kapetanovic, L. A. Hockaday, and J. T. Butcher. Three-dimensional printed trileaflet valve conduits using biological hydrogels and human valve interstitial cells. *Acta Biomaterialia*, 10(5):1836–1846, 2014.

[215] F. R. Vogenberg, C. Isaacson Barash, and M. Pursel. Personalized medicine. *Pharmacy and Therapeutics*, 35(10):560–576, 2010.

[216] A. Blaeser, Daniela F. Duarte C., and H. Fischer. 3D bioprinting of cell-laden hydrogels for advanced tissue engineering. *Current Opinion in Biomedical Engineering*, 2:58–66, 2017.

[217] W. Liu, Y. S. Zhang, M. A. Heinrich, F. De Ferrari, H. L. Jang, S. M. Bakht, et al. Rapid continuous multimaterial extrusion bioprinting. *Advanced Materials*, 29(3):1604630, 2017.

[218] J. Malda, J. Visser, F. P. Melchels, T. Jüngst, W. E. Hennink, W. J. A. Dhert, et al. 25th anniversary article: Engineering hydrogels for biofabrication. *Advanced Materials*, 25(36):5011–5028, 2013.

[219] Invetech. Organovo: NovoGen MMX Bioprinter^{TM}, 2018. Date of access: 10/01/2018, http://www.invetech.com.au.

[220] Jessica Mendoza. 3D-printing human skin: The end of animal testing?, 2018. Date of access: 10/01/2018, https://www.csmonitor.com.

[221] F. Marga, K. Jakab, C. Khatiwala, B. Shephard, S. Dorfman, and G. Forgacs. Organ printing: a novel tissue engineering paradigm. In *5th European Conference of the International Federation for Medical and Biological Engineering*, pages 27–30. Springer, 2011.

[222] W. W. L. Glenn, J. H. Hageman, A. Mauro, L. Eisenberg, S. Flanigan, and M. Harvard. Electrical stimulation of excitable tissue by radio-frequency transmission. *Annals of Surgery*, 160(3):338–350, 1964.

[223] N. M. Kiasari, S. Soltanian, B. Gholamkhass, and P. Servati. Environmental gas and light sensing using ZnO nanowires. *IEEE Transactions on Nanotechnology*, 13(2):368–374, 2014.

[224] J. Suehiro, N. Nakagawa, S.-I. Hidaka, M. Ueda, K. Imasaka, M. Higashihata, et al. Dielectrophoretic fabrication and characterization of a ZnO nanowire-based UV photosensor. *Nanotechnology*, 17(10):2567–2573, 2006.

[225] J. Zhou, Y. Gu, Y. Hu, W. Mai, P. H. Yeh, G. Bao, et al. Gigantic enhancement in response and reset time of ZnO UV nanosensor by utilizing Schottky contact and surface functionalization. *Applied Physics Letters*, 94(19):2007–2010, 2009.

[226] M. E. Swanwick, S. M.-L. Pfaendler, A. I Akinwande, and A. J. Flewitt. Near-ultraviolet zinc oxide nanowire sensor using low temperature hydrothermal growth. *Nanotechnology*, 23(34):344009, 2012.

[227] C. García Núñez, A. García Marín, P. Nanterne, J. Piqueras, P. Kung, and J. L. Pau. Conducting properties of nearly depleted ZnO nanowire UV sensors fabricated by dielectrophoresis. *Nanotechnology*, 24(41):415702, 2013.

[228] B. J. Coppa, R. F. Davis, and R. J. Nemanich. Gold Schottky contacts on oxygen plasma-treated, n-type ZnO(0001). *Applied Physics Letters*, 82(3):400–402, 2003.

[229] D. Calestani, M. Zha, R. Mosca, A. Zappettini, M.C. Carotta, V. Di Natale, et al. Growth of ZnO tetrapods for nanostructure-based gas sensors. *Sensors and Actuators B: Chemical*, 144(2):472 – 478, 2010.

[230] M. R. Alenezi, S. J. Henley, and S. R. P. Silva. On-chip fabrication of high performance nanostructured ZnO UV detectors. *Nature Scientific Reports*, 5:8516, 2015.

[231] Multifunctional ZnO-nanowire-based sensor. *Advanced Functional Materials*, 21(22):4342–4348, 2011.

[232] R. Orij, J. Postmus, A. T. Beek, S. Brul, and G. J. Smits. In vivo measurement of cytosolic and mitochondrial pH using a pH-sensitive GFP derivative in Saccharomyces cerevisiae reveals a relation between intracellular pH and growth. *Microbiology*, 155(1):268–278, 2009.

[233] T. R. Kießling, R. Stange, J. A. Käs, and A. W. Fritsch. Thermorheology of living cells - Impact of temperature variations on cell mechanics. *New Journal of Physics*, 15, 2013.

[234] W. Kowalski. UVGI Disinfection Theory. In *Ultraviolet Germicidal Irradiation Handbook: UVGI for Air and Surface Disinfection*, chapter 2, pages 17–50. Springer-Verlag Berlin Heidelberg, 1 edition, 2009.

[235] Y. Yang, W. Guo, K. C. Pradel, G. Zhu, Y. Zhou, Y. Zhang, et al. Pyroelectric nanogenerators for harvesting thermoelectric energy. *Nano Letters*, 12(6):2833–2838, 2012.

[236] S. N. Das, J. P. Kar, and K. Moon. Junction Properties and Applications of ZnO Single Nanowire Based Schottky Diode. In A. Hashim, editor, *Nanowires - Fundamental Research*, chapter 8, pages 161–182. InTech, 2011.

[237] R. Sharma. Temperature dependence of I-V characteristics of Au/n-Si Schottky barrier diode. *Journal of Electron Devices*, 8, 2010.

[238] E. H. Rhoderick. Metal-semiconductor contacts. *IEE Proceedings I - Solid-State and Electron Devices*, 129(1):1–, 1982.

[239] B. S. Kang, F. Ren, Y. W. Heo, L. C. Tien, D. P. Norton, and S. J. Pearton. pH measurements with single ZnO nanorods integrated with a microchannel. *Applied Physics Letters*, 86(11):112105, 2005.

[240] S. Borini, L. Boarino, and G. Amato. Slow conductivity relaxation and simple aging in nanostructured mesoporous silicon at room temperature. *Phys. Rev. B*, 75:165205, Apr 2007.

[241] J. S. Lee, R. I. Hornsey, and D. Renshaw. Analysis of CMOS Photodiodes. I. Quantum efficiency, year=2003, volume=50, number=5, pages=1233-1238,. *IEEE Transactions on Electron Devices*.

[242] M. Razeghi and A. Rogalski. Semiconductor ultraviolet detectors. *Journal of Applied Physics*, 79(10):7433–7473, 1996.

[243] A. Oyane, H.-M. Kim, T. Furuya, T. Kokubo, T. Miyazaki, and T. Nakamura. Preparation and assessment of revised simulated body fluids. *Journal of Biomedical Materials Research Part A*, 65A(2):188–195, 2003.

[244] T. Kokubo, H. Kushitani, S. Sakka, T. Kitsugi, and T. Yamamuro. Solutions able to reproduce in vivo surface-structure changes in bioactive glass-ceramic A-W3. *Journal of Biomedical Materials Research*, 24(6):721–734, 1990.

[245] R. de Levie. The electrolysis of water. *Journal of Electroanalytical Chemistry*, 476(1):92–93, 1999.

[246] Sigma Aldrich. Sigma Aldrich, 2018. Date of access: 05/02/2018, https://www.sigmaaldrich.com.

[247] D. F. Coutinho, S. Sant, H. Shin, J. T. Oliveira, E. G. Manuela, N. M. Neves, A. Khademhosseini, and R. L. Reis. Modified gellan gum hydrogels with tunable physical and mechanical properties. *Biomaterials*, 31(29):7494–7502, 2010.

[248] Ana H. Bacelar, Joana Silva-Correia, Joaquim M. Oliveira, and Rui L. Reis. Recent progress in gellan gum hydrogels provided by functionalization strategies. *J. Mater. Chem. B*, 4:6164–6174, 2016.

[249] M. M. Hossain, E. Shimizu, M. Saito, S. Ramachandra Rao, Y. Yamaguchi, and E. Tamiya. Non-invasive characterization of mouse embryonic stem cell derived cardiomyocytes based on the intensity variation in digital beating video. *Analyst*, 135:1624–1630, 2010.

[250] I. Ouchi, I. Nakai, M. Ono, and S. Kimura. Features of fluorescence spectra of polyethylene 2,6-naphthalate films. *Journal of Applied Polymer Science*, 105(1):114–121, 2007.

List of Publications

[1] S. R. Shin, B. Migliori, B. Miccoli, Y.-C. Li, P. Mostafalu, J. Seo, S. Mandla, A. Enrico, S. Antona, R. Sabarish, T. Zheng, L. Pirrami, K. Zhang, Y. S. Zhang, K.-T. Wan, D. Demarchi, M. R. Dokmeci, A. Khademhosseini. **Electrically driven microengineered bio-inspired soft robots**. *Advanced Materials*, 1704189, 2018, DOI https://doi.org/10.1002/adma.201704189.

[2] B. Miccoli*, V. Cauda*, A. Bonanno, A. Sanginario, K. Bejtka, F. Bella, M. Fontana. **One dimensional ZnO/gold junction for simultaneous and versatile multisensing measurements**. Scientific Reports, 6:29763, 2016, DOI doi:10.1038/srep29763.

[3] B. Miccoli, A. Bonanno, V. Cauda, A. Sanginario, and D. Demarchi. **Interface of a single ZnO-nanowire assembled onto custom-fabricated nanogap device for UV sensing applications**. In IEEE International Spring Seminar on Electronics Technology (ISSE), pages 431–435, Eger, Hungary, 2015, DOI 10.1109/ISSE.2015.7248035.

[4] A. Bonanno, A. Sanginario, S. Marasso, B. Miccoli, K. Bejtka, S. Benetto, D. Demarchi. **A multipurpose CMOS platform for nanosensing**. Sensors, 16(12):2034, 2016, DOI doi:10.3390/s16122034.

[5] A. Sanginario*, B. Miccoli*, D. Demarchi. **Carbon Nanotubes as an Effective Opportunity for Cancer Diagnosis and Treatment**. Biosensors, 7(1), 2017, DOI doi:10.3390/bios7010009.

[6] P. Motto Ros, B. Miccoli*, A. Sanginario, D. Demarchi. **Low-Power Architecture for Integrated CMOS Bio-Sensing**. 13th IEEE Biomedical and Life Science Circuits and Systems (BioCAS), 2017, *in press*.

[7] L. Racca, B. Dumontel, B. Miccoli, M. Canta, L. Serpe, R. Canaparo, C. Di Benedetto, A. Falqui, V. A. Cauda. **Investigation of cytotoxic effects of different ZnO nanostructures on living cancer cells**. Merck Young Chemists Symposium (MYCS 2016), Rimini, 25-27 November, page 158, 2016 .

Appendix A

Copyright and Reprinting Permissions

A.1 Reprinting permission for reference [1], ©2018 WILEY-VCH Verlag GmbH & Co. KGaA, Weinheim.

Terms and Conditions

- The materials you have requested permission to reproduce or reuse (the "Wiley Materials") are protected by copyright.

- You are hereby granted a personal, non-exclusive, non-sub licensable (on a stand-alone basis), non-transferable, worldwide, limited license to reproduce the Wiley Materials for the purpose specified in the licensing process. This license, **and any CONTENT (PDF or image file) purchased as part of your order,** is for a one-time use only and limited to any maximum distribution number specified in the license. The first instance of republication or reuse granted by this license must be completed within two years of the date of the grant of this license (although copies prepared before the end date may be distributed thereafter). The Wiley Materials shall not be used in any other manner or for any other purpose, beyond what is granted in the license. Permission is granted subject to an appropriate acknowledgement given to the author, title of the material/book/journal and the publisher. You shall also duplicate the copyright notice that appears in the Wiley publication in your use of the Wiley Material. Permission is also granted on the understanding that nowhere in the text is a previously published source acknowledged for all or part of this Wiley Material. Any third party content is expressly excluded from this permission.

- With respect to the Wiley Materials, all rights are reserved. Except as expressly granted by the terms of the license, no part of the Wiley Materials may be copied, modified, adapted (except for minor reformatting required by the new Publication), translated, reproduced, transferred or distributed, in any form or by any means, and no derivative works may be made based on the Wiley Materials without the prior permission of the respective copyright owner.**For STM Signatory Publishers clearing permission under the terms of the STM Permissions Guidelines only, the terms of the license are extended to include subsequent editions and for editions in other languages, provided such editions are for the work as a whole in situ and does not involve the separate exploitation of the permitted figures or extracts,** You may not alter, remove or suppress in any manner any copyright, trademark or other notices displayed by the Wiley Materials. You may not license, rent, sell, loan, lease, pledge, offer as security, transfer or assign the Wiley Materials on a stand-alone basis, or any of the rights granted to you hereunder to any other person.

- The Wiley Materials and all of the intellectual property rights therein shall at all times remain the exclusive property of John Wiley & Sons Inc, the Wiley Companies, or their respective licensors, and your interest therein is only that of having possession of and the right to reproduce the Wiley Materials pursuant to Section 2 herein during the continuance of this Agreement. You agree that you own no right, title or interest in or to the Wiley Materials or any of the intellectual property rights therein. You shall have no rights hereunder other than the license as provided for above in Section 2. No right, license or interest to any trademark, trade name, service mark or other branding ("Marks") of WILEY or its licensors is granted hereunder, and you agree that you shall not assert any such right, license or interest with respect thereto

- NEITHER WILEY NOR ITS LICENSORS MAKES ANY WARRANTY OR REPRESENTATION OF ANY KIND TO YOU OR ANY THIRD PARTY, EXPRESS, IMPLIED OR STATUTORY, WITH RESPECT TO THE MATERIALS OR THE ACCURACY OF ANY INFORMATION CONTAINED IN THE MATERIALS, INCLUDING, WITHOUT LIMITATION, ANY IMPLIED WARRANTY OF MERCHANTABILITY, ACCURACY, SATISFACTORY QUALITY, FITNESS FOR A PARTICULAR PURPOSE, USABILITY, INTEGRATION OR NON-INFRINGEMENT AND ALL SUCH WARRANTIES ARE HEREBY EXCLUDED BY WILEY AND ITS LICENSORS AND WAIVED BY YOU.

- WILEY shall have the right to terminate this Agreement immediately upon breach of this Agreement by you.
- You shall indemnify, defend and hold harmless WILEY, its Licensors and their respective directors, officers, agents and employees, from and against any actual or threatened claims, demands, causes of action or proceedings arising from any breach of this Agreement by you.
- IN NO EVENT SHALL WILEY OR ITS LICENSORS BE LIABLE TO YOU OR ANY OTHER PARTY OR ANY OTHER PERSON OR ENTITY FOR ANY SPECIAL, CONSEQUENTIAL, INCIDENTAL, INDIRECT, EXEMPLARY OR PUNITIVE DAMAGES, HOWEVER CAUSED, ARISING OUT OF OR IN CONNECTION WITH THE DOWNLOADING, PROVISIONING, VIEWING OR USE OF THE MATERIALS REGARDLESS OF THE FORM OF ACTION, WHETHER FOR BREACH OF CONTRACT, BREACH OF WARRANTY, TORT, NEGLIGENCE, INFRINGEMENT OR OTHERWISE (INCLUDING, WITHOUT LIMITATION, DAMAGES BASED ON LOSS OF PROFITS, DATA, FILES, USE, BUSINESS OPPORTUNITY OR CLAIMS OF THIRD PARTIES), AND WHETHER OR NOT THE PARTY HAS BEEN ADVISED OF THE POSSIBILITY OF SUCH DAMAGES. THIS LIMITATION SHALL APPLY NOTWITHSTANDING ANY FAILURE OF ESSENTIAL PURPOSE OF ANY LIMITED REMEDY PROVIDED HEREIN.
- Should any provision of this Agreement be held by a court of competent jurisdiction to be illegal, invalid, or unenforceable, that provision shall be deemed amended to achieve as nearly as possible the same economic effect as the original provision, and the legality, validity and enforceability of the remaining provisions of this Agreement shall not be affected or impaired thereby.
- The failure of either party to enforce any term or condition of this Agreement shall not constitute a waiver of either party's right to enforce each and every term and condition of this Agreement. No breach under this agreement shall be deemed waived or excused by either party unless such waiver or consent is in writing signed by the party granting such waiver or consent. The waiver by or consent of a party to a breach of any provision of this Agreement shall not operate or be construed as a waiver of or consent to any other or subsequent breach by such other party.
- This Agreement may not be assigned (including by operation of law or otherwise) by you without WILEY's prior written consent.
- Any fee required for this permission shall be non-refundable after thirty (30) days from receipt by the CCC.
- These terms and conditions together with CCC's Billing and Payment terms and conditions (which are incorporated herein) form the entire agreement between you and WILEY concerning this licensing transaction and (in the absence of fraud) supersedes all prior agreements and representations of the parties, oral or written. This Agreement may not be amended except in writing signed by both parties. This Agreement shall be binding upon and inure to the benefit of the parties' successors, legal representatives, and authorized assigns.
- In the event of any conflict between your obligations established by these terms and conditions and those established by CCC's Billing and Payment terms and conditions, these terms and conditions shall prevail.
- WILEY expressly reserves all rights not specifically granted in the combination of (i) the license details provided by you and accepted in the course of this licensing

transaction, (ii) these terms and conditions and (iii) CCC's Billing and Payment terms and conditions.

- This Agreement will be void if the Type of Use, Format, Circulation, or Requestor Type was misrepresented during the licensing process.
- This Agreement shall be governed by and construed in accordance with the laws of the State of New York, USA, without regards to such state's conflict of law rules. Any legal action, suit or proceeding arising out of or relating to these Terms and Conditions or the breach thereof shall be instituted in a court of competent jurisdiction in New York County in the State of New York in the United States of America and each party hereby consents and submits to the personal jurisdiction of such court, waives any objection to venue in such court and consents to service of process by registered or certified mail, return receipt requested, at the last known address of such party.

WILEY OPEN ACCESS TERMS AND CONDITIONS
Wiley Publishes Open Access Articles in fully Open Access Journals and in Subscription journals offering Online Open. Although most of the fully Open Access journals publish open access articles under the terms of the Creative Commons Attribution (CC BY) License only, the subscription journals and a few of the Open Access Journals offer a choice of Creative Commons Licenses. The license type is clearly identified on the article.
The Creative Commons Attribution License
The Creative Commons Attribution License (CC-BY) allows users to copy, distribute and transmit an article, adapt the article and make commercial use of the article. The CC-BY license permits commercial and non-
Creative Commons Attribution Non-Commercial License
The Creative Commons Attribution Non-Commercial (CC-BY-NC)License permits use, distribution and reproduction in any medium, provided the original work is properly cited and is not used for commercial purposes.(see below)

Creative Commons Attribution-Non-Commercial-NoDerivs License
The Creative Commons Attribution Non-Commercial-NoDerivs License (CC-BY-NC-ND) permits use, distribution and reproduction in any medium, provided the original work is properly cited, is not used for commercial purposes and no modifications or adaptations are made. (see below)
Use by commercial "for-profit" organizations
Use of Wiley Open Access articles for commercial, promotional, or marketing purposes requires further explicit permission from Wiley and will be subject to a fee.
Further details can be found on Wiley Online Library
http://olabout.wiley.com/WileyCDA/Section/id-410895.html

Other Terms and Conditions:

v1.10 Last updated September 2015

Questions? customercare@copyright.com or +1-855-239-3415 (toll free in the US) or +1-978-646-2777.

Gmail **Beatrice Miccoli <bea.miccoli@gmail.com>**

Reprinting Permission

Rights DE <RIGHTS-and-LICENCES@wiley-vch.de> 15 gennaio 2018 10:05
A: Beatrice Miccoli <beatrice.miccoli@polito.it>
Cc: Rights DE <RIGHTS-and-LICENCES@wiley-vch.de>

Dear Beatrice Miccoli,

We hereby grant permission for the requested use expected that due credit is given to the original source.

If material appears within our work with credit to another source, authorisation from that source must be obtained.

Credit must include the following components:

- Journals: Author(s) Name(s): Title of the Article. Name of the Journal. Publication year. Volume. Page(s). Copyright Wiley-VCH Verlag GmbH & Co. KGaA. Reproduced with permission.

If you also wish to publish your thesis in electronic format, you may use the article according to the Copyright transfer agreement:

3. Final Published Version.

Wiley-VCH hereby licenses back to the Contributor the following rights with respect to the final published version of the Contribution:

a. […]

b. Re-use in other publications. The right to re-use the final Contribution or parts thereof for any publication authored or edited by the Contributor (excluding journal articles) where such re-used material constitutes less than half of the total material in such publication. In such case, any modifications should be accurately noted. [This applies to each article, not the three articles in total].

Kind regards

Heike Weller

Rights Manager

Rights & Licenses

Wiley-VCH Verlag GmbH & Co. KGaA

Boschstraße 12

69469 Weinheim

Germany

www.wiley-vch.de

T +(49) 6201 606-585

F +(49) 6201 606-332

rightsDE@wiley.com

WILEY

Von: Beatrice Miccoli [mailto:beatrice.miccoli@polito.it]
Gesendet: Sonntag, 14. Januar 2018 8:33
An: Rights DE
Betreff: Reprinting Permission

[Testo tra virgolette nascosto]

A.2 Reprinting permission for reference [2], ©2015 IEEE.

Gmail **Beatrice Miccoli <bea.miccoli@gmail.com>**

Copyright Permission IEEE Article (ISSE2015)

Danilo Demarchi <danilo.demarchi@polito.it> 26 gennaio 2018 18:31
A: Beatrice Miccoli <beatrice.miccoli@polito.it>

Dear Beatrice,
of course yes.

danilo

> On 25 Jan 2018, at 18:06, Beatrice Miccoli <beatrice.miccoli@polito.it> wrote:
>
> Dear Professor Demarchi,
>
> as indicated by the IEEE reprinting guidelines (see attachment), I ask you, the senior author of the paper titled "Interface of a single ZnO-nanowire assembled onto custom-fabricated nanogap device for UV sensing applications" (DOI: 10.1109/ISSE.2015.7248035), the formal permission to reuse substantial portion of this paper for my PhD thesis.
>
> Best Regards,
>
> Beatrice Miccoli
> Ph.D. Student
> ----------
> Politecnico di Torino
> Dipartimento di Elettronica e Telecomunicazioni
> Corso Duca degli Abruzzi 24
> 10129 Torino - Italy
>
> Tel: +39 011 090 4004
> Email: beatrice.miccoli@polito.it
> ----------
> <Miccoli2015_ISSE.pdf>

A.3 Reprinting permission for reference [3], CC-BY 4.0.

A.4 Reprinting permission for reference [4], CC-BY 4.0.

Sensors **2016**, *16*(12), 2034; doi:10.3390/s16122034 Open Access Article

A Multipurpose CMOS Platform for Nanosensing

Alberto Bonanno [1], **Alessandro Sanginario** [2,*], **Simone L. Marasso** [3], **Beatrice Miccoli** [4], **Katarzyna Bejtka** [1], **Simone Benetto** [5] and **Danilo Demarchi** [4]

[1] Center for Sustainables Futures@PoliTo, Istituto Italiano di Tecnologia, C.so Trento 21, 10129 Torino, Italy
[2] Electronics Design Laboratory (EDL), Istituto Italiano di Tecnologia, Via Melen 83b, 16152 Genova, Italy
[3] CNR-IMEM, Parco Area delle Scienze 37, 43124 Parma, Italy
[4] Department of Electronics and Telecommunication, Politecnico di Torino, C.so Duca degli Abruzzi 24, 10129 Torino, Italy
[5] X-Lab Materials and Microsystems Laboratory, DISAT, Politecnico di Torino, Via Lungo Piazza d'Armi 6, 10034 Chivasso, Italy
* Author to whom correspondence should be addressed.

Academic Editors: Stefan Bosse, Ansgar Trächtler, Klaus-Dieter Thoben, Berend Denkena and Dirk Lehmhus

Received: 23 September 2016 / Revised: 17 November 2016 / Accepted: 23 November 2016 / Published: 30 November 2016

(This article belongs to the Special Issue System-Integrated Intelligence and Intelligent Systems)

Abstract

This paper presents a customizable sensing system based on functionalized nanowires (NWs) assembled onto complementary metal oxide semiconductor (CMOS) technology. The Micro-for-Nano (M4N) chip integrates on top of the electronics an array of aluminum microelectrodes covered with gold by means of a customized electroless plating process. The NW assembly process is driven by an array of on-chip dielectrophoresis (DEP) generators, enabling a custom layout of different nanosensors on the same microelectrode array. The electrical properties of each assembled NW are singularly sensed through an in situ CMOS read-out circuit (ROC) that guarantees a low noise and reliable measurement. The M4N chip is directly connected to an external microcontroller for configuration and data processing. The processed data are then redirected to a workstation for real-time data visualization and storage during sensing experiments. As proof of concept, ZnO nanowires have been integrated onto the M4N chip to validate the approach that enables different kind of sensing experiments. The device has been then irradiated by an external UV source with adjustable power to measure the ZnO sensitivity to UV-light exposure. A maximum variation of about 80% of the ZnO-NW resistance has been detected by the M4N system when the assembled 5 μ m × 500 nm single ZnO-NW is exposed to an estimated incident radiant UV-light flux in the range of 1 nW–229 nW. The performed experiments prove the efficiency of the platform conceived for exploiting any kind of material that can change its capacitance and/or resistance due to an external stimulus. View Full-Text

Keywords: CMOS interface; multipurpose sensing platform; CMOS post-processing; nanowires; nanosenors

▼ Figures

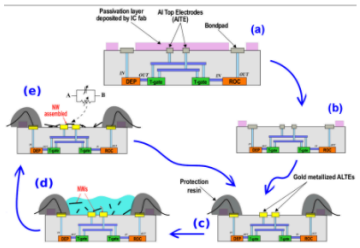

Figure 1